INCORPORATION OF 4*d* AND 5*d* TRANSITION METAL CYANOMETALLATES INTO MAGNETIC CLUSTERS AND MATERIALS

A Dissertation

by

MATTHEW GARY HILFIGER

Submitted to the Office of Graduate Studies of
Texas A&M University
in partial fulfillment of the requirements for the degree of

DOCTOR OF PHILOSOPHY

May 2010

Major Subject: Chemistry

INCORPORATION OF 4*d* AND 5*d* TRANSITION METAL CYANOMETALLATES INTO MAGNETIC CLUSTERS AND MATERIALS

A Dissertation

by

MATTHEW GARY HILFIGER

Submitted to the Office of Graduate Studies of
Texas A&M University
in partial fulfillment of the requirements for the degree of

DOCTOR OF PHILOSOPHY

Approved by:

Chair of Committee,	Kim R. Dunbar
Committee Members,	John P. Fackler
	Marcetta Y. Darensbourg
	Winfried Teizer
Head of Department,	David H. Russell

May 2010

Major Subject: Chemistry

ABSTRACT

Incorporation of 4*d* and 5*d* Transition Metal Cyanometallates into Magnetic Clusters and Materials.

(May 2010)

Matthew Gary Hilfiger, B.S., Grove City College

Chair of Advisory Committee: Dr. Kim R. Dunbar

The work presented herein describes efforts to synthesize and characterize new types of cyanide-bridged molecular materials encompassing both discrete clusters and extended solids. This investigation focused on the incorporation of anisotropic 4*d* and 5*d* transition metal ion building blocks into such materials. In this vein, systematic studies on the magnetic properties of families of these cyano-bridges species were conducted and these new materials represent a new addition to the field of cyanide chemistry incorporating for the first time the hexacyanometallates of $[Ru(CN)_6]^{3-}$ and $[Os(CN)_6]^{3-}$ into discrete molecules and extended networks. These compounds will serve as models for new theoretical studies in understanding the role of magnetic exchange interactions, both isotropic and anisotropic, in the study of nanomagnetic materials.

Results were obtained from using the well known octacyanometallates of Mo^V and W^V as building blocks for the synthesis and the magnetic investigation of both trigonal bipyramidal and pentadecanuclear clusters including the discovery of a new SMM. By expanding the research to previously unused hexacyanometallates, the

synthesis and characterization of the first known examples of clusters based on hexacyanoosmate(III) and hexacyanoruthenate(III) building blocks and their use in preparing new theoretical models of magnetic species. A novel pair of clusters is further detailed in the study of the trigonal bipyramidal clusters of $[Fe(tmphen)_2]_3[Os(CN)_6]_2$ and $[Fe(tmphen)_2]_3[Ru(CN)_6]_2$ and an in depth study of the CTIST behavior of these clusters using Mössbauer spectroscopy, variable temperature crystallography, epr, and variable temperature IR measurements. Finally, this work discusses new magnetic Prussian Blue analogs prepared from the hexacyanoosmate(III) and hexacyanoruthenate(III) anions with a comparison to the trigonal bipyramidal clusters presented based on these hexacyanoosmate(III) and hexacyanoruthenate(III) building blocks.

DEDICATION

To my wife Carolina who has been with me every step of the way. Without her love and support none of this would be possible.

> There is nothing like looking, if you want to find something. You certainly usually find something, if you look, but it is not always quite the something you were after.
>
> –JRR Tolkien

ACKNOWLEDGEMENTS

It is often said that we stand on the shoulders of giants. But it is not just giants; we are held up by our network of friends and co-workers who make our efforts possible. This being said there are a number of people whose influence and help have made a great impact on my research and career. First and foremost, I would like to thank my advisor, Prof. Kim R. Dunbar, for all of her guidance and help, as well as her patience in letting me pursue my goals. Her efforts have directly led to my success in the Ph.D. endeavor and have given me the skills to face future challenges.

I would also like to thank my committee, Prof. John P. Fackler, Prof. Marcetta Y. Darensbourg, and Prof. Winfried Teizer, for all of their support and time spent on this process.

Some of the research in this dissertation is made possible with measurements and theoretical calculations performed by our collaborators. I would like to thank Prof. Catalina Achim and Meimei Chen for all of their help over these past 4 years in making measurements and analyzing the highly complex behavior of the material presented in Chapter IV. I would especially like to thank them for graciously hosting me in my visit to their lab to understand the unique requirements of the Mössbauer measurements and sample preparation which they use. In addition I would like to thank Prof. Jan Musfeldt and Tatiana Brinzari for performing variable temperature IR analysis of the material presented in Chapter IV, as well as the theoretical contribution performed by Profs. Boris Tsukerblat and Sophia Klokisner and Drs. Andrey Palii and Sergei Ostrovsky

which was crucial in understanding the underlying exchange interactions in the work presented in Chapter III. Additionally I would like to thank Dr. Hanhua Zhao for all of his help especially in my first project which is explained in Chapter II. Finally, I would like to thank Dr. Nattamai Bhuvanesh for help with fitting the powder X-ray data in Chapter V and Dr. Wolfgang Wernsdorfer for the micro-SQUID measurements presented in Chapter II.

I am especially grateful to the close knit Dunbar group for all their help and support over the years, especially Prof. Michael Shatruk for his help and guidance in the beginning of this project; the members of the magnetic materials subgroup Ferdi Karadaş, Carolina Avendaño, Kristen Funck, and Dr. Andrey Prosvirin for all of those useful discussions and brainstorming sessions; and Daphne Aguirre and Alfredo Angeles for their great help and support over the years here. I would also like to thank the other members of the group for their advice and in providing the great atmosphere that we all enjoy working in, Dr. Hanhua Zhao, Dr. Helen Chifotides, Dr. Xinyi Wang, Dr. Akira Ota, Nazario López, Edward Funck, Ian Giles, Sarah Lane, Heather Southerland, Zhongyue Zhang, Darryl Stepien, and Codi Sanders.

I would also like to thank those whose work helped to guide me into this field in the first place, my undergraduate research advisor Dr. Harold Conder, whose confidence in me and tireless patience in teaching me the many skills necessary to prepare me for graduate school have been priceless. For steering me to chemistry in the first place, my high school chemistry teacher John Summerville has made a profound impact, where

despite teaching both chemistry and physics he always took some extra time to teach me a little more whenever I would bother him with all of my questions.

Finally, none of this would be possible without the strong network of support of my family. My parents Gary and Sharon have always been there to support me, listening to more than their fair share of my complaints; to my family here in College Station, Raul Avendaño and Angela Mejia, who have always been there for me; and to my family in Colombia, specially Raul, Luz Marina, and Dario for all their kind support through the last years. Most importantly though, I want to thank my wife, Carolina, who has been there with me every step of the way, both inside the lab and out.

TABLE OF CONTENTS

TABLE OF CONTENTS (CONT'D)

TABLE OF CONTENTS (CONT'D)

LIST OF TABLES

LIST OF TABLES (CONT'D)

LIST OF SCHEMES

LIST OF FIGURES

LIST OF FIGURES (CONT'D)

LIST OF FIGURES (CONT'D)

LIST OF FIGURES (CONT'D)

FIGURE Page

LIST OF FIGURES (CONT'D)

FIGURE Page

LIST OF FIGURES (CONT'D)

LIST OF FIGURES (CONT'D)

LIST OF FIGURES (CONT'D)

FIGURE Page

LIST OF FIGURES (CONT'D)

LIST OF COMPOUNDS

(1) $[Ni^{II}(tmphen)_2]_3[W^{V}(CN)_8]_2 \cdot 8CH_3OH \cdot 2H_2O$

(2) $[Ni^{II}(tmphen)_2]_3[Mo^{V}(CN)_8]_2 \cdot 5CH_3CN \cdot 8H_2O$

(3) $[Ni^{II}_9(tmphen)_6(CH_3OH)_6(H_2O)_6W^{V}_6(CN)_{48}] \cdot 6DMF$

(4) $[Ni^{II}_9(tmphen)_6(CH_3OH)_6(H_2O)_6Mo^{V}_6(CN)_{48}] \cdot 6DMF$

(5) $K_4Os(CN)_6$

(6) $K_4Ru(CN)_6$

(7) $[PPN]_3[Os(CN)_6]$

(8) $[PPN]_3[Ru(CN)_6]$

(9) $[Ni(tmphen)_2]_3[Os(CN)_6]_2 \cdot 12H_2O$

(10) $[Ni(tmphen)_2]_3[Ru(CN)_6]_2 \cdot 12H_2O$

(11) $[Mn(tmphen)_2]_3[Os(CN)_6]_2 \cdot 8H_2O$

(12) $[Mn(tmphen)_2]_3[Ru(CN)_6]_2 \cdot 8H_2O$

(13) $[Cr(tmphen)_2]_3[Ru(CN)_6]_2 \cdot 8MeCN$

(14) $[Co(tmphen)_2]_6[Ru(CN)_6]_3$

(15) $[Fe(tmphen)_2]_3[Os(CN)_6]_2$

(16) $[Fe(tmphen)_2]_3[Ru(CN)_6]_2$

(17) $Mn_3[Os(CN)_6]_2 \cdot 18H_2O$

(18) $Mn_3[Ru(CN)_6]_2 \cdot 22H_2O \cdot MeOH$

(19) $Fe_3[Os(CN)_6]_2 \cdot 19H_2O$

(20) $PPN_{0.6}Fe_{2.7}[Ru(CN)_6]_2 \cdot 14H_2O \cdot 2MeCN$

LIST OF COMPOUNDS (CONT'D)

(21) $Ni_3[Os(CN)_6]_2 \cdot 20H_2O \cdot 2MeCN$

(22) $Ni_3[Os(CN)_6]_2 \cdot 20H_2O \cdot MeOH$

(23) $Ni_3[Os(CN)_6]_2 \cdot 4H_2O$

(24) $Ni_3[Ru(CN)_6]_2 \cdot 20H_2O \cdot MeCN$

(25) $PPN_{0.2}Ni_{2.9}[Ru(CN)_6]_2 \cdot 16H_2O \cdot 2MeOH$

(26) $Ni_3[Ru(CN)_6]_2 \cdot 20H_2O \cdot 2MeOH$

CHAPTER I

INTRODUCTION

Collaborative research in chemistry and physics over the past two decades has spawned a major renaissance in the study of paramagnetic molecules and arrays. Arguably one of the most important discoveries in this period is the recognition of nanoscale magnetism in molecules and molecule based solids. One of the most active areas of research in molecular magnetism is that of cyanide molecules and solids. As an illustration of how rapidly research in cyanide materials has advanced, it is interesting to note that thirteen years ago, Dunbar and Heintz published a review chapter on "Modern Perspectives of Cyanide Chemistry" in the monograph series, *Progress in Inorganic Chemistry*[1] in which there were only several notable citations of magnetic properties of cyanide clusters at that time. In 2009 Shatruk, Avendano, and Dunbar published a second review for the same book series on developments in cyanide magnetism in which they limited the content to only discrete paramagnetic cyanide compounds due to the enormous amount of material. The article is a comprehensive coverage of molecular cyanide compounds up to mid 2008 with applications in molecular magnetism and includes 275 references.[2]

In addition to discrete clusters based on cyanide bridge there are many recent examples ranging from 1-D chains,[3, 4] 2-D,[5, 6] and 3-D[7-10] networks that exhibit a variety of properties ranging from high T_c values, spin crossover, photomagnetism, charge

---

This dissertation follows the style of the *Journal of the American Chemical Society*.

transfer induced spin transitions (CTIST), hydrogen storage materials, antidotes to radioactive poisoning, and single molecule magnetism. As is the case with many scientific discoveries, this rich field of cyanide chemistry is based on serendipity, in this case it is the accidental discovery of Prussian Blue over 300 years ago.

Prussian Blue Analogs

One of the earliest studied molecule-based magnetic materials is Prussian Blue (PB), $Fe_4[Fe(CN)_6]_3 \cdot 14\text{-}16H_2O$, a 3-dimensional solid based prepared from a simple reaction of soluble molecules, Fe^{III} and $[Fe(CN)_6]^{4-}$ ions. Prepared by the Berlin artist Diesbach in 1703 as a pigment[11], it is one of the oldest synthetic coordination compounds recorded. Historical accounts tell the story that when Diesbach was attempting to make red dye of cochineal, the chemist that he was working with, Dippel, provided him with potash which had been contaminated with animal blood.[12] When Diesbach attempted to prepare the red dye, much to his surprise, an insoluble dark Blue precipitate formed, soon to be dubbed Prussian Blue. The dye was an instant success in terms of uses in panting and other applications, due to the fact that it was much cheaper than alternatives derived from indigo and mineral sources, such as aquamarine, and more importantly because its color never faded. Diesbach and his apprentices were the only manufacturers of Prussian Blue until a full recipe was published by Woodward nearly 20 years later.[13] Since then the dye has enjoyed remarkable success as a paint pigment, being used by many prominent artists such as Hokusai and Picasso in his blue period (Figure 1), as well as the many magnetic properties which have been previously mentioned. It was not until 1814, after the realization that cyanide was composed of only

Figure 1. Examples of paintings incorporating the Prussian Blue pigment.[13,14]

carbon and nitrogen, that a purely inorganic route was envisioned for the synthesis of PB. The reaction of charcoal, potash, and iron fillings in atmospheric nitrogen led to the formation of the ferrocyanide ion, which was further reacted with ferric salts leading to a more standard procedure for the preparation of Prussian Blue.[14] Of course, these days a much more facile synthesis is available, through the direct reaction of potassium ferrocyanide with Fe salts (Scheme 1).

Prussian Blue's attraction, however, is not only limited to its use as a pigment, but also from its optical and magnetic properties which have been heavily investigated. At Bell labs in 1956 a half page paper with the simple title *New Low Temperature Ferromagnets* was published. The subject of the study, Prussian Blue, was shown to order at 5.6K.[15] This rather unassuming paper was the first example of a ferromagnet based on a coordination compound, and it spawned the field of modern cyanide chemistry. As the field of molecular magnetism progressed, the desire to understand the magnetic properties of such materials grew and the development of theoretical methods to explain existing properties and predict new ones became a priority.

In general, molecular magnets share some similar behavior to their bulk magnet counterparts, which come from three different scenarios: (a) A ferromagnet where neighboring spins align in a parallel fashion with the magnetic field and retain their directionality even when the field is removed; (b) An antiferromagnet wherein the spins of neighboring centers couple in an antiparallel fashion leading to a total cancellation of spin; and (c) A ferrimagnet where the neighboring spins are antiferromagnetically coupled, but due to differing numbers of electrons between the two, do not completely

Scheme 1. General synthetic scheme of Prussian Blue analogs, M' = V,Cr, Fe, Co, M = V, Cr, Mn, Fe, Ni , L = labile ligand or solvent molecule.

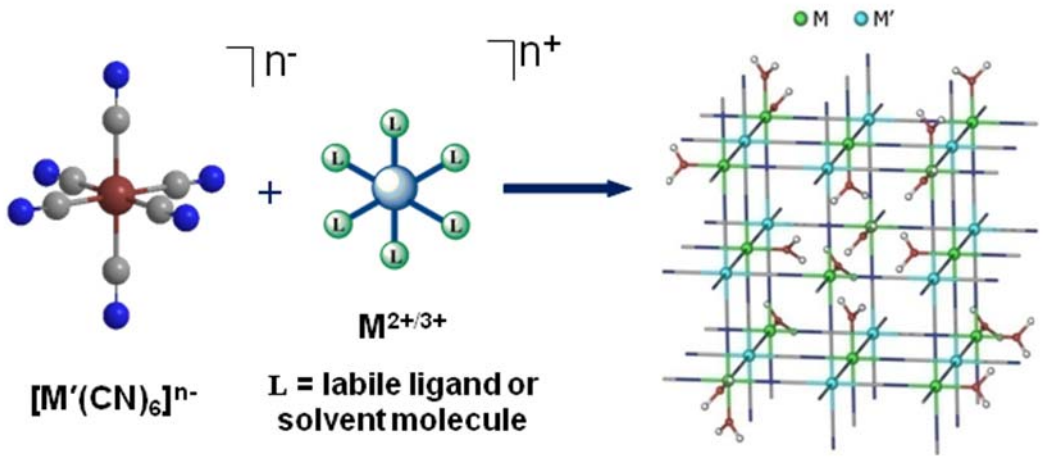

cancel, and the remaining unpaired spins align with the field as a ferromagnet does (Scheme 2a). Although these magnetic properties were first studied in bulk minerals, Goodenough and Kanamori developed simple rules governing the expected ferromagnetic or antiferromagnetic coupling of complexes that could be extended to molecular systems. Regardless of the type of magnetic materials however, a pathway must exist for spin-spin interactions to take place. This can be provided by a direct bond or through a bridging ligand, and the strength of the interactions is described by an exchange coupling constant *J*, which may be negative or positive. For the typical convention which is used in our group, H = -2*J* where *J* is negative for antiferromagnetic coupling and positive for ferromagnetic coupling. These rules worked quite well especially for cyanide based materials owing to the small size of the bridging linker which aids in stronger coupling, and the relative simplicity in understanding the orbital interactions of the metal center with the empty π orbitals of the cyanide ligand (Scheme 2b).

The exchange model for Prussian Blue materials can be phenomenologically rationalized from the orbital overlap of the metals (in this case in an idealized O_h symmetry) with the cyanide ligand. A M'-C≡N-M system in which unpaired electrons in the neighboring metal centers are in orthogonal orbitals, for example one metal having unpaired electrons solely in the t_{2g}, (d_{xy}, d_{xz}, d_{yz}) orbitals while the other metal has only unpaired electrons in the e_g, (d_{z2}, d_{x2-y2}) orbitals, will by the Goodenough-Kanamori

Scheme 2. (a) A schematic representation of the different types of magnetic ordering and (b) orbital depiction of the exchange pathway through the π* orbitals of the cyanide ligand.

(a)

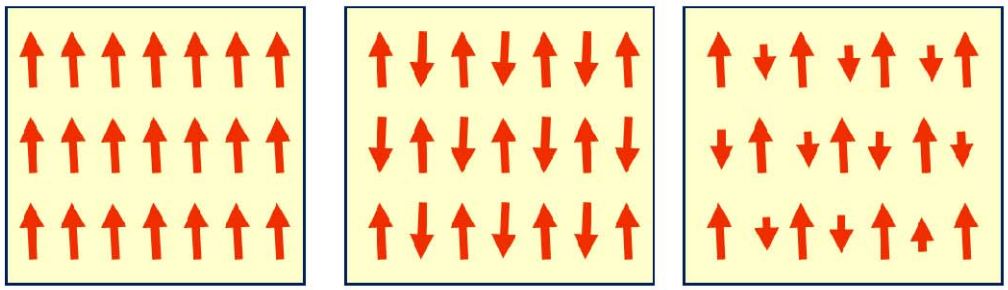

ferromagnet

Long-range ordering, metal centers coupled ferromagnetically with all moments magnetized in the direction of the magnetic field and has net magnetization.

antiferromagnet

Long-range ordering, metal centers coupled antiferromagnetically, moments are aligned antiparallel, hence, no net magnetization

ferrimagnet

Metal centers coupled antiferromagnetically, but there is not total spin cancellation. Remaining moments are magnetized in the direction of the field and there is net magnetization.

(b)

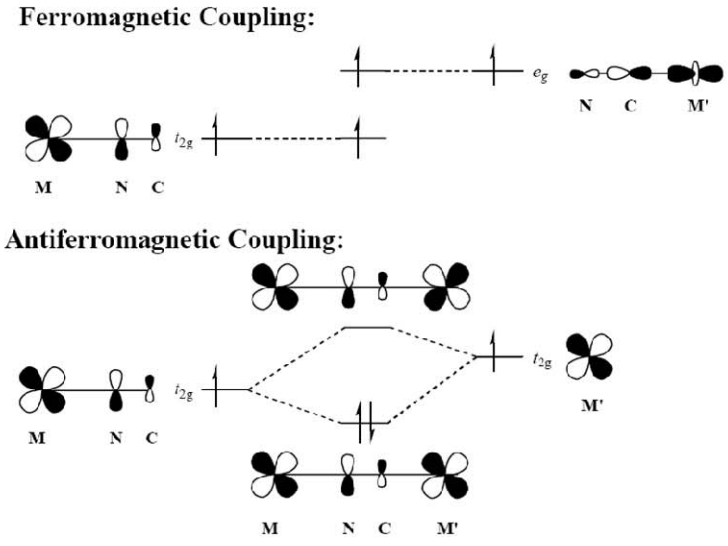

rules, lead to ferromagnetic coupling (Scheme 2b). Conversely, for systems in which there are available unpaired electrons in only the t_{2g} orbitals, this non orthogonality leads to a spin paired antiferromagnetic ground state. By applying this simple "rule of thumb", complexes can be designed to provide specific interactions, for example: (a) $Ni_3[Fe(CN)_6]_2$ PB[16] with Fe^{III}, $t_{2g}^5eg^0$ and Ni^{II}, $t_{2g}^6e_g^2$ can only engage in ferromagnetic interactions. (b) $KV[Cr(CN)_6]$ PB[10], where there are only unpaired electrons in the t_{2g} orbitals V^{II}, t_{2g}^3, and Cr^{III}, t_{2g}^3, or (c) $Cs_2Mn[V(CN)_6]$ PB[17] which has competing numbers of ferromagnetic and antiferromagnetic interactions with are unpaired electrons in both the t_{2g} and e_g orbitals of the Mn^{II} ion ($t_{2g}^3eg^2$) and t_{2g} spins in the V^{II} (t_{2g}^3). The application of the Goodenough-Kanamori rules in the description of the exchange pathway in these systems is not only useful for Prussian Blue analogs, but can also be extended to discrete clusters and other low dimensional solids. The ability to easily tune the properties by judicious choice of metal ions and capping ligands has led to the formation of a number a species with wealth of properties.[2, 18, 19]

This simplified approach to magnetic interactions works well for the majority of Prussian Blue analogs, however it does not work for the original Prussian Blue. Using the Goodenough-Kanamori rules, one would expect almost no exchange interaction to take occur, as the Fe^{III} sites are interacting with nearest neighbor diamagnetic $[Fe^{II}(CN)_6]^{4-}$ ions. This analysis would seemingly lead to a hypothesis of a paramagnetic solid of isolated Fe^{III} ions. As previously mentioned however, the solid does in fact order at 5.6K. The early work of Peter Day on this issue, focused on the mixed valency

of the material, where he was able to show that this electronic property was what gave rise to the weak ferromagnetic ordering.[20]

Since this initial discovery, much work has been accomplished in the synthesis of new molecular magnets from Prussian blue analogs. The PB solids which exhibit the highest ordering of any known Prussian Blue analogs are shown in Table 1. One of the initial discoveries of these high T_c magnets was by Girolami and Ently in 1995,[17] who reacted $[V^{II}(CN)_6]^{4-}$ with Mn^{II} ions to yield $Cs_2Mn^{II}[V^{II}(CN)_6]$, which orders at 230K. At the same time Verdaguer *et al.*[21] reported a Prussian Blue analog that orders at 315K formulated as $V^{II}_{0.42}V^{III}_{0.58}[Cr^{III}(CN)_6]_{0.86}\cdot 2.8H_2O$ (Figure 2a). The problem with these reported 3D magnets, are that they are amorphous solids, precluding the collection of structural data by powder diffraction. Through the use of sol-gel processes Girolami and Holmes were able to prepare a micro-crystalline Prussian Blue complex formulated as $KV^{II}[Cr^{III}(CN)_6]\cdot 2H_2O\cdot 0.1KOTf$, which, to this date, exhibits the highest ordering temperature of any PB, 376K (Figure 2b), making it the only molecular based magnet stable above the boiling point of water.[10]

In addition to finding new high temperature magnets, one of the most widely studied phenomenon of the PB family, is in the magnetic bistability exhibited by some analogs. For example, $K_{0.2}Co_{1.4}[Fe(CN)_6]6.9H_2O$,[22] and $Rb_{0.91}Mn_{1.05}[Fe(CN)_6]\cdot 0.6H_2O$,[23] exhibit bistability governed by charge transfer induced spin transitions, (CTIST) and the bistability of $CsFe[Cr(CN)_6]\cdot 1.3H_2O$[24] is governed by spin crossover. Application of additional external stimuli, such as light allowed for the discovery of photomagnetism in the $K_{0.2}Co_{1.4}[Fe(CN)_6]6.9H_2O$ PB, first observed

Table 1. List of high T_c Prussian Blue analogs and their ordering temperatures.

MM'	Compound	Configuration	T_c	Ref.
$Cr^{III}V^{II}$	$KV[Cr(CN)_6]\cdot 2\ H_2O$	$t_{2g}^3–t_{2g}^3/t_{2g}^2$	376	10
$Cr^{III}V^{II}/V^{III}$	$K_{0.058}V[Cr(CN)_6]_{0.79}(SO_4)_{0.058}$	$t_{2g}^3–t_{2g}^3/t_{2g}^2$	372	27
	$K_{0.50}V[Cr(CN)_6]_{0.95}\cdot 1.7\ H_2O$	$t_{2g}^3–t_{2g}^3/t_{2g}^2$	350	27
	$V[Cr(CN)6]_{0.86}\cdot 2.8\ H_2O$	$t_{2g}^3–t_{2g}^3/t_{2g}^2$	315	21
	$V[Cr(CN)_6]_{0.69}(SO_4)_{0.23}\cdot 3.0\ H_2O$	$t_{2g}^3–t_{2g}^3/t_{2g}^2$	315	28
$Cr^{III}Cr^{II}$	$[Cr_5(CN)_{12}]\cdot 10\ H_2O$	$t_{2g}^3–t_{2g}^3e_g^1$	240	29
$Mn^{II}V^{II}$	$(Et_4N)_{0.5}Mn_{1.25}[V(CN)_5]\cdot 2H_2O$	$t_{2g}^3\ e_g^2–t_{2g}^3$	230	17

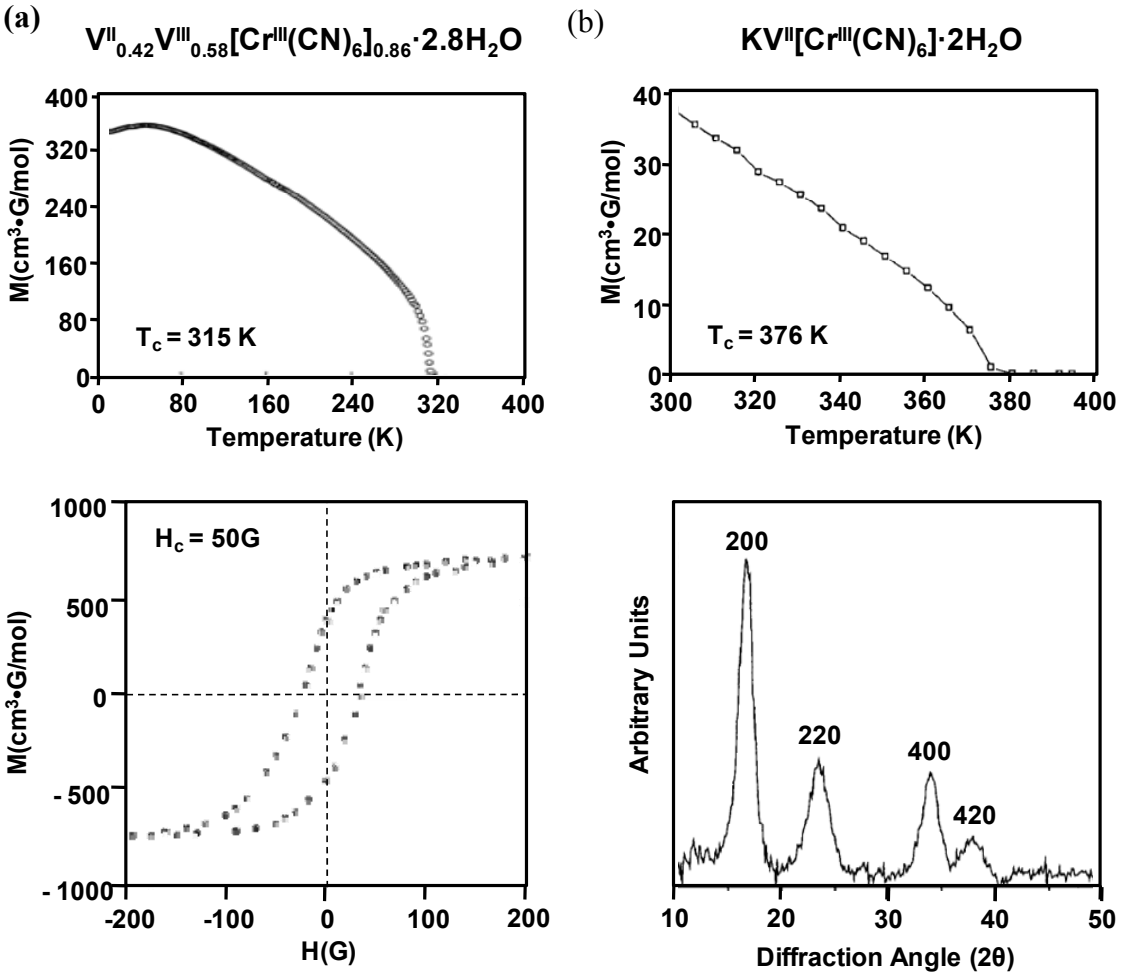

Figure 2. Magnetic data for the ordering of the Prussian Blue analogs (a) $V^{II}_{0.42}V^{III}_{0.58}[Cr^{III}(CN)_6]_{0.86}\cdot 2.8H_2O$, Tc = 315K, Hc = 50G. and (b) $KV^{II}[Cr^{III}(CN)_6]\cdot 2H_2O\cdot 0.1KOTf$, T_c = 376K, with the powder diffraction data. (Adapted from Verdaguer *et al.*,[21] and Girolami *et al.*[10])

nearly simultaneously by Hashimoto *et al*.[25] and by Verdaguer[26]. This material exhibits a CTIST around 250K corresponding to a change from $Fe^{III}_{L.S.}$-$Co^{II}_{H.S.}$ at room temperature to $Fe^{II}_{L.S.}$-$Co^{III}_{L.S.}$ at low temperatures. Irradiation at low temperatures leads to a photomagnetic state wherein the material is excited back to the $Fe^{III}_{L.S.}$-$Co^{II}_{H.S.}$ configuration observed at room temperature (Figure 3). Further work by Ohkoshi also showed this phenomenon occurs in the $Rb_{.91}Mn_{1.05}[Fe(CN)_6]\cdot 0.6H_2O$ PB material. [23] More recently, bistability due to spin crossover in the $CsFe^{II}[Cr^{III}(CN)_6]1.3H_2O$ Prussian Blue was also demonstrated by Ohkoshi *et al*. The Fe^{II} sites in the Prussian Blue material undergo a high spin to low spin transition in with a wide thermal hysteresis over the temperature range from 200-250K.[24] In all of these cases, these materials are highly sensitive to the ratio of the metal ions used in the reaction, as well as the alkali metal cation present, which in some cases, dramatically affects the properties of the system (Figure 4).[30]

Overall, the synthesis of Prussian Blue and its analogs has yielded a wide range of compounds that exhibit a wide range of interesting and useful properties as described above. The promise of discovering new analogs with as yet unexplored cyanometallate ions, as well as the ability to combine multiple properties into one material is high. Importantly, in addition to their extraordinary magnetic and photomagnetic properties, [23, 25] they have also seen widespread study as hydrogen storage materials, [31] as well as antidotes for radiation poisoning. [32, 33] With all this in mind, Prussian Blue is, as Andreas Ludi so eloquently stated, an “Inorganic Evergreen”.[34]

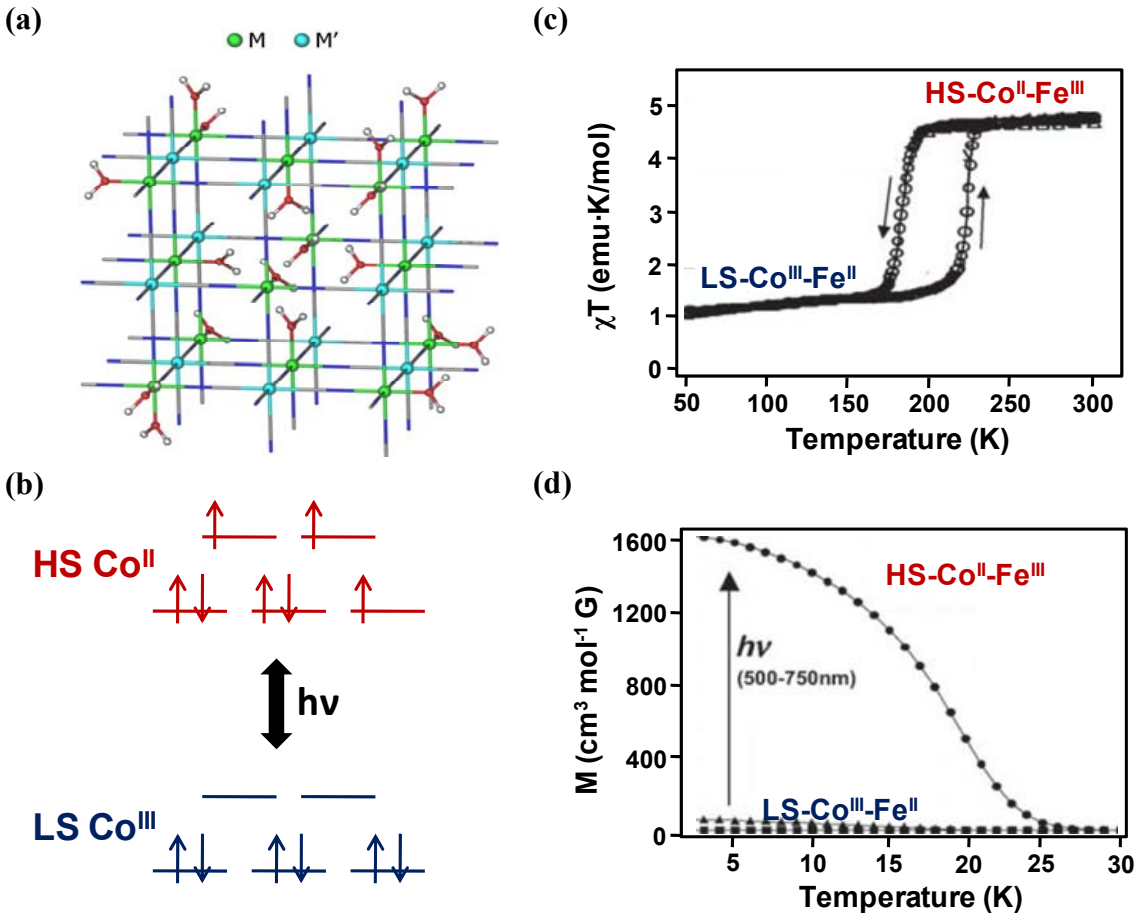

Figure 3. Photomagnetism in $Co_x[Fe(CN)_6]_y$ PB: (a) idealized structure; (b) electron transfer coupled with spin state change in Co; (c) thermal hysteresis in the CTIST and (d) photomagnetic behavior stable until 25K. (Adapted from Sato *et al.*[22])

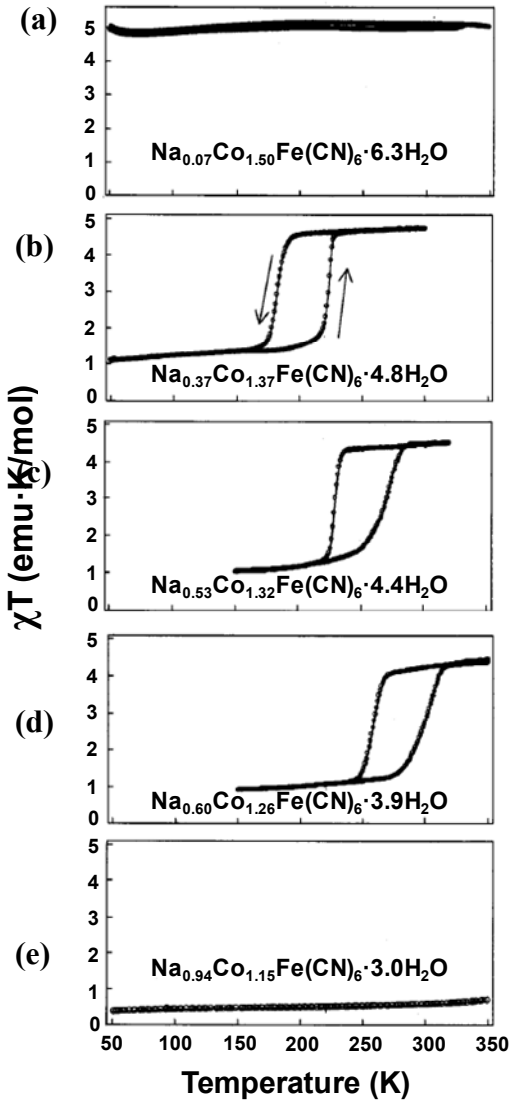

Figure 4. Cation ratio dependence on CTIST for $Co_x[Fe(CN)_6]_y$ PB. Decreasing Co content causes a change from (a) H.S. Co^{II} stable over all temperatures, to (b) thermal hysteresis centered at 200K, continuing to (c) thermal hysteresis centered at 250K, (d) following with thermal hysteresis centered at 280K and finally to a (e) complete L.S. Co^{III} at all temperatures. (Adapted from Ohkoshi *et al.*[30])

Cyanide Bridged Discrete Clusters as Models for Prussian Blue Analogs

Clearly Prussian Blue and its analogs exhibit a rich chemistry, but there are some drawbacks. These materials are often amorphous, and single crystals are rarely obtained for structure-property correlations. In order to take advantage of the remarkable properties exhibited by Prussian Blue analogs, many groups have turned to the use of cyanometallates as building blocks in combination with convergent metal precursors, i.e. metal centers with capping ligands to prevent the formation of extended networks. This approach allows for the isolation of stochiometrically pure complexes with well defined structures that exhibit the full range of physical properties including as spin crossover, charge transfer induced spin transitions, and photomagnetism.[2]

Spin Crossover

Spin crossover was first observed by Cambi *et al*. for the tris(N,N-dialkyl-dithiocarbamatoiron^{III} complexes in 1931.[35] Since then, a majority of the complexes studied have been based on Fe^{II}, especially the $Fe(phen)(NCS)_2$ complex reported by König and Madeja in 1961 and its subsequent derivatives.[36] This research has been greatly aided by the discovery of the Mössbauer technique which can monitor changes in the oxidation states of the Fe centers. The development of this technique has led to a great deal of study in spin crossover, incorporating a variety of clusters and extended solids which exhibit this phenomenon.[37-39]

The spin crossover transition takes place when an external stimulus such as pressure, temperature, or light, induces a change in the delicate balance in the ligand field environment, which leads to a change in the electronic configuration of the metal

centers from a high spin to a low spin state or vice versa. This phenomenon can most easily be studied by analyzing the magnetic properties where the change in Fe^{II} from a paramagnetic H.S. state, S = 2, to a low spin diamagnetic S = 0 ground state. The most useful technique for precise measurements is Mössbauer spectroscopy, which provides quantitative percentages of the population of various oxidation and spin states of Fe at a given temperature. While the spin transition occurs at the molecular level, in order to exhibit true bistability the effect must be propagated throughout the solid, an effect known as cooperativity.[40] By increasing the cooperativity it is possible to take a transition from broad, to sharp, and in some cases open up a hysteresis loop (Figure 5). In order to have high cooperativity, the Fe centers must be able to 'feel' the effects of the change of nearby Fe centers, by "mechanical" coupling through direct bonding or intermolecular forces which can propagate the changes in the metrical parameters at the Fe sites. As such, in order to increase this cooperativity one approach is the design of molecular clusters with more than one metal center that can undergo the transition. The use of cyanide based building blocks offer such possibility due to the relative ease of designing molecular systems of a desired geometry. Such examples of this approach have been shown previously by Dunbar *et al*. in the $[Fe(tmphen)_2]_3[Fe(CN)_6]_2$ and $[Fe(tmphen)_2]_3[Co(CN)_6]_2$ (tmphen = 3,4,7,8 tetramethylphenanthroline) trigonal bipyramidal clusters,[37] where the equatorial Fe^{II} sites undergo a spin transition centered near 280K (Figure 6a). In addition, the $[Fe(bpy)_2CN]_4$ square of Oshio *et al*. (Figure 6b),[41] engages in a two step spin transition where the transition occurs independently over two different temperature ranges in the two unique Fe sites. Not surprisingly most

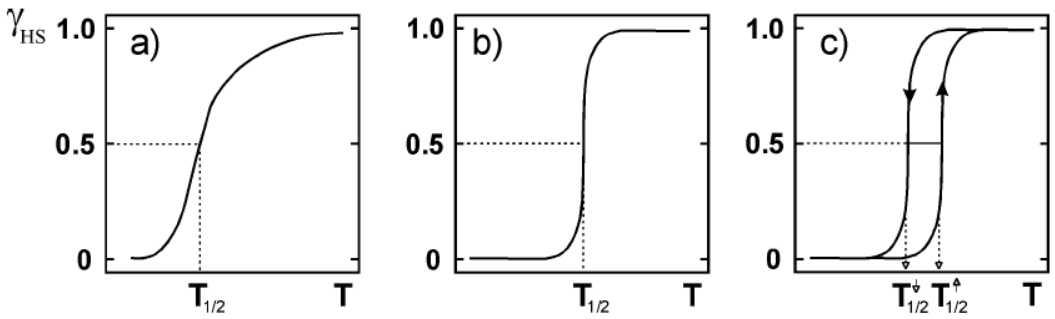

Figure 5. Examples of increasing cooperativity, from left to right: (a) gradual transition, (b) sharp transition, and (c) sharp transition with hysteresis. (Adapted from Gütlich *et al*.[39])

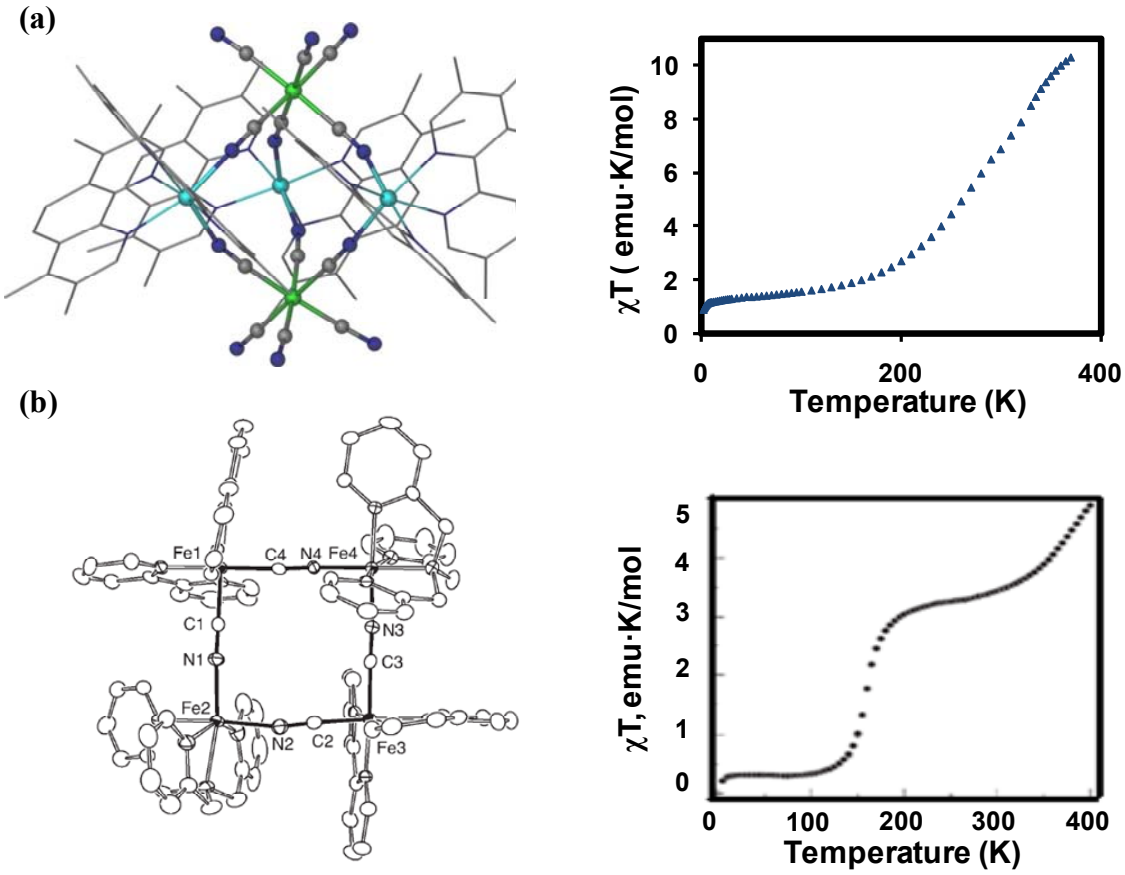

Figure 6. (a) $Fe^{II}_3Fe^{III}_2$ TBP exhibiting spin crossover behavior with a gradual transition centered at 280K. (b) Fe_4 square exhibiting a two step spin transition. (Adapted from Dunbar *et al*.[37] and Oshio *et al*.[41])

efforts in the area of new SCO materials focus on increasing the cooperativity such that the transition occurs at or very near room temperature with hysteresis. Devices based on spin crossover complexes have already been prepared and continue to play a leading role in fueling further development in the area of molecule based magnetic materials (Figure 7).[42]

Charge Transfer Induced Spin Transition (CTIST) and Photomagnetism

The charge transfer induced spin transition phenomenon was first observed for the $Co_x[Fe(CN)_6]_y$ and $RbMn[Fe(CN)_6]_y$ Prussian Blue Analogs.[22, 23, 26]and has been widely studied in these materials. Such solids exhibit a reversible electron transfer from the room temperature configuration in $Co_x[Fe(CN)_6]_y$ PB, where the Fe^{III}-Co^{II} pair converts to Fe^{II}-Co^{III} at low temperatures, an event accompanied by a change in the spin state of the Co ions from H.S. to L.S (Figure 3). The properties of these Prussian Blue analogs are highly dependent on moisture content, metal ratios, and alkali metal content. A change in these conditions lead to a broad spectrum of behavior for the materials, where only high spin Co^{II} is present, to only low spin Co^{III} being present, and a wide range of CTIST temperatures and thermal hysteresis widths between those two extremes, (Figure 4).

In order to carefully study this phenomenon in microscopic detail it is imperative to be able to correlate the structure with the magnetic properties. To achieve this situation it is necessary to prepare discrete molecules as models for $Co_x[Fe(CN)_6]_y$ PB materials. The first example in this class is the $[Co(tmphen)_2]_3[Fe(CN)_6]_2$ TBP cluster reported by Dunbar *et al*., in 2004 which engages in charge transfer between the Fe^{III} and

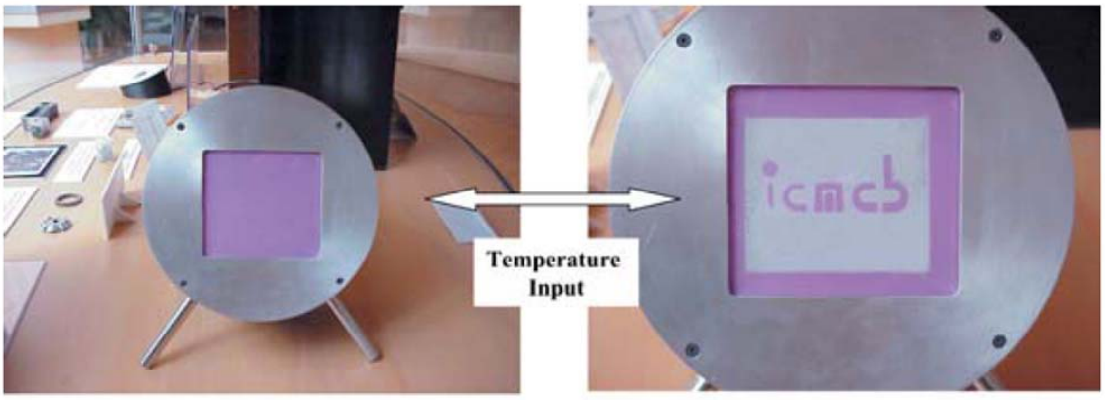

Figure 7. A display device based on thermally induced spin crossover (Adapted from Létard *et al*.[42])

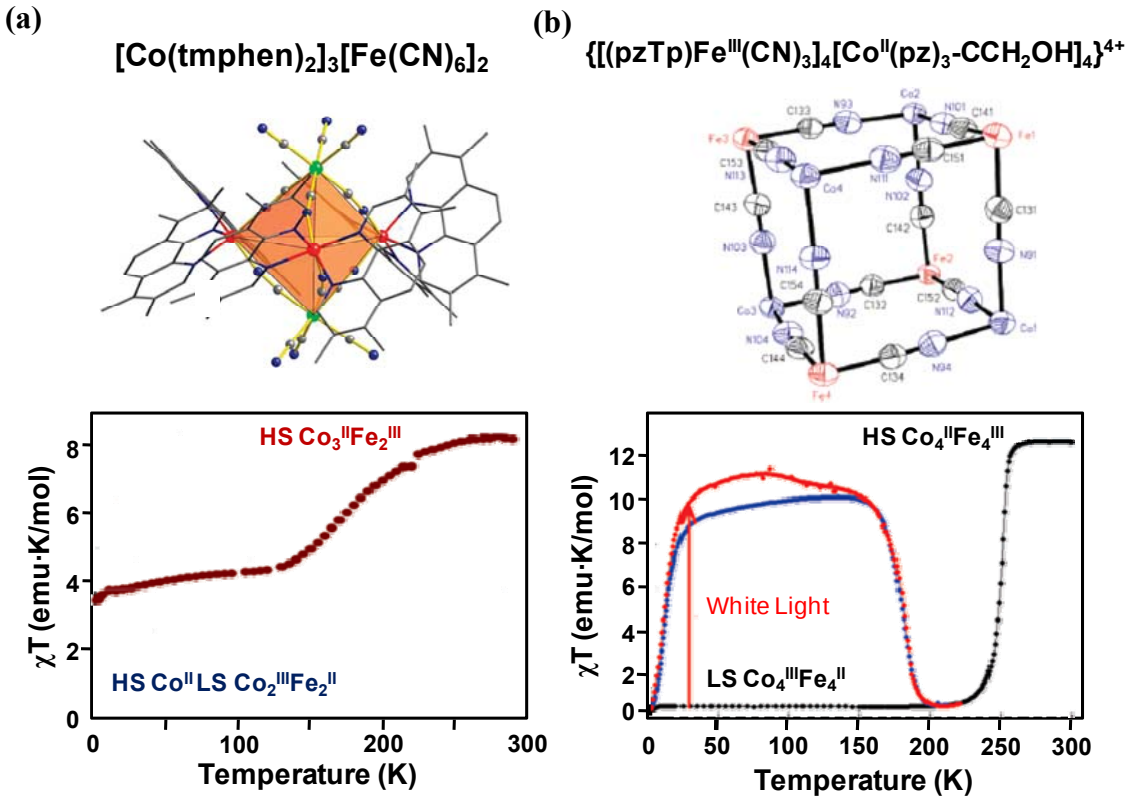

Figure 8. (a) CTIST behavior for $[Co(tmphen)_2]_3[Fe(CN)_6]_2$ TBP and (b) $\{[(pzTp)Fe^{III}(CN)_3]_4[Co^{II}(pz)_3\text{-}CCH_2OH]_4[ClO_4]_4\}$ square, the latter shows a sharp transition at 250K and photomagnetism stable up to 200K. (Adapted from Dunbar *et al*.[44] and Holmes *et al*.[45])

Co^{II} centers (Figure 8a).[43, 44] More recently a cube based on the same metal ions, $[(pzTp)Fe^{III}(CN)_3]_4[Co^{II}(pz)_3\text{-}CCH_2OH]_4[ClO_4]_4$ was prepared by Holmes *et al* which exhibits a sharp CTIST near 250K (Figure 8b).[45]

In addition to reversible CTIST behavior, the $Co_x[Fe(CN)_6]_y$ analogs may also exhibit photomagnetism, where light can induce the low temperature configuration to be converted to a metastable state identical to the room temperature configuration. This photomagnetic state in the PB phases is stable up to 150K in some cases and has been observed for the aforementioned discrete model compounds as well. To this date, molecular analogs of the $RbMn[Fe(CN)_6]$ Prussian Blue, such as those represented by the trigonal bipyramidal cluster $\{[Mn(tmphen)_2]_3[Fe(CN)_6]_2\}$, have not shown any CTIST or photomagnetic behavior.[46]

Single Molecule Magnetism (SMM)

Origins of SMM Behavior

The research presented previously highlights the success that has been made in synthesizing molecular models of Prussian Blue analogs which mimic the properties of the bulk materials. While these molecular analogs are able to exhibit related phenomena, it was not thought that single molecules could model the ability of Prussian Blue analogs to behave as magnets below a critical temperature. Bulk magnets, even those which are synthesized from molecular building blocks, have magnetic domains, which give rise to the ability of the materials to be magnetized through classical mechanisms of domain wall movement and collapse (Figure 9a). Even by decreasing the size to a single domain particle (Figure 9b), magnetic behavior can still be observed.

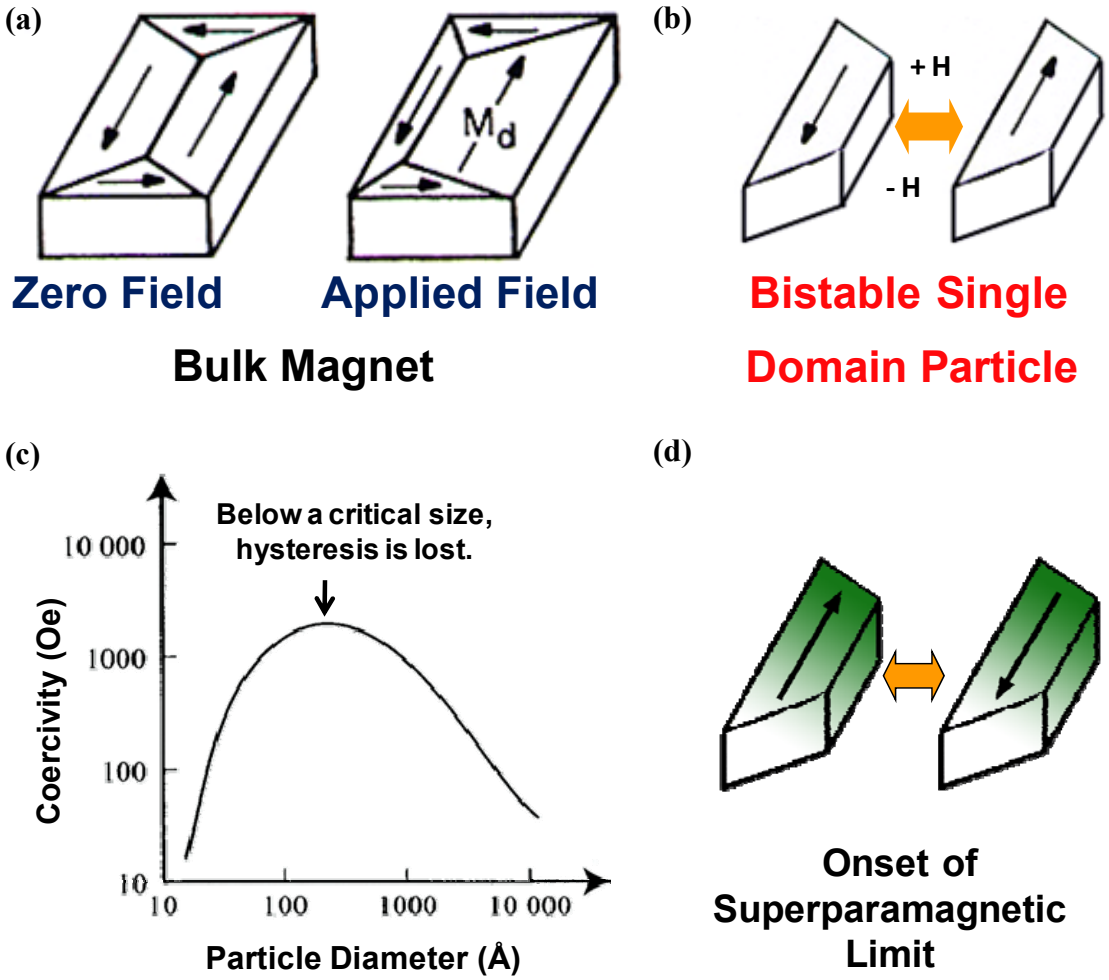

Figure 9. (a) Magnetization of a bulk magnet via domain wall movement and collapse in an applied field. As size decrease to a certain limit, a particle consisting of (b) a single domain can form, which is the smallest size that can exhibit bulk magnetism. Particle size vs. coercivity: below a certain size threshold (c), the superparamagnetic limit is reached where (d) the particle acts as one spin in an applied field, however there is no temperature below which the magnetization is blocked, i.e they behave as paramagnets with no remnant magnetization at zero field. (Adapted from Spaldin[48])

Due to an inherent energy barrier based on the anisotropy and the volume as demonstrated by Néel,[47] E = KV where K is the anisotropy constant and V is the size of the particle, a critical limit in the barrier of the magnetization can be reached where it is equivalent with the thermal bath of its surroundings, thereby losing permanent magnetization (Figure 9c). With this decrease in size, any given material below some threshold size value, will only behave in what is referred to as a superparamagnet, in which there is a large magnetic response in the direction of the applied field, however no remnant magnetization at zero field (Figure 9d).

With this scenario in mind, a major breakthrough occurred in 1993 when a single molecule was shown to exhibit magnetic bistability[49], defying classical magnetic theory. It is not classical behavior, however, that is responsible for this phenomenon, as explained in the next passage. Moreover in going from extended phases to the molecular level, there is an onset of quantum behavior and classical effects become less prevalent.

The first compound found to exhibit this peculiar behavior is the by now well known Mn_{12} acetate molecule (Figure 10a), $Mn_{12}O_{12}(O_2CCH_3)_{16}(H_2O)_4$, first synthesized by Lis in 1980.[50] In 1993 the Gatteschi group in Florence, shortly followed by the Christou and Hendrickson groups in 1994, reported the observation of magnetic bistability for this cluster, giving birth to the field of single molecule magnetism (Figure 10b).[49, 51] The bistability is achieved by the existence of a barrier to the reversal of magnetization (Figure 10c), which is a necessary prerequisite for single molecule magnetism. This barrier is given by the formula $\Delta E = S^2|D|$ and $(S^2\text{-}1/4)|D|$ for integer and half-integer spin molecules, respectively. The ground state spin value of the cluster

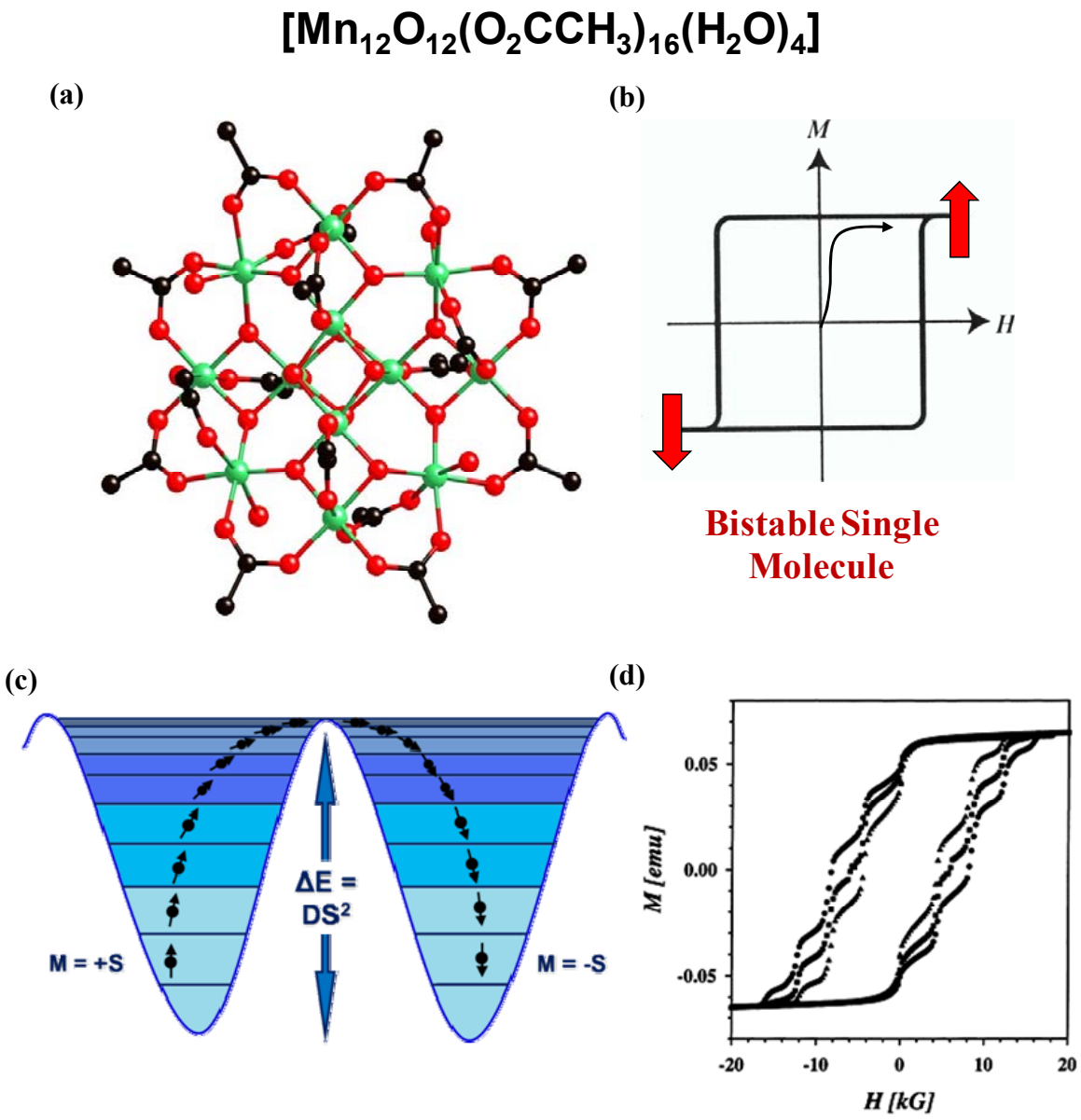

Figure 10. (a) Molecular structure of the first reported single molecule magnet, Mn_{12}. (b) idealized hysteresis for a single molecule magnet; (c) energy well diagram for the Mn_{12} SMM; (d) hysteresis loop for Mn_{12}-acetate, which clearly shows steps due to quantum tunneling through the barrier. (Adapted from Gatteschi *et al*.[52])

is S and D is the axial anisotropy, which must be negative for a barrier to form (Figure 10c). The energy barrier to this observed bistability however, is not equivalent to the maximum possible barrier given by ΔE, above, but rather is the effective barrier height, U_{eff}, which is affected by the relaxation time of the molecule in interactions with the phonon bath of its surroundings as well as quantum tunneling of the spins in the molecule (Figure 10d). This energy barrier, U_{eff}, is always lower than the maximum possible given by ΔE, but still allows for a magnetized ground state to stay stable until the barrier is traversed by magnetizing the material in a field of the opposite direction. This behavior can only be observed below a critical blocking temperature, T_B, in essence creating the smallest unit of binary storage that can be envisaged.

Another crucial phenomenon of some single molecule magnets is the existence of quantum tunneling, which can be discerned from the steps in the hysteresis loops (Figure 10d). [53] These steps represent the tunneling of the spins through the spin reversal barrier, and may hold promise in applications such as quantum computing.[54, 55] While a great deal of new SMM's have been prepared, [56-62] Mn_{12} still holds the current SMM record of the highest T_B at 8K (as measured from the AC signal at 1kHz)[63] and is known to retain this bistability for months when kept below 3K.[64]

The Mn_{12} cluster is prepared by a self assembly process which does not typically lead to predictable results.[58] Therefore, some researchers have sought a building block approach using cyanometallates. These efforts have led to the formation of a number of cyanide based SMM's, but most of them exhibit very low blocking temperatures where the verification of hysteresis in these compounds requires the use of specialized

measurements such as a micro-squid apparatus to obtain low temperature measurements, down to 0.04K.[59, 61, 65-68] One such example of a cyanide based SMM was reported by Dunbar *et al*. in 2003 and was later studied by Micro-SQUID measurements with the aid of Prof. Wolfgang Wernsdorfer in 2009.[62, 69]

Incorporation of Highly Anisitropic Metal Ions

The use of the building block approach has proven to be useful for the synthesis of SMM's but has failed to yield examples with higher blocking temperatures, a requirement for any useful application in data storage or processing. In the very simplistic model, to increase the blocking temperature of an SMM, the barrier height ($\Delta E = S^2|D|$ or $(S^2 - ¼)\ |D|$ for integer and half-integer spin molecules, respectively) would need to be increased. From this standpoint, it makes sense that since the S value is squared that it should have the largest effect. Indeed early work focused on preparing large clusters with high S values, such as those exemplified by the work of Annie Powell *et al*.[56] with a cluster of Mn_{19}, S = 89/2 and George Christou *et al*.[60, 70] with Mn_{25}, and Mn_{84} clusters with ground state spin values of S = 51/2 and S = 6 respectively (Figure 11). Unfortunately these clusters are very low temperature SMM's, with the blocking temperature less than 1K for all three, remarkably lower than that of the original SMM, Mn_{12}.

Rather than focusing on increasing S, a number of researchers began to focus on incorporating metals with strong anisotropy in the form of D. A recent paper by Waldmann[71] in 2007 addressed this issue, where he outlined an argument that the simplified method of relying on the exact interpretation of the barrier height $\Delta E = S^2|D|$

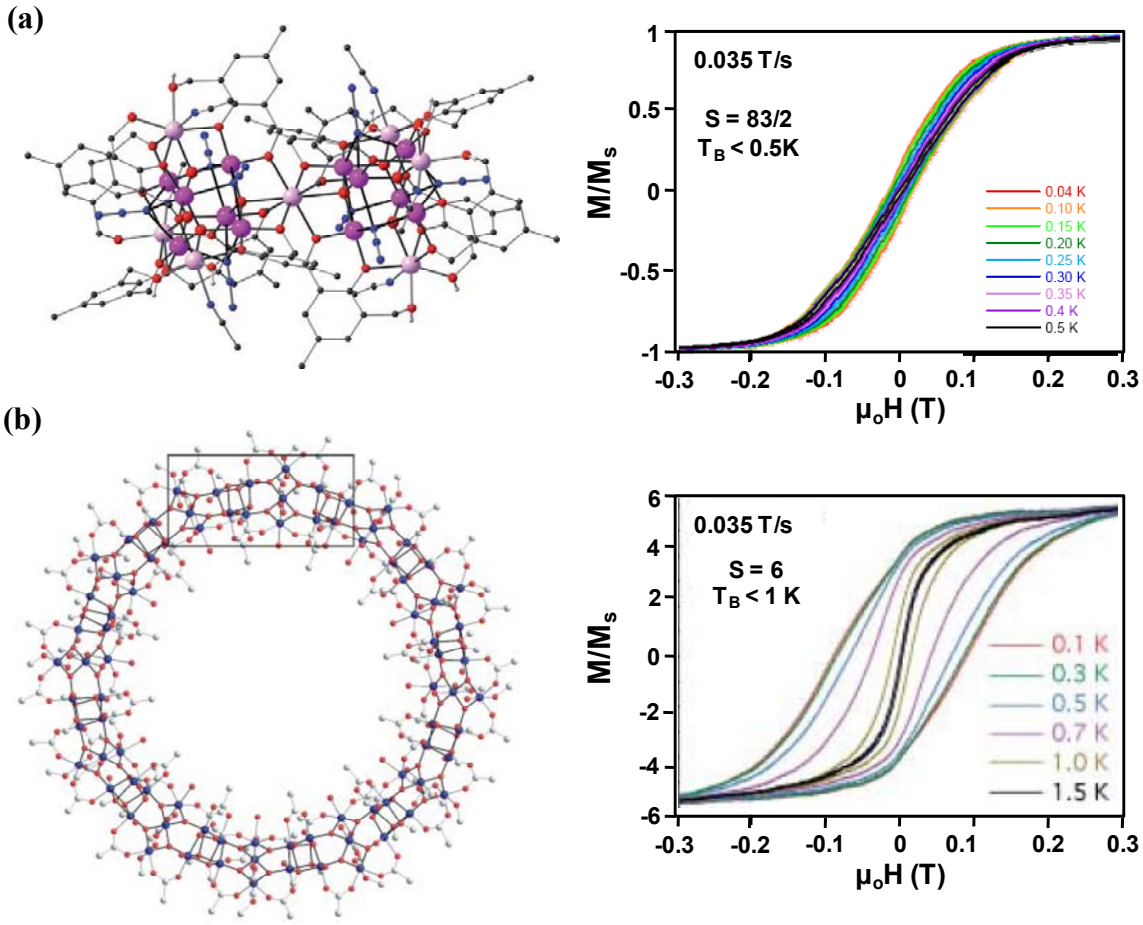

Figure 11. Molecular structure and micro-SQUID measurements for (a) $[Mn^{III}_{12}Mn^{II}_{7}(\mu^4\text{-}O)_8(\mu3,\eta^1\text{-}N_3)_8(HL)_{12}(MeCN)_6]Cl_2\cdot10MeOH\cdot MeCN$ (Mn_{19}) cluster (S = 83/2 ground state and T_B < 0.5 K) (b) $[Mn_{84}O_{72}(O_2CMe)_{78}(OMe)_{24}(MeOH)_{12}\text{-}(H_2O)_{42}(OH)_6]\cdot xH_2O\cdot yCHCl_3$ (Mn_{84}) cluster (S = 6 and T_B < 1 K). (Adapted from Powell *et al.*[56] and Christou *et al.*[70])

equation may very well be misleading, and that S could have very little impact compared to that of having a strong axial anisotropy. This idea was expanded by Ruiz and Alvarez, who not only proposed the mathematical reasons for this phenomenon, but began to include experimental data into this model, coming to the conclusion that it may not be even possible to have a coexistence of both a high anisotropy and a high ground state spin value, and that the most important issue should be a focus on increasing the anisotropy parameter, D, rather than the spin, S.[72]

One such method of increasing the anisotropy of the clusters is by using building blocks based on 4d and 5d metal ions, which have a larger anisotropy stemming from the increased spin orbit coupling. While this method does in fact increase anisotropy, the use of 4d and 5d metals also makes the S no longer a valid quantum number, as such the use of these metal ions adds yet another layer of complexity into the SMM field. The first 4d and 5d metal complexes to be widely studied were the $[Mo^{V}(CN)_8]^{3-}$ and $[W^{V}(CN)_8]^{3-}$ building blocks, with a number of interesting results.[9, 45, 73-77] These ions have been used to synthesize large pentadecanuclear clusters of M'_6M_9 of the general formula $[M^{II}\{M^{II}(MeOH)_3\}_8(\mu\text{-}CN)_{30}\{M'^{V}(CN)_3\}_6]_x\bullet MeOH_y\bullet H_2O$ where M' = Mo,W and M = Ni, Mn, Co. These molecules are unstable due to the loss of solvent molecules from the periphery of the cluster, but in some cases they were reported to exhibit SMM behavior, as in the W_6Co_9 analog.[74] In order to increase the stability, the bpy ligand was used as a capping ligand which led to the isolation of $[Ni^{II}\{Ni^{II}(bpy)(H_2O)\}_8\{W^{V}(CN)_8\}_6]\cdot 23H_2O$, which was found to exhibit SMM behavior.[78] Another rarely used octacyanometallate $[Nb^{IV}(CN)_8]^{4-}$ has been used in some

cluster chemistry to prepare octahedral complexes such as the $Mn^{II}_4Nb^{IV}_2$ cluster, which does not exhibit SMM behavior but is one of the first documented case of the $[Nb^{IV}(CN)_8]^{4-}$ building block.[79] To a lesser extent, clusters based on cyanometallates of Re have also been studied and have led to new SMM's. The first such cluster with Re^{II} to show SMM behavior was synthesized by Dunbar *et al*. in 2004.[80] When the salt $[Et_4N][Re^{II}(triphos)(CN)_3]$ was reacted with labile Mn^{II} ions, the cubic complex $[\{Mn^{II}Cl\}_4\{Re^{II}\text{-}(triphos)(CN)_3\}_4]$ was formed which exhibited SMM behavior at low temperatures (Figure 12a). Later, Long's group reported the first homoleptic Re cyanometallate complex, the $[Re^{IV}(CN)_7]^{3-}$ ion, which was reacted with $[(PY_5Me_2)Mn^{II}(MeCN)](PF_6)_2$ to yield a pentanuclear star-like cluster $[(PY_5Me_2)_4Mn^{II}_4Re^{IV}(CN)_7](PF_6)_5\cdot 6H_2O$ with a blocking temperature of 5K (as measured from AC at 1kHz), the highest blocking temperature reported for a cyanide based SMM (Figure 12b).[65]

To more deeply understand SMM behavior and its relationship to spin-orbit coupling, theoreticians began studying more complex building blocks, such as 3d metals with higher inherent anisotropy, e.g. $[Fe(CN)_6]^{3-}$ and $[Mn(CN)_6]^{3-}$ due to their unquenched orbital angular momentum[81, 82], as well as the lesser studied 4d and 5d cyanometallates with large spin orbit coupling, $[Mo^{III}(CN)_7]^{4-}$ and $[Os^{III}(CN)_6]^{3-}$.[67, 83, 84] One difficulty in modeling such systems, is that the spin quantum number S is no longer valid. Instead the quantum number *J* must used, where *J* = L + S (note that the quantum number *J* is not the same as the *J* for exchange coupling). Theoretical barrier heights have been calculated for the $[Mn^{II}(tmphen)_2]_3[Mn^{III}(CN)_6]_2$ TBP[85] as well as the

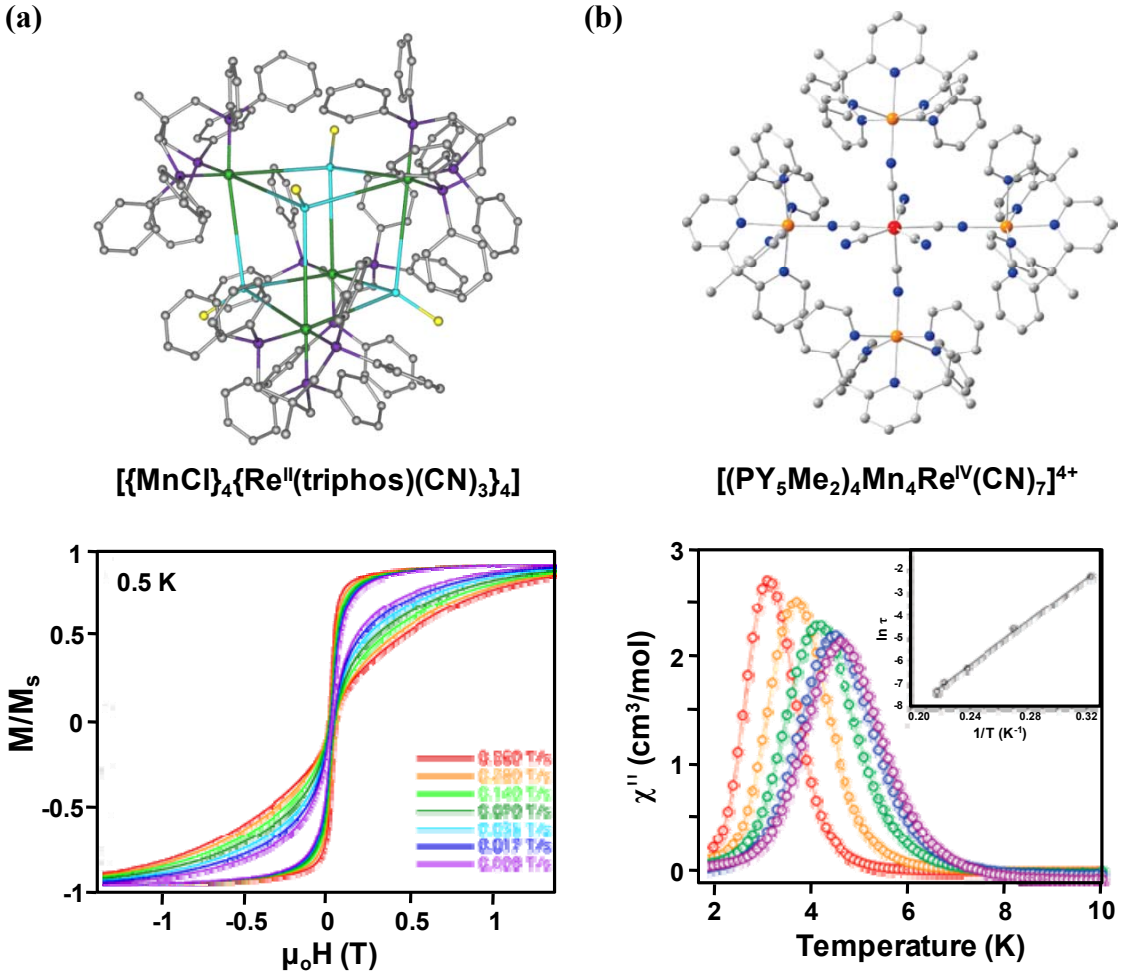

Figure 12. (a) Molecular structure and sweep rate dependence of the $Re^{II}_4Mn^{II}_4$ cube at 0.5 K from micro-SQUID data and (b) molecular structure and AC data for the $Re^{IV}Mn^{II}_4$ molecule with a $T_B < 5$ K (at 1kHz). (Adapted from Dunbar *et al.*[61] and Long *et al.*[65])

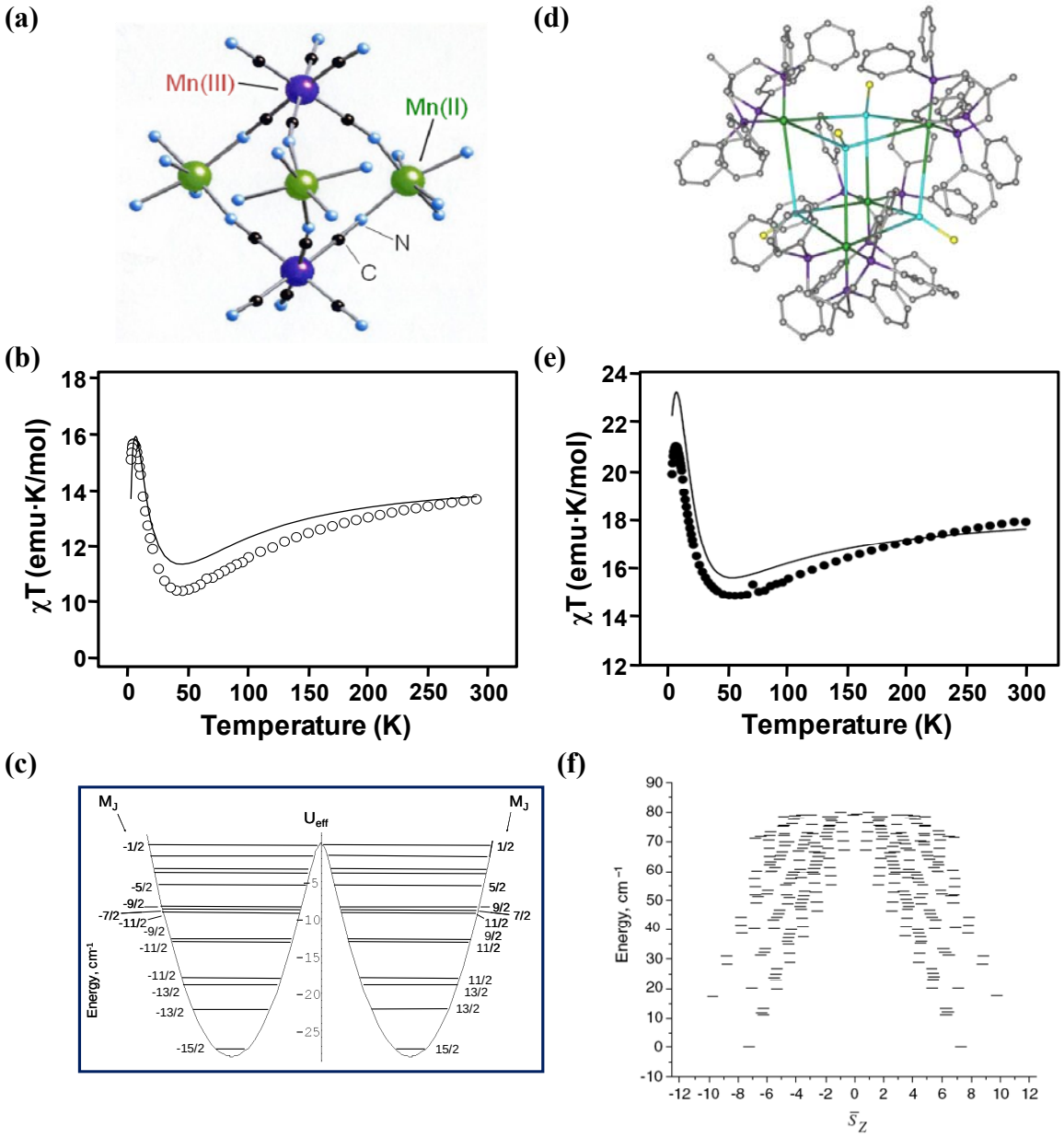

Figure 13. Plots are results of theoretical calculations of the magnetic susceptibility (b,e), and barrier height (c,f) of $[Mn^{II}(tmphen)_2]_3[Mn^{III}(CN)_6]_2$ TBP (a), and $[MnCl]_4[Re^{II}(triphos)(CN)_3]_4$ cube (d). (Adapted from Klokishner and Tsukerblat *et al.*[85, 86])

$[\{Mn^{II}Cl\}_4\{Re^{II}\text{-(triphos)}(CN)_3\}_4]$ cube,[86] where the barrier height is defined by multiples m_j of J. These models were able to simulate the behavior of the magnetic susceptibility data (Figure 13) as well. Predictions based on calculations of anisotropic metals indicated that molecules that would incorporate building blocks with a very large single ion anisotropy should produce higher blocking temperatures due the increase in the cluster anisotropy primarily through anisotropic exchange interactions. In a fundamental sense, anisotropic exchange occurs when the magnetic exchange interactions are no longer equivalent in all directions between metal centers, and there can be a J_x, J_y, J_z component which can have a large difference in magnitude.[82, 87, 88] There are comparatively few studies that focus on increasing anisotropy versus those that concentrate increasing spin, most likely due from to the difficulty in working with many of the suitable building blocks for such studies. The use of 4*d* and 5*d* transition metals is very important for addressing the validity of current theoretical predictions about the possibility of preparing SMM's with higher blocking temperatures. Due to the limited number of systems available for study, the synthesis and characterization of materials with these anisotropic building blocks will provide valuable experimental data for the study of the impact of both spin orbit coupling and anisotropic exchange on the magnetic properties of materials.

The work described in this thesis focuses on the use of 4*d* and 5*d* cyanometallates as building blocks for the study of magnetic properties. Chapter II describes results obtained from using the well known octacyanometallates of Mo^V and W^V as building blocks for the synthesis and magnetic investigation of both trigonal

bipyramidal and pentadecanuclear clusters. Chapter III outlines the synthesis and characterization of the first known examples of clusters based on hexacyanoosmate(III) and hexacyanoruthenate(III) building blocks. The topic of Chapter IV is a detailed study of the trigonal bipyramidal clusters of $[Fe(tmphen)_2]_3[Os(CN)_6]_2$ and $[Fe(tmphen)_2]_3[Ru(CN)_6]_2$ and an in depth study of the CTIST behavior of these clusters using Mössbauer spectroscopy, variable temperature crystallography, epr, and variable temperature IR measurements. Chapter V, discusses new Prussian Blue analogs prepared from the hexacyanoosmate(III) and hexacyanoruthenate(III) anions with a comparison to the trigonal bipyramidal clusters presented in Chapters III and IV.

CHAPTER II

TRIGONAL BIPYRAMIDAL AND PENTADECANUCLEAR CLUSTERS BASED ON $M^{V}(CN)_8$ (M = Mo, W) AND Ni^{II}*

Introduction

Recent decades have witnessed a flurry of activity involving the magnetic properties of transition metal clusters[2] with fascinating results having emerged including spin crossover,[38-40, 42, 89, 90] photomagnetism,[45, 91] and single molecule magnetism.[49, 52, 60, 61, 65, 66, 92, 93] One of the reasons for the high level of excitement is the fact that there is growing evidence that molecular properties can be exploited for use in new devices,[42] particularly those that pertain to quantum computing and spintronics applications.[54, 55, 94, 95]Among the most well-studied molecule-based magnetic materials is Prussian Blue (PB)[96] and its analogues.[17, 21, 24] In an effort to understand and model the magnetic behavior of these typically defective and often poorly defined materials, researchers have turned to methods for isolating low-dimensional analogues of PB that involve the use of blocking ligands to limit the growth of the structure to 2-D nets,[97, 98] 1-D chains,[3, 4, 99] and 0-D discrete multinuclear complexes.[45, 46, 65, 100, 101] Among these categories, 2009discrete cyanide clusters are of special interest due to their contributions to the area of single molecule magnetism.[57, 59, 61, 62, 65, 66]

*Portions of this chapter are reprinted with permission from "Molecules based on M(V) (M = Mo, W) and Ni(II) ions: a new class of trigonal bipyramidal cluster and confirmation of SMM behavior for the pentadecanuclear molecule $\{Ni^{II}[Ni^{II}(tmphen)(MeOH)]_6[Ni(H_2O)_3]_2[\mu\text{-}CN]_{30}[W^{V}(CN)_3]_6\}$", Hilfiger, M.G.; Zhao H.; Prosvirin, A.; Wernsdorfer, W.; Dunbar K.R. Dalton Trans. **2009,** *26***,** 5155-5163.

Both spin and anisotropy play crucial roles in determining the blocking temperature for reversing the magnetization of a particular SMM, with a negative axial zero field splitting value (−D) being an absolute requirement for the establishment of a barrier according to the traditional definition wherein the energy barrier is $\Delta E = S^2|D|$ and $S^2|1/4 - D|$ for integer and half-integer spin molecules, respectively. A different paradigm for introducing anisotropy into SMMs, and indeed molecular magnets in general, is to use 4d and 5d transition metal ions with significant unquenched orbital angular momentum.[61, 65, 77, 102, 103] The group 6 elements Mo and W in the form of the pentavalent octacyanometallates are among the most widely investigated in this category.[74, 76-78, 103-105] A persistent geometry that has emerged for clusters based on $[M^V(CN)_8]^{3-}$ ions is that of the $M_9M'_6$ pentadecanuclear six-capped body-centered cube[77,73, 76, 106] (M = Mn, Ni, Co and M′ = W, Mo). The first $M_9M'_6$ clusters to be reported[77,106] were capped solely by coordinated alcohol molecules, a situation that renders them relatively unstable, especially under the application of a vacuum such as that necessary to make SQUID measurements. This unfortunate circumstance led to difficulty in correctly interpreting the magnetic data, notably in the case of the Mn_9Mo_6 cluster first reported as a 51/2 ground state,[76] but later proven by a combination of DFT and polarized neutron diffraction studies to be, in fact, an S = 39/2 molecule.[107] In an effort to prepare more stable analogues of these molecules, Lim *et al.* successfully used the bpy ligand to cap some of the peripheral sites of the cluster. These authors reported the observation of SMM behavior for the Ni_9W_6 analogue $[Ni[Ni(bpy)(H_2O)]_8[W(CN)_8]_6]\cdot 23H_2O$ as judged by low temperature AC susceptibility

data.[78, 104] Other studies have focused on such clusters as building blocks for larger extended magnetic networks.[8] In spite of a growing number of papers dedicated to the topic of these fascinating clusters, no detailed low temperature magnetic analyses have been performed.

In order to further probe the use of the Mo^V and W^V octacyanometallate building blocks for engendering SMM behavior, we carried out reactions of the cyanometallates with Ni^{II} ions in the presence of tmphen (tmphen = 3,4,7,8-tetramethyl-1,10-phenanthroline). For the first time in such chemistry, both trigonal bipyramidal (TBP) and pentadecanuclear clusters were obtained with the result being dependent on the metal ratios involved. Specifically, the new compounds $[Ni^{II}(tmphen)_2]_3[W^V(CN)_8]_2$, $[Ni^{II}(tmphen)_2]_3[Mo^V(CN)_8]_2$, $[Ni^{II}_9(tmphen)_6(CH_3OH)_6(H_2O)_6W^V_6(CN)_{48}]$, and $[Ni^{II}_9(tmphen)_6(CH_3OH)_6(H_2O)_6Mo^V_6(CN)_{48}]$, **1–4** respectively, were obtained. As the TBP geometry is known to be prevalent in cyanide chemistry, indeed we have capitalized on this fact to prepare homologous series of molecules for detailed magnetic modeling studies,[37, 43, 46, 62, 102, 108] but the present results constitute the first instances in which the octacyanometallate building block has led to a TBP cluster. In addition to the TBP molecules, we also obtained two new examples of M_9M_6 clusters. The structures were confirmed by X-ray crystallography and magnetic studies of all four new molecules were undertaken, including modeling of the data and a comparison to recently reported theoretical calculations.[109] The present analyses of the magnetic parameters of the two M_9M_6 clusters constitute the first time the data of these large clusters have been

subjected to fitting. Finally, single molecule magnetic behavior was definitively confirmed by microSQUID measurements performed on the Ni_9W_6 cluster.

Experimental Section

Syntheses

Reagents. The tmphen ligand was purchased from Aldrich and used without further purification. The metal starting materials $MoCl_5$ (Aldrich), WCl_5 (Aldrich), $NiCl_2$ (Strem), and $Ni(BF_4)_2{\cdot}4H_2O$ (Aldrich) were used as received. The compounds $[(C_4H_9)_3NH]_3Mo(CN)_8$ and $[(C_4H_9)_3NH]_3W(CN)_8$ were prepared according to literature procedure.[110] Reagent grade methanol (MeOH), acetonitrile (MeCN) and dimethylformamide (DMF) were purchased from Aldrich and used as received.

$[Ni^{II}(tmphen)_2]_3[W^V(CN)_8]_2{\cdot}8CH_3OH{\cdot}2H_2O$ (1). A solution of 71 mg (0.30 mmol) of tmphen in 4 mL of MeOH was slowly added to a solution of 36 mg (0.15 mmol) of $NiCl_2{\cdot}6H_2O$ in 4 mL MeOH–DMF (3 : 1 v/v) with constant stirring. The resulting solution was layered in the dark with a solution of 95 mg (0.10 mmol) $[(C_4H_9)_3NH]_3W(CN)_8$ in 8 mL of MeOH. Red needle-like crystals were obtained after the course of a week. The crystals were collected by filtration, washed with MeOH, and dried *in vacuo*. Yield = 68 mg (51%, based on W). Elemental analysis: Calcd. for $W_2Ni_3O_{10}N_{28}C_{120}H_{132}$: C, 53.97%; H, 4.98%; N, 14.69%; Found: C, 53.69%; H, 4.55%; N, 15.03%. IR (Nujol), υ(C≡N) cm^{-1}: 2135, 2157, 2181.

$[Ni^{II}(tmphen)_2]_3[Mo^V(CN)_8]_2{\cdot}5CH_3CN{\cdot}8H_2O$ (2). Quantities of $NiBF_4{\cdot}6H_2O$ (51 mg, 0.15 mmol) and tmphen (70 mg, 0.30 mmol) were stirred in 20 mL of acetonitrile for 30

min. The resulting dark red solution was quickly combined in the dark with a solution of 86 mg (0.10 mmol) of $[(C_4H_9)_3NH]_3Mo(CN)_8$ in 20 mL of acetonitrile. The mixture was filtered and the filtrate was left to stand undisturbed for about a week. After this period of time, burgundy red crystals were collected by filtration, washed with acetonitrile (2 × 10 mL), and dried *in vacuo*. Yield: 41 mg (24%). Elemental analysis: Calcd. for $C_{122}H_{127}Mo_2N_{33}Ni_3O_8$: C, 57.42%; H, 5.02%; N, 18.12%; Found: C, 57.38%; H, 5.00%; N, 16.46%. IR (Nujol), υ(C≡N) cm^{-1}: 2137, 2157, 2185.

$[Ni^{II}_9(tmphen)_6(CH_3OH)_6(H_2O)_6W^{V}_6(CN)_{48}]\cdot 6DMF$ (3). A solution of tmphen (47 mg, 0.20 mmol) in MeOH (3 mL) was slowly added to a solution of 71 mg (0.30 mmol) $NiCl_2\cdot 4H_2O$ in 4 mL MeOH–DMF (3 : 1 v/v) with constant stirring. The solution was layered in the dark with a solution of 190 mg (0.20 mmol) of $[(C_4H_9)_3NH]_3W(CN)_8$ in 10 mL of MeOH. Red block-shaped crystals were obtained after several days. Yield: 57 mg (68% based on W). Elemental analysis: Calcd. for $W_6Ni_9C_{168}H_{174}N_{66}O_{18}$: C, 40.09%; H, 3.80%; N, 18.37%; Found: C, 39.91; H, 3.35%; N, 17.42%. IR (Nujol), υ(C≡N), cm^{-1}: 2179, 2136, 2111.

$[Ni^{II}_9(tmphen)_6(CH_3OH)_6(H_2O)_6Mo^{V}_6(CN)_{48}]\cdot 6DMF$ (4). A solution of 47 mg (0.20 mmol) of tmphen in 3 mL of MeOH was slowly added to a solution of 71 mg (0.30 mmol) of $NiCl_2\cdot 4H_2O$ in 4 mL MeOH–DMF (3 : 1 v/v) with constant magnetic stirring. The resulting solution was layered in the dark with a solution of 173 mg (0.20 mmol) $[(C_4H_9)_3NH]_3Mo(CN)_8$ in 10 mL of MeOH. Red block-shape crystals were obtained after three days. Yield: 50 mg (67% based on Mo). Elemental analysis: Calcd. for

$Mo_6Ni_9C_{168}H_{174}N_{66}O_{18}$: C, 44.77%; H, 3.79%; N, 20.52%; Found: C, 46.10%; H, 3.84%; N, 20.08%. IR (Nujol), υ(C≡N), cm^{-1}: 2177, 2134, 2100.

Single Crystal X-Ray Crystallography

In a typical experiment, the crystal selected for study was suspended in paraffin oil and mounted on a cryoloop which was placed in an N_2 cold stream. Single crystal X-ray data were collected on a Bruker APEX diffractometer equipped with a CCD detector at 110 K (Table 4). The data sets were recorded as ω-scans at a 0.3° step width and integrated with the Bruker SAINT[111] software package. The absorption correction (SADABS[112]) was based on fitting a function to the empirical transmission surface as sampled by multiple equivalent measurements. Solution and refinement of the crystal structures were carried out using the SHELX[113] suite of programs and the graphical interface X-SEED.[114] All the structures were solved by direct methods which resolved the positions of all the metal atoms and most of the C and N atoms. The remaining non-hydrogen atoms were located by alternating cycles of least squares refinements and difference Fourier maps. Hydrogen atoms were placed at calculated positions, with the exception of some water molecules, for which the hydrogen atoms were located from the difference Fourier maps. Whenever disordered solvent molecules were present in a structure, their bond distances were restrained to chemically meaningful values. The final refinement was carried out with anisotropic thermal parameters for all non-hydrogen atoms, except for the non-hydrogen atoms of the disordered solvent molecules which were refined isotropically. This methodology applies to the following chapters.

Results and Discussion

Syntheses and Infrared Spectroscopy

Reactions of $[(C_4H_9)_3NH]_3M^V(CN)_8$ (M = Mo or W), $NiX_2{\cdot}6H_2O$ (X = Cl, NO_3 or BF_4), and 3,4,7,8-tetramethyl-1,10-phenanthroline in a 2 : 3 : 6 ratio afforded compounds **1** and **2**. In a typical preparation of trigonal bipyramidal (TBP) clusters, the precursor complex was prepared *in situ* by combining 1 equivalent of the metal salt with **2** equivalents of tmphen in acetonitrile or methanol. Crystalline forms of both compounds were obtained by performing bulk reactions in acetonitrile, as well as by layering a solution of the octacyanometallate anion over a solution of NiX_2 and tmphen in a mixture of methanol and dimethylformamide. Compounds **3** and **4** were obtained from a layering reaction performed with a 2 : 3 : 2 ratio of M : Ni : tmphen starting materials. It is important to note that the reactions must be carried out under low light conditions, as both the $[W^V(CN)_8]^{3-}$ and $[Mo^V(CN)_8]^{3-}$ precursors are readily photo-reduced to $[M^{IV}(CN)_8]^{4-}$. The dried products are air-stable and may be stored without specific precautions for prolonged periods of time in the absence of light. The steric bulk afforded by the tmphen ligands on the perimeter of the molecule renders the cluster much more stable than the analogues with only solvent molecules as the capping ligands.

The IR spectra (Appendix A) reveal $\nu(C{\equiv}N)$ stretches (cm^{-1}) at 2135, 2157, 2181 for **1**; 2137, 2157, 2185 for **2**; 2177, 2134, 2100 for **3**; and 2136, 2111 for **4**. The lowest energy stretches are attributed to the terminal CN^- ligands on the octacyanometallates as compared to the precursors, $[(C_4H_9)_3NH]_3Mo^V(CN)_8$ (2141, 2121 cm^{-1}) and $[(C_4H_9)_3NH]_3W^V(CN)_8$ (2143, 2123 cm^{-1}). The higher energy vibrations are assigned to

bridging modes of the CN^- ligand, which have been well documented in the literature.[1, 46].

Single Crystal X-ray Studies

Single crystal X-ray diffraction studies revealed that compounds **1** and **2** are isostructural and crystallize in the monoclinic space group $P2_1/c$ (Table 2). A side view displaying the core of the cluster (left) and an axial view showing the pseudo C_3 symmetry (right) for **1** and **2** are depicted in Figure 14. The molecular structures consist of a pentanuclear core composed of CN-bridged Ni^{II} and M^{V} ions. The two $[M(CN)_8]^{3-}$ ions are in a distorted bicapped trigonal prismatic geometry in which $[M(CN)_8]^{3-}$ occupies the axial positions of the TBP core. Three CN^- ligands of each octacyanometallate unit act as bridges, and the other five terminal CN^- ligands point away from the cluster. The three equatorial Ni^{II} ions are in pseudo-octahedral coordination environments consisting of two bidentate tmphen molecules and two bridging CN^- ligands. Each tmphen ligand bound to the Ni(2) center engages in an intramolecular π-π contact with a tmphen ligand from a neighboring Ni(1) or Ni(3) center. In contrast, only one tmphen ligand from the Ni(1) or Ni(3) center is involved in an intramolecular π-π interaction with a tmphen ligand bound to a Ni(2) site.

Compounds **3** and **4** are isostructural and adopt a six-capped body-centered cube arrangement of metal ions that has been previously observed for related clusters. The molecules contain fifteen metal atoms with nine Ni^{II} ions in a pseudo-octahedral

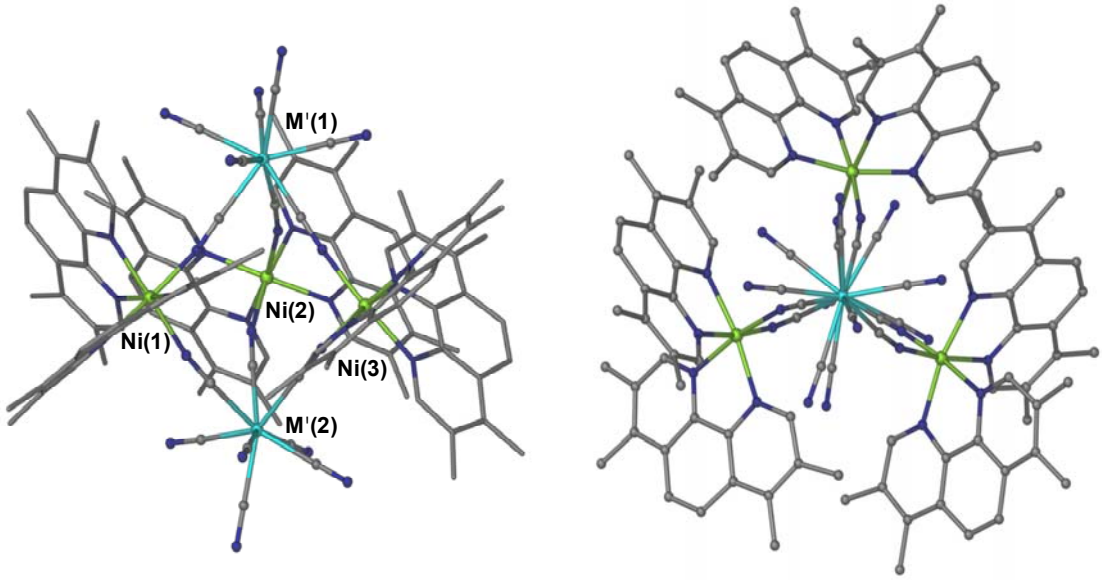

Figure 14. Equatorial and axial views of the cores in the trigonal bipyramidal molecules **1** and **2**. Equatorial sites are comprised of the Ni atoms and the axial sites are occupied by either $Mo(CN)_8$ or $W(CN)_8$ units.

Table 2. Crystal structure data and refinement parameters for compounds **1–4.**

Formula	$W_2Ni_3N_{30}C_{112}H_{120}O_4$ (**1**)	$Mo_2Ni_3N_{33}C_{122}H_{127}O_8$ (**2**)	$W_6Ni_9C_{168}H_{174}N_{66}O_{18}$ (**3**)	$Mo_6Ni_9C_{168}H_{174}N_{66}O_{18}$ (**4**)
Space group	$P2_1/c$	$P2_1/c$	$R\bar{3}$	$R\bar{3}$
Unit cell	a = 31.859(6) Å	a = 31.229(6) Å	a = 32.270(5) Å	a = 32.214(5) Å
	b = 16.435(3) Å	b = 16.302(3) Å	b = 32.270(5) Å	b = 32.214(5) Å
	c = 28.926(6) Å	c = 28.862(6) Å	c = 21.161(4) Å	c = 21.074(4) Å
	β= 116.12(3)°	β = 114.73(3)°	α= β = 90°, γ= 120°	α = β = 90°, γ= 120°
Unit cell volume, V/Å^3	13 599(5)	13 346(5)	19 084(5)	18 939(5)
Z	3	3	9	9
Density, ρ_c/g cm^{-3}	0.98	1.226	1.315	1.185
Abs. coeff., μ/mm^{-1}	1.616	0.662	3.406	0.999
Crystal color and habit	Red plate	Red plate	Red block	Red block
Crystal size/mm	0.36 × 0.26 × 0.09	0.23 × 0.12 × 0.04	0.27 × 0.22 × 0.018	0.16 × 0.14 × 0.08
Temperature/K	110	110	150	150
Radiation, λ/Å	Mo-K α, 0.71073	Mo-K α, 0.71073	Mo-K α, 0.71073	Mo-K α, 0.71073
Min. and max. θ/°	1.41 to 27.57	1.55 to 28.61	1.21 to 27.61	1.75 to 28.76
Reflections collected	117 802 [R_{int} = 0.0539]	152 144 [R_{int} = 0.0535]	48 537 [R_{int} = 0.1186]	73 793 [R_{int} = 0.1367]
Independent reflections	30 969	32 249	9650	10 423
Data/parameters/restraints	28 986/1258/0	20 136/1496/1.055	4057/404/7	3548/409/1
R [$F_o > 4\sigma$ (F_o)]	R_1 = 0.0570	R_1 = 0.0822	R_1 = 0.0915	R_1 = 0.1197
	wR_2 = 0.1741	wR_2 = 0.2895	wR_2 = 0.3493	wR_2 = 0.4215
G.o.f. on F^2	1.075	1.055	1.003	1.129
Max., min. residual densities/e Å^{-3}	0.696, −0.273	3.141, −2.182	2.947, −1.210	1.724, −0.844

Table 3. Average metal to ligand bond distances (Å) and bond angles (°) in the crystal structures of compounds **1–4**.

Ni_3W_2 (**1**)				Ni_3Mo_2 (**2**)			
$Ni(1)–N_{(N\equiv C)}$	2.039	Ni(1)–N≡C	165.4	$Ni(1)–N_{(N\equiv C)}$	2.041	Ni(1)–N≡C	163.7
$Ni(2)–N_{(N\equiv C)}$	2.049	Ni(2)–N≡C	164.2	$Ni(2)–N_{(N\equiv C)}$	2.048	Ni(2)–N≡C	168.6
$Ni(3)–N_{(N\equiv C)}$	2.049	Ni(3)–N≡C	168.9	$Ni(3)–N_{(N\equiv C)}$	2.035	Ni(3)–N≡C	168.3
W(1)–C	2.157	$W(1)–C\equiv N_{bridging}$	176.9	Mo(1)–C	2.148	$Mo(1)–C\equiv N_{bridging}$	177.4
W(2)–C	2.161	$W(2)–C\equiv N_{bridging}$	175.2	Mo(2)–C	2.152	$Mo(2)–C\equiv N_{bridging}$	175.4
$C\equiv N_{bridging}$	1.144			$C\equiv N_{bridging}$	1.144		
$C\equiv N_{terminal}$	1.150			$C\equiv N_{terminal}$	1.147		
Ni_9W_6 (**3**)				Ni_9Mo_6 (**4**)			
$W–C_{term}$	2.173	$W–C\equiv N_{term}$	175.7	$Mo–C_{term}$	2.149	$Mo–C\equiv N_{term}$	176.4
$W–C_{bridge}$	2.119	$W–C\equiv N_{bridge}$	176.3	$Mo–C_{bridge}$	2.136	$Mo–C\equiv N_{bridge}$	177.1
$Ni_{peripheral}–N$	2.055	$Ni_{peripheral}–N\equiv C$	177.2	$Ni_{peripheral}–N$	2.057	$Ni_{peripheral}–N\equiv C$	176.7
$Ni_{central}–N$	2.024	$Ni_{central}–N\equiv C$	176.8	$Ni_{central}–N$	2.023	$Ni_{central}–N\equiv C$	175.8

coordination environment and six M^V (M = W, Mo) centers in a bicapped trigonal prismatic geometry. A central Ni^{II} atom is bound to six peripheral $[M^V(CN)_8]^{3-}$ units.

The asymmetric unit is shown in Figure 15. The peripheral $[M^V(CN)_8]^{3-}$ groups are linked *via* CN^- bridges to four Ni^{II} ions with three of the CN^- ligands remaining terminal. Each of six Ni^{II} ions are coordinated to one tmphen ligand and one MeOH molecule, with the remaining two Ni^{II} ions, located axially, being coordinated to three water molecules. Representative views of the clusters in compounds 3 and **4** are depicted in Figure 16a. The core of such clusters is typically described as belonging to an idealized O_h point group.[77] The addition of the tmphen blocking ligand has the effect of lowering the overall symmetry of the system to an approximate C_{3v} point group. Compounds **3** and **4** both pack in hexagonal ABC layers and it can be seen that the central cluster cores are well separated from each other. The π-stacking in the layers of the clusters gives rise to a highly symmetric packing pattern as can be observed in Figure 16b. The resulting space group is $R\bar{3}$ which is the highest observed for the $M_9M'_6$ family. Table 2 lists representative structural data and Table 3 contains a listing of selected bond distances and angles.

Magnetic Properties

The DC susceptibility data for compounds **1–4** were measured from 2–300 K in an applied magnetic field of 1000 G (Appendix A). All compounds showed a rapid increase in χT as the temperature is lowered, an indication of ferromagnetic exchange interactions between the W^V, Mo^V and the Ni^{II} centers mediated through the cyanide bridge. This behavior was also confirmed by low temperature magnetization data. To

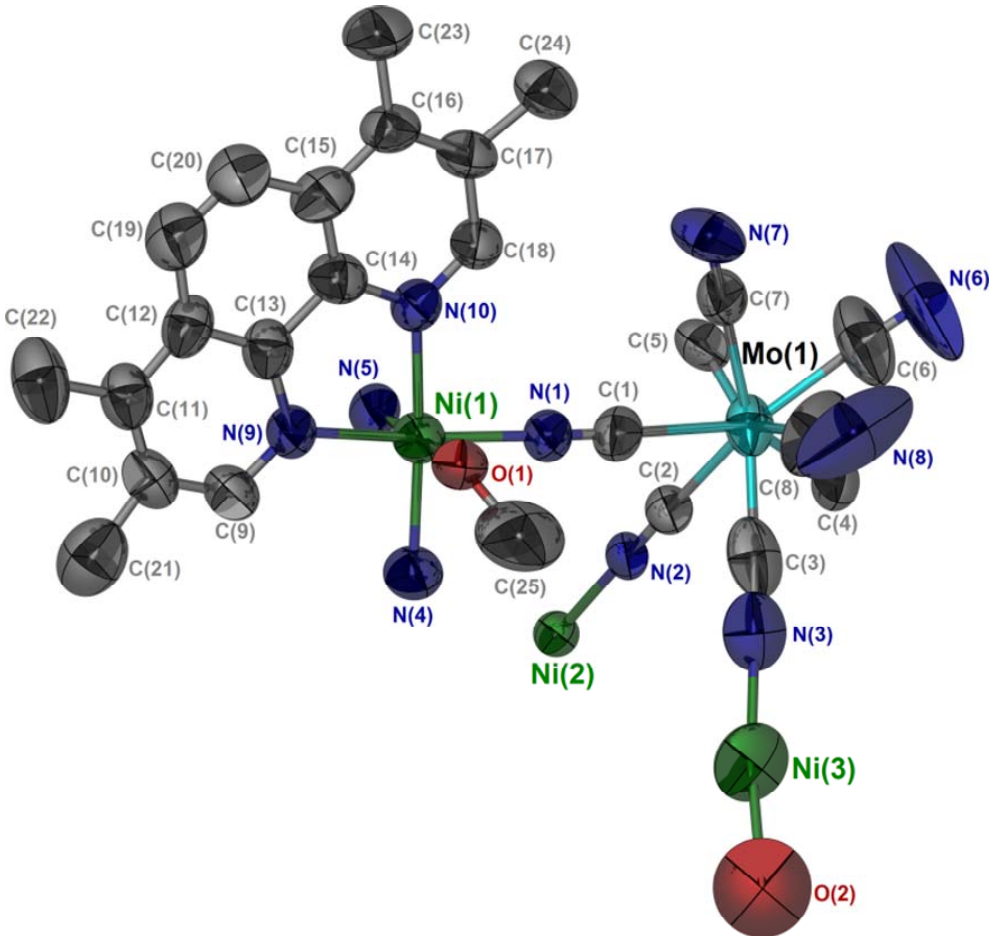

Figure 15. Depiction of the asymmetric unit of 3 (thermal ellipsoids at the 50% probability level; H atoms removed for clarity).

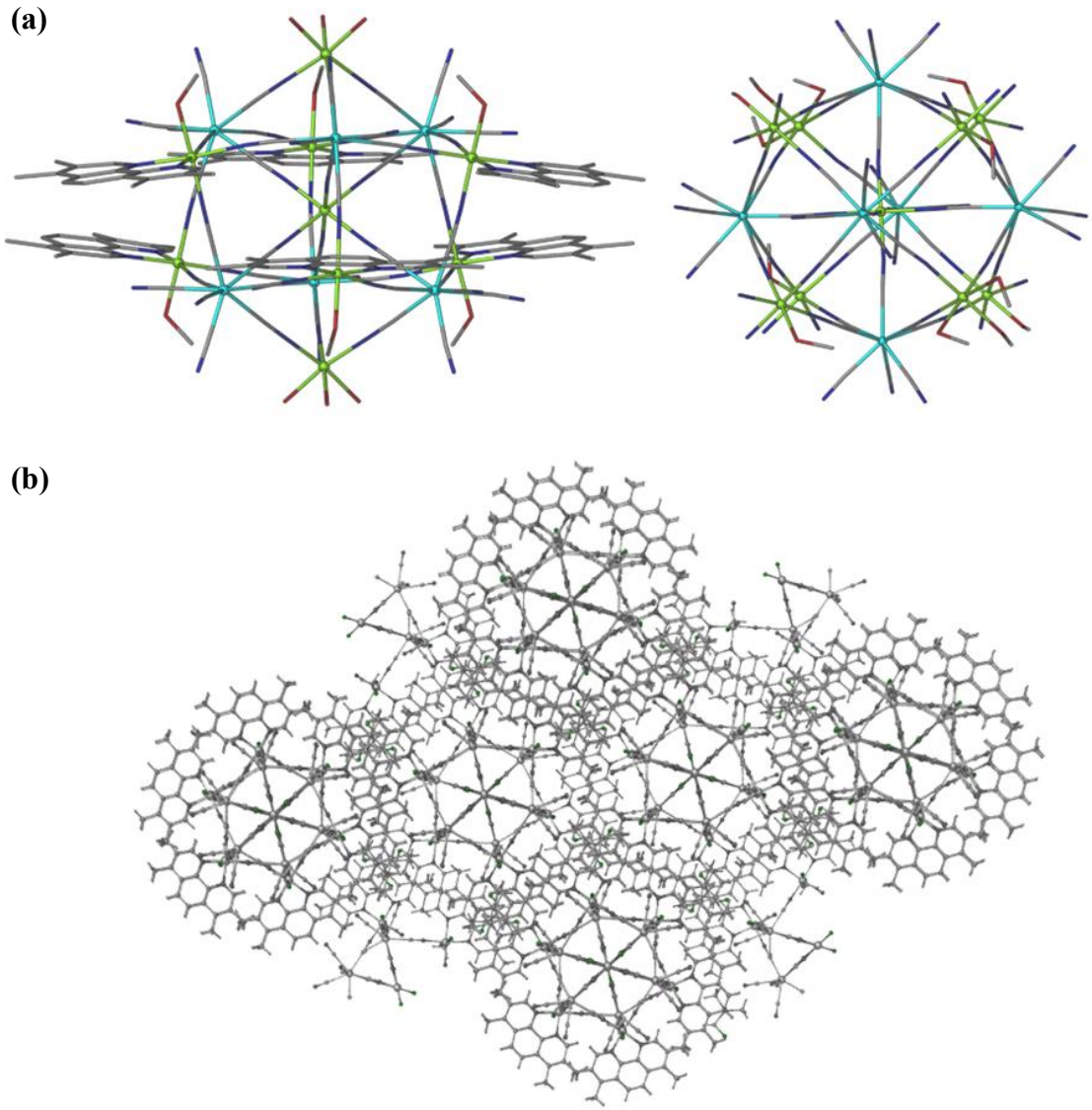

Figure 16. (a) Model of the crystal structures of compound 3 depicting the arrangement of tmphen ligands enveloping the core (left) and the core without the tmphen ligands (right). (b) View of the crystal packing of 3 as viewed approximately down the *c* axis.

model the magnetic behavior of compounds **1** and **2** the isotropic Heisenberg–Dirac–Van Vleck Hamiltonian was applied:

$$H = -2J_{Ni-M}(S_{M1} + S_{M2})(S_{Ni1} + S_{Ni2} + S_{Ni3}) - 3D[S^{z}_{Ni}{}^{2} - S_{Ni}(S_{Ni} + 1)/3] + \beta H[g_{M}(S_{M1} + S_{M2}) + g_{Ni}(S_{Ni1} + S_{Ni2} + S_{Ni3})] \quad (1)$$

J is the isotropic exchange constant and M corresponds to the axial Mo^{V} or W^{V} atoms. The simulation of the χT *vs.* T curves were carried out using MAGPACK.[115] Compounds **3** and **4** were modeled using MAGPACK as well:

$$H = -2J[S_{W1}(S_{Ni1} + S_{Ni7} + S_{Ni2} + S_{Ni3} + S_{Ni8}) + S_{W2}(S_{Ni1} + S_{Ni2} + S_{Ni3} + S_{Ni4} + S_{Ni9}) + S_{W3}(S_{Ni1} + S_{Ni3} + S_{Ni4} + S_{Ni5} + S_{Ni8}) + S_{W4}(S_{Ni1} + S_{Ni4} + S_{Ni5} + S_{Ni6} + S_{Ni9}) + S_{W5}(S_{Ni1} + S_{Ni5} + S_{Ni6} + S_{Ni7} + S_{Ni8}) + S_{W6}(S_{Ni1} + S_{Ni6} + S_{Ni7} + S_{Ni2} + S_{Ni9})] \quad (2)$$

where J is the isotropic exchange constant, Ni1 and Ni2–9 correspond to the central and peripheral Ni^{II} ions, respectively.

$[Ni^{II}(tmphen)_2]_3[W^{V}(CN)_8]_2\cdot 8CH_3OH\cdot 2H_2O$ (1). The room temperature χT value for **1** is 4.87 emu mol^{-1} K which is slightly higher than expected for a spin-only case of two uncoupled W^{V} (S = 1/2) and three Ni^{II} (S = 1) ions (χT = 4.55 emu mol^{-1} K) due to the spin–orbit coupling of the W ion. The χT value continuously increases as the temperature is lowered, an indication of ferromagnetic coupling between the Ni^{II} and W^{V}

ions (Figure 17). This observation is in agreement with theoretical studies regarding the origin of ferromagnetic coupling for d^1 octacyanometallate compounds.[116] The MAGPACK simulation of the χT *vs.* T data based on the Hamiltonian (eqn (1)) with the parameter $g_W = 2.00$ led to $g_{Ni} = 2.25$, an intermolecular cluster interaction $zJ' = -0.02$ cm^{-1}, and an isotropic exchange constant of $J = 9.5$ cm^{-1}. The negligible value of zJ' reflects the absence of appreciable inter-cluster interactions. The *J* value is slightly higher than that of the reported 1st row analogue, namely the corresponding Ni_3Cr_2 TBP cluster,[46] for which $J = 8.5$ cm^{-1}. Although the compounds cannot be directly compared given that the Cr^{III} centers are S = 3/2 and W^V is S = 1/2, the *J* values are surprisingly similar. The value of χT reaches a maximum of 11.45 emu mol^{-1} K at 8 K, in accord with a ground state spin value of S = 4. A fitting of the reduced magnetization data using ANISOFIT 2.0[117] led to a zero field splitting parameter of $D_{Ni} = -0.24$ cm^{-1} (Figure 18). Although a negative value gave a slightly better fit, we realize that this method is not absolutely reliable for determining the sign of D. The field dependence of magnetization at 1.8 K was fitted to the Brillouin function for S = 4 and $g_{avg} = 2.15$ (Figure 19). Given that previously reported cyanide compounds with the same metal ions have been reported to exhibit single molecule magnetic behavior,[78] compound **1** was subjected to AC magnetic susceptibility studies. Indeed, the sample exhibits a weak frequency-dependent out-of-phase signal which hints at possible SMM behavior (Figure 18 inset), but, as this criterion is not definitive (particularly when there is no maximum), the

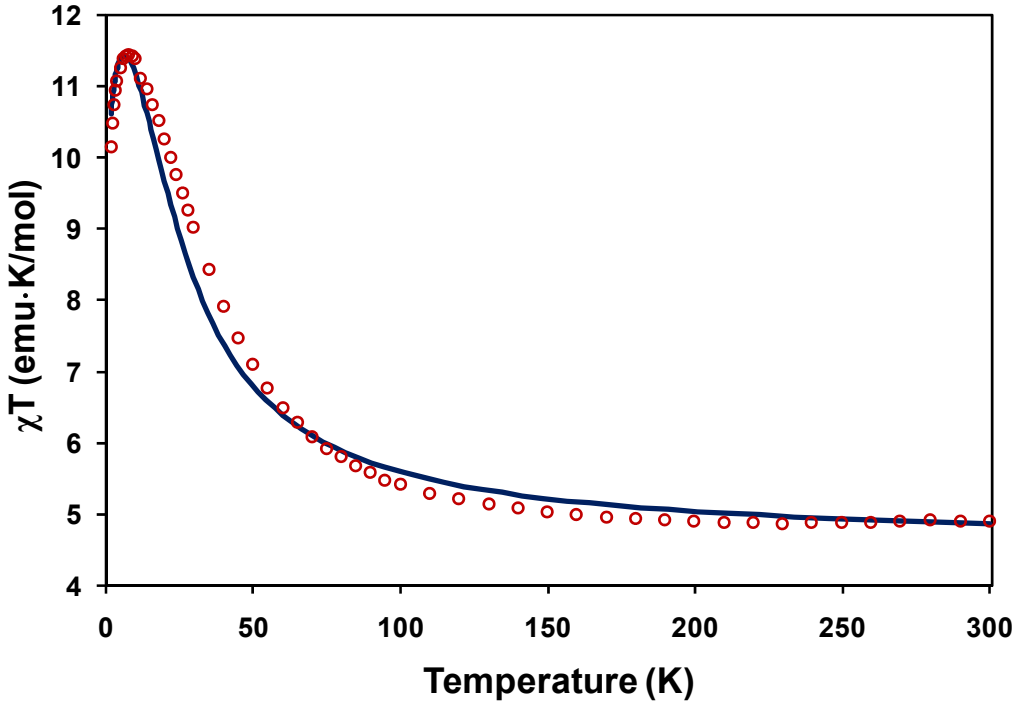

Figure 17. Temperature dependence of the χT product for **1** (O). The solid line corresponds to the MAGPACK simulation (g_{Ni} = 2.25, g_W = 2.0, J = 9.5 cm^{-1}, zJ' = -0.02 cm^{-1}, $R2$ = 0.998). Inset: Field dependent magnetization. The solid line corresponds to the best fit using MAGPACK.

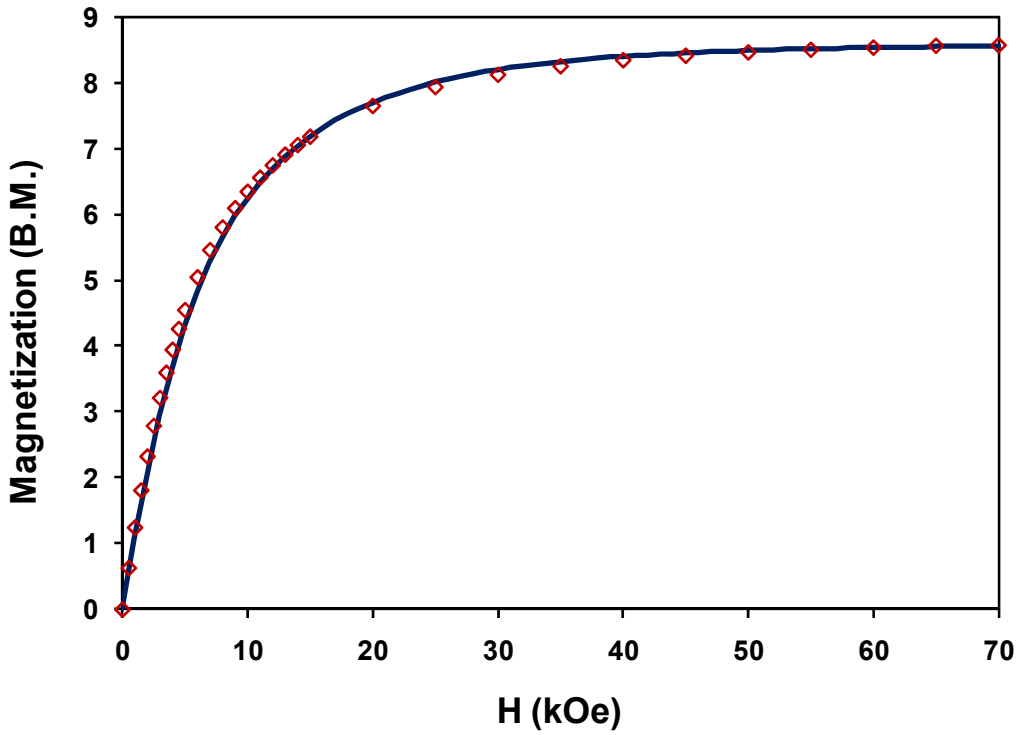

Figure 18. Field dependent magnetization for compound **1**. The solid line corresponds to the best fit using MAGPACK: S = 4, g = 2.15, D = - 0.22 cm^{-1}.

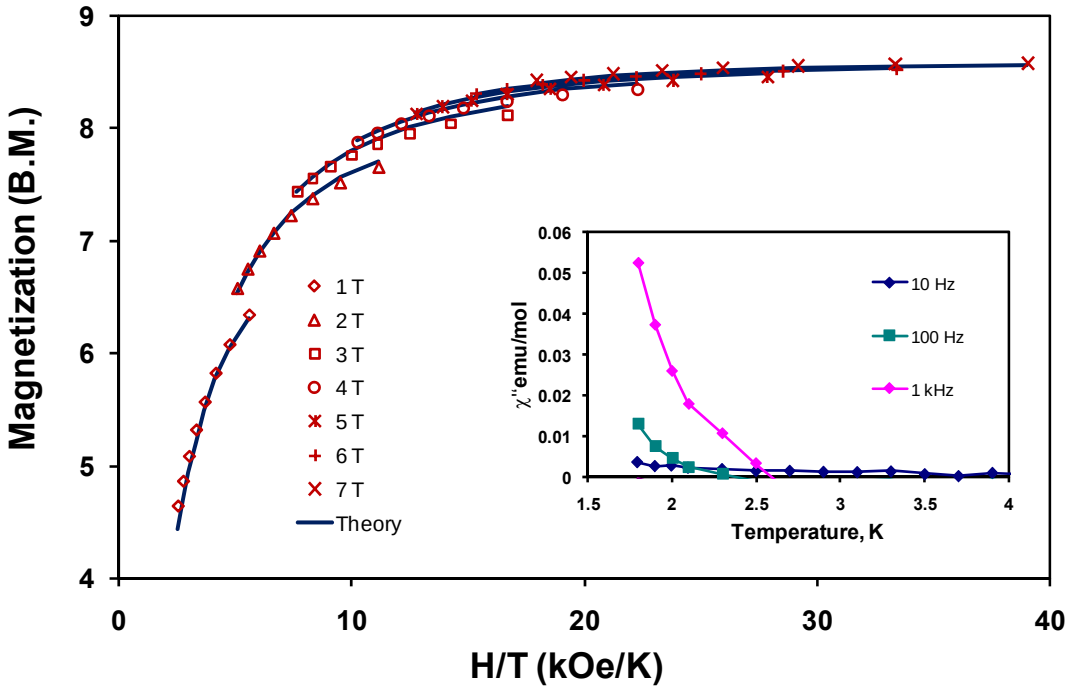

Figure 19. Reduced magnetization data for **1** at different external fields. Lines show the best-fit assuming S = 4, g_{avg} = 2.15, and D = -0.24 cm^{-1}. Inset: Imaginary part (χ'') of AC magnetic susceptibility at different frequencies under applied magnetic field H_{AC} = 3 Oe and H_{DC} = 0 Oe (solid lines are guides for the eye).

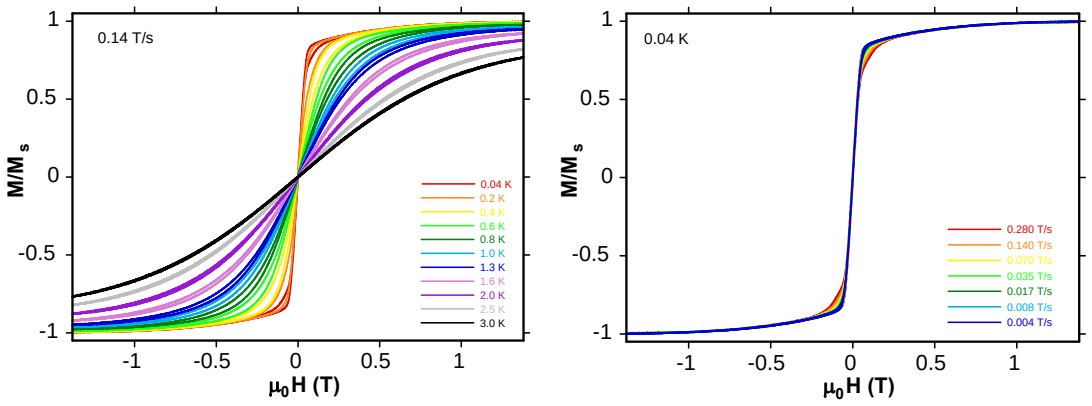

Figure 20. Magnetization data from Micro-SQUID measurements for a crystal of **1** with a variation in temperature at a constant scan rate of 0.14T/s (left) and with a variation of the scan rate at a constant temperature of 0.04 K (right).

behavior was further probed using a micro-SQUID apparatus at temperatures below 1 K. Temperature dependent scans (Figure 20) revealed that, down to 0.04 K, there is essentially no hysteresis, incontrovertible evidence that the cluster is *not* a single molecule magnet. As has been pointed out many times by others in the field, the beginning of an out-of-phase signal in the AC experiment is not sufficient evidence for concluding that a molecule is a SMM and this is a case where these data alone would have led to a false conclusion.

$[Ni^{II}(tmphen)_2]_3[Mo^{V}(CN)_8]_2\cdot 8CH_3OH\cdot 2H_2O$ (2). A cluster analogous to **1** with Mo^{V} was prepared, and the properties were found to be quite similar. The χT value for **2** at 300 K is 4.81 emu mol^{-1} K (Figure 21), which is slightly higher than the spin-only value expected for two uncoupled Mo^{V} and three Ni^{II} ions (χT = 4.68 emu mol^{-1} K). As in the case of the W^{V} derivative, the χT value increases at lower temperatures, an indication of ferromagnetic coupling between the Ni^{II} and Mo^{V} ions. A MAGPACK simulation of the χT *vs.* T data based on the Hamiltonian (eqn (1)) with the parameter g_{Mo} = 2.00 led to g_{Ni} = 2.23, zJ' = −0.005 cm^{-1}, and an isotropic exchange constant J = 10 cm^{-1} which is similar to the value for compound **1**. The χT value reaches a maximum of 11.56 emu mol^{-1} K at 1.8 K, which supports the ground state spin value of S = 4. The field dependence of magnetization at 1.8 K was fitted using MAGPACK for S = 4 and g_{avg} = 2.15 (Figure 21 inset). The cluster did not exhibit any appreciable zero field splitting based reduced magnetization data. Indeed, no evidence for a frequency dependent signal in the AC susceptibility data was detected.

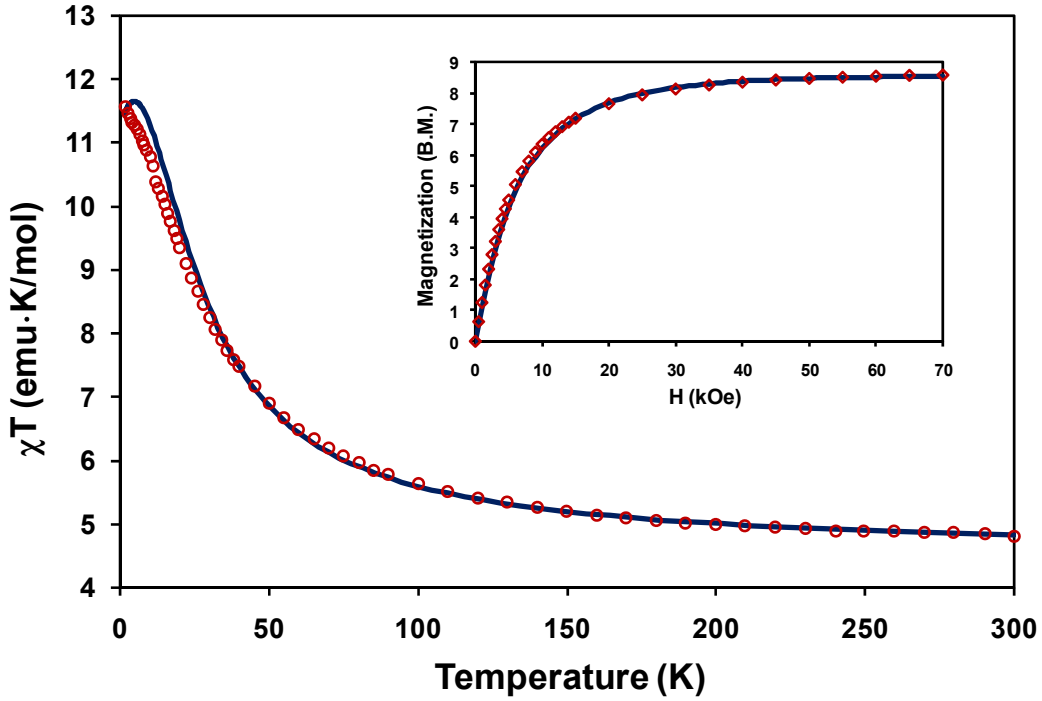

Figure 21. Temperature dependence of the χT product for **2** (O). The solid line corresponds to the MAGPACK simulation (g_{Ni} = 2.23, g_{Mo} = 2.0, J = 10 cm^{-1}, zJ' = -0.005 cm^{-1}, $R2$ = 0.999). Inset: Field dependent magnetization: The solid line corresponds to the best fit to the Brillouin function (S = 4, g_{avg} = 2.15).

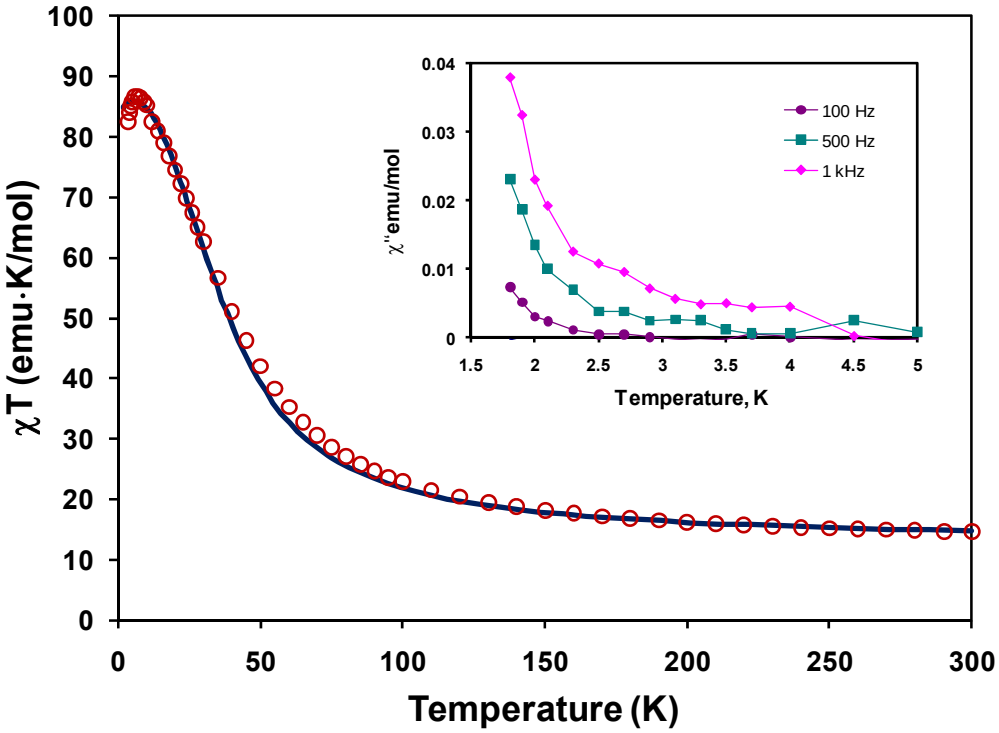

Figure 22. Temperature dependence of the χT product for **3** (O) The solid line corresponds to the MAGPACK simulation (g_{Ni} = 2.12, g_W = 2.0, *J* = 12.0 cm-1, *J′* = -0.005 cm-1, *z*J' = -0.0006 cm-1, *R*2 = 0.999. Inset: Imaginary part (χ") for **3** of AC magnetic susceptibility at different frequencies under applied magnetic field H_{AC} = 3 Oe and H_{DC} = 0 Oe (solid lines are guides for viewing, not fit parameters).

$[Ni^{II}_9(tmphen)_6(CH_3OH)_6(H_2O)_6W^{V}_6(CN)_{48}]\cdot 6DMF$ (3). The room temperature χT value for **3** is 14.28 emu mol^{-1} K (Figure 22), slightly higher than expected for a spin only case of six uncoupled W^V (S = 1/2) and nine Ni^{II} (S = 1) ions (χT = 12.36 emu mol^{-1} K) due to spin orbit coupling from the W^V centers. As the temperature is lowered, the χT value increases from room temperature, slowly at first, then rapidly to reach a maximum of 86.62 emu mol^{-1} K at 6 K which corresponds to the ground state spin value of S = 12. The magnetic interactions between the nearest neighbor magnetic centers were modeled by using an upgraded version of MAGPACK. Using g_W = 2.00 we obtained g_{Ni} = 2.12, $zJ' = -0.0006$ cm^{-1} and an isotropic exchange constant J_{W-Ni} = 12 cm^{-1}. These values for g and *J* are reasonable and correspond well with compounds **1** and **2**.[57] The field dependence of magnetization at 1.8 K was fitted to the ground state S = 12 with g_{avg} = 1.91, (Figure 23 inset). The χT data combined with the field dependent magnetization data support the assignment of ferromagnetic interactions between the Ni^{II} and W^V centers. A fitting of the reduced magnetization plot (Figure 23) of data measured between 1.8 to 4 K with variable fields ranging from 1–7 T using the ANISOFIT 2.0 software led to an assignment of the anisotropy of the cluster as D = −0.039 cm^{-1}. The magnetization reversal dynamics of compound **3** were probed by AC magnetic susceptibility measurements which revealed an out of phase signal in χ_m", characteristic of SMM behavior (Figure 22, inset). The low D value combined with the ground state spin value leads to a theoretical barrier height of only 5.6 K, based on $\Delta E = S_z^2|D|$. Given the low barrier, it was necessary to obtain magnetic data below 2 K. Magnetization data

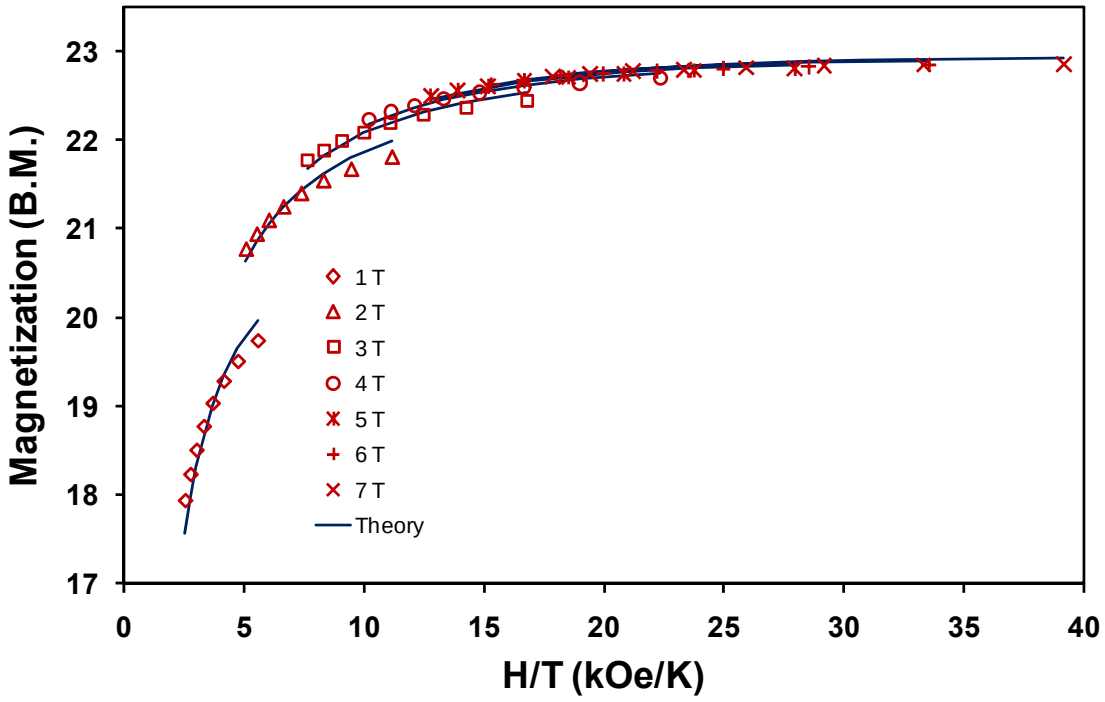

Figure 23. Reduced magnetization data for **3** under the application of different external fields. The lines indicate the best-fit for S = 12, g_{avg} = 1.91, and D = - 0.039 cm^{-1}. Inset: Field dependent magnetization of **3**. The solid line corresponds to the best fit using MAGPACK: S = 12, g_{avg} = 1.91.

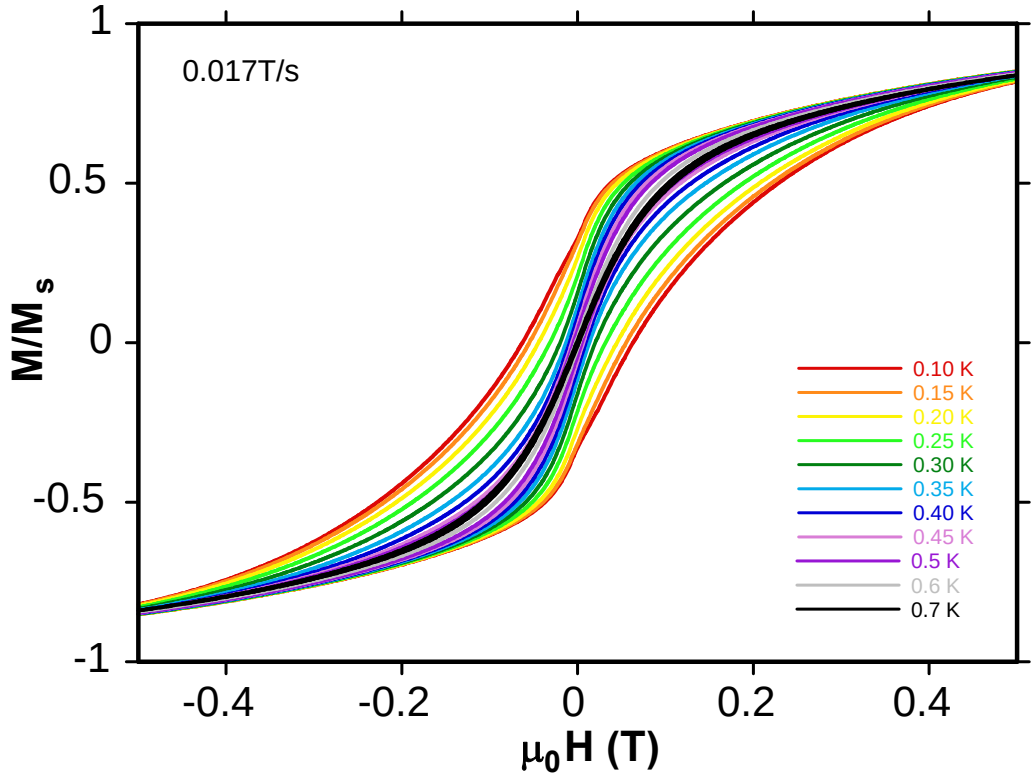

Figure 24. Micro-SQUID measurements from 700 to 100 mK at a field sweep rate of 0.017 T s^{-1}. Sample shows coercivity at zero field indicating remnant magnetization, the required behavior for a magnet, in this case proving the material is an SMM.

were collected on easy-axis oriented single crystal samples using a micro-SQUID apparatus and the data (Figure 24) revealed hysteretic behavior with strong temperature and sweep rate dependent coercivity, confirming that compound **3** is a SMM below 1 K. **$[Ni^{II}_9(tmphen)_6(CH_3OH)_6(H_2O)_6Mo^{V}_6(CN)_{48}]\cdot 6DMF$ (4).** The χT value at 300 K for **4** is 14.37 emu mol^{-1} K (Figure 25) which is slightly higher than expected for a spin only case of six uncoupled Mo^V and nine Ni^{II} ions (χT = 12.36 emu mol^{-1} K) due to the spin orbit coupling of the Mo^V ions. As the temperature decreases, the χT value continuously increases reaching a maximum of 82.01 emu mol^{-1} K at 6 K and decreases thereafter. The maximum observed corresponds to the stabilization of the high-spin ground state of S = 12. The abrupt drop from the maximum can be attributed to the zero field splitting of the Ni^{II} atoms in the cluster. The magnetic interactions between the nearest neighbor magnetic centers were modeled, as in the previous example, with an upgraded version of MAGPACK, assuming a g_{Mo} = 2.00 which led to a g_{Ni} = 2.12, zJ' = −0.005 cm^{-1} and an isotropic exchange constant $J_{Mo–Ni}$ = 12.2 cm^{-1}. The field dependent magnetization data supported the assignment of ferromagnetic interactions between the Ni^{II} and Mo^V centers. The field dependence of magnetization at 1.8 K was fit using MAGPACK for S = 12 and g_{avg} = 1.93 (Figure 26). A fitting of the reduced magnetization plot (Figure 25, inset) for a sample of **4** measured from 1.8 to 4 K with variable fields ranging from 1–7 T with ANISOFIT 2.0 led to the D value 0.053 cm^{-1}. As was the case for the Ni_3Mo_2 TBP cluster, the AC data did not contain an out-of-phase signal. This trend wherein only the W^V congener appears to exhibit SMM behavior was also noted for bipyridine modified Ni_9M_6 clusters.[78, 104] Recently Zhang *et al.*[109] published a detailed theoretical

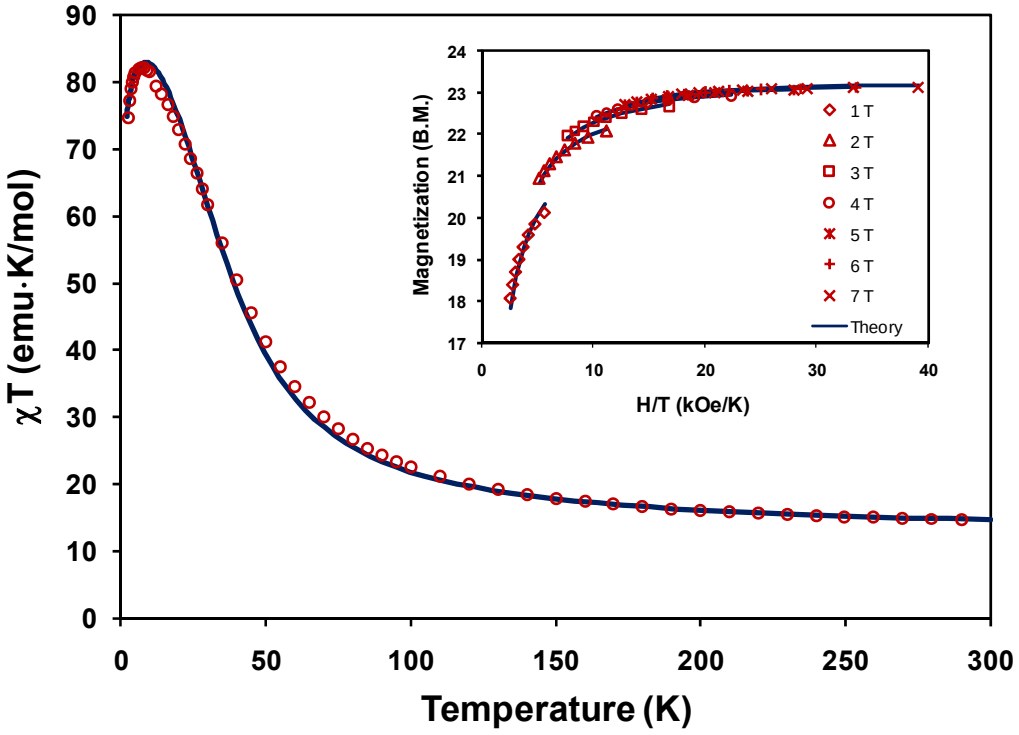

Figure 25. Temperature dependence of the χT product for **4** (O). The solid line corresponds to the MAGPACK simulation (g_{Ni} = 2.12, g_{Mo} = 2.0, J = 12.2 cm^{-1}, J' = -0.005 cm^{-1}, zJ' = -0.005 cm^{-1}, $R2$ = 0.999). Inset: Reduced magnetization data for **4** with different external fields. Lines show the best-fit assuming S = 12, and D = 0.053 cm^{-1}.

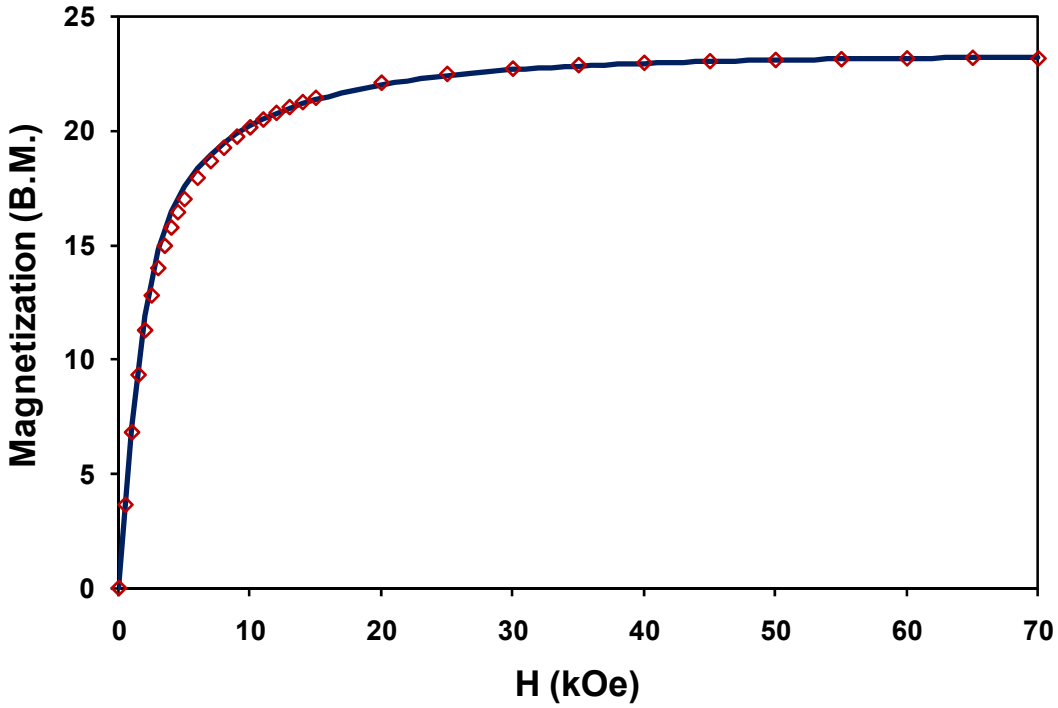

Figure 26. Field dependent magnetization data for **4**. The solid line corresponds to the best fit using MAGPACK: S = 12, g = 1.94, D = + 0.07 cm^{-1}.

Table 4. Summary of magnetic data for compounds **1-4.**

Compound	J_{avg}/cm^{-1}	D/cm^{-1}	Ref.
Ni_3W_2 (**1**)	9.5	−0.24	[118]
Ni_3Mo_2 (**2**)	10	~0	[118]
Ni_9W_6 (**3**)	12.0	−0.034	[118]
Ni_9Mo_6 (**4**)	12.2	0.053	[118]
Ni_9W_6	12.4	—	[109]
Ni_9Mo_6	11.9	—	[109]
Ni_9W_6	12.8	—	[119]

study of the Ni_9M_6 systems where M = Mo, W. Combining theoretical calculations with experimental results is a crucial step in understanding not only the exchange pathways but what factors affect SMM behavior. The same group reported a DFT based approach to probe the exchange coupling and calculated the values to be 12.4 cm^{-1} and 11.9 cm^{-1} for the Ni_9W_6 and Ni_9Mo_6, respectively. Both apical and equatorial *J* values were calculated and, when combined to an average *J* value for the cluster for comparison, the calculated parameters are in good agreement with the present experimental fits for **3** and **4**. In addition, the Ni_9W_6 cluster, $\{Ni^{II}[Ni^{II}(CH_3OH)_3]_8[\mu\text{-}CN]_{30}[W^{V}(CN)_3]_3\}$, was studied by polarized neutron diffraction and DFT calculations by Gillon *et al.*[119] Analysis of their data reveals that the average *J* value of the cluster is 12.8 cm^{-1} (based on the $-2J$ convention), also in excellent agreement with both Zhang *et al.* and the magnetic analysis reported herein. The parameters for these systems are summarized in Table 4.

Conclusions

A systematic study of four complexes based on octacyanometallates has been presented and it has been shown that the Ni_9W_6 cluster definitively exhibits SMM behavior. For the first time a detailed fitting of the magnetic properties of the pentadecanuclear clusters has been presented which allows for a good estimation of the exchange coupling between 3*d* and 4*d* or 5*d* metal ions through the cyanide ligand. In addition, this work has allowed us to corroborate current theoretical results providing an important bridge between theoretical predictions and experimental results. By studying

two sets of structurally identical clusters, a detailed comparison emphasizes that the nature of the octacyanometallate plays a key role in the presence of slow relaxation of the magnetization of the clusters. While it is obvious that the effect must be due to the differences in single ion and global anisotropy of these clusters, the basic or fundamental cause is still unknown. Further experimental work, in particular EPR studies, are required to obtain precise anisotropy parameters. On-going efforts in our laboratories involve the synthesis of other TBP clusters with Mn^{II}, Co^{II}, and Fe^{II} to elucidate their magnetic properties in an effort to add to the body of knowledge on the magnetochemistry of octacyanometallate based clusters of d^1 Mo^{V} and W^{V} ions.

CHAPTER III

TRIGONAL BIPYRAMIDAL CLUSTERS BASED ON $[Os(CN)_6]^{3-}$ AND $[Ru(CN)_6]^{3-}$ BUILDING BLOCKS

Introduction

As mentioned in the previous chapter and the introduction, the use of 4d and 5d metals in the chemistry of molecular magnetism is of high interest due to their single ion anisotropies. Currently the only molecular clusters based on homoleptic cyanide building blocks of the 4d and 5d transition metals are octacyano- and heptacyanometallates based on Mo^{V}, W^{V}, Nb^{IV}, and Re^{IV} but they do not provide a useful comparison to the respective first row metals in the family which are mainly six-coordinate.[73, 74, 79] One of the most attractive group of metals allowing for a comparison between members of the same group is Group 8 because the Fe, Ru, and Os homoleptic cyanide complexes are known for both the divalent and trivalent oxidation states.[120-123] While the chemistry of both the ferrocyanide and ferricyanide ions has been one of the most prolific of the transition metals due to their abundance and stability, hexacyanoosmate(II/III) and hexacyanoruthenate(II/III) (with the exception of early work in the 1970's of Prussian Blue analogues of the divalent species),[124] have not been used to design discrete compounds. Moreover no known extended structures have been reported for the paramagnetic trivalent species. Over the years, several salts of the $[Ru^{III}(CN)_6]^{3-}$ and $[Os^{III}(CN)_6]^{3-}$ anions have been probed by X-ray crystallography, magnetism and spectroscopy, but no reactivity studies were reported.[121-123] The main

reason for the lack of activity is most likely the challenge in working with these species as they are not trivial to prepare. Moreover the Ru^{III} derivative is unstable in water.[123, 125]

Given the large body of work that has emerged from our laboratories regarding the synthesis and characterization of trigonal bipyramidal molecules, this geometric scaffold is clearly an excellent choice for comparing 3d complexes with the 4d and 5d congeners. A homologous series of Group 8 TBP's allows for a detailed comparison of the magnetic properties as a function of the role of the anisotropic metal. In this chapter five new TBP clusters, as well as a double trigonal bipyramidal cluster are reported for 4d and 5d hexacyanometallate building blocks, the first of their kind.

Experimental Section

Syntheses

Given our prior success in non-aqueous cyanometallate chemistry, we focused on a method for preparing useful organic soluble salts of hexacyanoruthenate(III) and hexacyanoosmate(III). By a modification of known literature procedures,[120] we prepared $K_4[M^{II}(CN)_6]$ (M = Ru, Os), in high yields and treated them with $Ce^{IV}(SO_4)_2$ in water to form the oxidized species. Addition of hot PPNCl (PPN = Bis(triphenylphosphine)iminium) to the aqueous solutions yielded pure samples of $PPN_3[M^{III}(CN)_6]$.[126] As previously mentioned, the $[Ru^{III}(CN)_6]^{3-}$ ion is unstable in water, and early attempts to synthesize this salt in large yields involved the sparging of a DMF solution with oxygen, which only resulted in incomplete oxidation.[127] Alternatively, this problem was solved by the addition of methanol to an aqueous

solution of $K_4[Ru^{II}(CN)_6]$ before the oxidant was added. The addition of methanol stabilizes the trivalent species as it forms, thus allowing for the isolation of the pure salt. The PPN salts are very soluble in alcohols, acetonitrile, dichloromethane, dimethylformamide, and nitromethane which opens up a realm of possibilities for their chemistry.

Reagents. $Ni(BF_4)_2 \cdot 6H_2O$, $Ni(NO_3)_2 \cdot 6H_2O$, $Mn(NO_3)_2 \cdot 4H_2O$, and $Mn(ClO_4)_2 \cdot 6H_2O$ and 3,4,7,8-tetrametylphenanthroline were purchased from Aldrich and used as received. Acetonitrile was dried over 3 Å sieves and distilled prior to use. $Cr_2(O_2CCF_3)_4 \cdot 2THF$ was prepared by reacting $CrCl_2$ and CF_3COONa in stoichiometric ratio in refluxing THF for 6 h. The solution was filtered and evaporated to dryness. The obtained purple solid was extracted with toluene. The solution was filtered, and the solvent was removed *invacuo* to obtain the final product. Concentrations of the reactants given below were found to produce the best quality crystals for structural determination by X-ray crystallography for the reactions which yielded crystals, however the yields have not been optimized in all cases.

$K_4Os(CN)_6$. A sample of OsO_4 (1g, 4 mmol) obtained from a sealed ampoule was carefully added to a 125 mL Erlenmeyer flask containing 50 mL of water. The ampoule was broken along the score mark and the contents were poured into the flask in a well ventilated fumehood; the fragments of the ampoule were then added to the flask as well to ensure complete transfer. **CAUTION: OsO_4 sublimes near room temperature and is highly toxic. Caution must be used when handling this material.** The compound OsO_4 does not readily dissolve in the water, but upon the addition of KOH (2 g, 36 mmol) an

instantaneous reaction occurs to yield a red brown solution. After stirring for 5-10 minutes to allow for complete consumption of the OsO_4, the glass fragments were removed and KCN was added (6 g, 92 mmol) which led to the formation of darker red solution. The reaction was heated to near boiling which led to a color change from dark red to dark green with gradual lightening occurring as the contents of the flask were taken to dryness. The flask was then heated on a hot plate after the material was dry and the solid changed from purple to white. A 30 mL aliquot of H_2O 25-30 was then added to re-dissolve the solid and the heating was continued to the point of dryness once again until all of the solid is snow white. The compound is then redissolved in 50 mL of water to give forming a colorless solution which is treated with 80 mL of methanol to yield a white precipitate. The solid was collected by filtration and washed with methanol and diethyl ether. Yield 1.8g (89%).

$K_4Ru(CN)_6$. $RuCl_3$ (1g, 4.8 mmol) was added to a 125 mL Erlenmeyer flask containing 50 mL of water to give red-green solution and treated with KOH (2g, 36 mmol) to form a red brown solution. After the mixture had been stirred for 5-10 minutes, KCN was added (6g, 92 mmol) to give a darker red solution and the flask was heated to near boiling and taken to dryness. The dry flask was further heated on a hot plate until the color changed from purple to white. A 25-30 mL aliquot of H_2O was added to redissolve the solid and the solution was evaporated to dryness. Once dry, the flask was heated until the solids were converted to a snow white material. The compound was redissolved in 50 mL of water and treated with 80 mL of methanol to give a white

precipitate which was removed by suction filtration and washed with methanol followed bydiethyl ether. Yield 1.6g (81%).

$[PPN]_3[Os(CN)_6]$. A sample of $K_4Os(CN)_6$ (1g, 2mmol) was dissolved in 50 mL of H_2O and stirred for 20 minutes to give a clear, colorless solution and treated with $Ce^{IV}(SO_4)_2$ (0.662g, 2mmol) which led to an instantaneous change to yellow and then dark green and finally back to bright yellow. The yellow was quickly filtered and then slowly added to a hot solution of PPNCl (3.4g, 6mmol) which led to the formation of a yellow solid which was filtered, washed with 3 x 100 mL of hot water to dissolve impurities and finally washed with 100 mL of diethyl ether and vacuum dried. Anal. Calcd for $C_{114}H_{90}N_9OsP_6$: N, 6.42; C, 69.7; H, 4.62. Found: N, 6.44; C, 68.98; H, 4.62%.

$[PPN]_3[Ru(CN)_6]$. A sample of $K_4Ru(CN)_6$ (0.75g, 1.8 mmol) was dissolved in 60 mL of H_2O and 40 mL of MeOH and stirred for 5 minutes after which time $Ce^{IV}(SO_4)_2$ (0.6g, 1.8 mmol) was added to give a yellow solution. After stirring for 45 minutes the solution was quickly filtered and slowly added to a hot solution of PPNCl (3.1g, 5.4 mmol). Upon addition, a yellow precipitate had formed which was filtered, washed 3 x 250 mL of hot water to remove impurities. Finally the product was washed with 100 mL of diethyl ether and vacuum dried. Anal. Calcd for $C_{114}H_{90}N_9RuP_6$: N, 6.73; C, 73.0; H, 4.84. Found: N, 6.69; C, 72.13; H, 6.69%.

$[Ni(tmphen)_2]_3[Os(CN)_6]_2 \cdot 12H_2O$ (5). A quantity of $Ni(BF_4)\cdot 6H_2O$ (0.136 g, 0.402 mmol) and tmphen (0.213 mg, 0.904 mmol) were combined in 80 mL of acetonitrile, and the solution was stirred for 30 minutes in air. The resulting clear pink solution was quickly combined with a solution of 0.70 g (0.356 mmol) of $[PPN]_3[Os(CN)_6]$ in 80 mL

of acetonitrile in a 500 mL screwcap jar. The mixture was left to stand undisturbed for 4-5 days. After this period of time, a crop of orange-red crystals suitable for X-ray diffraction was collected by filtration, washed with acetonitrile (3 x 30 mL). Yield 123 mg (29.6%) of crystals. Elemental analysis and TGA analysis indicated the presence of interstitial water molecules after exposure to air. Anal. Calcd for $C_{108}H_{114}Ni_3N_{24}O_9Os_2$ (12·H2O): O, 7.66; N, 13.43; C, 51.78; H, 4.83. Found: O, 6.84; N, 13.42; C, 51.76; H, 4.72%.

$[Ni(tmphen)_2]_3[Ru(CN)_6]_2 \cdot 12H_2O$ (6). A sample of $Ni(NO_3)\cdot 6H_2O$ (0.048 g, 0.165 mmol) and tmphen (0.068 mg, 0.287 mmol) were combined in 20 mL of acetonitrile and the solution was stirred for 30 minutes in air. The resulting clear pink solution was divided into two 10 mL portions and quickly combined with a solution of 0.20 g (0.107 mmol) of $[PPN]_3[Ru(CN)_6]$ in 20 mL of acetonitrile also split into two 10 ml portions, in two 20 mL vials which were left undisturbed for 4-5 days. After this period of time, a crop of orange-red crystals suitable for X-ray diffraction was harvested and washed with acetonitrile (3 x 30 mL). Yield 24 mg (21.2%) of crystals. Elemental analysis and TGA analysis indicated the presence of interstitial water molecules after exposure to air. Anal. Calcd for $C_{108}H_{114}Ni_3N_{24}O_9Ru_2$ (12·H_2O): O, 8.26; N, 14.46; C, 55.8; H, 5.21. Found:O, 8.82; N, 13.97; C, 55.40; H, 5.25%.

$[Mn(tmphen)_2]_3[Os(CN)_6]_2 \cdot 8H_2O$ (7). Samples of $Mn(NO_3)\cdot 6H_2O$ (0.043 g, 0.151 mmol) and tmphen (0.071 mg, 0.300 mmol) were combined in 20 mL of methanol, and the solution was stirred for 30 minutes in air. The resulting clear yellow solution was layered in thin tubes on solutions of 0.250g (0.127 mmol) of $[PPN]_3[Os(CN)_6]$ in 18 mL

of acetonitrile and 2 mL of H_2O in 6 thin tubes (5mm inner diameter). The tubes were left to stand undisturbed for 2 weeks after which time a crop of olive crystals suitable for X-ray diffraction were observed at the interface of the two solutions. The crystals were collected by filtration and washed with acetonitrile (3 x 10 mL). Yield 6 mg (4%) of crystals. Elemental analytical and TGA data indicated the presence of interstitial water molecules after exposure to air. Anal. Calcd for $C_{108}H_{114}Mn_3N_{24}O_9Os_2$ ($8\cdot H_2O$): N, 13.87; C, 53.51; H, 4.66. Found: N, 13.20; C, 53.86; H, 4.89%.

$[Mn(tmphen)_2]_3[Ru(CN)_6]_2\cdot 8H_2O$ (8). A sample of $Mn(ClO_4)_2\cdot 6H_2O$ (0.026 g, 0.1 mmol) was combined with tmphen (0.054 mg, 0.230 mmol) in 20 mL of acetonitrile and the solution was stirred for 10 minutes in air. The resulting clear yellow solution was quickly added to a solution of 0.150 g (0.08 mmol) of $[PPN]_3[Ru(CN)_6]$ in 20 mL of acetonitrile and stirred for 5 minutes during which time an olive green precipitate formed. The powder was collected by filtration and washed with acetonitrile (3 x 30 mL). Yield 36 mg (43%) yield.

$[Cr(tmphen)_2]_3[Ru(CN)_6]_2\cdot 8MeCN$ (9). A sample of $Cr_2(O_2CCF_3)_4\cdot 2THF$ (0.076 g, 0.1 mmol) was combined with two equivalents of tmphen (0.053 mg, 0.23 mmol) in 20 mL of acetonitrile and stirred for 30 minutes under in a N_2 filled dry box. The resulting clear dark green solution was divided into two 10 mL portions and each was quickly combined with 10 mL aliquots of a solution of 0.150 g (0.1 mmol) of $(PPN)_3[Ru(CN)_6]$ in 20 mL of acetonitrile. After being left to stand undisturbed for 2 days a crop of blue-green crystals suitable for X-ray diffraction was collected by filtration and washed with acetonitrile (3 x 30 mL). Yield 16 mg (19.2%) of crystals.

$[Co(tmphen)_2]_6[Ru(CN)_6]_3$ (10). A quantity of $CoCl_2$ (0.011 g, 0.09 mmol) was reacted with tmphen (0.048 mg, 0.2 mmol) in 20 mL of acetonitrile. After stirring for 30 minutes under a nitrogen atmosphere in the dry box, the resulting clear yellow solution was divided into two 10 mL portions and combined with 10 mL aliquots of a solution of 0.150g (0.1 mmol) of $[PPN]_3[Ru(CN)_6]$ in 20 mL of acetonitrile. After 5 days, a crop of red-orange crystals suitable for X-ray diffraction was collected by filtration and washed with acetonitrile (3 x 30 mL). Yield 9 mg (11%) of crystals.

Results and Discussion

Syntheses

Reactions between divergent hexacyanometallate anions, $[M^{III}(CN)_6]^{3-}$ (M = Ru, Os), and a convergent mononuclear precursor of the type $[M'^{II}(tmphen)_2X_2]^{0/2+}$ (M' = Cr, Mn, Ni; X = Cl, CH_3CN) produce pentanuclear, cyanide bridged complexes $[M'^{II}(tmphen)_2]_3[M^{III}(CN)_6]_2$. The compounds were prepared in air with the exception of the Cr_3Ru_2 molecule which was prepared in an inert atmosphere dry box. Elemental and TGA analyses support the conclusion that interstitial acetonitrile molecules are replaced with water molecules when the compounds are stored in air for analysis, which has been observed in previously reported TBP complexes as well- see TGA and elemental data noted in the experimental section.[37, 46] As such, all analysis of the magnetic properties, structure, and IR spectroscopic measurements were undertaken with precautions to limit exposure to air once the sample had been removed from the mother liquor.

An exception to the general synthetic method is the preparation of the Mn_3Os_2 analog. Typical materials of Mn^{II} were used in the typical methods that involve the use of methanol or DMF versus acetonitrile, but in all cases the reactions produced only powders. In addition, many trial combinations were performed using thin tubes as a vessel for the reaction to slow down the reaction time. Eventually the Mn_3Os_2 cluster was isolated by layering a mixture of the hexacyanoosmate in acetonitrile/water with the $Mn(tmphen)_2$ being dissolved in methanol and layered on top of the cyanometallate solution. Unfortunately, given the instability of the hexacyanoruthenate(III) ion in water over extended periods of time, these conditions were unsuitable for growing crystals of the Mn_3Ru_2 TBP. This situation notwithstanding, the reaction between $[Mn(tmphen)_2]^{2+}$ and $[Ru(CN)_6]^{3-}$ was performed using the same solvent conditions, except the reagents were rapidly combined to give an olive green precipitate. The powder proved to be amorphous but it was characterized by magnetic measurements and IR spectroscopy (Appendix A) which support the identity of the product as being a TBP cluster.

Single Crystal X-ray Studies

Trigonal Bipyramidal Clusters. With the exception of two compounds, the new TBP molecules (Table 5) crystallize in the $P2_1/c$ space group as found for previously 3d cyanometallate congeners. The equatorial $[M(tmphen)_2]^{2+}$ sites of each TBP are homochiral, *i.e.* each cluster is either Δ, Δ, Δ or Λ, Λ, Λ and the crystal contains a racemic mixture of the two optical isomers. The TBP clusters exist as π – dimers,

Table 5. Crystal structural data and refinement parameters.

Formula	**Ni_3Os_2**	**Ni_3Ru_2**	**Mn_3Os_2**
Space group	$P2_1/c$	$C2/c$	$P2_1/c$
Unit cell	a= *19.403(14)*Å b = 25.613(18) Å c =24.962(17) Å β = 98.152(10)	a = 25.57(2) Å b = 24.122(19) Å c = 22.722(18) Å □=□=*90* β = 109.426(13) °	a= *19.9739(16)* Å b = 25.284(2) Å c =24.2912(19) Å β = 99.5480(10)
Unit cell volume, V	12280(15) Å^3	13215(18) Å^3	12097.6(17) Å^3
Z	5	4	5
Density, ρ_{calc}	1.340 g/cm^3	1.228 g/cm^3	1.460 g/cm^3
Abs. coeff., μ	2.570 mm^{-1}	0.701 mm^{-1}	3.053 mm^{-1}
Crystal color and habit	Orange-brown needle	Red-orange needle	Olive green needle
Crystal size, mm^3	.40x.20x.05	0.22x0.23x0.10	.18x.17x.10
Temperature	110 K	110 K	110 K
Radiation, λ	Mo-Kα, 0.71073 Å	Mo-Kα, 0.71073 Å	Mo-Kα, 0.71073 Å
Min. and max. θ	1.33 to 24.16 º	1.34 to 28.41 º	1.17 to 28.32 º
Reflections collected	83299 [R_{int} =.1331]	62957 [R_{int} =0.0898]	141255 [R_{int} =.0680]
Independent reflections	19015	15980	29441
Data/parameters/restraints	19015 /1308 /0	15980 /702 /0	29441 /1279 /0
R [$F_o > 4\sigma(F_o)$]	R_1 = 0.0892 wR_2 = 0.2310	R_1 = 0.0864 wR_2 = 0.2363	R_1 = 0.1026 wR_2 = 0.2712
G.o.f. on F^2	1.149	1.024	1.141
Max./min. residual densities, e·Å^{-3}	2.95, -1.98	2.17, -0.75	3.86,-2.89
Formula	**Cr_3Ru_2**	**Co_6Ru_3 DTBP**	
Space group	$P3221$	$P2_1/c$	
Unit cell	a = 24.568(5)Å b = 24.568(5) Å c =20.356(6) Å □=□=*90*, β=120°	a = 19.042(8)Å b =25.260(12) Å c =24.803(14) Å β =97.392(14) °	
Unit cell volume, V	10641(4) Å^3	11831(10) Å^3	
Z	13	5	
Density, ρ_{calc}	1.734g/cm^3	1.407 g/cm^3	
Abs. coeff., μ	1.594 mm^{-1}	0.675 mm^{-1}	
Crystal color and habit	Red-purple needle	Red-purple needle	
Crystal size, mm^3	0.14x0.11x0.05		
Temperature	110 K	110 K	
Radiation, λ	Mo-Kα, 0.71073 Å	Mo-Kα, 0.71073 Å	
Min. and max. θ	0.96 to 28.62 º	1.08 to 28.29º	
Reflections collected	96292 [R_{int} =0.211]	84792 [R_{int} =0.141]	
Independent reflections	17627	27498	
Data/parameters/restraints	17627 / 721 /0	27498 /1246 /31	
R [$F_o > 4\sigma(F_o)$]	R_1 = 0.1287 wR_2 = 0.2877	R_1 = 0.0916 wR_2 = 0.2230	
G.o.f. on F^2	0.973	1.007	
Max./min. residual densities, e·Å^{-3}	1.59, -2.30	1.82, -1.42	

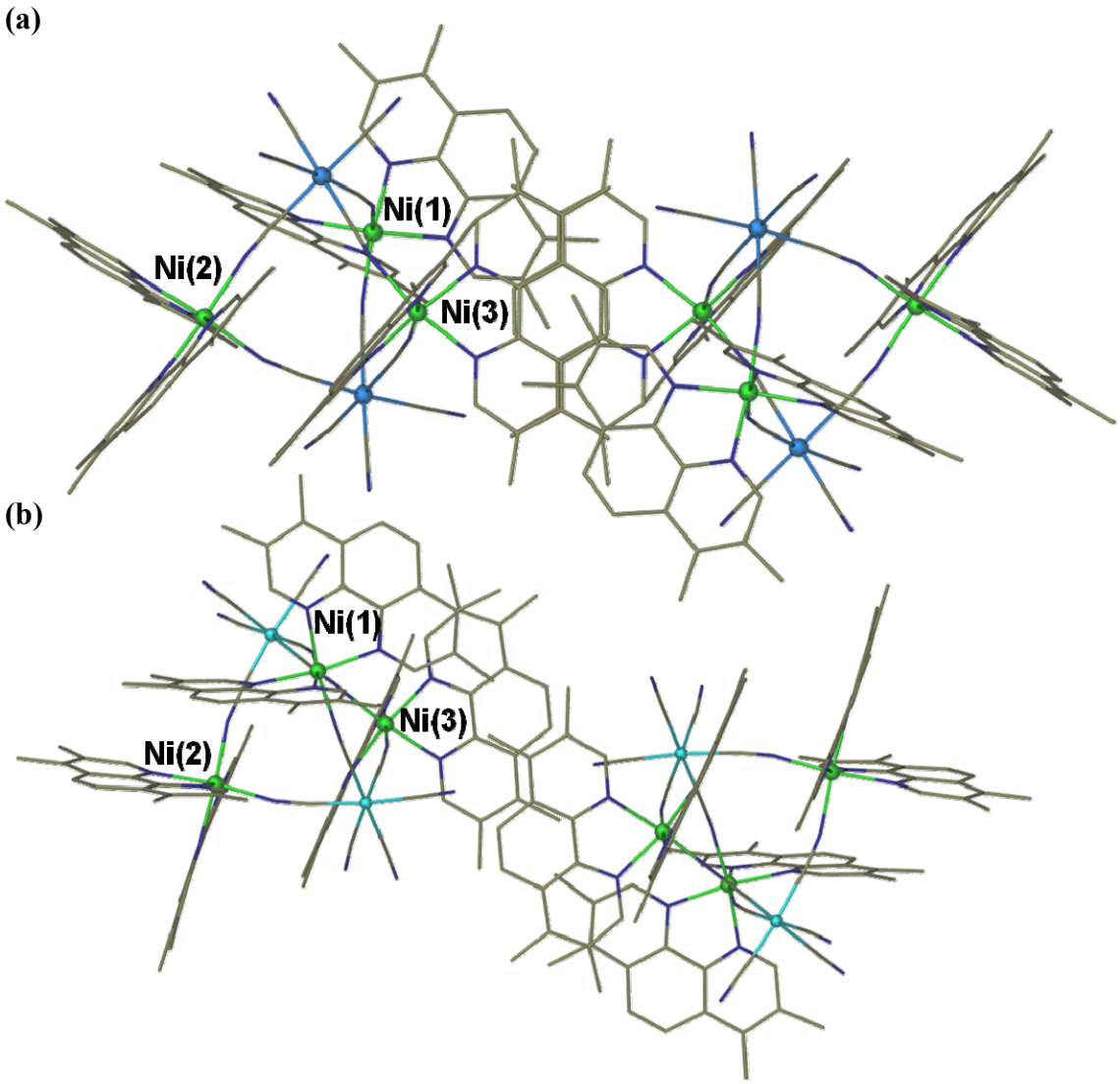

Figure 27. (a) Depiction of the π-overlap pattern that leads to sets of dimers for the Ni_3Os_2 TBP cluster in the packing arrangement and (b) depiction of a pair of Ni_3Ru_2 TBP clusters that do not exhibit significant π-overlap.

composed of tmphen units that engage in π stacking interactions (Figure 27a). The only exception to this situation is the Ni_3Ru_2 TBP cluster which crystallizes in the space group $C2_{/c}$ and does not engage in intermolecular π-stacking interactions (Figure 27b). The only other structural "outlier" is the Cr_3Ru_2 TBP which forms crystals in the hexagonal space group of $P3_221$ with a higher symmetry for the TBP core. The molecule exhibits a nearly perfect C_3 axis of symmetry (Figure 28).

$[Co(tmphen)_2]_6[Ru(CN)_6]_3$ An unexpected product was encountered in the course of these studies which was isolated as a few crystals. Although the structure was determined, the limited quantity precludes evaluation of physical and magnetic properties. Specifically, the reaction of the $[PPN]_3[Ru(CN)_6]$ with $CoCl_2$ and tmphen did not lead to crystals of the expected TBP but instead produced a low yield of crystals of a double trigonal bipyramidal cluster composed of three $[Ru(CN)_6]^{4-}$ and six $[Co(tmphen)_2]^{2+}$ units, namely a nonanuclear cluster (Figure 29). The typical TBP cluster is thought to be the main product isolated under typical conditions due to the neutrality of the cluster (two $[M^{III}(CN)_6]^{3-}$ units combine with 3 $[M^{II}(tmphen)_2]^{2+}$ units for an overall charge of zero on the cluster). In the case of the double TBP, those oxidation states would not lead to a neutral cluster, but if the units are composed of $[M^{II}(CN)_6]^{4-}$, then this would, in fact, lead to an overall neutral cluster. In this case the initial oxidation state of the Ru is not the desired paramagnetic oxidized Ru^{III} species, but rather Ru^{II}. These results hint at the possibility of obtaining these DTBP structures by using only divalent precursors rather than a mixture of trivalent and divalent, but, to date, no further examples have been prepared.

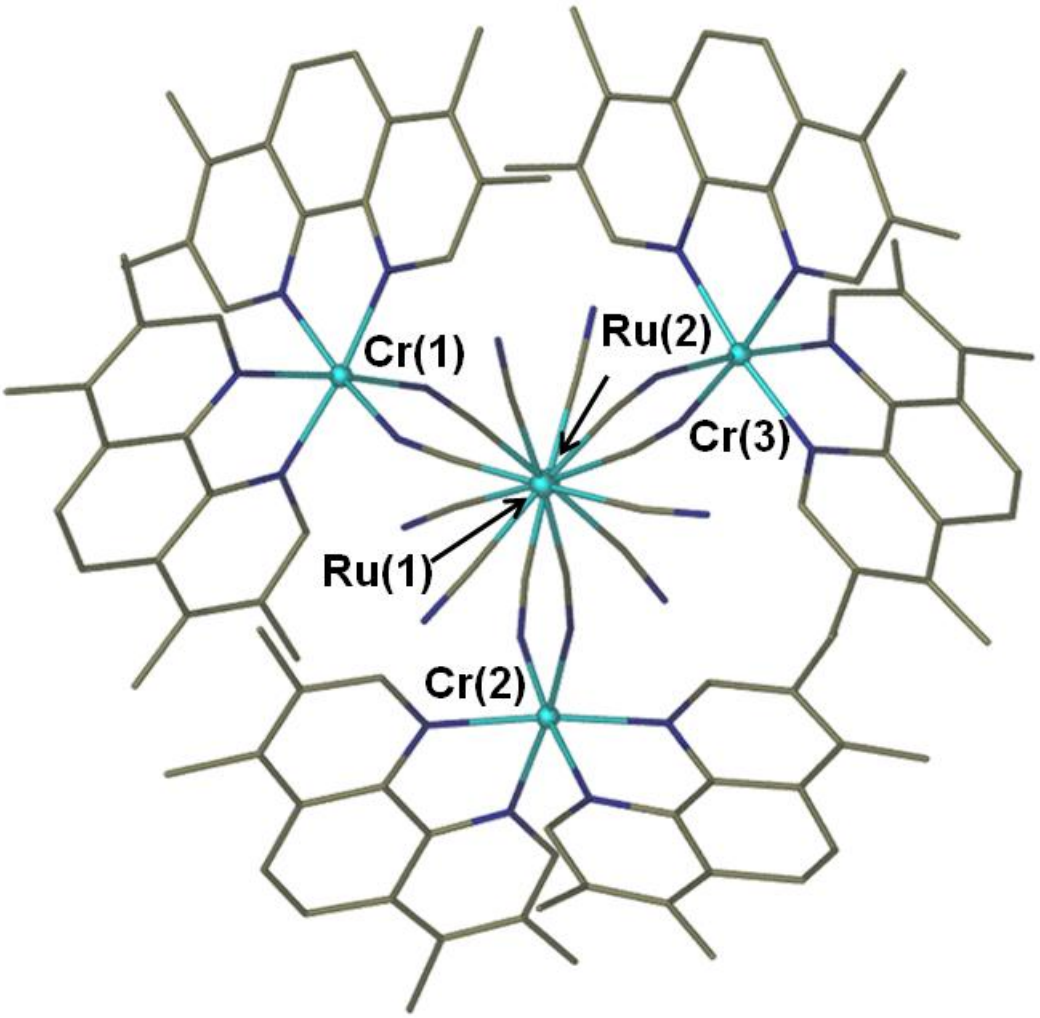

Figure 28. Axial view of the Cr_3Ru_2 TBP cluster that emphasizes the near perfect C_3 symmetry looking down the axial direction of the cyanometallates.

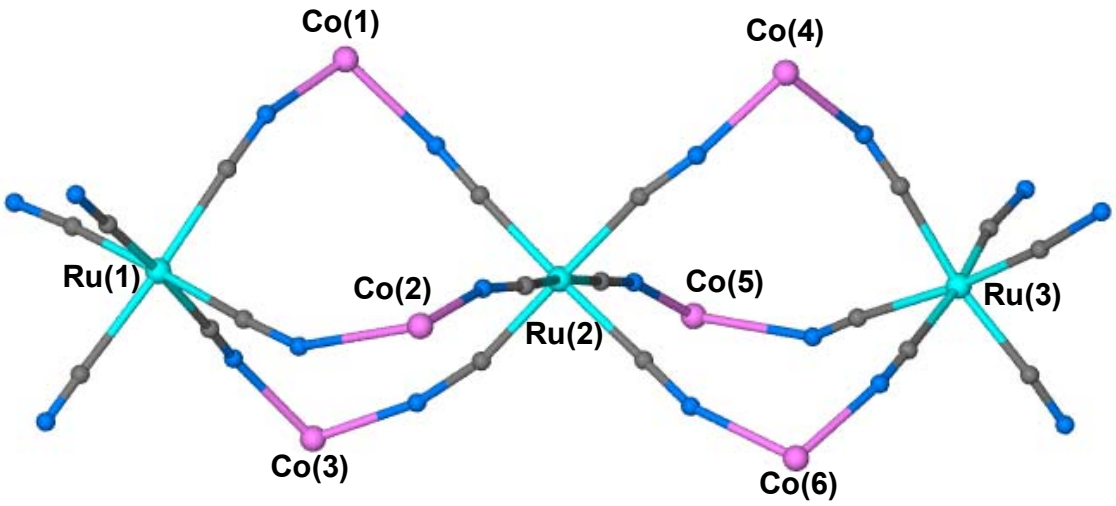

Figure 29. Molecular structure of the Co_6Ru_3 double TBP cluster. Tmphen ligands were removed so that the core of the molecule can be seen clearly.

Infrared Spectroscopy

Measurements were performed on a Thermo-nicolet FTIR spectrometer on nujol mulls between two KBr plates. The data are summarized in Table 6. The $[PPN]_3[Os^{III}(CN)_6]$ and $[PPN]_3[Ru^{III}(CN)_6]$ salts exhibit doublets at 2085, 2076 cm^{-1} and 2093, 2084 cm^{-1} respectively. As expected, these values represent a shift to higher frequencies from the divalent analogs where $[PPN]_4[Os^{II}(CN)_6]$ and $[PPN]_4[Ru^{II}(CN)_6]$ exhibit CN stretches of 2044 and 2056 cm^{-1} respectively. The CN stretching frequencies of the PPN salts are in good agreement with the TBA salts.[128] The isostructural TBP complexes of Ni_3Os_2 and Mn_3Os_2 exhibit a terminal CN stretch at 2099 and 2097 cm^{-1} which are slightly shifted from the CN stretch for the free $[Os(CN)_6]^{3-}$ anion located at 2085 cm^{-1}. Each TBP exhibits two bridging modes: 2129 and 2148 for Ni_3Os_2 and 2119 and 2142 cm^{-1} for the Mn_3Os_2 derivative. The Ni_3Ru_2 TBP exhibits a broad terminal stretch at 2057 and two bridging cyanide features at 2106 and 2138 cm^{-1}. The slightly lower energy of these stretches is thought to be due to the hydrogen bonding interactions of the CN ligands with nearby tmphen ligands. The difference between the two Ni TBP clusters originates from the change in structure, with the Ni_3Ru_2 TBP engaging in more hydrogen bonding interactions between the terminal cyanides on the cluster with H atoms on the tmphen ligands in the neighboring clusters. This is due to the closer proximity of the Ni_3Ru_2 cluster (Figure 30). Despite not having structural data for the Mn_3Ru_2 compound, the IR data reveal a markedly similar behavior to the Ni_3Ru_2 cluser

Table 6. IR stretches in the $\nu_{C\equiv N}$ region.

Compound	**$\nu_{C\equiv N}$ in cm^{-1}**
$PPN_4Os(CN)_6$	2048 (s)
$PPN_4Ru(CN)_6$	2055 (s)
$TBA_4Ru(CN)_6$	2040[127] (s)
$PPN_3Os(CN)_6$	2076,2085 (s)
$PPN_3Ru(CN)_6$	2084,2093 (s)
$TBA_3Ru(CN)_6$	2090[127] (s)
Ni_3Os_2 TBP	2099 (s), 2129 (w), 2148 (w)
Ni_3Ru_2 TBP	2057 (s), 2106 (w), 2138(w)
Mn_3Os_2 TBP	2097(s), 2119(w), 2142(w)
Mn_3Ru_2 TBP	2055(s), 2096(w), 2126(w)

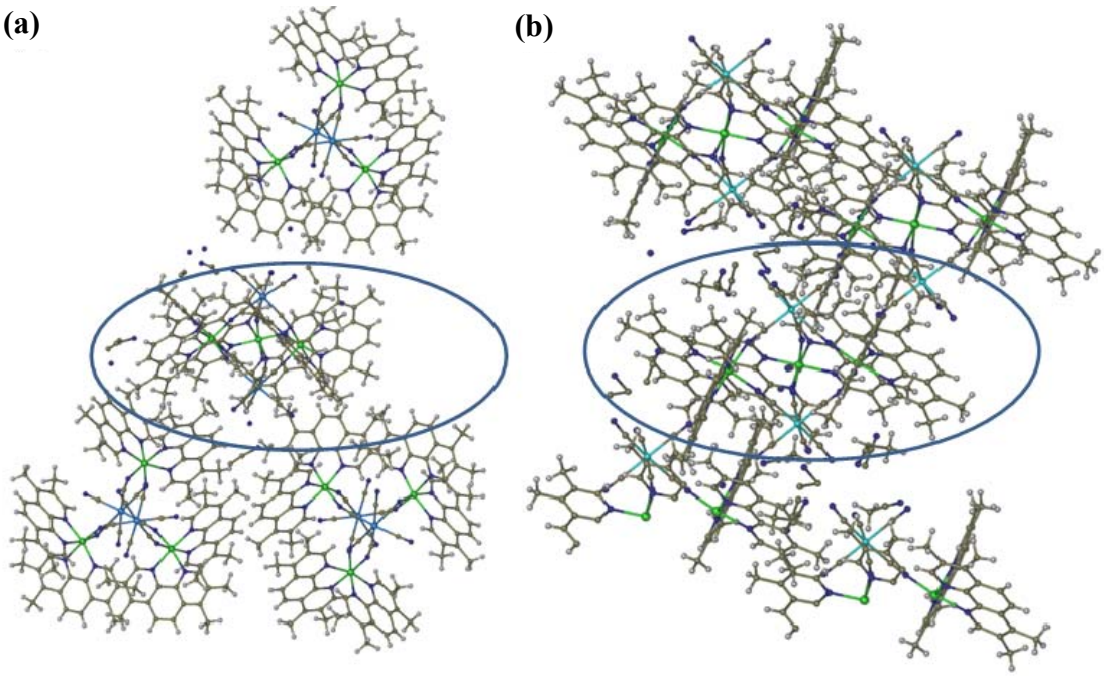

Figure 30. (a) Axial packing of Ni_3Os_2 TBP (b) axial packing of Ni_3Ru_2 showing stronger interactions along the axial sites.

with a terminal stretching mode at 2056 cm^{-1} and the two cyanide bridging modes at 2096 and 2126 cm^{-1}, which supports the conclusion that the Mn_3Ru_2 product has a similar structure as the Ni_3Ru_2 compound. In Chapter V, a discussion will be presented regarding comparisons between Prussian Blue analogs based on these metal ion combinations with the TBP clusters.

Magnetic Properties

The magnetic properties of the clusters were investigated by magnetic susceptibility measurements in the temperature range of 2–300 K and field dependent magnetization measurements in applied fields up to 7 Tesla. AC susceptibility measurements were carried out to ascertain SMM behavior in select instances. Measurements were carried out on crushed crystals with the exception of the $[PPN]_3[Os(CN)_6]$, $[PPN]_3[Ru(CN)_6]$, and Mn_3Ru_2 TBP which were carried out on powder samples.

$[PPN]_3[Os(CN)_6]$ and $[PPN]_3[Ru(CN)_6]$. Both metal precursors are d^5 low spin s = 1/2 ions, which, for an isotropic S = 1/2 system, exhibits a room temperature χT value of 0.375 emu K/mol. Analysis of the magnetic properties of the compounds indicated that at 300K the compound exhibits a negative signal due to the diamagnetic contributions from the organic components; the molecular weight of the starting material is 1962 g/mol with only one unpaired electron. The diamagnetic contribution is consistent and can be accurately subtracted, but below a certain temperature where the paramagnetic component of the signal overcomes the diagmagnetic contribution, a discontinuity in the χT vs T plots occurs (Figures 31 and 32). Beginning at 300 K and decreasing thereafter,

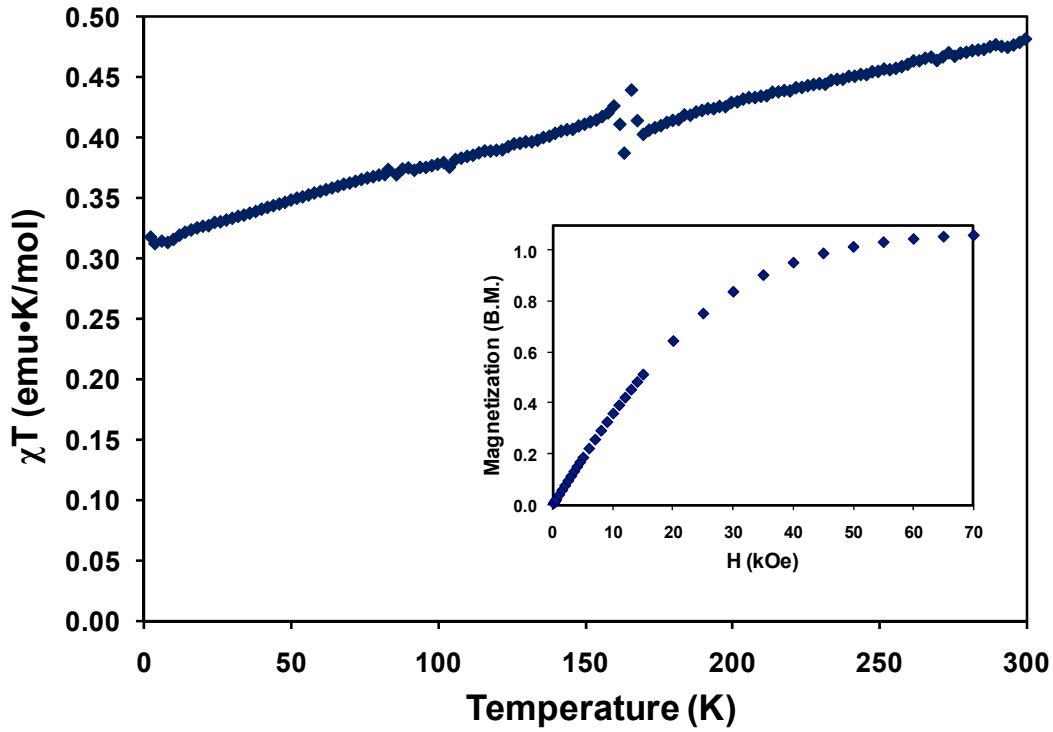

Figure 31. Temperature dependence of χT for $[PPN]_3[Os(CN)_6]$ Slope is due to slight TIP. Inset: Field dependent magnetization corresponding to an S = ½ ground state as expected.

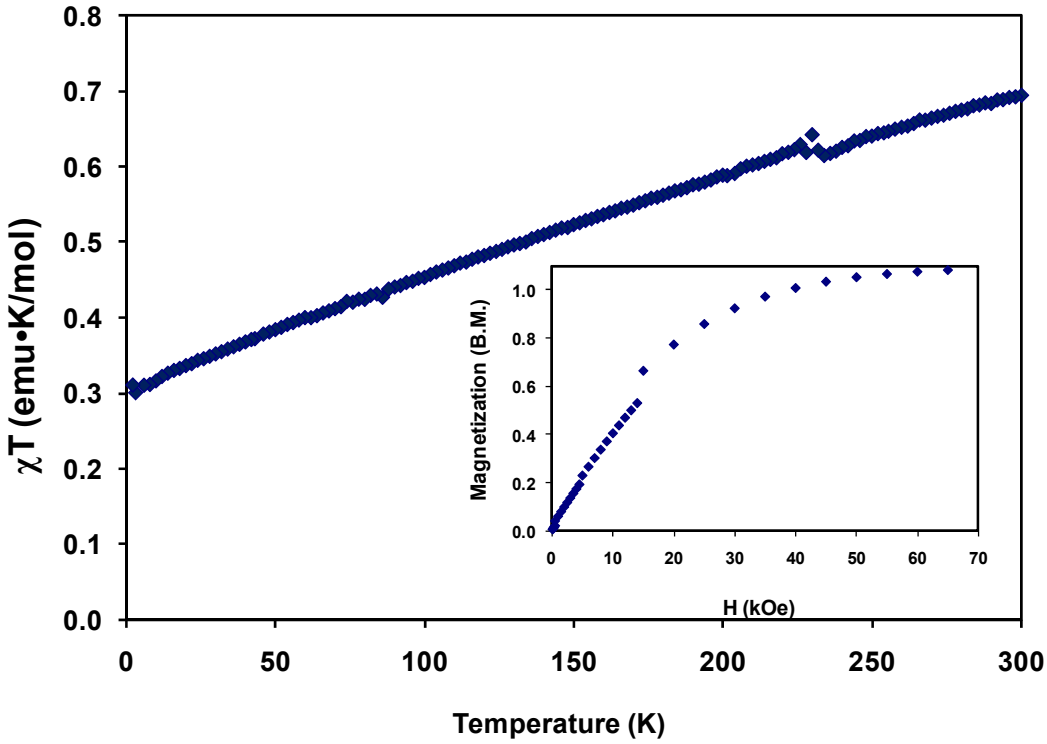

Figure 32. Temperature dependence of χT for $[PPN]_3[Ru(CN)_6]$ Slope is due to slight TIP. Inset: Field dependent magnetization corresponding to an S = ½ ground state as expected.

some degree of temperature independent paramagnetism (TIP) is observed, but at low temperatures the contribution can be ascertained as being 0.32 emu K/mol for both precursors. Magnetization data collected from 1-7 T also indicate only 1 unpaired electron is present in each system, as expected for a low spin d^5 S = ½ configuration (Figures 31 and 32 inset).

$[Ni(tmphen)_2]_3[Os(CN)_6]_2 \cdot 12H_2O$. A χT value of 4.73 emu K mol^{-1} was observed at 300 K which is higher than the expected value for three S = 1 and two S = 1/2 spin centers in the absence of magnetic interactions (3.64 emu K mol^{-1}) which is due to an orbital contribution from the Ni^{II} ions (Figure 33). (Note that the "expected" value was calculated using the experimental room temperature value of the $[PPN]_3[Os(CN)]_6$ starting material which is 0.32 emu K mol^{-1}). A plot of χT versus T shows a slight increase as the temperature is lowered and reaches a maximum of 5.29 emu K mol^{-1} at 21.6 K. Such behavior is indicative of weak ferromagnetic coupling between the Ni^{II} and Os^{III} centers. The magnetic properties were modeled taking into account the effects of intracluster superexchange and zero field splitting:

$$\text{Eqn 3: } H = -2J_{Ni-Os}(S_{Os1} + S_{Os2})(S_{Ni1} + S_{Ni2} + S_{Ni3}) - 3D[S_{zNi2} - S_{Ni}(S_{Ni} + 1)/3] \quad (3)$$
$$+ \beta H[g_{avg}(S_{Os1} + S_{Os2} + S_{Ni1} + S_{Ni2} + S_{Ni3})]$$

A fitting of this Hamiltonian using Magpack[115] resulted in best fit parameters of g_{avg} = 2.09, J_{Ni-Os} = 2.3 cm^{-1}, and D_{Ni} = 19.5 cm^{-1}, confirming the ferromagnetic coupling between Ni^{II} and Os^{III} ions. Clearly the D parameter is unrealistically large for the Ni^{II} ion, but it must be emphasized that the model cannot account for the spin–orbit coupling

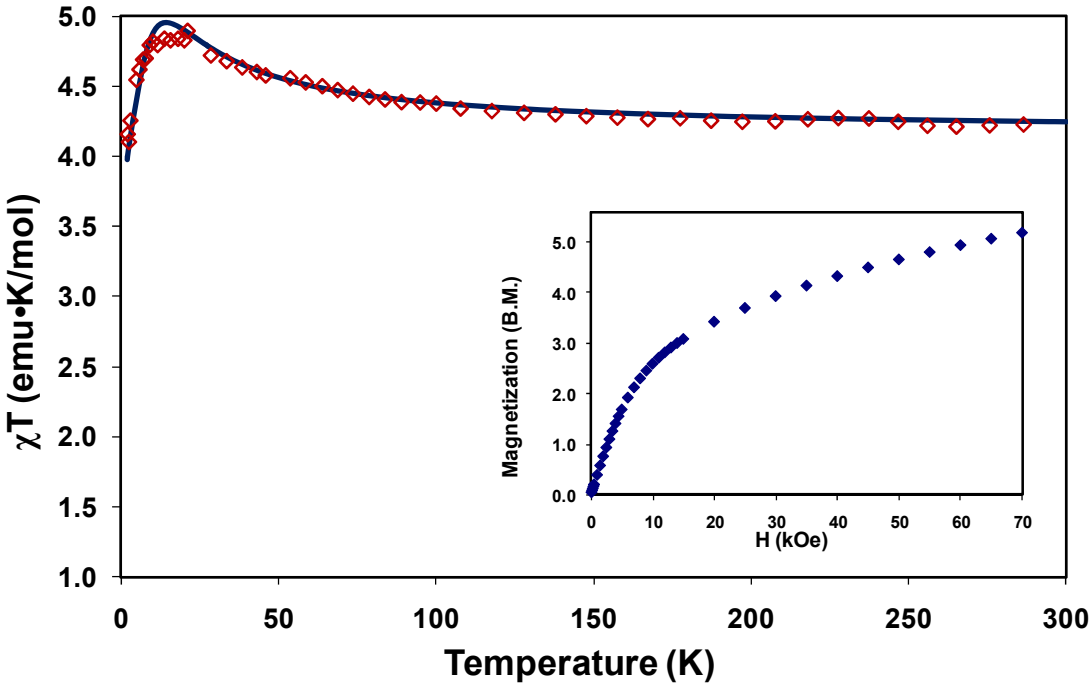

Figure 33. Temperature dependence of χT for the Ni_3Os_2 TBP (O). The solid line corresponds to the MAGPACK simulation (g_{avg} = 2.09, $J_{Ni–Os}$ = 2.3 cm^{-1}, and D_{Ni} = 19.5 cm^{-1}). Inset: Field dependent magnetization, unsaturation of the magnetization is indicative of low lying excited states.

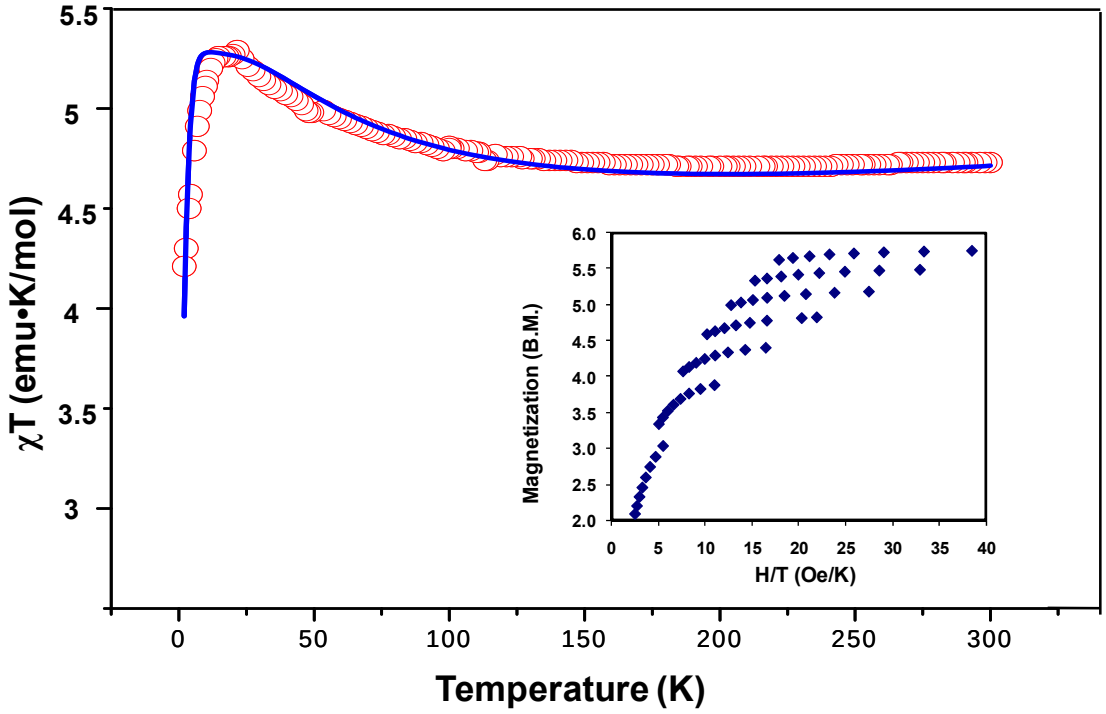

Figure 34. Temperature dependence of χT for Ni_3Os_2 TBP (O). The solid line corresponds to a theoretical fitting of the data incorporating anisotropic exchange parameters of the cluster (g_{Os} = 1.55 g_{Ni} = 2.2, $J_{||} = 23.8\ cm^{-1}$, $J_{\perp} = 1.2\ cm^{-1}$, $\chi_{TIP} = 1.4 \cdot 10^{-3}\ cm^{-1}$). Inset: Field dependent magnetization unsaturation of the magnetization is indicative of low lying excited states.

.

effects of the Os^{III} centers or anisotropic superexchange. Contributions from these factors would account for an overestimation of the D value. The strong magnetic anisotropy of the cluster is clearly evident from the variable temperature reduced magnetization curves (Fig. 34 inset). It is important to point out at this stage that a theoretical study was recently undertaken by Mironov[83] (whose work appeared before our experimental results) in which the behavior of a hypothetical $M_3^{II}Os_2^{III}$ trigonal bipyramidal clusters (M = a 3d metal ion) was modeled in an effort to identify possible candidates for SMM behavior. In the case of the Ni_3Os_2 analog, the results indicated that the molecule would be unlikely to be a SMM due to the presence of low lying excited states that facilitate relaxation of the magnetization. Indeed, AC magnetic susceptibility data do not exhibit an out of-phase signal down to 1.8 K. Moreover, the field dependent magnetization curve of 1 at 1.8 K does not saturate (Fig. 33 inset), which is in accord with the presence of low lying excited states as predicted from theory.

In order to probe the magnetic properties further, and investigate the artificially large D value, the magnetic and structural data was analyzed by our collaborators, Professor Boris Tsukerblat at Ben Gurion University together with Professor Sophia Klokishner, Dr. Andre Palii, and Dr. Sergei Ostrovsky at Kishinev University Moldova. These physicists specialize in studying the magnetic interactions in cyanide bridged complexes incorporating both spin orbit coupling and anisotropic exchange.[67, 81] Their analysis involved theoretical modeling of the experimental data with the inclusion of anisotropic exchange the results of which are the parameters $J_{||} = 23.8\ \mathrm{cm}^{-1}$, $J_{\perp} = 1.2\ \mathrm{cm}^{-1}$, $\chi_{\mathrm{TIP}} = 1.4 \cdot 10^{-3}\ \mathrm{cm}^{-1}$ which are able to nicely reproduce the

experimental data (figure 34).[129] It is important to note that the cluster could be fit only with a Hamiltonian that takes into account the anisotropic exchange of the system, $H_{(ex)}(1,3) = -2J_{\parallel}\tau_{z_{13}}(1)S_{z_{13}}(3) - 2J_{\perp}[\tau_{x_{13}}(1)S_{x_{13}}(3) + \tau_{y_{13}}(1)S_{y_{13}}(3)]$. It was determined that the zero field splitting of the system is not the cause of the anisotropy and that the behavior results from an interplay between the $J_{\perp}$ and $J_{\parallel}$ components (Figure 35). This is the first cluster to include the hexacyanoosmate(III) building block and the results indicate that it is an excellent building block for engendering anisotropy in the form of anisotropic exchange for transition metal clusters.

$[Ni(tmphen)_2]_3[Ru(CN)_6]_2 \cdot 12H_2O$. As shown in Figure 36, a χT value of 3.03 emu K mol^{-1} was observed at 300 K which is slightly lower than the expected value of 3.64 emu K $mol^{-1}$for three S = 1 and two S = 1/2 spin centers in the absence of magnetic interactions which was calculated using the experimental value of the $[PPN]_3[Ru(CN)]_6$ starting material (0.32 emu K mol^{-1}). A plot of χT vs. T is constant as the temperature is lowered until 34 K where it begins to increase and reaches a maximum of 3.24 emu K mol^{-1} at 4.9 K. These data are indicative of ferromagnetic coupling as expected from the orthogonality of the magnetic orbitals (t_{2g} for the Ru ions and e_g for the Ni ions), and is similar to the behavior observed for the Ni_3Os_2 compound. There is a stark contrast between the two analogs, however, in the reduced magnetization data. The Ni_3Os_2 cluster exhibits a pronounced non-superposition of the curves which is an indication of a strong degree of anisotropy which is supported by the results of the MAGPACK fitting and theoretical calculations. In the Ni_3Ru_2 TBP, however the reduced magnetization

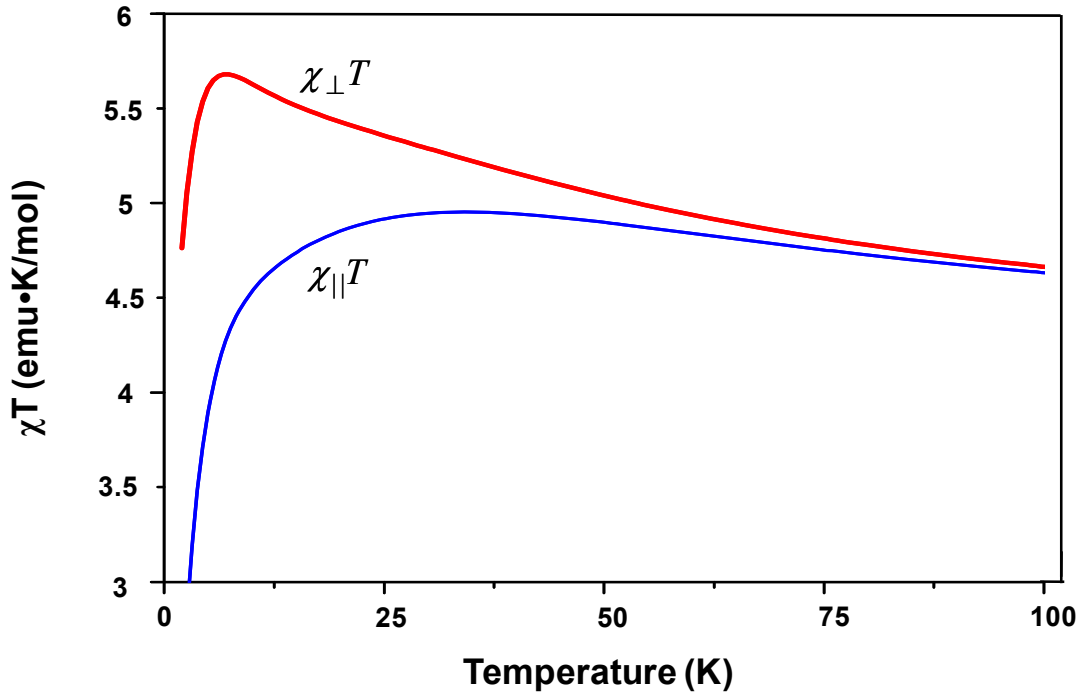

Figure 35. Theoretical $\chi_{||}T$ vs. T and $\chi_{\perp}T$ vs. T curves calculated with $g_{eff}(\mathrm{Os}) = 1.55$, $g(\mathrm{Ni}) = 2.2$, $J_{||} = 23.8\ \mathrm{cm}^{-1}$, $J_{\perp} = 1.2\ \mathrm{cm}^{-1}$.

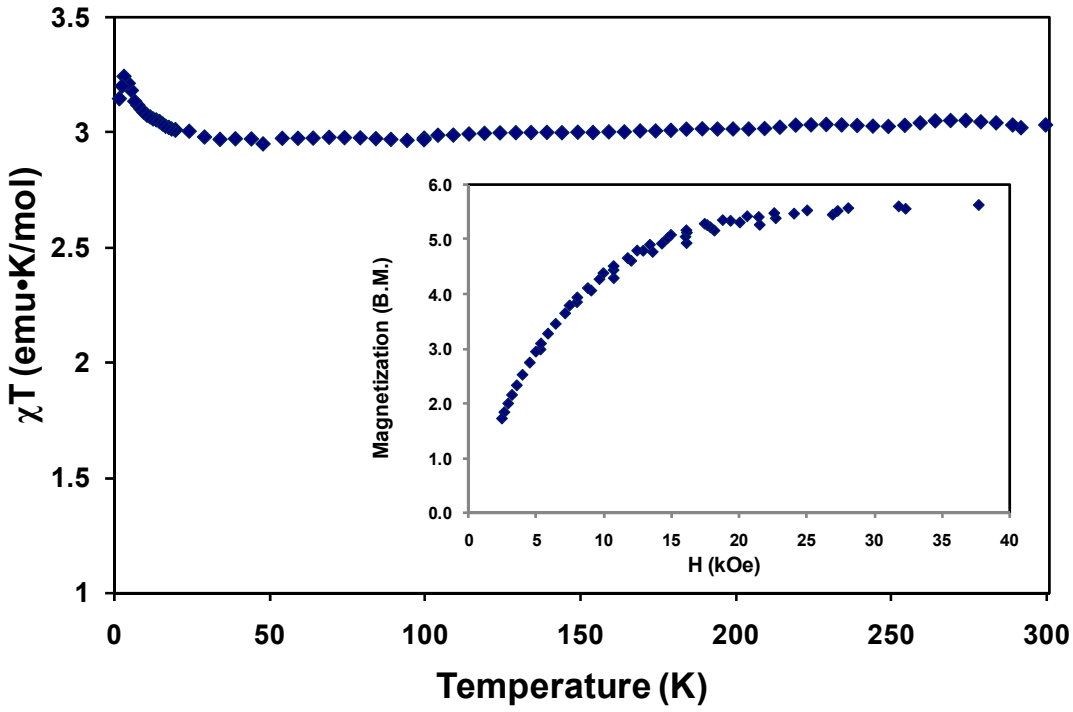

Figure 36. Temperature dependence of χT for the Ni_3Ru_2 TBP cluster. Inset: Reduced magnetization plots, essentially no differences are observed in the field lines indicating a lack of anisotropy.

experiment clearly shows a lack of appreciable anisotropy being exhibited and was unable to be modeled using the MAGPACK software and will be the subject of future theoretical analysis. It should be noted, however, that the Ru cluster crystallizes in a higher symmetry, a factor which will need to be taken into account in theoretical calculations in future work since the geometries around the metal centers is no longer the same as for the previous Ni_3Os_2 TBP cluster.

$[Mn(tmphen)_2]_3[Os(CN)_6]_2 \cdot 8H_2O$ TBP. The χT value for the cluster at 300 K is 12.83 emu mol^{-1} K (Figure 37), slightly lower than the expected free ion value of 13.86 emu mol^{-1} K for 3 HS Mn^{II} and 2 Os^{III} ions. The susceptibility exhibits a steady drop as the temperature decreases, followed by a more rapid decrease beginning at 20K, indicative of antiferromagnetic coupling in the system, which is expected for non-orthogonal t_{2g} magnetic orbitals of the metal centers. A simulation using the MAGPACK program to elucidate the exchange coupling could not be performed due to the highly unquenched orbital angular momentum of the Os^{III} ion. Similar behavior has been noted for the Mn_3Fe_2 TBP cluster, which exhibits the same trend in the magnetic susceptibility data due to the unquenched orbital angular momentum of the Fe^{III} ion.[46] Further analysis by magnetization data shows a lack of saturation which is a signature of low lying excited states being important even at low temperatures. The anisotropy of the cluster was investigated by measuring the reduced magnetization which clearly shows a strong splitting of the isofield lines (Figure 38b). Clearly there a strong anisotropy operative in this cluster as found for the Ni_3Os_2 TBP. AC susceptibility data revealed a frequency dependent out-of-phase signal at low temperatures, the maximum of which

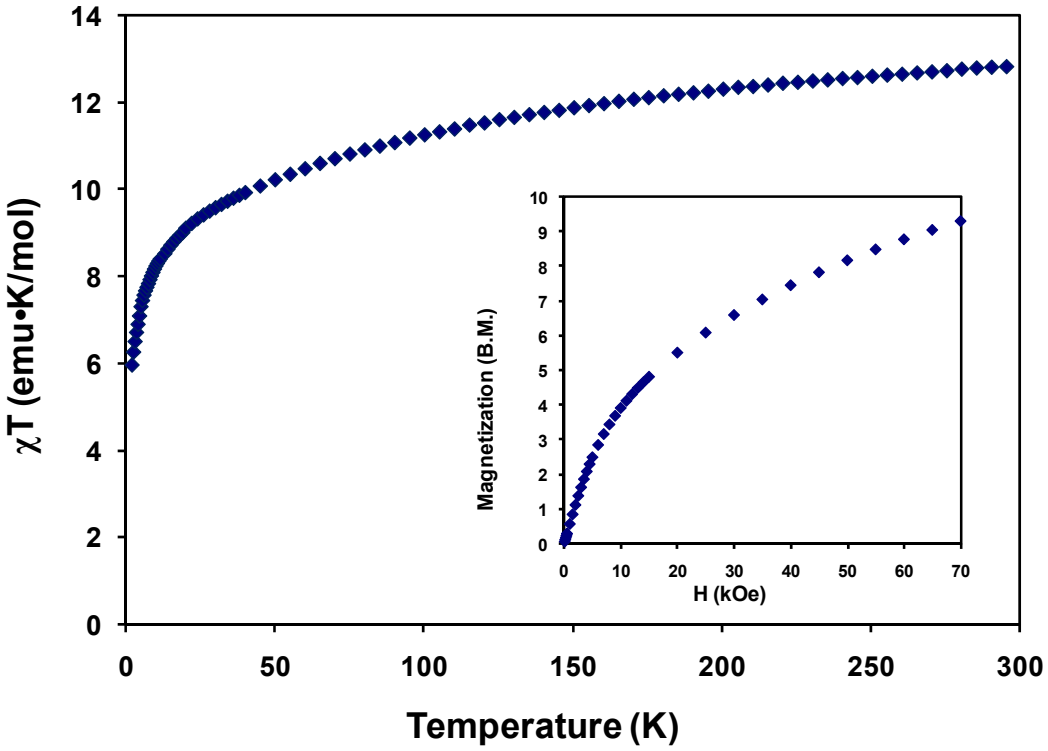

Figure 37. Temperature dependence of χT for the Mn_3Os_2 TBP cluster indicative of antiferromagnetic coupling. Inset: Field dependent magnetization is unsaturated, indicating the presence of low lying excited states due to a large anisotropy.

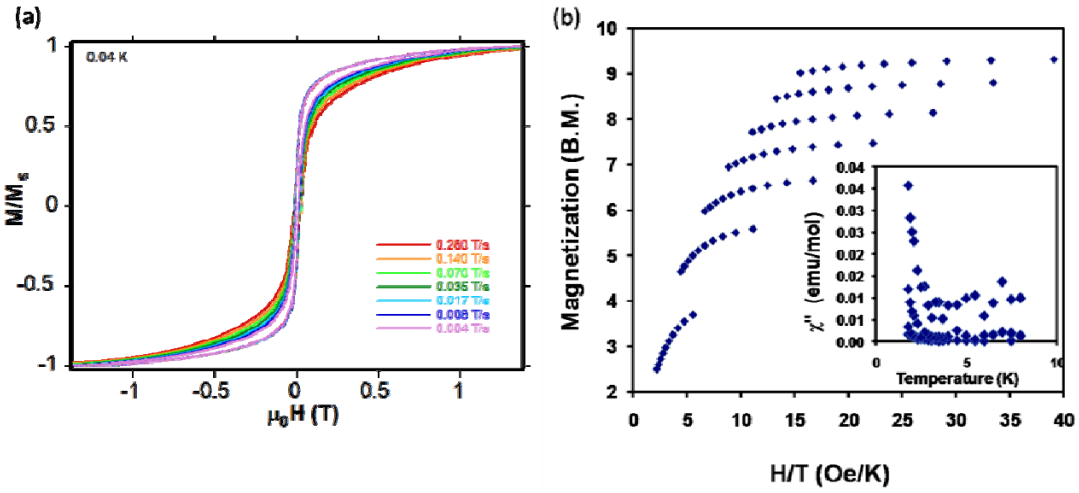

Figure 38. (a) Micro-SQUID measurements from 0.28 to 0.004 Ts^{-1} at 0.04K. (b)Reduced magnetization data, splitting of the isofield lines indicates a large anisotropy. Inset: imaginary part (χ'') of AC magnetic susceptibility from 1Hz to 1 kHz under a weak applied field of H_{AC} = 3 Oe and H_{DC} = 0 Oe.

could not be observed (Figure 38 inset). MicroSquid measurements indicate that this cluster is in fact an SMM below 1.8K (Figure 38a).

Prevailing theory in the field provides much inspiration for continuing to study this combination of ions. In a theoretical study that included the Ni_3Os_2 TBP, Mironov devotes much of the paper to calculations that support the conclusion that the combinations of Mn^{II} and Os^{III} in a trigonal bipyramidal cluster should form an SMM with a high blocking temperature.[83] The current magnetic data indicate that this cluster is an SMM, albeit not one with a high blocking temperature. A highly valuable tool in the field of molecular magnetism is to be able to explain observed behavior *and* to predict behavior for unknown compounds. These clusters are valuable in that they provide the first experimental data with which to test these theoretical predictions.

$[Mn(tmphen)_2]_3[Ru(CN)_6]_2 \cdot 8H_2O$. No crystalline material was obtained from these reactions because the use of slow diffusion methods with water leads to decomposition of the $[Ru(CN)_6]^{3-}$ ion as previously noted in the literature.[125] This being said, the assignment of the material as the TBP is supported by the magnetic and infrared analysis, however structural characterization still needs to be performed. Measurements were carried out, however, on the rapidly formed olive green powder which precipitates from the reaction when the reagents are mixed with stirring. The olive green color of the powder is the same color as the Mn_3Os_2 TBP crystals and the characteristic IR bands match the Ni_3Ru_2 TBP. The χT value for the cluster at 300 K is 13.51 emu mol^{-1} K (Figure 39) dropping slightly as the temperature decreases, followed by a rapid decrease

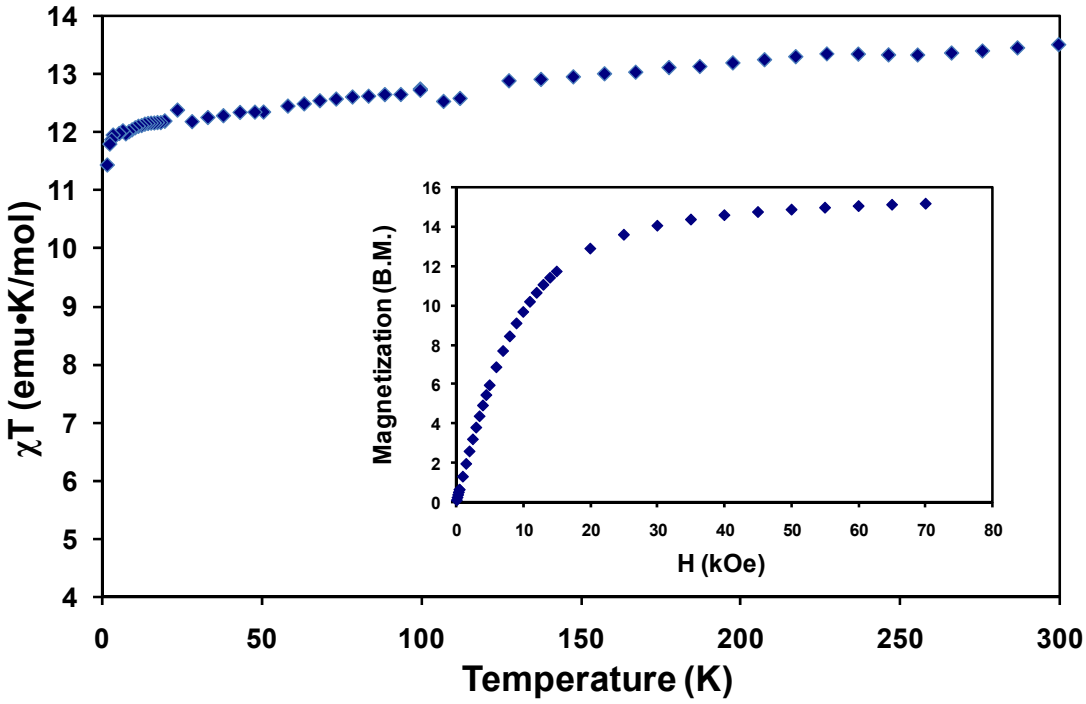

Figure 39. Temperature dependence of χT for the Mn_3Ru_2 TBP cluster, overall showing a weak antiferromagnetic coupling. Inset: Field dependent magnetization, lack of saturation is indicative of low lying excited states.

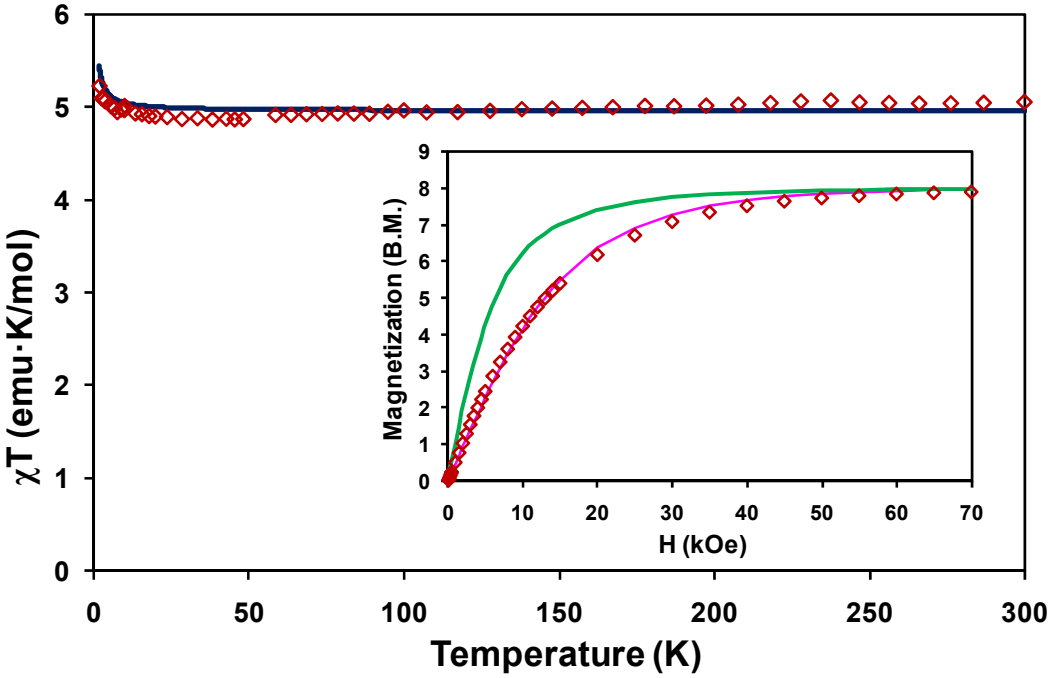

Figure 40. Temperature dependence of χT for the Cr_3Ru_2 TBP cluster. MAGPACK simulation of the χT *vs.* T data gave best fit parameters g_{CrIII} = 2.00 led to g_{CrII} = 2.2, , and an isotropic exchange constant J = 0.03 cm^{-1} indicating weak ferromagnetic coupling through the diamagnetic Ru^{II} center. Inset: Field dependent magnetization: the green line is the theoretical fit for two Ru^{III} and three LS Cr^{II} ions and the pink line is for two Ru^{II} and two LS Cr^{III} and one LS Cr^{II} ion.

at 5K. An inspection of the magnetization data revealed a value of 15.1 at 7 T which is not saturated but is approaching the 17 e^- system one would expect for cluster. Analysis of the magnetic data support the assignment of a TBP cluster with two Ru^{III} and three HS Mn^{II} ions which would yield 13.875 emu mol^{-1} K almost identical to the measured value of 13.51 emu K mol^{-1}.

$[Cr(tmphen)_2]_3[Ru(CN)_6]_2 \cdot 8MeCN$. The χT value at 300 K is 5.06 emu mol^{-1} K (Figure 40) which is slightly higher than the spin-only value expected for two Ru^{III} and three Cr^{II} ions that are magnetically isolated (χT = 4.27 emu mol^{-1} K). As the temperature decreases, there is little change in the susceptibility and only at 4.9 K is there a slight increase in the susceptibility which hints at ferromagnetic coupling. As the corresponding Cr_3Fe_2 TBP cluster is unknown there is no basis for convenient comparison, but from the Goodenough Kanamori rules, one would expect antiferromagnetic coupling since the unpaired electrons in both metal centers are in the t_{2g} orbitals. Further insight is provided by the magnetization data which saturate at 8 B.M, which is expected for a G.S of S = 4. Attempts to fit the magnetization data, however, do not reproduce the curvature when using a model of two Ru^{III} and three LS Cr^{II} centers (Figure 40 inset). Another possibility for the cluster is that electron transfer occurs between the Ru and Cr centers leading to a configuration of two Ru^{II} S = 0 ions, two Cr^{III} S = 3/2 ions, and one LS Cr^{II} ion. The expected room temperature χT value of this electronic isomer is 4.96 emu mol^{-1} K, which is very close to the experimental value moreover a fitting of the magnetization data with this model is excellent. A MAGPACK simulation of the χT *vs.* T data with the new model gave best fit parameters g_{CrIII} = 2.00,

g_{CrII} = 2.2, and an isotropic exchange constant of J = 0.03 cm^{-1} indicating that there is very weak ferromagnetic coupling occurring through the diamagnetic Ru^{II} centers.

Conclusions

The clusters reported in this chapter are the first examples of their type with the hexacyanoruthenate(III) and hexacyanoosmate(III) anions. Both the Mn_3Os_2 and Ni_3Os_2 TBPs exhibit very strong anisotropy, the origin of which appears to be anisotropic exchange as predicted by recently reported theoretical work. The only fully characterized Ru analog does not exhibit any appreciable anisotropy, and exhibits much weaker ferromagnetic coupling. These clusters represent the only experimental evidence thus far for any 4d or 5d hexacyanometallate based magnetic molecules. The lack of experimental data has hampered efforts thus far in advancing theory and understanding of cyanide exchange interactions for the heavier elements. Our new experimental support in this project will allow for more detailed analyses to be performed in order to fine tune the theory for predicting complex magnetic behavior. Future work in the field of cyanide based magnetic materials is expected to be greatly impacted by these new findings as they involve two underexplored hexacyanometallate building blocks. Of highest interest is the chemistry of the hexacyanoosmate(III) anion which is clearly an anisotropic building block as compared to the Ru derivative and whose mixed metal cyanide complexes open up a new venue for correlating theory and experiment for understanding the effects of increased spin orbit coupling on magnetic properties of designer molecules.

CHAPTER IV

CHARGE TRANSFER COUPLED SPIN TRANSITION AND SPIN CROSSOVER BEHAVIOR OF $[Fe(TMPHEN)_2]_3[Os(CN)_6]_2$ AND $[Fe(TMPHEN)_2]_3[Ru(CN)_6]_2$ TRIGONAL BIPYRAMIDAL CLUSTERS

Introduction

The study of paramagnetic cyanide compounds is one of the most active research areas in the field of coordination chemistry. Remarkable properties have been documented for both molecules[2] and extended phases, including high temperature magnetic ordering,[17, 21] single molecule magnetism,[59, 61, 62, 65, 103, 130] single chain magnetism,[4, 99] photomagnetism,[45, 91, 131] spin crossover (SCO),[24, 37] and a less common phenomenon known as a charge transfer induced spin transition (CTIST) or, charge transfer coupled spin transition (CTCST) as the exact mechanism of the transition is not yet known.[22, 43, 45, 132] The CTCST involves formal intramolecular electron transfer and spin state changes at the metal ions within a molecule or material and creates the potential for the control of the magnetic and optical properties by changes in temperature or with irradiation. The reason for the high interest in these compounds is the fact that the accessibility of two states that differ in electronic and magnetic properties is crucial for the possible implementation of molecule-based materials in future technological devices.[42, 90]

The first compounds that were recognized as exhibiting CTCST behavior are the Prussian Blue analogs $Rb_{0.88}Mn_{0.96}\cdot 0.5H_2O$, $Na_{0.32}Co[Fe(CN)_6]_{0.74}\cdot 3.4H_2O$ and $K_{0.2}Co_{1.4}[Fe(CN)_6]\cdot 6.9H_2O$.[23, 25, 30, 133, 134] These findings were followed by the discovery of a similar CTCST in $Co^{II}_3[W^V(CN)_8]_2(pyrimidine)_4\cdot 6H_2O$ that can be induced by either temperature or light.[132] These exciting properties prompted efforts in our laboratories on the topic of facile electron-transfer in cyanide bridged assemblies, which led to the first documented case of a discrete molecule-based material containing both Fe and Co centers, $\{[Co(tmphen)_2]_3[Fe(CN)_6]_2\}.xH_2O$, that exhibits CTCST. The compound is one of a large family of related trigonal bipyramidal (TBP) cyanide clusters that contain in the axial positions $[M(CN)_6]^{3-}$ and in the equatorial sites $[M'(tmphen)]^{2+}$ fragments.[43, 45] A few years later, a cyanide-bridged Fe/Co cube cluster was prepared and found to also undergo a sharp CTCST at 250K.[45] To date, in all the systems in which the CTCST involves iron ions, their transition is between LS Fe^{II} and LS Fe^{III} states. The reason for the high interest in these compounds is the fact that the accessibility of two different states that differ in electronic and magnetic properties is crucial for the possible implementation of molecule-based materials in future technological advances.[42, 90]

Herein a detailed study is reported of the metal ions in the Fe group, in combination with the earlier reported $[Fe(tmphen)_2]_3[Fe(CN)_6]_2$ cluster,[37] the remaining two members of the family, $[Fe(tmphen)_2]_3[M(CN)_6]_2$ (M = Ru, Os), have been prepared providing the first example of three isostructural clusters, which is the first such series with 3d, 4d or 5d metal in the family. The Fe_3Os_2 TBP cluster exhibits a thermally

induced CTCST phenomenon centered at room temperature which was documented by variable temperature x-ray crystallography, variable temperature IR, magnetic susceptibility, and Mössbauer spectroscopy. The Fe_3Ru_2 TBP analog was also studied by variable temperature crystallography, IR, magnetic susceptibility, and Mössbauer spectroscopy and the results indicate that this molecule exhibits both spin crossover and a charge transfer coupled spin transition (CTCST).

Experimental Section

Syntheses

Reagents. The anhydrous $FeCl_2$ (Strem), and 3,4,7,8-tetramethyl-1,10-phenanthroline (tmphen; Lancaster) were used as received. Acetonitrile was dried over 3 Å molecular sieves and distilled prior to use. The compounds were prepared under anaerobic conditions in an nitrogen-filled dry box. Concentrations of the reactants given below were found to produce the best quality single crystals for structural determination by X-ray crystallography. All of the reactions, however, can be scaled up to obtain products in larger quantities.

$[Fe(tmphen)_2]_3[Os(CN)_6]_2$ (15). Quantities of $FeCl_2$ (0.052 g, 0.413 mmol) and tmphen (0.216 mg, 0.914 mmol) were combined in 80 mL of acetonitrile and the solution was stirred for 30 minutes. The resulting dark-red solution was quickly combined with a solution of 0.659 g (0.336 mmol) of $(PPN)_3[Os(CN)_6]$ in 80 mL of acetonitrile in a 500 mL screwcap jar. The mixture was left undisturbed for 4-5 days. After this period of time, a crop of purple-red crystals was collected by filtration, and washed with

acetonitrile (3 x 30 mL). Yield 117.8 mg (30.7%). Elemental analysis and TGA the presence of 9 interstitial water molecules after exposure to air during the test. Anal. Calcd for $C_{108}H_{114}Fe_3N_{24}O_9Os_2$ (·$9H_2O$): O, 5.89; N, 13.76; C, 53.08; H, 4.70. Found:O, 5.98; N, 13.89; C, 53.64; H, 4.85%.

$[Fe(tmphen)_2]_3[Ru(CN)_6]_2$ (16). Quantities of $FeCl_2$ (0.055 g, 0.437 mmol) and tmphen (0.220 mg, 0.931 mmol) were combined in 80 mL of acetonitrile, and the solution was stirred for 30 minutes in the dry box. The resulting clear dark-red solution was mixed with a solution of 0.70g (0.374 mmol) of $(PPN)_3[Ru(CN)_6]$ in 80 mL of acetonitrile in a 500 mL screwcap jar and was left undisturbed for 4-5 days. After this period of time, a crop of purple-red crystals was collected by filtration, washed with acetonitrile (3 x 30 mL). Yield 152.1 mg (38.7%). TGA and Elemental analysis confirm the presence of 8 interstitial water molecules after exposure to air during the test. Anal. Calcd for $C_{108}H_{112}Fe_3N_{24}O_8Ru_2$ (·$8H_2O$): O, 5.71; N, 14.97 ; C, 57.74; H, 5.03. Found:O, 5.78; N, 15.21; C, 56.87; H, 5.01%.

Single Crystal X-ray Crystallography

In a typical experiment, the crystal selected for study was suspended in paraffin oil and mounted on a cryoloop which was placed in an N_2 cold stream set to variable temperatures depending on the experiment. Single crystal X-ray data were collected on a Bruker APEX diffractometer equipped with a CCD detector at 110 K (Table 7). The data sets were recorded as ω-scans at a 0.3° step width and integrated with the Bruker SAINT[54] software package. The absorption correction (SADABS[55]) was based on fitting a function to the empirical transmission surface as sampled by multiple equivalent

measurements. Solution and refinement of the crystal structures were carried out using the SHELX[55] suite of programs and the graphical interface X-SEED.[56] All the structures were solved by direct methods which resolved the positions of all the metal atoms and most of the C and N atoms. The remaining non-hydrogen atoms were located by alternating cycles of least squares refinements and difference Fourier maps. Hydrogen atoms were placed at calculated positions, with the exception of some water molecules, for which the hydrogen atoms were located from the difference Fourier maps. Whenever disordered solvent molecules were present in a structure, their bond distances were restrained to chemically meaningful values. The final refinement was carried out with anisotropic thermal parameters for all non-hydrogen atoms, except for the non-hydrogen atoms of the disordered solvent molecules which were refined isotropically (Fig. 41).

Results and Discussion

Syntheses

Reactions between divergent hexacyanometallate anions, $[M^{III}(CN)_6]^{3-}$ (M = Ru, Os), and a convergent mononuclear precursor of the type $[Fe^{II}(tmphen)_2X_2]^{0/2+}$ (X = Cl, CH_3CN) produce pentanuclear, cyanide bridged complexes of the type $[Fe^{II}(tmphen)_2]_3[M^{III}(CN)_6]_2$. The compounds were prepared under nitrogen in an inert atmosphere glove box, but are stable in solid form in air for an indefinite time. TGA analyses were performed to determine the number of interstitial solvent molecules in the samples and the thermal stability of the complexes. Gradual solvent loss occurred when the compounds were heated from room temperature to 320 °C. No solvent loss occurred

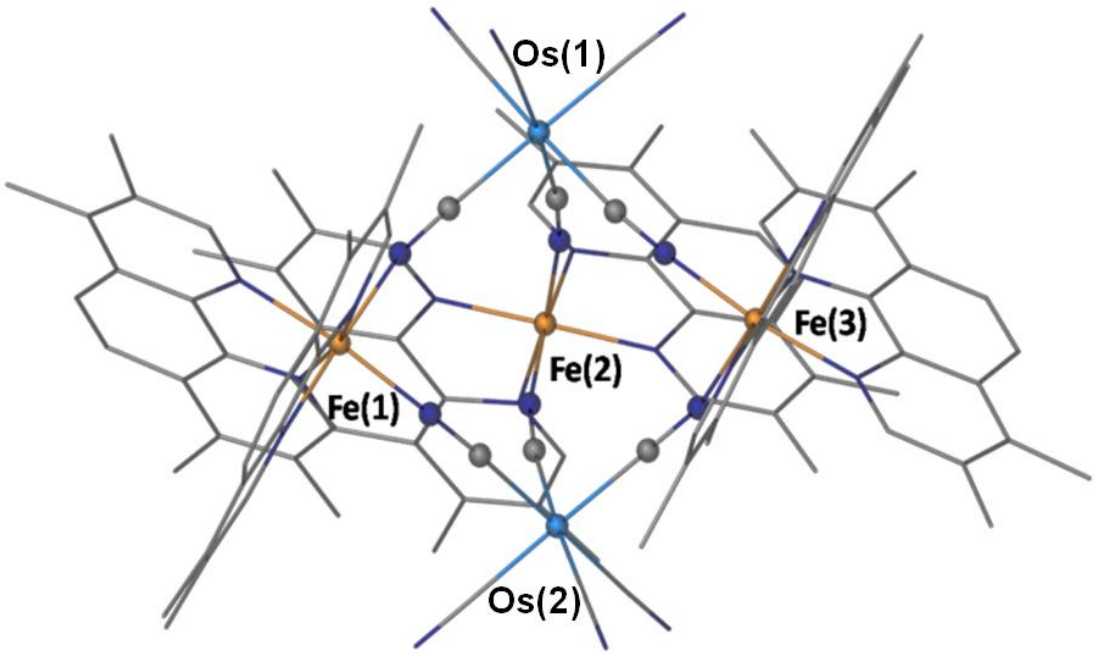

Figure 41. Molecular structure of Fe_3Os_2 TBP plotted from the X-ray coordinates. Hydrogen atoms are not shown for the sake of clarity.

after 280 °C and the compounds decomposed at 300 °C. The solvent content determined by this method varied between 5.6 and 5.8% by mass, depending on the compound. This mass difference corresponds to 8-9 molecules of water per molecule of complex, which is in agreement with the result of elemental analysis. Thus, thermo gravimetric and elemental analyses support the conclusion that interstitial acetonitrile molecules are replaced with water molecules when the compounds are stored in air. Given the hydroscopic nature of the compounds, all analysis of the magnetic properties, structure, IR and variable temperature IR, as well as Mössbauer spectroscopic measurements were performed on samples that had not been exposed to air. To determine the effect that excess water may have on the samples, crystals of the more stable of the two TBP clusters, the Fe_3Os_2 compound, were filtered and placed into a small vial containing water. After one week, the crystal structure and magnetic properties were measured.

Single Crystal X-ray Studies

The Fe_3Os_2 and Fe_3Ru_2 clusters are isostructural, and crystallize in the $P2_1/c$ space group (Table 7 and 8), which is the same space group found for the Fe_3Fe_2 cluster as well. The equatorial $[Fe(tmphen)_2]^{2+}$ sites of each TBP are homochiral, *i.e.* each cluster is either Δ, Δ, Δ or Λ, Λ, Λ and the crystal contains a racemic mixture of the two optical isomers. The TBP clusters exist as π – dimers, namely the tmphen units engage in inter-molecular π stacking (Figure 42). This behavior has been the discussion of a recent Forum article in Inorganic chemistry published by our group.[69]

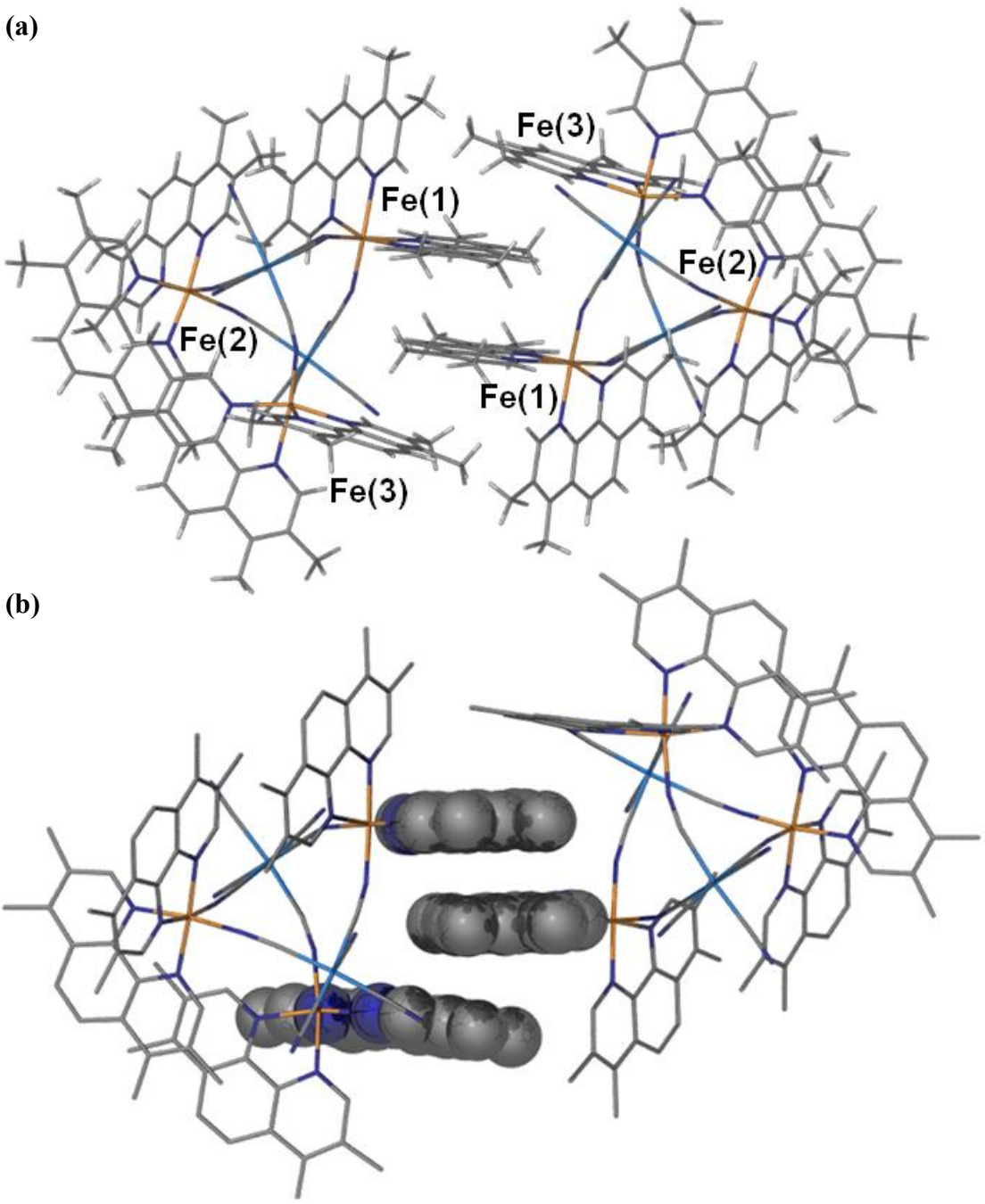

Figure 42. View of TBP clusters forming (a) dimeric unit through (b) π-stacking interactions.

Table 7. Crystal structural data and refinement parameters for Fe_3Os_2 TBP at 110 K, 250 K and 300 K.

Formula	**Fe_3Os_2 110K**	**Fe_3Os_2 250K**	**Fe_3Os_2 300K**
Space group	$P2_1/c$	$P2_1/c$	$P2_1/c$
Unit cell	*a= 19.2135(16)*Å	*a* = 19.356(8) Å	*a* =19.474(19)Å
	b = 24.956(2)Å	*b* = 25.411(11) Å	*b* = 25.47(2) Å
	c =24.734(2)Å	*c* = 25.144(11) Å	*c* = 25.32(2)Å
	β = 97.2540(10)	β = 97.642(6) °	β =97.431(13) °
Unit cell volume, *V*	11764.5(17)Å^3	12257(9) Å^3	12450(21) Å^3
Z	5	5	5
Density, ρ_{calc}	1.367 g/cm^3	1.241 g/cm^3	1.519 g/cm^3
Abs. coeff., μ	2.571 mm^{-1}	2.462 mm^{-1}	3.030 mm^{-1}
Crystal color and habit	Red-purple needle	Red-purple needle	Red-Purple needle
Crystal size, mm^3	0.53x0.29x0.20	0.44x0.25x0.10	0.44x0.25x0.10
Temperature	110 K	220 K	300 K
Radiation, λ	Mo-Kα, 0.71073 Å	Mo-Kα, 0.71073 Å	Mo-Kα, 0.71073 Å
Min. and max. θ	1.51 to 24.94 º	1.33 to 28.40 º	1.32 to 28.26º
Reflections collected	109978 [R_{int} =0.770]	114741 [R_{int} =0.188]	138372 [R_{int} =0.128]
Independent reflections	20537	29218	29832
Data/parameters/restraints	20537/ 1218/ 24	29218/1262/0	29832/622/0
R [$F_o > 4\sigma(F_o)$]	R_1 = 0.0647	R_1 = 0.1151	R_1 = 0.0885
	wR_2 = 0.1707	wR_2 = 0.2673	wR_2 = 0.2418
G.o.f. on F^2	1.108	1.151	1.048
Max./min. residual densities, e·Å^{-3}	1.537, -1.15	2.30, -1.30	1.81, -1.24

Table 8. Crystal structural data and refinement parameters for a hydrated sample of Fe_3Os_2 TBP at 110 K and Fe_3Ru_2 TBP at 110 K and 300 K.

Formula	**Fe_3Os_2-H_2O 110K**	**Fe_3Ru_2 110K**	**Fe_3Ru_2 300K**
Space group	$P2_1/c$	$P2_1/c$	$P2_1/c$
Unit cell	a = 19.809(3) Å b = 24.850(3)Å c =24.805(3)Å β=99.0810(10)°	a = 19.042(8)Å b =25.260(12) Å c =24.803(14) Å β=97.392(14) °	a = 19.41(2)Å b = 25.22(3)Å c =24.90(2)Å β=98.468(13) °
Unit cell volume, V	12058(3) Å^3	11831(10) Å^3	12057(20) Å^3
Z	5	5	5
Density, ρ_{calc}	1.437 g/cm^3	1.407 g/cm^3	1.446 g/cm^3
Abs. coeff., μ	2.527 mm^{-1}	0.675 mm^{-1}	0.810 mm^{-1}
Crystal color and habit	Red-purple needle	Red-purple needle	Red-purple needle
Crystal size, mm^3	0.47x0.12x0.15	0.36x0.11x0.08	0.41x0.14x0.11
Temperature	110 K	110 K	300 K
Radiation, λ	Mo-Kα, 0.71073 Å	Mo-Kα, 0.71073 Å	Mo-Kα, 0.71073 Å
Min. and max. θ	1.17 to 28.32 º	1.08 to 28.29º	1.33 to 28.29 º
Reflections collected	100709 [R_{int} =0.101]	84792 [R_{int} =0.141]	33093 [R_{int} =0.123]
Independent reflections	28302	27498	20821
Data/parameters/restraints	28302 /1323 /0	27498 /1246 /31	20821/1193 /0
R [$F_o > 4\sigma(F_o)$]	R_1 = 0.0776 wR_2 = 0.2177	R_1 = 0.0916 wR_2 = 0.2230	R_1 = 0.1589 wR_2 = 0.3618
G.o.f. on F^2	1.039	1.007	1.072
Max./min. residual densities, e·Å^{-3}	2.12, -1.92	1.82, -1.42	2.71, -2.05

$[Fe(tmphen)_2]_3[Os(CN)_6]_2$ TBP (15). Crystallographic data for the cluster were collected at 110 K and 300K (Table 9). Interestingly, while the average Fe–N(tmphen) bond length for Fe(2) is constant 2.00±0.05 Å at both temperatures, the corresponding bond distances for Fe(1) and Fe(3) increased by ~0.2 Å in going from 110K and 300 K, an indication that a change in the oxidation or spin state of these two metal ions takes place between the two temperatures. The observed change in the Fe-N bond length by 0.2 Å is typically observed in spin transitions of Fe^{II} from LS to HS states.[135] Most importantly we have observed SCO behavior and documented the accompanying changes in bond lengths at the Fe(1) and Fe(3) sites of the $\{[Fe(tmphen)_2]_3[Fe(CN)_6]_2\}$ and $\{[Fe(tmphen)_2]_3[Co(CN)_6]_2\}$ clusters.[69] The fact that the Fe(1) and Fe(3) sites undergo the transition and are distinct from Fe(2) is likely due to the nature of the packing of the TBP clusters. As recently described,[69] the clusters pack as sets of dimers (Figure 42) wherein there is strong π-overlap between the tmphen ligands of Fe(1) and Fe(3), which mediate the magnetic properties. While this similarity in the changes in the average Fe-N bond length is suggestive of a LS Fe^{II} to HS Fe^{II}, it does not preclude a transition from LS Fe^{II} to HS Fe^{III}. To the best of our knowledge, no HS Fe^{III} ion with two bidentate ligands coordinated through imine nitrogens and two other independent nitrogen ligands, has been documented, so we have no reference compound for the present data. The most that can be said is that the X-ray structural data indicate that the core in the cluster is $[(LS\ Fe^{II})_3(Os^{III})_2]$ at low temperature and that two of the three iron sites become HS Fe^{II} *or* HS Fe^{III}, at 300K. The 4.2 K EPR spectrum of the cluster is indicative of an S = ½ signal characteristic of LS Os^{III} thus corroborating the assignment

Table 9. Fe-N and Os-C bond distances (Å) in the Fe_3Os_2 TBP at 110K, 250K, 300K.

Temperature	Fe1-N	Fe2-N	Fe3-N	Os1-C	Os2-C
110K	1.914(10)	1.917(10)	1.922(9)	2.014(12)	2.024(11)
	1.919(9)	1.919(9)	1.947(9)	2.027(10)	2.041(11)
	1.992(9)	1.953(10)	1.982(9)	2.041(12)	2.044(10)
	1.995(9)	1.963(9)	1.984(9)	2.048(13)	2.046(12)
	1.998(10)	1.964(9)	1.998(9)	2.050(12)	2.059(10)
	2.002(11)	1.973(9)	1.998(9)	2.066(13)	2.062(10)
Avg M-L	*1.97(1)*	*1.95(1)*	*1.97(1)*	*2.04(1)*	*2.05(1)*
250K	1.965(13)	1.934(12)	1.966(13)	1.968(14)	1.996(17)
	2.024(14)	1.941(13)	1.964(14)	1.995(16)	2.05(2)
	2.127(12)	2.015(15)	2.133(11)	2.010(16)	2.011(17)
	2.127(13)	2.016(13)	2.167(13)	2.053(17)	2.065(19)
	2.162(13)	2.019(14)	2.185(13)	2.036(15)	2.09(2)
	2.200(13)	2.011(13)	2.212(13)	2.088(19)	2.077(18)
Avg M-L	*2.10(1)*	*1.99(1)*	*2.10(1)*	*2.02(1)*	*2.05(1)*
300K	1.989(11)	1.959(11)	1.974(10)	1.985(12)	2.026(12)
	2.032(11)	1.956(11)	2.011(10)	2.021(12)	2.028(13)
	2.142(11)	2.042(11)	2.152(10)	2.031(14)	2.039(14)
	2.140(10)	2.033(11)	2.165(10)	2.036(14)	2.034(13)
	2.165(10)	2.043(12)	2.185(10)	2.031(12)	2.062(16)
	2.182(10)	2.074(11)	2.201(11)	2.071(15)	2.04(2)
Avg M-L	*2.11(1)*	*2.02(1)*	*2.12(1)*	*2.03(1)*	*2.04(1)*

Table 10. Fe-N, Os-C, and Ru-C bond distances (Å) for the hydrated Fe_3Os_2 TBP at 110 K and the Fe_3Ru_2 TBP cluster at 110 K and 300 K.

Hydrated Fe_3Os_2 TBP					
Temperature	**Fe1-N**	**Fe2-N**	**Fe3-N**	**Os-C**	**Os-C**
110K	1.943(11)	1.920(12)	1.974(10)	1.994(11)	1.971(14)
	1.963(10)	1.928(10)	1.991(11)	2.016(14)	1.999(13)
	2.083(10)	2.002(11)	2.111(10)	2.028(17)	2.019(17)
	2.096(10)	2.020(10)	2.126(10)	2.038(16)	2.056(14)
	2.102(10)	2.028(14)	2.175(10)	2.049(12)	2.050(14)
	2.114(10)	2.028(12)	2.177(9)	2.057(13)	2.089(15)
Avg M-L	*2.05(1)*	*1.99(1)*	*2.09(1)*	*2.03(1)*	*2.03(1)*
Fe_3Ru_2 TBP					
Temperature	**Fe1-N**	**Fe2-N**	**Fe3-N**	**Ru-C**	**Ru-C**
110K	1.961(6)	1.941(6)	1.962(6)	1.985(9)	1.974(7)
	1.971(7)	1.963(6)	1.987(6)	1.987(7)	2.000(7)
	2.146(6)	1.976(6)	2.108(6)	2.032(7)	2.020(7)
	2.163(6)	1.981(6)	2.111(6)	2.034(8)	2.047(8)
	2.191(6)	1.987(6)	2.117(5)	2.067(9)	2.055(8)
	2.196(6)	1.941(6)	2.166(6)	2.072(8)	2.069(7)
Avg M-L	*2.10(1)*	*1.96(1)*	*2.07(1)*	*2.03(1)*	*2.03(1)*
300K	1.980(14)	1.973(14)	1.988(13)	1.972(17)	1.90(3)
	2.006(13)	2.054(15)	1.995(15)	1.969(16)	2.01(2)
	2.127(12)	2.03(2)	2.124(14)	2.01(2)	2.024(16)
	2.153(13)	2.064(15)	2.157(15)	2.04(2)	2.023(16)
	2.175(14)	2.094(15)	2.190(14)	2.09(2)	2.071(14)
	2.211(13)	2.061(14)	2.222(13)	2.13(2)	2.070(17)
Avg M-L	*2.11(1)*	*2.05(1)*	*2.14(1)*	*2.04(1)*	*2.02(1)*

of an [(LS Fe_3^{II} Os_2^{III})] distribution of oxidation states in the cluster at low temperatures.

Fe_3Os_2 TBP crystal soaked in water. After exposure to water for 1 week, the crystals were removed and some were discovered to still be suitable for xray diffraction studies. At 110K there is a change in the bond distances, a slight lengthening approaching that observed of the room temperature Fe_3Os_2 TBP (Table 9). The structure was found to have ~ 14 H_2O molecules and curiously still 1 MeCN molecule from crystallography. The interstitial water has a strong effect on the properties of this system, clearly from the bond distances not all 3 Fe centers in the material are completely L.S. Fe^{II}.

Fe_3Ru_2 crystal strutures at 110K and 300K. At 110K, the Fe_3Ru_2 TBP exhibits a strong difference compared to that of the Fe_3Os_2 TBP, already two of the Fe centers exhibit bond distances which more closely match H.S. $Fe^{II/III}$ (Table 10). To investigate the effect of increasing the temperature on the bond distances an additional data set was collected at 300 K. From the table, there is in fact a slight increase overall in the bond distances of 0.02 to 0.04 Å, indicating that a transition is continuing to occur in this temperature range.

Infrared Spectroscopy

$[Fe(tmphen)_2]_3[Os(CN)_6]_2$ TBP (15). Variable temperature infrared spectroscopic measurements were performed in Dr. Janice Musfeldt's group at the University of Tennessee, where they have provided us with the data and assistance in analyzing these single crystal measurements. An IR spectrum of the Fe_3Os_2 TBP at 4.2 K showed a $\nu_{C\equiv N}$ bridging stretch at 2100 and 2120 cm^{-1} and terminal stretching mode at 2098 cm^{-1} (Figure 43) which are similar to the frequencies recorded for other members of the

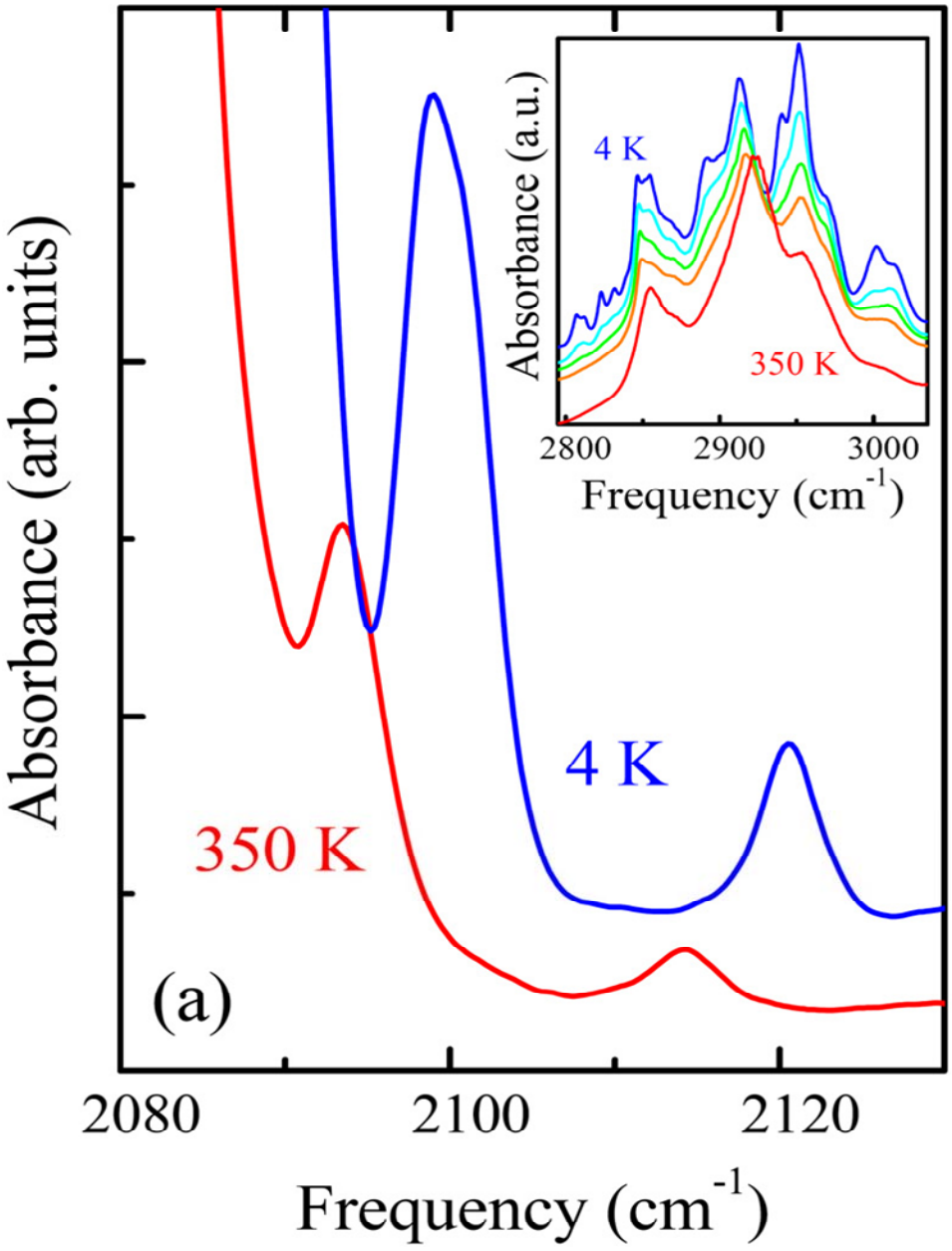

Figure 43. IR spectra of a crystalline sample of Fe_3Os_2 TBP (frequency range characteristic for cyanide vibrations). The frequency change indicates the change in oxidation state of the $Os(CN)_6$ unit. The inset displays C-H stretching region of the IR spectrum at 4, 110, 190, 250, and 350 K.

family of TBP clusters.[69, 102] At 350 K the bridging and terminal $\nu_{C\equiv N}$ stretches occur at 2115, 2095 cm^{-1} and 2080 cm^{-1}, respectively. The change in these particular stretches is not as large as expected, terminal $[Os^{II}(CN)_6]^{3-}$ stretches should appear near 2050 cm^{-1}, but this issue has been attributed to competing interactions in the crystal lattice with hydrogen bonding of the solvent as well as the tmphen ligands with the terminal cyanides on the cluster. If the Fe^{II} sites in the cluster simply undergo SCO, one would expect a slight shift in the IR frequency of the bridging cyanide and also of the C-H stretching modes of the tmphen ligand bound to the iron centers as a function of temperature but no appreciable change in the terminal cyanide stretches of $[Os^{III}(CN)_6]^{3-}$ If, however, the oxidation states of both Fe and Os in the cluster change as is the case for a CTCST, substantial changes in both the bridging and terminal cyanide modes are anticipated. As the aforementioned data attest, a shift of the $\nu_{C\equiv N}$ vibrational modes by toward higher frequencies as well as of the C-H stretching modes of the tmphen ligands occurs in going from 350 K to 4.2 K (Inset of Figure 43). A shift of the $\nu_{C\equiv N}$ vibrational mode toward higher energies with decreasing temperature correlates with electron transfer and the gradual oxidation of Os centers. Hence, these vibrational data confirm that one observes a shift toward higher frequencies of the $\nu_{C\equiv N}$ stretching mode at low temperatures and support the assignment of the behavior of the cluster as a CTCST rather than to a LS Fe^{II} to a HS Fe^{II} transition (See physical methods in Appendix A).

$[Fe(tmphen)_2]_3[Ru(CN)_6]_2$ TBP (16). Room temperature IR data collected on crushed crystals suspended in mineral oil show four distinct $\nu_{C\equiv N}$ stretches at 2019, 2048, 2078 and 2125 cm^{-1}. The features at 2019 and 2078 cm^{-1} correspond to both terminal

stretches associated with $[Ru^{II}(CN)_6]^{4-}$ and $[Ru^{III}(CN)_6]^{3-}$ which are lowered from their free values of 2035 and 2085 cm^{-1} respectively, which is attributed to hydrogen bonding corresponding to the uptake of water in the cluster. The shifts at 2048 and 2125 cm^{-1} are due to the bridging modes of the cyanide, which is typically increases going from M-C≡N to M-C≡N-M′ bonding. These sets of stretches indicate the presence of both Ru^{II} and Ru^{III} at room temperature.

Magnetic Properties

$[Fe(tmphen)_2]_3[Os(CN)_6]_2$ TBP (15). A polycrystalline sample was subjected to variable temperature magnetic susceptibility measurements carried out in an applied DC field of 1000 Oe (Figure 44), and an abrupt decrease in χT was observed from 9.07 emu·K/mol at 350K to 1.83 emu·K/mol at 200K, followed by a slow decrease to 1.2 emu·K/mol at 50K. The ~ 7.3 emu·K/mol change in χT between 200 and 350 K is indicative of a gradual change in the spin state at the metal ions either due to SCO or a redox reaction between the Fe and Os ions. Specifically, the change in χT could be either a L.S. Fe^{II} to H.S. Fe^{II} transition affecting 46% of the iron ions at 300K and 81% at 350 K, or a CTCST from [L.S. Fe^{II}-Os^{III}] to [H.S. Fe^{III}-Os^{II}] affecting 34% at 300K and 56% of the iron centers at 350K. A previously studied molecule, the $[Fe(tmphen)_2]_3[Fe(CN)_6]_2$ TBP cluster exhibited a nearly identical change in χT which was determined by Mössbauer spectroscopy to exhibit SCO behavior. Being in the same family as $[Fe(CN)_6]^{3-}$ the corresponding Os based cluster may be expected to exhibit SCO behavior. To unambiguously discern whether this is true, Mössbauer spectroscopy studies were employed at variable temperatures. Magnetization measurements at 1.8K

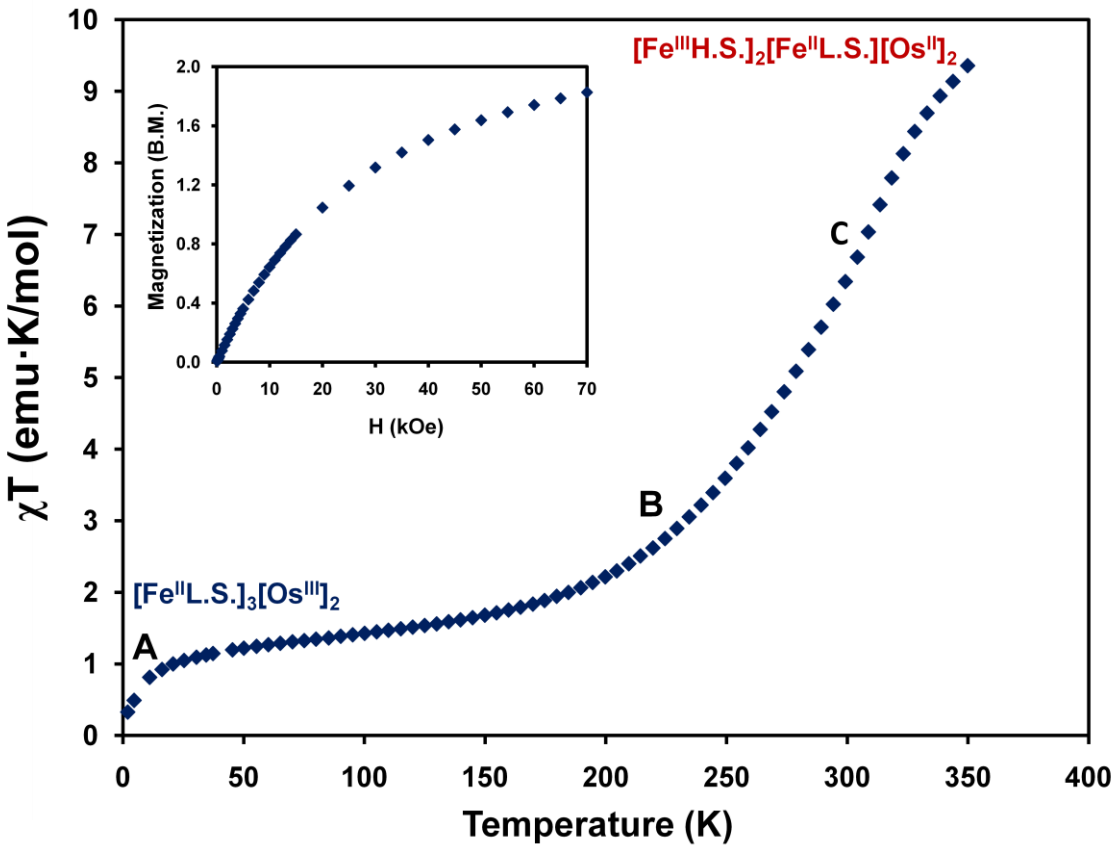

Figure 44. Temperature dependence of χT for a polycrystalline sample of Fe_3Os_2 TBP. A, B, C correspond to Mössbauer measurement data points. Inset: Magnetization at 1.8K, sample does not saturate completely, but is nearly saturated approaching two unpaired electrons, which is expected for two isolated Os^{III} (S = 1/2) and three L.S. Fe^{II} ions (S = 0).

were unable to provide information on the ground state of the cluster, due to lack of saturation, which is indicative of the presence of low lying excited states. While the data can be seen to be approaching 2 μB, the expected value for three isolated L.S. Fe^{II} and two Os^{III} S = ½ ions, it cannot conclusively prove a two electron ground state. These results notwithstanding, the magnetization data combined with epr and crystallographic data are all consistent with the low temperature electronic structure as being three L.S. Fe_3^{II} Os_2^{III}. For details of magnetic physical methods see Appendix A.

$[Fe(tmphen)_2]_3[Os(CN)_6]_2$ TBP in water. The magnetic properties of the hydrated Fe_3Os_2 TBP material, which was prepared from the same batch as the sample reported above, were measured in order to have a reference point to assure that the samples being measured had not already converted to a hydrated form (Figure 45). The value at 110K of 2.1 emu·K/mol is higher than what would be possible for three L.S. Fe^{II} (S = 0) and two Os^{III} ions (S = ½) , 0.75 emu·K/mol, indicating that there is some amount of H.S. Fe present in the sample at that temperature, but it is less than a full equivalent of Fe ions that have undergone the transition. Further evidence of this is noted when analyzing the 110K Fe-N bond distances, which are slightly higher than what are typically observed for L.S. Fe^{II} in the same environment for the nonhydrated Fe_3Os_2 TBP, but are not as large as those observed for H.S. Fe^{II} or H.S. Fe^{III}. At 300 K a χT value of 3.9 is observed and the data show a clear transition, however this once again does not match what would be observed for a full transition of one equivalent of Fe atoms. For H.S. Fe^{II} this would correspond to a change of 3 emu·K/mol, and for H.S. Fe^{III} a change of 4.3 emu·K/mol.

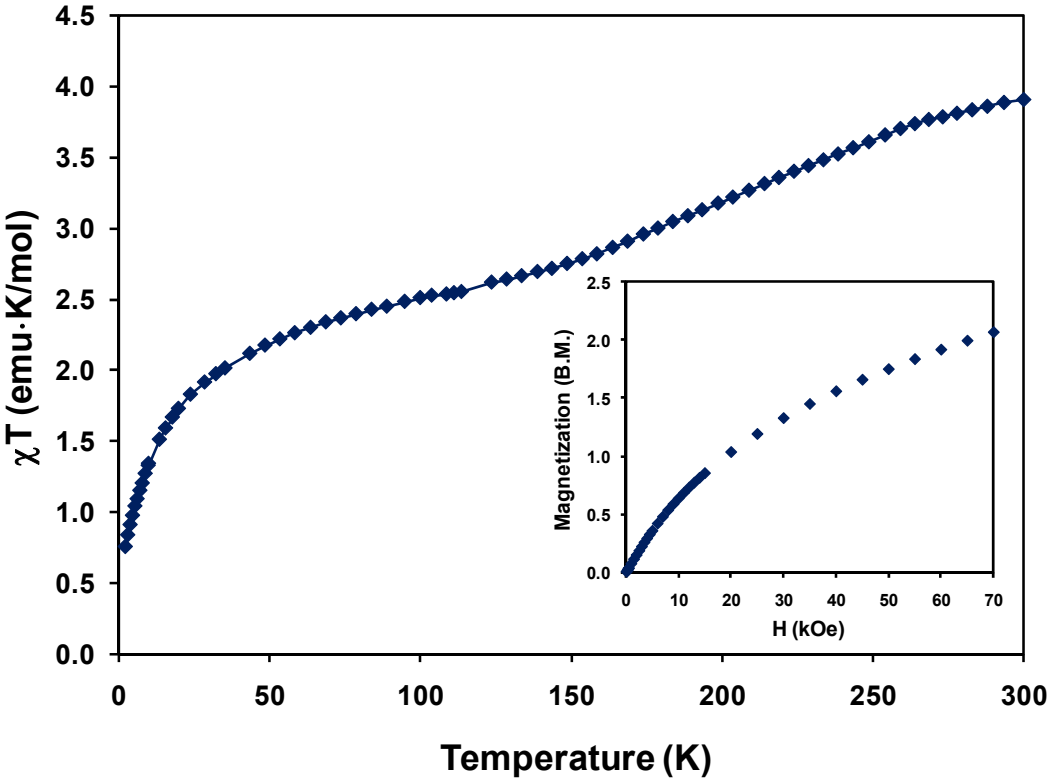

Figure 45. Temperature dependence of χT for a polycrystalline sample of hydrated Fe_3Os_2 TBP. The gradual spin transition is centered at ~200K. Inset: Magnetization at 1.8K shows that the sample does not saturate indicating the presence of low lying excited states.

A spin transition is clearly occurring, but the exact nature is difficult to determine in this case.

$[Fe(tmphen)_2]_3[Ru(CN)_6]_2$ TBP (16). A polycrystalline sample of the compound was subjected to variable temperature magnetic susceptibility measurements in an applied DC field of 1000 Oe (Figure 46). At 350 K the room temperature χT is 10.57 emu·K/mol and, as the temperature decreases, beginning at 325 K a gradual decrease in χT is observed plateauing at 4.9 emu·K/mol at 140 K, with an abrupt decrease beginning at 50 K. The ~5.66 emu·K/mol change in χT between 70 and 270 K is indicative of a gradual change in the spin state at the metal ions either due to SCO or CTCST. This cluster does not exhibit a near diamagnetic to highly paramagnetic transition as found in the Fe_3Os_2 system. At 350K, there are two possible electronic configurations which could lead to a room temperature value of 10.56 emu·K/mol. The scenario is two H.S. Fe^{III} and one H.S. Fe^{II} sites giving rise to an expected spin only value of 11.75 and the second case is one H.S. Fe^{III}, two H.S. Fe^{II}, and one Ru^{III} leading to a value of 10.75 emu·K/mol . The second situation matches almost identically with the experimental value. The decrease of 5.66 emu·K/mol, is a hint that there must be two types of transitions occurring, as a conversion of just one H.S. Fe^{III} to a L.S. Fe^{II}, would be a change of only 4.37 emu·K/mol. An additional transition of 3 emu·K/mol would include a complete HS Fe^{II} to LS Fe^{II} transition, but would bring the overall χT value to 3.2 emu·K/mol, which is lower than the observed value of 4.9 emu·K/mol. To aid in the determination of the ground state of the cluster, magnetization data were collected at

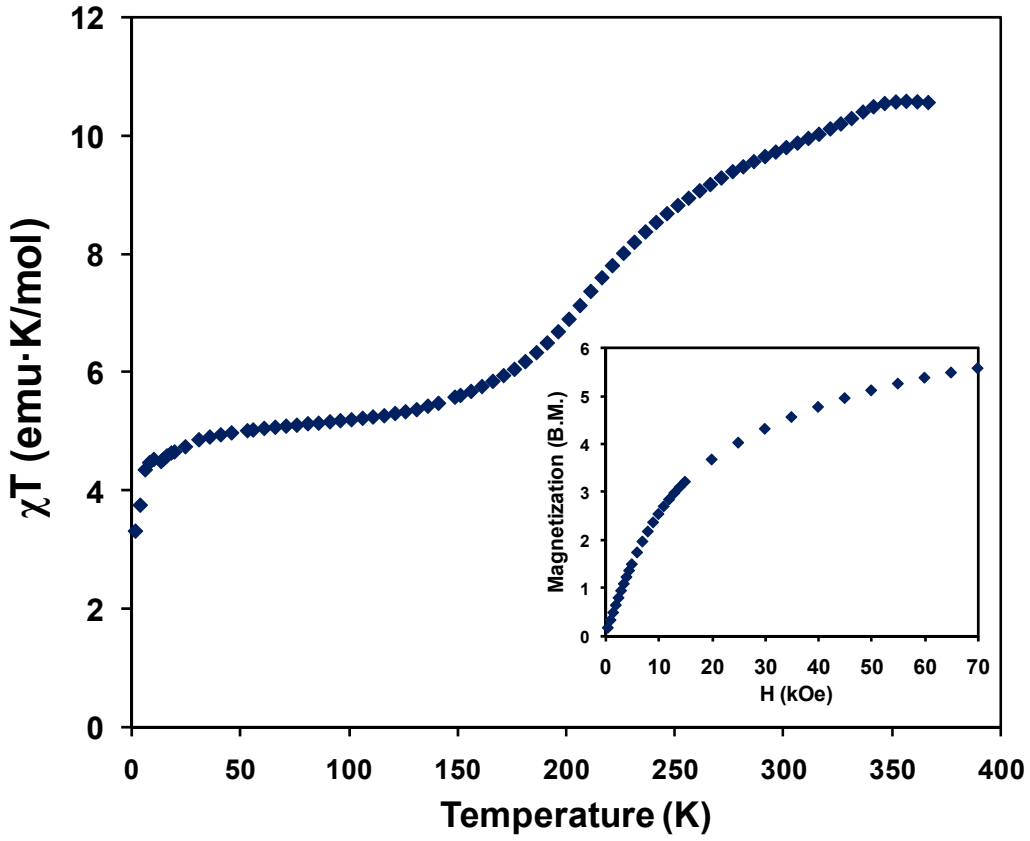

Figure 46. Temperature dependence of χT for a polycrystalline sample of Fe_3Ru_2 TBP with a gradual spin transition centered at ~225K. Inset: Field dependent magnetization where the lack of saturation is indicative of low lying excited states.

varying fields at a constant temperature of 1.8 K. For this cluster, however, no saturation value is observed, but it begins to slow in curvature near 5.5 B.M. A configuration at low temperatures of one HS Fe^{II}, two LS Fe^{II}, and two Ru^{III} would lead to a value of 6 emu·K/mol, which is very close to the observed value (Figure 46 inset). These data reveal that at the lowest measureable temperature there is a strong support for the proposed electronic configuration, but with some population of low lying excited states.

Further analysis by Mössbauer spectroscopy as described in the next section, help to elucidate the nature of the transition for the cluster. This is crucial as the magnetic properties alone cannot confirm if both CTCST and SCO behavior occurring throughout the material.

Mössbauer Spectroscopy

$[Fe(tmphen)_2]_3[Os(CN)_6]_2$ TBP (15). To directly investigate the oxidation and spin state of the Fe sites in the cluster as a function of temperature, we have obtained ^{57}Fe Mössbauer spectra at temperatures between 4.2 K and 300 K and in applied magnetic fields of up to 8T. This work was carried out by Prof. Catalina Achim at Carnegie Mellon University. The dominant feature of the 4.2 K spectrum for the sample that was used for the magnetic susceptibility measurements plotted in Figure 44 exhibits a quadrupole doublet with isomer shift δ of 0.36 mm/s and a quadrupole splitting ΔE_Q of 0.40 mm/s., which represents more than 85% of the Fe in the sample (red line in Figure 47A). The δ and ΔE_Q parameters are characteristic of LS Fe^{II}. The slight asymmetry of

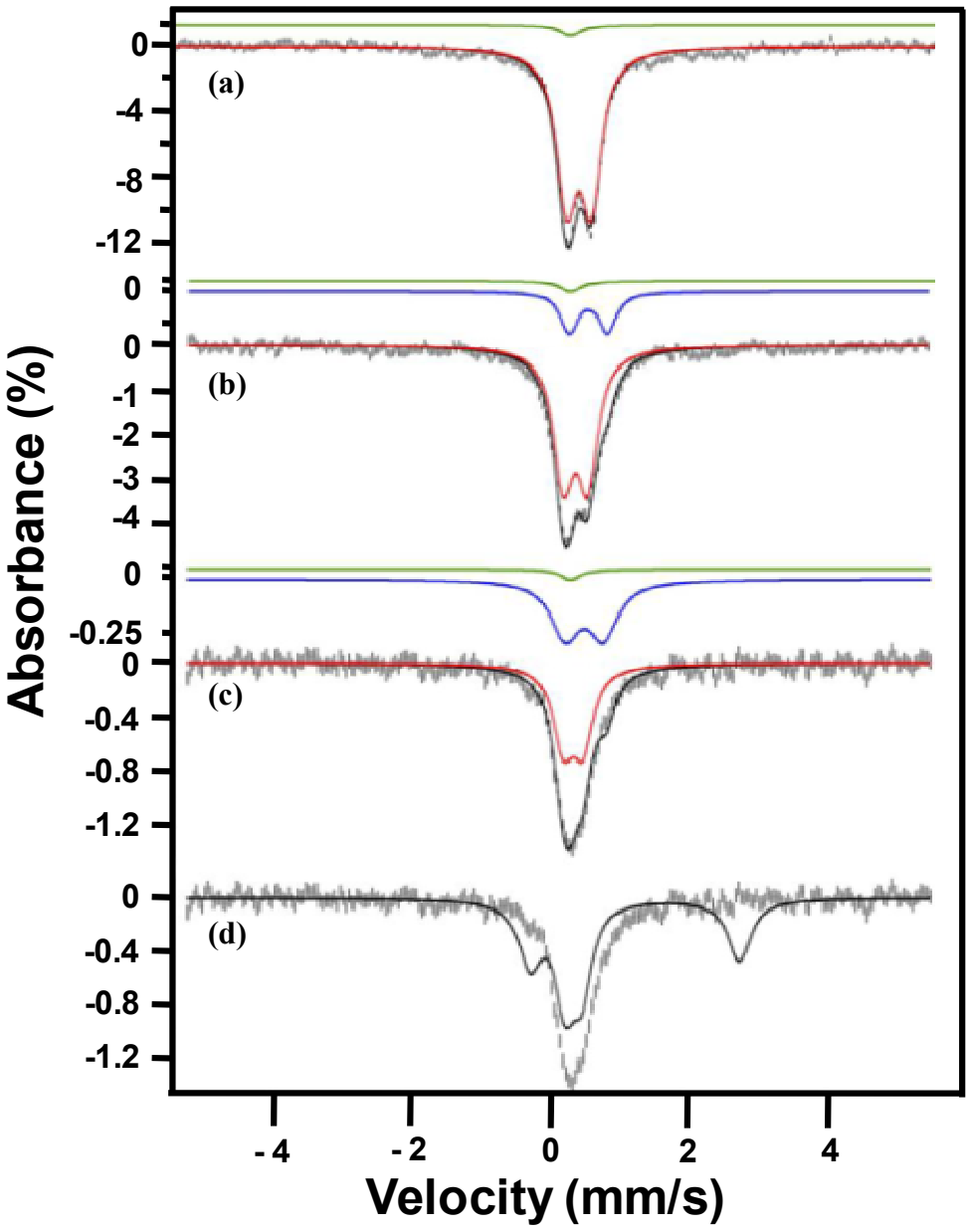

Figure 47. Mössbauer spectra at (a) 4.2 K, (b) 220 K and (c) 300K. The plot in (d) represents a simulation of HS Fe^{II} at 300K. The red trace is the simulated contribution of LS Fe^{II}, the blue line is HS Fe^{III} and the green line represents a LS Fe^{II} impurity. The black line represents the sum of contributions for all types of Fe in the sample.

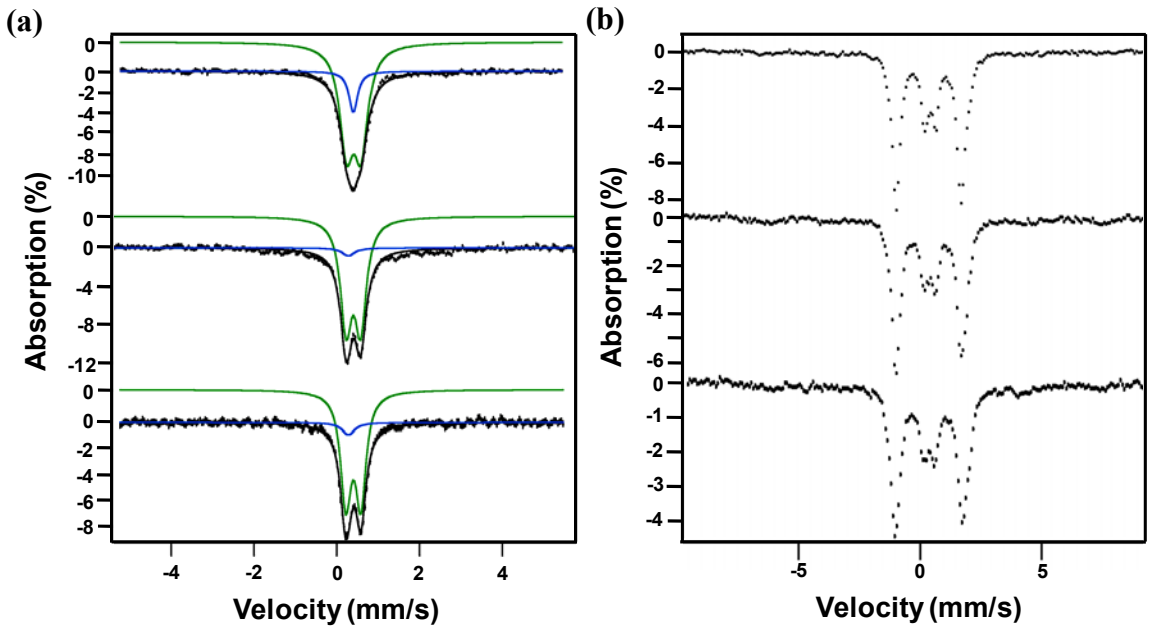

Figure 48. Mössbauer spectra for Fe_3Os_2 TBP clusters from three different synthetic batches, labeled A-C. The dotted black line represents the raw data. (a) Low field 4.2 K spectra. The green and blue lines are the majority and minority LS Fe^{II}, respectively. (b) High field (8T), 4.2 K Mössbauer spectra. The minority HS Fe^{III} is most easily identified by the small area between the straight line marking the baseline of each spectrum and the experimental data at velocities of < -1.5 mm/s and > 2 mm/s.

the quadrupole doublet of this majority iron component reflects the presence of a small amount of LS Fe^{II}, which represents at most 5% of the Fe in the sample. A spectrum obtained at 4.2 K and 8 T for the same sample confirmed the fact that the majority of the iron in the sample is LS Fe^{II} and revealed that the sample contains also HS Fe^{III} which is, at most 10% of the Fe in the sample, accounted for due to an incomplete transition in the sample (Figure 48). Examination of several samples of compound **15** obtained from different synthetic batches showed that they all contain a minority LS Fe^{II} and HS Fe^{III} species at 4.2K (Figure 49, Table 11). If a LS Fe^{II} to HS Fe^{II} transition takes place in **15**, Mössbauer spectra obtained at 220 K and 300 K would show the appearance of a quadrupole doublet with $\delta \sim 1$ mm/s and $\Delta E_Q \sim 3$ mm/s, whose right line would be easiest to observe at > 2 mm/s (Figure 47D). The lack of absorption at > 2 mm/s in the 300 K spectrum excludes the possibility that a LS Fe^{II} to HS Fe^{II} spin transition takes place for **15**. If HS Fe^{III} forms from LS Fe^{II} by CTCST, the HS Fe^{III} would be represented in the Mössbauer spectra at $T \geq 220$K by a quadrupole doublet with $\delta \sim 0.5$ mm/s and $\Delta E_Q \sim 0.5$ mm/s, which would be observed as a shoulder on the right side of the doublet of LS Fe^{II}. Indeed such a spectral feature is observed in the 220 and 300 K spectra (blue line in Figures 47 B,C). Therefore the Mössbauer data rules out a spin crossover transition at the Fe^{II} sites and is compatible with the manifestation of a CTCST from LS-Fe^{II}-Os^{III} to HS Fe^{III}-Os^{II}, experimental values of which are reported in Table 12. As noted above, not all of the sample undergoes a complete CTCST, and the minority LS Fe^{II} and HS Fe^{III} which are present in the samples at 4.2 K and shown also

Table 11. Sample composition for different batches of the Fe_3Os_2 TBP cluster. The % of HS Fe^{III} in each sample was estimated based on the high field Mössbauer spectra and the % of LS Fe^{II} was estimated based on the low field spectra. A, B and C are the samples for which the high field and low field spectra are shown in Figure 48.

Sample	Fe type	Shift (mm/s)[a]	ΔEq (mm/s)[a]	%[b]
A	LS Fe^{II} -I	0.40	0.36	93
	LS Fe^{II} -II	0.28	0.00	7
	HS Fe^{III}	0.45	0.55	<10
B	LS Fe^{II} -I	0.40	0.35	95
	LS Fe^{II} -II	0.28	0.00	5
	HS Fe^{III}	0.45	0.55	<12
C	LS Fe^{II} –I	0.41	0.35	83
	LS Fe^{II}-II	0.40	0.00	17
	HS Fe^{III}	0.45	0.55	<7

[a] The precision for both the isomer shift and the quadrupole splitting of the LS Fe^{II} and HS Fe^{III} is ±0.01 mm/s and 0.02 mm/s, respectively.

[b] Each sample contains HS Fe^{III} and LS Fe^{II}. The percentage reported for HS Fe^{III} is calculated with respect to all the Fe in the sample. For LS Fe^{II}, we report relative distribution of types A and B with respect to the total amount of LS Fe^{II} present in the sample, thus excluding the HS Fe^{III}.

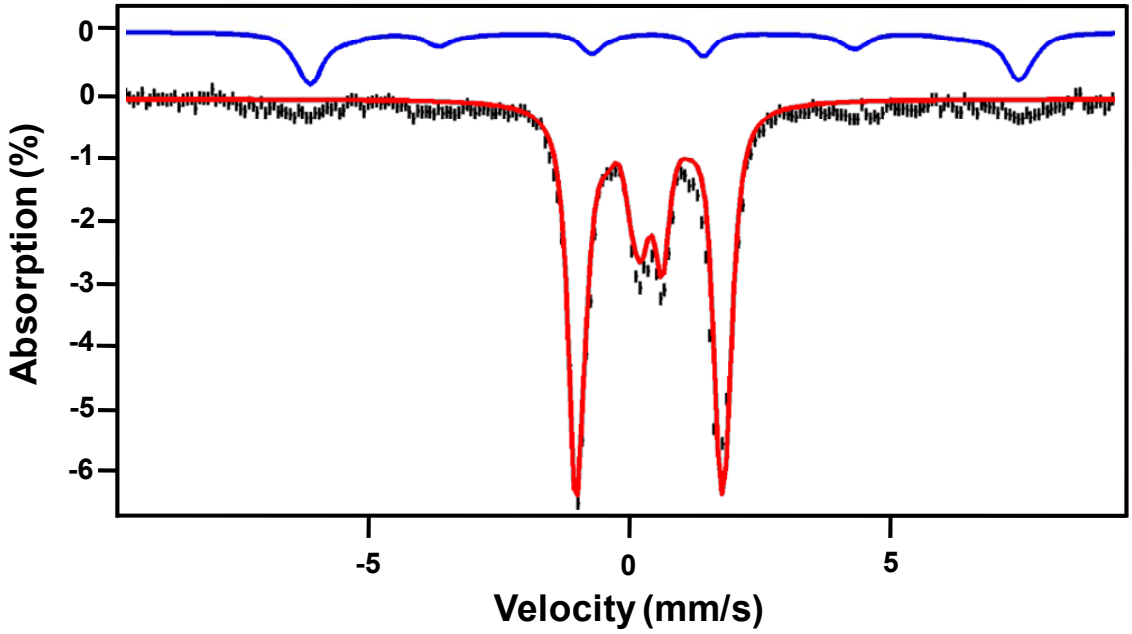

Figure 49. High field (8T) 4.2 K Mössbauer spectra for Fe_3Os_2 TBP clusters. The dotted black line represents the raw data. The red and blue lines are the theoretical simulations of LS Fe^{II} and HS Fe^{III} respectively.

Table 12. Mössbauer parameters for a polycrystalline sample of Fe_3Os_2 TBP.

T (K)	Fe site	d (mm/s)	DE_Q (mm/s)	%
4.2	LS Fe^{II}	0.40	0.35	95
	LS Fe^{II}*	0.28	0.00	5
220	LS Fe^{II}	0.35	0.35	72
	HS Fe^{III}	0.54	0.55	22
	LS Fe^{II}*	0.28	0.00	6
300	LS Fe^{II}	0.32	0.28	66
	HS Fe^{III}	0.50	0.55	27
	LS Fe^{II}*	0.28	0.00	6

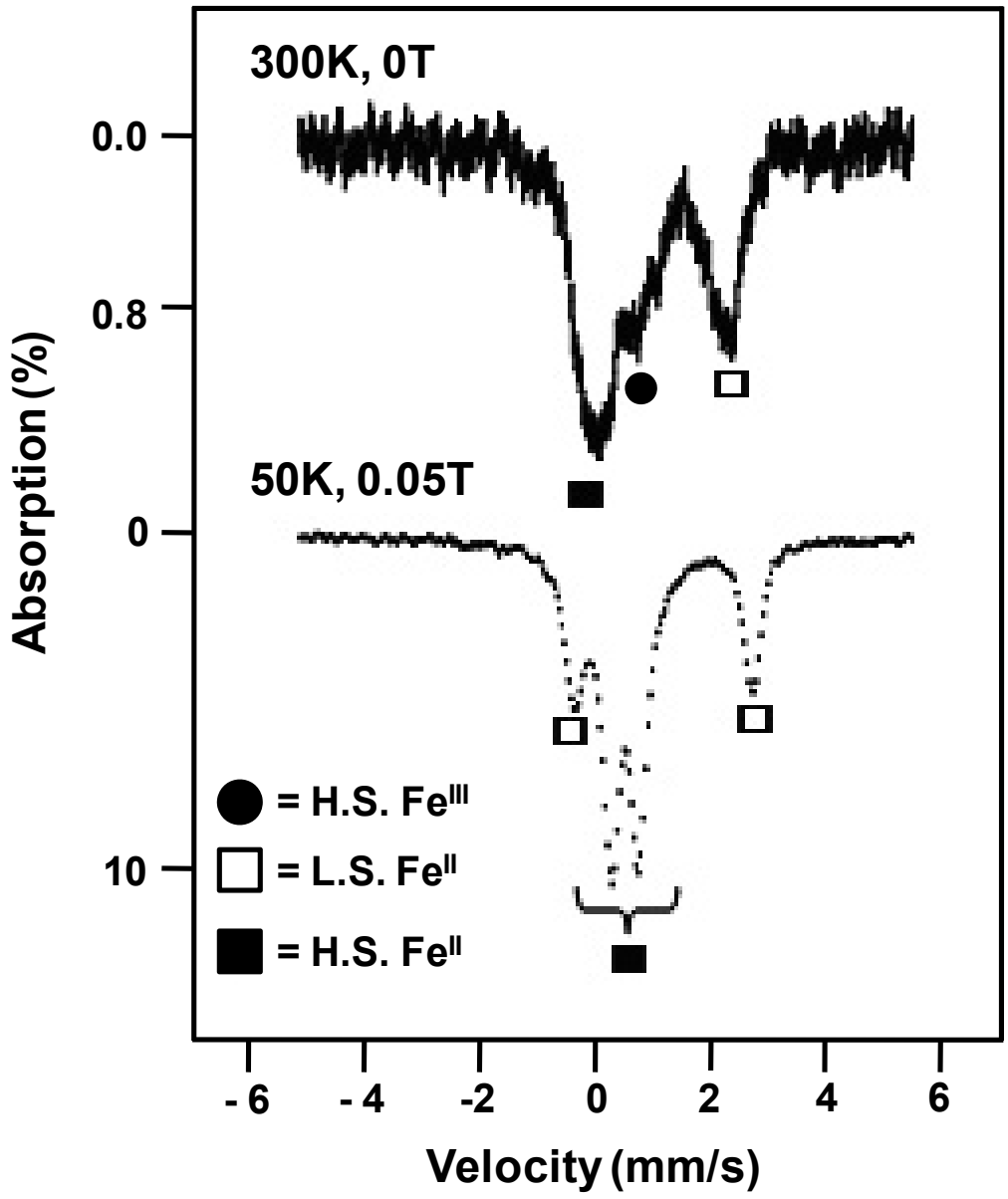

Figure 50. Mössbauer spectra at 50 K and 300 K for Fe_3Ru_2 TBP. (■) indicates H.S. Fe^{II} and (□) indicates L.S. Fe^{II} both of which are present at 50K. (●) represents H.S. Fe^{III} which forms as the temperature is increased to 300 K, in addition to the growth of H.S. Fe^{II} and decrease in amount of L.S. Fe^{II}.

in Table 11 is likely a population of <10% clusters that are "locked" into HS Fe^{III}-Os^{II} form at low temperature (Figure 48).

$[Fe(tmphen)_2]_3[Ru(CN)_6]_2$ TBP (16). Preliminary Mössbauer spectroscopic measurements indicate that this cluster, as apparent from the magnetic properties is a highly complex system (Figure 50). At 50 K both low spin Fe^{II} and HS Fe^{II} are present and as the temperature increases to 300 K there is a slight increase in the feature at > 2 mm/s with a quadrupole doublet of $\delta \sim 1$ mm/s and $\Delta E_Q \sim 3$ mm/s, which is due to increasing concentration of H.S. Fe^{II}. The major change observed at 300 K in the sample, is the observation of a quadrupole doublet with $\delta \sim 0.5$ mm/s and $\Delta E_Q \sim 0.5$ mm/s, which is seen as a shoulder on the right side of the doublet of LS Fe^{II}. This indicates the increasing percentage of HS Fe^{III} in the sample as the temperature increases, which supports the notion that HS Fe^{III} is forming postulated from the analysis of the magnetic data. At low temperatures in both the Mössbauer measurements and the magnetic data, the best fit of the data indicates the presence of both HS Fe^{II} and LS Fe^{II}. As the temperature increases, the postulated high temperature electronic configuration of one HS Fe^{III}, one HS Fe^{II}, one LS Fe^{II}, one Ru^{II} and one Ru^{III} is also supported by the appearance of HS Fe^{III} in the Mössbauer measurements. The combined results of the two methods are augmented by the IR data which reveal 4 different types of CN stretches and support this electronic configuration. It appears that the Fe_3Ru_2 cluster exhibits a combination of the properties exhibited by the other two members of the Fe_3M_2 family of clusters. While the Fe_3Fe_2 TBP compound exhibits only a HS to LS Fe^{II} transition, and the Fe_3Os_2 TBP exhibits only a CTCST, the Fe_3Ru_2 cluster appears to

be capable of undergoing both phenomena to some extent. This is the first instance of this type of complex behavior to be recognized. For physical methods details of the Mössbauer measurements, see Appendix A.

Conclusions

In summary we have studied the new cyanide-bridged $[Fe(tmphen)_2]_3[Os(CN)_6]_2$ and $[Fe(tmphen)_2]_3[Ru(CN)_6]_2$ clusters by a full characterization of their structural, spectroscopic and magnetic properties. The $[Fe(tmphen)_2]_3[Os(CN)_6]_2$ compound clearly exhibits CTCST behavior. The $[Fe^{III}(tmphen)_2(NC)_2]^{2+}$ units present in the complex at high temperature are the first structurally characterized examples of HS Fe^{III} ions with an all nitrogen ligand environment. The data collected on bond distances and Mössbauer parameters constitutes a useful database for comparing results for new iron compounds in the future. Most importantly, however, our studies revealed an unprecedented type of reversible, temperature-induced, charge transfer coupled spin transition between [LS Fe^{II}-Os^{III}] to [HS Fe^{III}–Os^{II}] centered at room temperature, one of the highest CTCST temperatures reported to date. This discovery constitutes a new and unique addition to the relatively rare CTCST phenomenon literature and provides a heretofore unknown mechanism for such a transition.

Arguably, the biggest impact of this work however, is that this study provides the only complete study on a family of isostructural clusters in which a trend in the SCO/CTCST properties is correlated to a single variable, namely the identities of the metal ion of the cyanometallate, all of which belong to the same group of LS d^5 metals.

As one traverses down the family from 3d to 5d ions, it is observed that the Fe_3Fe_2 complex exhibits SCO behavior, the Fe_3Ru_2 exhibits a mixture of CTCST and SCO phenomena, and finally the Fe_3Os_2 cluster exhibits only CTCST behavior. These findings will be a valuable source of information for theoretical study into the nature of both spin crossover and charge transfer induced spin transition properties in related compounds.

CHAPTER V

NEW PRUSSIAN BLUE ANALOGS BASED ON THE 4*d* AND 5*d* HEXACYANOMETALLATES $[Ru(CN)_6]^{3-}$ AND $[Os(CN)_6]^{3-}$

Introduction

As described in Chapter I, the history of Prussian Blue and its well defined analogs constitute a crucial backdrop for the studies in this dissertation. If one is to access truly new Prussian Blue analogs with fascinating properties however, it is necessary to go beyond modification of the existing ones by cation substitution and metal ion ratio changes as previously mentioned. It is important to synthesize new analogs based on elusive cyanometallates that have not been explored as building blocks. Theoretical work on this topic has proposed a number of possible metal ion combinations[136] (Table 13) which could lead to high temperature ordered magnets, but unfortunately these necessary building blocks are often much less stable than the classic cyanometallates used in the aqueous chemistry of Prussian Blue and related derivatives of the first row transition metals. For example, theoretical calculations predict that the best magnets will be those based on $[Mo(CN)_6]^{3-}$, $[Mn(CN)_6]^{3-}$, and $[V(CN)_6]^{3-}$. Of the three anions, the first one has only been isolated as an unstable product,[137] and the latter two are unstable in aqueous media.[62, 138] The difficult nature of this chemistry is exemplified by reports of the reactivity of the $[V(CN)_6]^{3-}$ anion by Joel Miller *et al*. who attempted to incorporate this building block into Prussian Blue analogs with divalent

Table 13. Theoretical T_c values for new Prussian Blue analogs.

M,M'	T_c (K)
$Mn^{III}V^{II}$	480
$Mo^{III}V^{II}$	552
$Cr^{III}Mo^{II}$	355
$V^{III}V^{II}$	344
$Cr^{III}V^{II}$	315
$Cr^{III}Mo^{II}$	185
$Mo^{III}Cr^{II}$	308
$Mn^{III}Cr^{II}$	147
$Cr^{III}Cr^{II}$	116

M = hexacyanometallate, M' = free metal ion

Mn, Fe, Co, and Ni ions.[138] The reactions were carried out under an inert atmosphere in acetonitrile and tetrahydrofuran. With the exception of the Mn^{II} case, the reactions result in either redox chemistry or labilization of the CN ligand. In addition to these problems, another issue that arises with non-aqueous synthesis is that the complexes are amorphous which precludes their analyses by powder diffraction. Discrete cyanide bridged molecular clusters are important to have in hand so that the corresponding Prussian Blue analogs can have a benchmark for expected magnetic properties and infrared spectral features.

Given that we now have a number of new clusters with unusual metal ion combinations in hand, it was an obvious question to ask whether the Prussian Blue analogs could be prepared as well. In this chapter, the synthesis of the various Prussian Blue analogs was undertaken to investigate how closely the properties are for extended networks and molecular counterparts. Materials were prepared using the $[Os(CN)_6]^{3-}$ and $[Ru(CN)_6]^{3-}$ building blocks in both aqueous mixtures as well as organic solvents with Mn^{II}, Fe^{II}, and Ni^{II} ions. The Ni^{II} analogs which all exhibit ferromagnetic ordering have been subjected to a solvent study in order to track the changes in magnetic properties for products prepared in the polar non-H bonding solvent acetonitrile, the protic solvent methanol, and a mixture of methanol and water. This is the first such study of its kind for Prussian Blue analogs.

Experimental Section

Syntheses

The preparation of the $[PPN]_3[Os(CN)_6]$ and $[PPN]_3[Ru(CN)_6]$ were carried our as described in (see Chapter III). Nitrate salts of Mn^{II}, Fe^{II}, and Ni^{II} were purchased from Aldrich and used as received. Elemental analyses were performed by Chemisar in Guelph, Ontario. It should be noted that elemental analysis for Prussian Blue complexes, especially for amorphous products are much more variable than those for discrete clusters. As such, the elemental analyses will be reported here with the corresponding formula, but for simplicity sake, an abbreviated notation of the formula of the Prussian Blue phases will be used throughout. The samples are synthesized in their respective solvents, however, they rapidly exchange entrapped solvent from the reaction rapidly exchanges for water molecules when dried in air. The products consistently exhibit between 18 and 22 molecules of solvent (mostly water) per formula unit.

$Mn_3[Os(CN)_6]_2 \cdot 18H_2O$. A sample of $Mn(NO_3)_2 \cdot 4H_2O$ (0.039 g, 0.156 mmol) was dissolved in 20 mL of a 50:50 mixture of H_2O/MeOH, and the solution was stirred for 10 minutes until all solids dissolved to form a colorless solution. The resulting solution was quickly combined with a solution of 0.20 g (0.101 mmol) of $(PPN)_3[Os(CN)_6]$ in 20 mL of a 60:40 MeOH/H_2O mixture in a 50 mL Erlenmeyer flask. The mixture was stirred for 5 minutes during which time a tan solid immediately precipitated. The flask was placed in a 10° refrigerator overnight. After this period of time, the product was removed by filtration and washed with methanol (3 x 30 mL). Yield 33 mg product (77%). Elemental analysis and TGA data led to the conclusion that there are between 17-18 H_2O

molecules in the sample. Anal. Calcd for: C, 13.60; H, 2.28; N, 15.87; Mn, 13.83 . Found: C, 12.63; H, 2.29; N, 14.31; Mn, 12.39%.

$Mn_3[Ru(CN)_6]_2 \cdot 22H_2O \cdot MeOH$. A quantity of $Mn(NO_3)_2 \cdot 4H_2O$ (0.030 g, 0.12 mmol) was dissolved in 20 mL of MeCN, and the solution was stirred for 10 minutes. The resulting colorless solution was combined with a solution of 0.150 g (0.081 mmol) of $[PPN]_3[Ru(CN)_6]$ in 20 mL MeCN in a 50 mL Erlenmeyer flask which led to the instantaneous precipitation of a tan solid. After stirring for 5 minutes, the flask was placed in a 10° refrigerator overnight. After this period of time, the product was filtered in air and washed with methanol (3 x 30 mL). Yield 22 mg product (82%). Elemental analysis indicated the presence of interstitial water molecules after exposure to air during the test which is additionally confirmed by TGA showing between 18-19 H_2O molecules lost upon heating, slightly less than determined by the elemental analysis which was used to determine the formula Anal. Calcd for: C, 16.03; H, 3.40; N, 17.72; Mn, 15.45. Found: C, 15.09; H, 3.12; N, 16.60; Mn, 18.74%.

$Fe_3[Os(CN)_6]_2 \cdot 19H_2O$. A quantity of $Fe(NO_3)_2 \cdot 6H_2O$ (0.049 g, 0.19 mmol) was dissolved in 20 mL of MeCN, and the solution was stirred for 10 minutes to yield a pale yellow solution which was quickly combined with a solution of 0.250 g (0.127 mmol) of $[PPN]_3[Os(CN)_6]$ in 20 mL of MeCN in a 50 mL Erlenmeyer flask. The mixture was stirred for 5 minutes during which time a dark blue solid was observed to appear which was filtered and washed with methanol (3 x 30 mL). Yield 48 mg product (88 %). A combination of elemental TGA analysis led to the estimation of 19 H_2O molecules per

formula unit. Anal. Calcd for: C, 11.94; H, 3.17; N, 13.93; Fe, 13.91 . Found: C, 12.47; H, 2.89; N, 12.24; Fe, 13.11%.

$PPN_{0.6}Fe_{2.7}[Ru(CN)_6]_2 \cdot 14H_2O \cdot 2MeCN$. A sample of $Fe(NO_3)_2 \cdot 6H_2O$ (0.043 g, 0.17 mmol) was dissolved in 20 mL of MeCN, and the solution was stirred for 10 minutes to give a pale yellow solution. The solution was quickly combined with 20 mL of an acetonitrile solution of 0.20 g (0.108 mmol) of $[PPN]_3[Ru(CN)_6]$ in a 50 mL Erlenmeyer flask. The mixture was stirred for 5 minutes and the resulting dark blue solid was collected by filtration in air and washed with methanol (3 x 30 mL). Yield 26 mg (70%). The number of interstitial solvent molecules were determined to be approximately 14 water molecules from a combination of elemental and TGA data. Anal. Calcd for: C, 34.07; H, 3.95; N, 15.44; Fe, 11.40 . Found: C, 34.10; H, 4.00; N, 13.29; Mn, 10.27%.

$Ni_3[Os(CN)_6]_2 \cdot 20H_2O \cdot 2MeCN$. A sample of $Ni(NO_3)_2 \cdot 6H_2O$ (0.052 g, 0.18 mmol) was dissolved in 20 mL of MeCN, and the solution was stirred for 10 minutes until all solids dissolved and a pale green solution was observed. The resulting solution was quickly combined with a solution of 0.25 g (0.127 mmol) of $[PPN]_3[Os(CN)_6]$ in 20 mL of MeCN in a 50 mL Erlenmeyer flask. The mixture was stirred for 5 minutes to give an orange-brown precipitate and the flask was placed in a refrigerator at 10° overnight. After this period of time the product was collected by filtration in air and washed with methanol (3 x 30 mL) Yield 42 mg (77%). The interstitial solvent content of the solid by elemental and TGA analyses led to the evaluation that between 18-19 H_2O molecules and one MeCN molecule are present per formula unit slightly less than the elemental

analysis used to determine the formula. Anal. Calcd for: C, 14.63; H, 3.53; N, 14.91; Ni, 13.24 . Found: C, 14.46; H, 2.91; N, 13.51; Ni, 12.29%.

$Ni_3[Os(CN)_6]_2 \cdot 20H_2O \cdot MeOH$. A sample of $Ni(NO_3)_2 \cdot 6H_2O$ (0.054 g, 0.186 mmol) was dissolved in 20 mL of MeOH and resulting pale green solution was stirred for 10 minutes after which time it was combined with a solution of 0.25 g (0.127 mmol) of $[PPN]_3[Os(CN)_6]$ in 20 mL of MeOH in a 50 mL Erlenmeyer flask. The mixture was stirred for 5 minutes and an orange-brown solid was observed to rapidly precipitate. The flask was placed in a refrigerator overnight at 10° and then collected by filtration in air and washed with methanol (3 x 30 mL) Yield 45 mg (83%). Elemental analysis and TGA revealed 19 H_2O molecules and one MeOH molecule as the interstitial solvent content slightly less than found in the elemental analysis which was used for the formula.Anal. Calcd for: C, 12.72; H, 3.28; N, 13.70; Ni, 14.17. Found: C, 12.69; H, 2.84; N, 14.00; Ni, 11.04%.

$Ni_3[Os(CN)_6]_2 \cdot 4H_2O$. A quantity of $Ni(NO_3)_2 \cdot 6H_2O$ (0.031 g, 0.106 mmol) was dissolved in 20 mL of 50:50 MeOH/H_2O and the solution was stirred for 10 minutes to give a pale green solution which was treated with a solution of 0.198 g (0.1 mmol) of $[PPN]_3[Os(CN)_6]$ in 20 mL of a 60:40 MeOH/H_2O mixture in a 50 mL Erlenmeyer flask. The mixture was stirred for 5 minutes which led to the formation of an orange-brown solid. After the flask had been chilled in a refrigerator overnight at 10° the solution was filtered in air and the solid was washed with methanol (3 x 30 mL) Yield 37 mg (86%) Elemental Calculated: C 15.20, H 0.91, N 17.74, O 7.26, Ni 18.35, Os 40.53. Found: C 15.01, H 0.90, N 17.20, O 7.15, Ni 17.30.

$Ni_3[Ru(CN)_6]_2 \cdot 20H_2O \cdot MeCN$. A sample of $Ni(NO_3)_2 \cdot 6H_2O$ (0.06 g, 0.2 mmol) was dissolved in 20 mL of MeCN, and the solution was stirred for 10 minutes to give a pale green solution. The resulting solution was quickly combined with a solution of 0.250g (0.13 mmol) of $(PPN)_3[Ru(CN)_6]$ in 20 mL MeCN in a 50 mL Erlenmeyer flask The mixture was stirred for 5 minutes which led to the formation of an orange-brown precipitate. After storage in a refrigerator overnight the product was collected by filtration and washed with methanol (3 x 30 mL). Yield 36 mg (81%). Elemental analysis and TGA led to the conclusion that an average of 20 H_2O molecules and one acetonitrile solvent molecule are trapped in the material. Anal. Calcd for: C, 15.4; H, 3.97; N, 16.6; Ni, 15.9 . Found: C, 14.54; H, 3.99; N, 15.13; Ni, 12.47%.

$PPN_{0.2}Ni_{2.9}[Ru(CN)_6]_2 \cdot 16H_2O \cdot 2MeOH$. A sample of $Ni(NO_3)_2 \cdot 6H_2O$ (0.058 g, 0.19 mmol) was dissolved in 20 mL of MeOH and after stirring the pale green solution for 10 minutes it was combined with a solution of 0.150 g (0.13 mmol) of $[PPN]_3[Ru(CN)_6]$ in 20 mL MeOH in a 50 mL Erlenmeyer falsk. The mixture was stirred for 5 minutes during which time an orange-brown solid formed; the flask was stored in a refrigerator overnight at 10° . After chilling, the solution was filtered in air and washed with methanol (3 x 30 mL) Yield 22 mg (80%). Elemental analysis and TGA support the assignment of 15-16 interstitial H_2O molecules and 2 MeOH molecules on the average per formula unit. Anal. Calcd for: C, 22.24; H, 4.05; N, 14.93; Ni, 14.69 . Found: C, 23.29; H, 3.83; N, 14.84; Ni, 15.20%.

$Ni_3[Ru(CN)_6]_2 \cdot 20H_2O \cdot 2MeOH$. A sample of $Ni(NO_3)_2 \cdot 6H_2O$ (0.035 g, 0.12 mmol) was dissolved in 20 mL of a 50:50 MeOH/H_2O mixture to give a pale green soliution.

After 10 minutes of stirring, the solution was treated with was a solution of 0.150g (0.08 mmol) of $(PPN)_3[Ru(CN)_6]$ in 20 mL og a 60:40 MeOH/H_2O mixture in a 50 mL Erlenmeyer flask. The orange-brown solid that immediately precipitated was stored in the mother liquor in a refrigerator overnight at 10° The product was then filtered and washed with methanol (3 x 30 mL) Yield 23 mg (82%). Elemental analysis and TGA support the assignment of 20 interstitial H_2O molecules and 2 MeOH molecules on the average per formula unit. Anal. Calcd for: C, 15.58; H, 4.11; N, 15.58; Ni, 16.12. Found: C, 14.82; H, 3.81; N, 14.61; Ni, 15.89%.

Results and Discussion

Synthesis

The typical synthetic strategy used to prepare Prussian Blue materials is to react a hydrated transition metal cation with a solution of a hexacyanometallate in water. In our synthesis however, we are using solvents that dissolve the PPN salts of $[Ru(CN)_6]^{3-}$ and $[Os(CN)_6]^{3-}$ in order to prevent decomposition from occurring, especially in the case of the notoriously unstable Ru^{III} derivative. The starting materials are reacted in a 2:3 ratio of the hexacyanometallate with the labile metal precursor, which is based on the idealized formula of $M^{II}_3[M^{III}(CN)_6]_2$ in acetonitrile or a mixture of H_2O and methanol. To ascertain the effects of solvent on the ordering temperature of the complex, the syntheses of the Ni_3Ru_2 and Ni_3Os_2 PB analogs were performed in three different solvent environments, namely H_2O/MeOH, MeOH, and MeCN. In all cases the reactions led to the formation of the Prussian Blue as an insoluble microcrystalline powder.

Powder Diffraction Studies

It is well known that single crystals of Prussian Blue and its analogs are very difficult to obtain, but the necessity of obtaining single crystal data is mitigated by the fact that powder X-ray diffraction is quite useful for such high symmetry materials and, indeed, it is the standard method for confirming the existence of an extended Prussian Blue framework. All samples were collected on a holder composed of a single silicon crystal to minimize background interference. Samples were ground and gently pressed onto the surface and the data were collected from 5 – 55° in 2θ at room temperature (Appendix A). The data were fit to a face centered cubic unit with the unit cell parameter on average of 10.4(1) Å for the various PB analogs (for detailed fitting data see Appendix B), Figures 51 and 52. This unit cell is similar to the closest known example to these present materials, namely the $K_{1.2}Ru_{3.6}[Ru(CN)_6]_3 \cdot 16H_2O$ PB analog recently reported by the Long research group for which the unit cell parameter for the FCC cell is 10.42 Å.

Infrared Spectroscopy

Analysis of the $\nu_{C\equiv N}$ stretches were performed by FTIR spectroscopy (Appendix A) for all of the materials at room temperature (Table 14). In the case of the Mn Prussian Blue analogs, two stretches are observed one very broad peak ranging from 2000-2100 cm^{-1} for the Mn_3Ru_2 PB, and 2030-2100 cm^{-1} for the Mn_3Os_2 These stretches are consistent with both Ru^{II}, Ru^{III} and Os^{II}, Os^{III} being present in each compound respectively. Both of these materials also exhibit weak IR features at 2170 and 2164 cm^{-1} which correspond to bridging modes for both Ru^{III} and Os^{III} as determined from data for

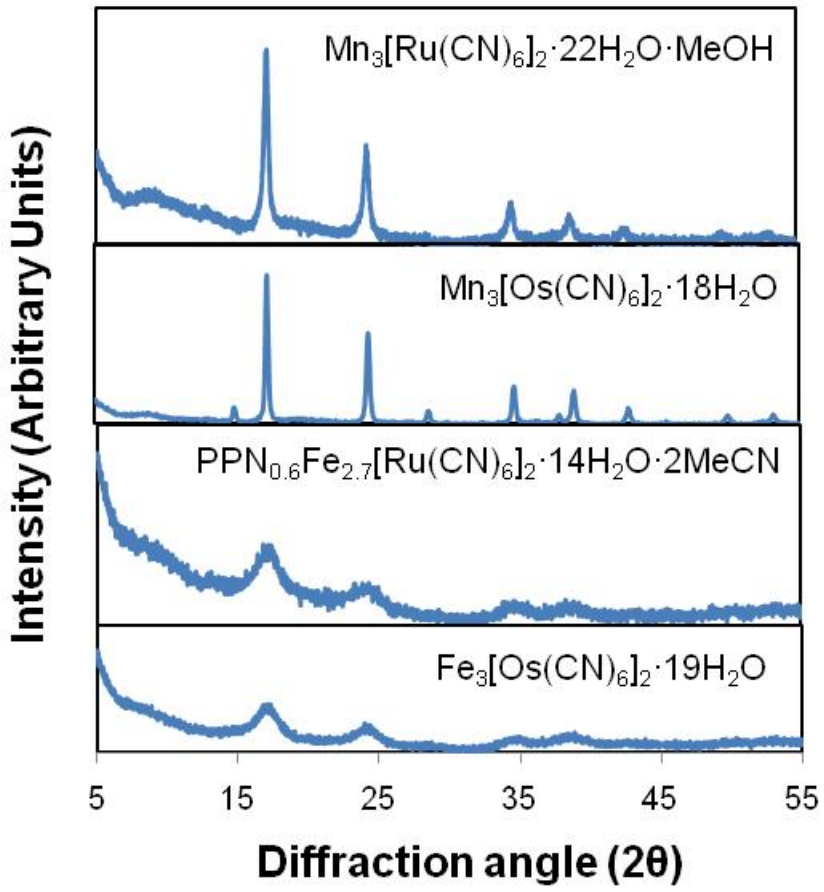

Figure 51. Powder X-ray diffraction patterns collected from 5-55° in 2θ for the Mn and Fe Prussian blue samples.

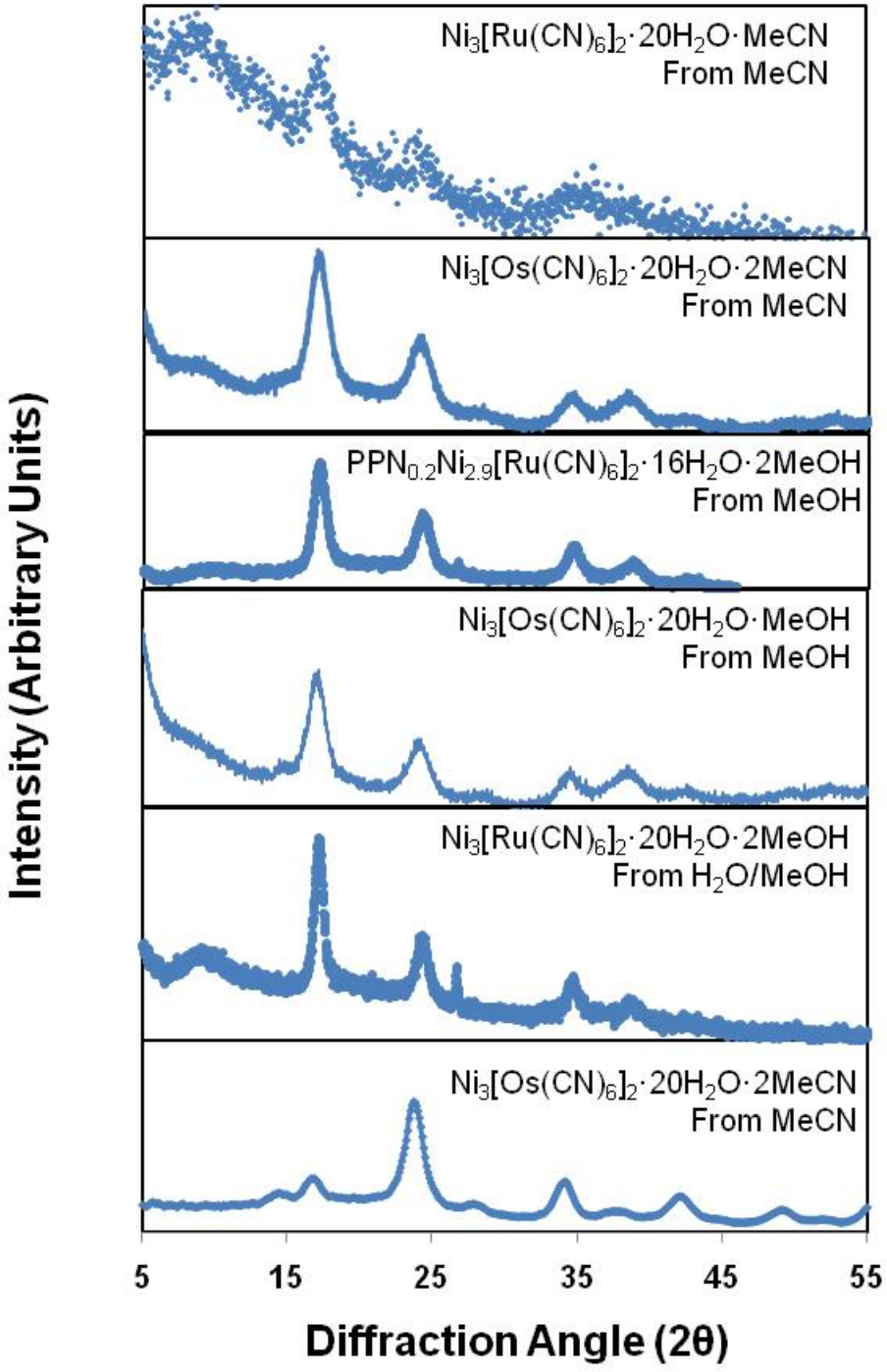

Figure 52. Powder X-ray diffraction patterns collected from 5-55° in 2θ for the above Prussian blue samples.

T**able 14.** IR $\upsilon_{C\equiv N}$ stretches for Prussian Blue materials and TBP clusters.

Compound	**$\nu_{C\equiv N}$ stretches (cm^{-1})**
$Mn_3[Os(CN)_6]_2 \cdot 18H_2O$	2030-2100(broad), 2170(weak)
Mn_3Os_2 TBP	2097 (b, s), 2119 (m), 2142(m)
$Mn_3[Ru(CN)_6]_2 \cdot 22H_2O \cdot MeOH$	2000-2100 (b), 2164 (w)
Mn_3Ru_2 TBP	2055 (s), 2096 (w), 2126 (w)
$Fe_3[Os(CN)_6]_2 \cdot 19H_2O$	2068 (b), 2160 (m)
Fe_3Os_2 TBP 4.2K	2098 (s), 2120 (w)
$PPN_{0.6}Fe_{2.7}[Ru(CN)_6]_2 \cdot 14H_2O \cdot 2MeCN$	2074 (b,s), 2157 (m)
$Ni_3[Os(CN)_6]_2 \cdot 4H_2O$ H_2O/MeOH	2102 (b,s), 2141(m)
$Ni_3[Os(CN)_6]_2 \cdot 20H_2O \cdot MeOH$ From MeOH	2088 (b,s), 2142 (s)
$Ni_3[Os(CN)_6]_2 \cdot 20H_2O \cdot 2MeCN$ From MeCN	2089 (b,s), 2142 (s)
Ni_3Os_2 TBP	2099 (s), 2129(m), 2148(m)
$Ni_3[Ru(CN)_6]_2 \cdot 20H_2O \cdot 2MeOH$ From H_2O/MeOH	2098 (b,s), 2153 (m)
$PPN_{0.2}Ni_{2.9}[Ru(CN)_6]_2 \cdot 16H_2O \cdot 2MeOH$ From MeOH	2100 (b,s), 2156 (m)
$Ni_3[Ru(CN)_6]_2 \cdot 20H_2O \cdot MeCN$ From MeCN	2095 (b,s), 2147(m)
Ni_3Ru_2 TBP	2057(s), 2106(m), 2138(m)

b = broad, s = strong intensity, m = medium intensity, w = weak intensity

the well-characterized TBP cluster analogs. The Fe_3Ru_2 and Fe_3Os_2 PB phases exhibit intense and broad stretches at 2074 and 2068 cm^{-1} respectively which correspond the terminal cyanide frequencies for the cyanometallate. Bridging modes are observed at 2157 and 2160 cm^{-1} for the Fe_3Ru_2 and Fe_3Os_2 materials respectively. For the different products of the solvent study for the Ni_3Ru_2 and Ni_3Os_2 PBs the terminal stretches are found in the range 2088-2098 cm^{-1} and the bridging cyanide stretching frequencies occur in the range 2140-2160 cm^{-1}. The PB analogs for the Ni_3Os_2 systems correspond most closely to their TBP cluster counterparts because the electronic states in both the molecules and the Prussian Blues are the same at room temperature, namely Ni^{II} and Os^{III}. These results constitute the first such study in which a comparison of cyanide bridged clusters with the corresponding Prussian Blue phases based on combinations of the 3d metals with those of the 4d and 5d series has been reported. A summary of the IR data for each new PB and its corresponding TBP cluster is provided in Table 14.

Magnetic Properties

$Mn_3[Ru(CN)_6]_2 \cdot 22H_2O \cdot MeOH$. Magnetic measurements were carried out on powder samples of the materials from the same batches used for powder X-ray diffraction studies (Figure 53) for physical methods of all magnetic measurements see Appendix A. The room temperature χt value is 12.5 emu·K/mol, a value that remains constant until low temperatures with a steady decrease being observed below 25 K. If one assumes that the product is$[HS\ Mn^{II}]_3[Ru^{III}(CN)_6]_2$ the expected room temperature value would be 13.87 emu·K/mol for three S = 5/2 and two S = ½ non-interacting magnetic centers

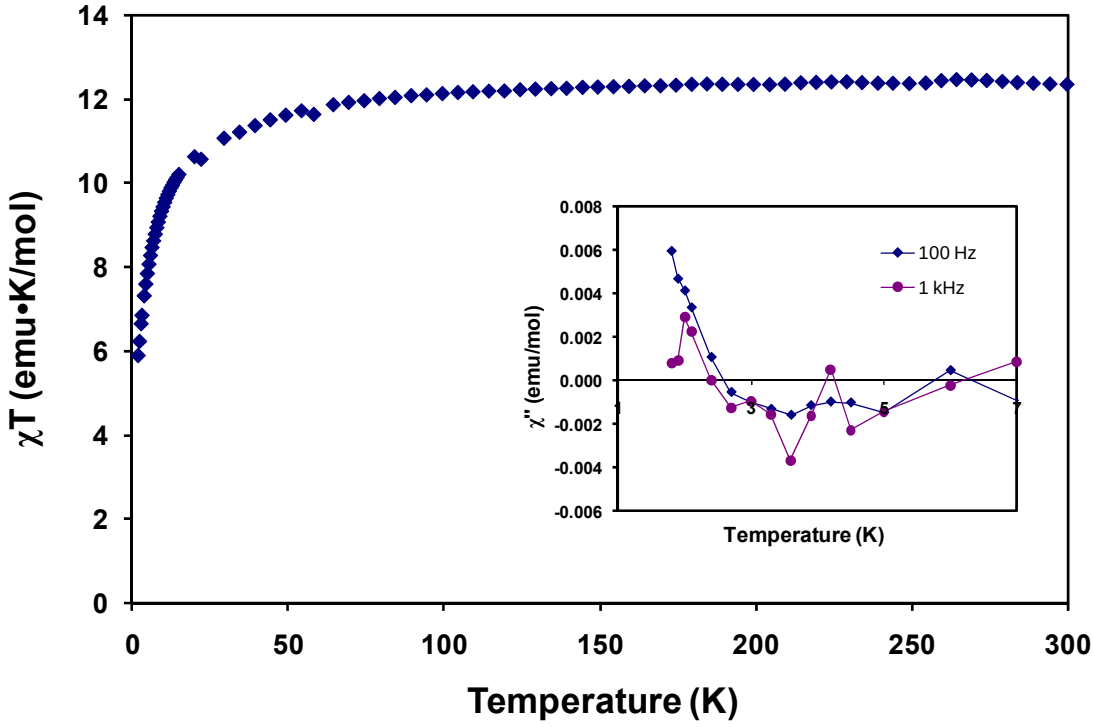

Figure 53. Temperature dependence of the χT from 300 K to 2 K for Mn_3Ru_2 PB. Inset: Imaginary part (χ'') of AC magnetic susceptibility at different frequencies under very weak applied magnetic field H_{AC} = 3 Oe and H_{DC} = 0 Oe.

which is only slightly higher than the observed value. The slightly lower than expected value could be due to partial electron transfer occurring which would mean a certain amount of HS Mn^{III} and Ru^{II} sites which would decrease the number of spin centers (HS Mn^{III} is an S = 2 ion and Ru^{II} is diamagnetic). The plateau in the magnetic properties is consistent with perhaps a very weak or no coupling which is similar to the behavior observed for the Mn_3Ru_2 TBP cluster. AC susceptibility data revealed no long range ordering occurs in this material.

$Mn_3[Os(CN)_6]_2 \cdot 18H_2O$. The osmium congener behaves in an essentially identical fashion to the Mn_3Ru_2 PB (Figure 54). The room temperature χT value is 11.67 emu·K/mol which remains nearly constant (it decreases slightly) until low temperatures where it begins to decrease more rapidly toward zero at 50 K. Using the same argument as advanced above, the expected 300K value would be 13.87 emu·K/mol for three S = 5/2 and two S = ½ centers, higher than the observed data. In this material, the degree of electron transfer must be slightly higher to account for this result. The IR data are in accord with mixtures of different oxidation states as the CN stretching frequencies are quite broad pointing to the conclusion that both Os^{II} and Os^{III} are present in the material. AC susceptibility measurements indicate that a weak long range ordering may be taking place below 1.8 K. The observed onset of a χ'' signal with a slight frequency dependence typically observed for disordered (glassy) materials undergoing long range ordering, but the signal is only slightly perceptible above the baseline, signifying only a very small

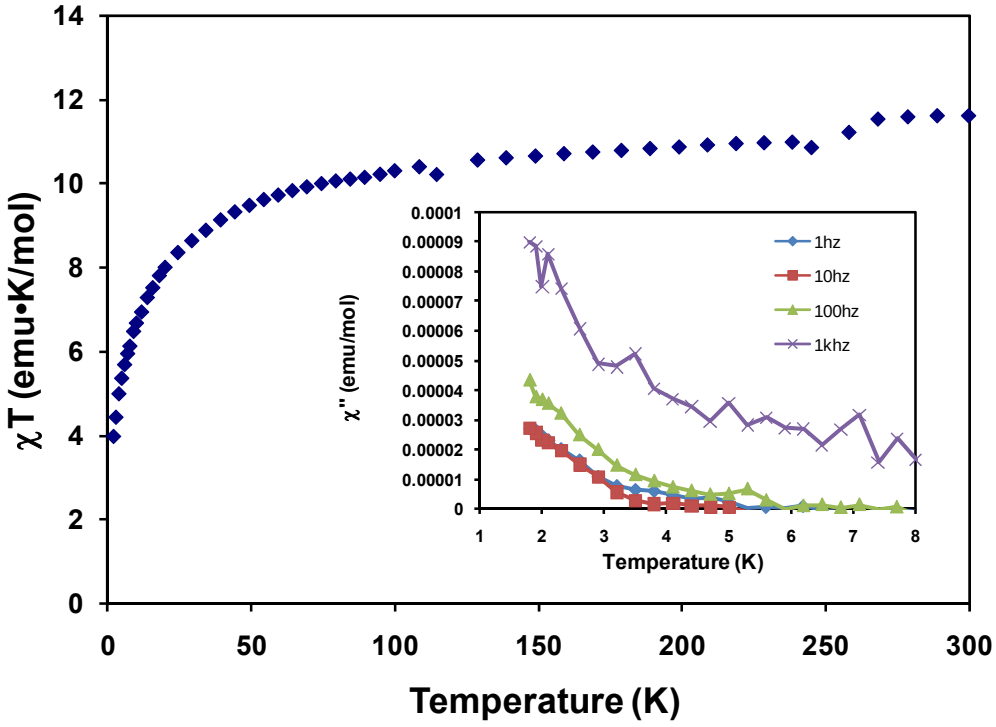

Figure 54. Temperature dependence of χT from 300 K to 2 K for the Mn_3Os_2 PB. Inset: Imaginary part (χ'') of AC magnetic susceptibility at different frequencies with H_{AC} = 3 Oe and H_{DC} = 0 Oe, out of phase signal is indicative of very weak ordering.

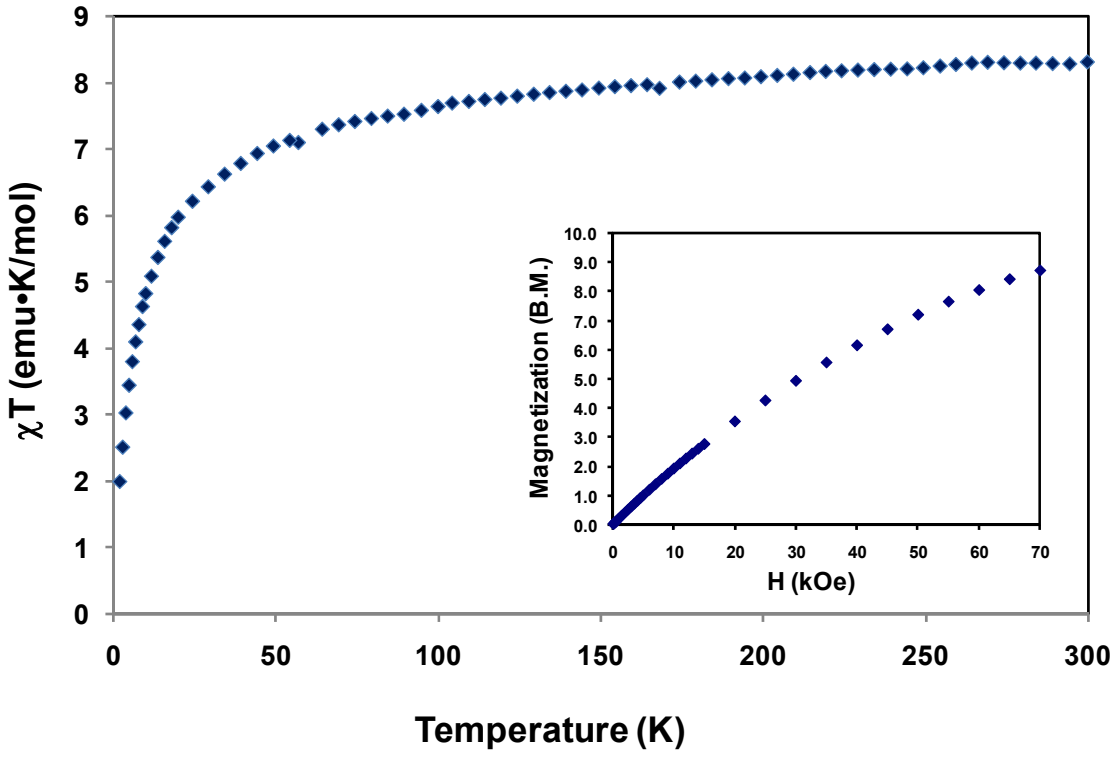

Figure 55. Temperature dependence of χT from 300 K to 2 K for the Fe_3Ru_2 PB. Inset: magnetization versus field data reveal no obvious saturation value.

degree of magnetic ordering which could be due to some small quantity of a ferromagnetic impurity.

$PPN_{0.6}Fe_{2.7}[Ru(CN)_6]_2 \cdot 14H_2O \cdot 2MeCN$. The room temperature χT value is 8.31 emu·K/mol which slowly decreases at low temperatures where it begins to decrease more rapidly toward zero at 50K (Figure 55). Previous attempts to synthesize the earlier member "all iron" member of the family, namely the "$[Fe^{II}]_3[Fe^{III}(CN)_6]_2 \cdot x\ H_2O$" analog led to an erroneous claim that the material existed.[139] The product, dubbed Turnbull's Blue, was originally thought to be different from Prussian Blue (which is $[Fe^{III}]_4[Fe^{II}(CN)_6]_3 \cdot 14H_2O$) but it was later shown that the combination of $[Fe^{III}(CN)_6]^{3-}$ with Fe^{II} always leads to an irreversible electron transfer to form the same material as the original Prussian Blue complex. With this situation in mind, analysis of the possible spin states is necessary in order to decide what the oxidation states are on average in the present case. If an electron transfer occurs the material could be $[HS\ Fe^{III}]_4[Ru^{II}]_3$ with a room temperature χT value of 17.4 for four S = 5/2 magnetic centers. The second case, where the ions remain in their original oxidation state would mean the sample is $[H.S.\ Fe^{II}]_3[Ru^{III}(CN)_6]_2$ which would exhibit a room temperature χT value of ~ 9.75 emu·K/mol. The observed value of 8.31 is slightly lower than this value, likely due to the presence of trapped diamagnetic impurities of the $[PPN]^+$ ions as noted in the experimental section. Clearly, the $[H.S.\ Fe^{II}]_3[Ru^{III}(CN)_6]_2$ case is the closest match with the experimental data. Further experimental evidence for this conclusion is found in the IR spectral data. Recently Long's group reported the $Fe_4[Ru(CN)_6]_3 \cdot 18H_2O$ Prussian Blue analog,[140] with Fe^{III} and Ru^{II} which exhibits a $\upsilon_{C\equiv N}$ stretch at 2045 cm^{-1}, consistent

with Ru^{II}. In our material, however, the IR data contain two stretches at 2074 and 2157 cm^{-1} consistent with Ru^{III} terminal and bridging stretches. AC susceptibility measurements were performed to check for long range ordering, but no signal was observed.

Of interest to point out, however, is that since no spontaneous electron transfer appears to be occurring, the material is a Ru analog to the match to elusive Turnbull Blue. Most importantly, however, we note that the TBP cluster is *not stable* as a simple redox isomer and that it exhibits much more complex electronic and magnetic properties that are not observed for the bulk 3-D solid (see Chapter IV). Additional studies are underway to attempt preparation of a spin crossover material based on this PB metal ion combination, in a manner akin to the known SCO material $CsFe[Cr(CN)_6]$.[24]

$Fe_3[Os(CN)_6]_2 \cdot 19H_2O$. The room temperature χT value was observed to be 9.81 emu·K/mol which slowly decreases t low temperature where it begins to decrease more rapidly toward zero at 50K (Figure 56.). As in the case of the Fe_3Ru_2 analog, an analysis of the possible spin states ead to two scenarios, the first being an electron transfer which in this case would lead to $[H.S.\ Fe^{III}]_3[Os^{II}]_2$ with a room temperature χT value of 17.5 emu·K/mol for four S = 5/2 ions. The second case would be $[H.S.\ Fe^{II}]_3[Os^{III}(CN)_6]_2$ which leads to a theoretical room temperature χT value of 9.75 emu·K/mol which is very close to the observed value. These results are conclusive evidence that the Prussian Blue phase exists in the H.S. Fe^{II} state without an electron transfer having occurred. As is the case for the $PPN_{0.6}Fe_{2.7}[Ru(CN)_6]_2 \cdot 14H_2O \cdot 2MeCN$ material, no ordering is observed, which is as expected, because at low temperatures antiferromagnetic coupling

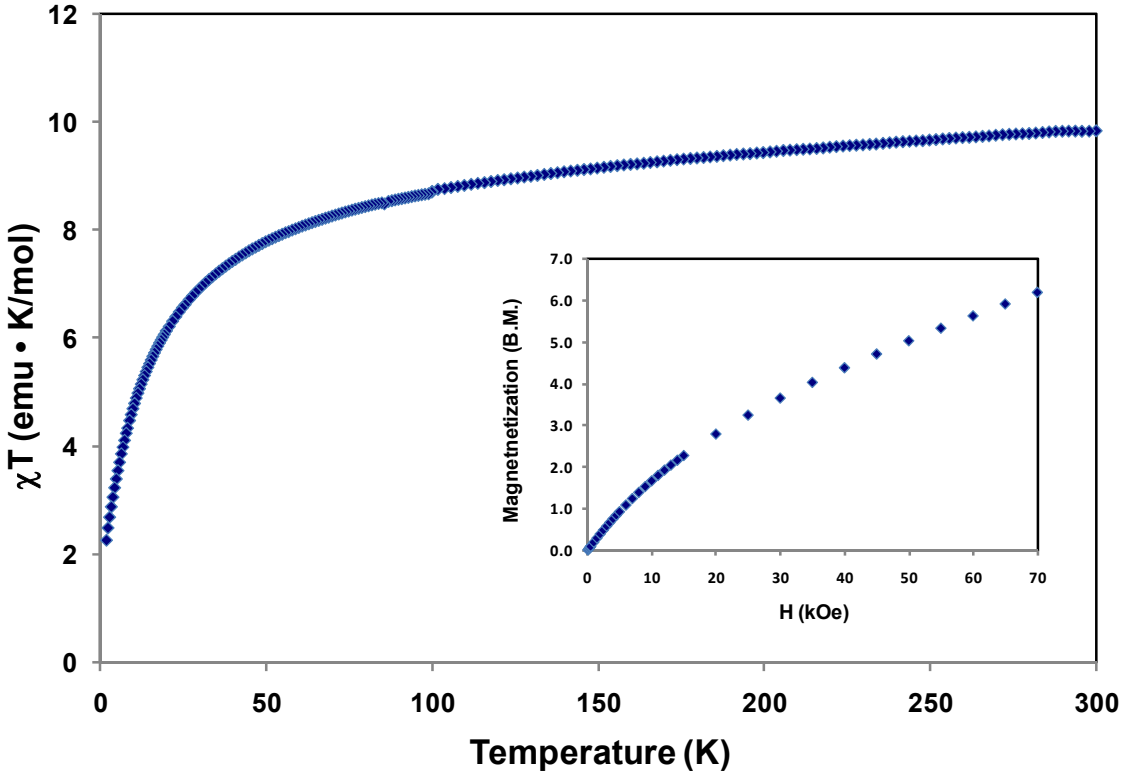

Figure 56. Temperature dependence of χT in the range 300 K to 2 K for the Fe_3Os_2 PB indicative of antiferromagnetic coupling. Inset: magnetization vs. field plot which does not reach a saturation value.

dominates, and no mixed valence double exchange is possible unlike the classical Prussian Blue case to explain the ordering mechanism. Similar to the Ru_3Fe_2 Prussian Blue and TBP pair, the behavior of the Fe_3Os_2 TBP cluster is quite different than that the Prussian Blue. For the TBP cluster there is a reversible electron transfer mechanism coupled with a spin transition. Modifications of the PB material with different cations or solvents may lead to the onset of spin crossover or perhaps even the charge-transfer coupled spin transition (CTCST) behavior observed for the discrete TBP molecule in the solid state.

Ni_3Os_2 and Ni_3Ru_2 PB Analogs

The previous Prussian Blue analogs were found to undergo antiferromagnetic coupling or no coupling at all, findings that are in accord with the corresponding properties of their TBP counterparts. The only TBP clusters that exhibit ferromagnetic coupling are the Ni congeners so it was of obvious interest to probe if this would be the case for the extended PB phases as well. The Ni_3Os_2 and Ni_3Ru_2 PB analogs were prepared and are rare cases of magnetic Prussian Blue analogs for the 4d and 5d metals, the only other being the $Fe_4[Ru(CN)_6]_3 \cdot 18H_2O$ prepared by long, in which the 4d metal in this case is diamagnetic Ru^{II}.[140] An analysis of the magnetic properties of these materials revealed that they undergo ferromagnetic ordering at low temperatures. The nature of these particular materials were further studied by changing the reaction solvent from pure MeCN, to pure MeOH, to H_2O/MeOH in order to probe the effects that reaction conditions, hence trapped solvent, has on the magnetic properties.

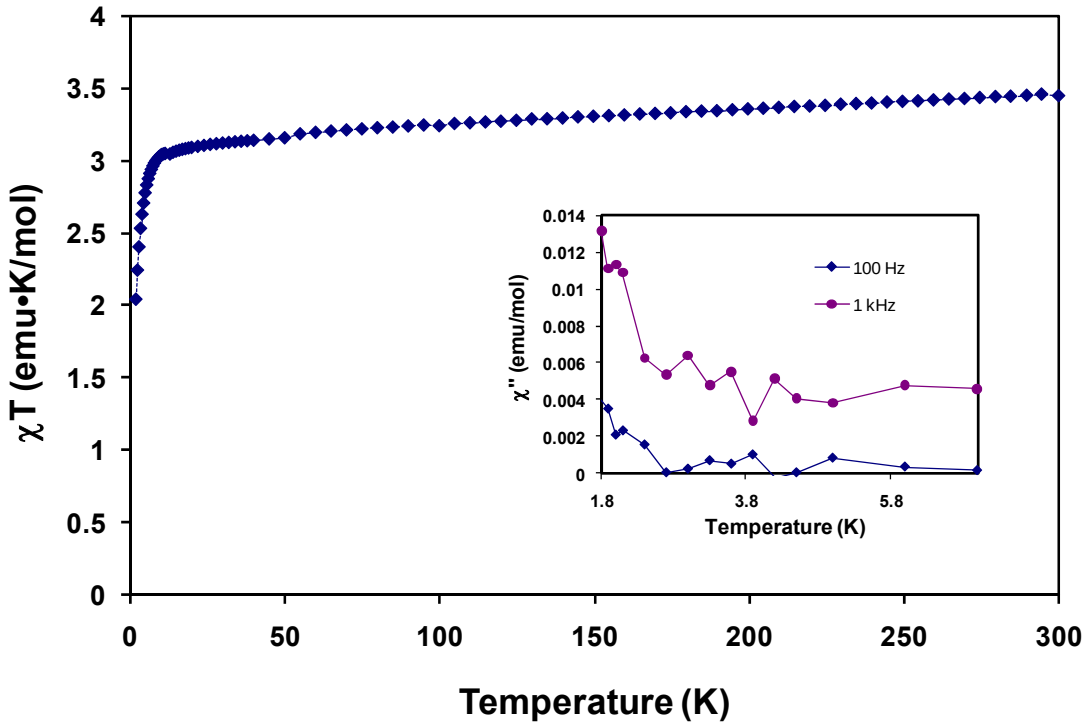

Figure 57. Temperature dependence of χT in the range 300 K to 2 K for the Ni_3Ru_2 PB phase prepared in acetonitrile. Inset: imaginary part (χ'') of AC magnetic susceptibility at different frequencies (H_{AC} = 3 Oe and H_{DC} = 0 Oe), the weak response is indicative of low temperature ordering.

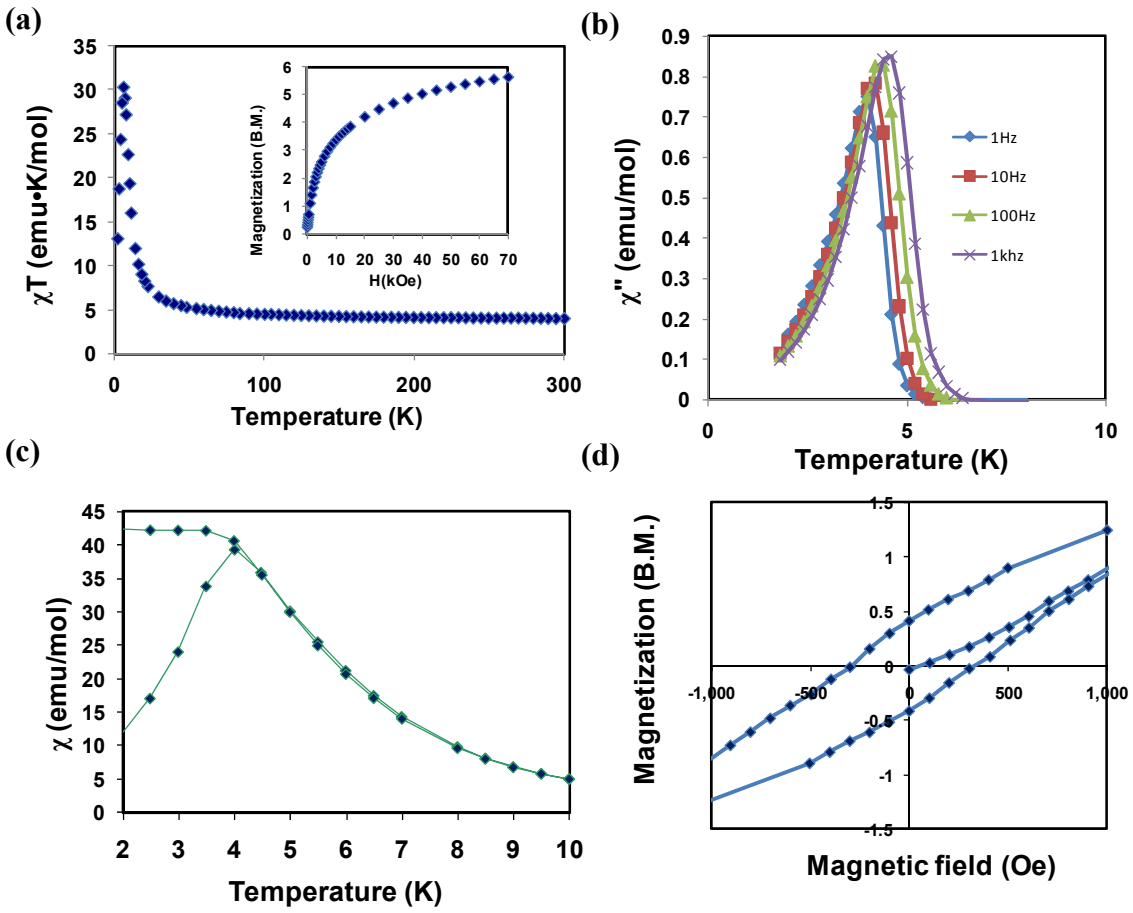

Figure 58. (a) Temperature dependence of χT from 300K to 2K for the Ni_3Os_2 PB prepared in acetonitrile. Inset: magnetization versus field plot at 1.8 K and (b) the imaginary part (χ") of AC magnetic susceptibility at different frequencies (H_{AC} = 3 Oe and H_{DC} = 0 Oe) which shows ordering at ~4 K (c) and confirmed by ZFC/FC divergence at 4.2 K. (d) The hysteresis loop was performed at 1.8 K with an H_c of 300 Oe.

$Ni_3[Ru(CN)_6]_2 \cdot 20H_2O \cdot MeCN$ and $Ni_3[Os(CN)_6]_2 \cdot 20H_2O \cdot 2MeCN$ prepared in acetonitrile. Magnetic measurements were performed on powder samples after confirming the structural pattern by powder X-ray diffraction methods. The room temperature χT values for Ni_3Ru_2 (Figure 57) and Ni_3Os_2 PB (Figure 58) are 3.5 and 3.9 emu·K/mol respectively. As the temperature decreases, almost no change is observed for the Ni_3Ru_2 analog until 12 K when a sudden decrease is observed that is attributed to zero field splitting effects. The data for the Ni_3Os_2 analog, however, begins to increase slowly at 54 K and then rapidly to reach a maximum χT value of 29 emu·K/mol. These data are indicative of ferromagnetic coupling and ordering in the sample. AC susceptibility and ZFC/FC measurements confirmed this behavior. The Ni_3Os_2 sample orders at 4.3K but a lack of signal for the Ni_3Ru_2 analog confirms the lack of ordering for this material. One possible explanation for the behavior of the Ni_3Ru_2 compound is the very high degree of amorphous character of the material as observed from the PXRD data as well as the large number of defects in the material which translates to fewer pathways for 3D magnetic ordering by limiting the size of the domains that have continuous cyanide exchange pathways.

$PPN_{0.2}Ni_{2.9}[Ru(CN)_6]_2 \cdot 16H_2O \cdot 2MeOH$ and $Ni_3[Os(CN)_6]_2 \cdot 20H_2O \cdot MeOH$ prepared in MeOH. Room temperature χT values for the Ni_3Ru_2 (Figure 59) and Ni_3Os_2 (Figure 60) products are 3.14 and 4.19 emu·K/mol respectively. As the temperature decreases the χT value for Ni_3Ru_2 decreases slightly and the Ni_3Os_2 remains constant. As the temperature is further lowered for the Ni_3Ru_2 sample a sudden increase occurs at 35 K to reach a maximum χT value of 3.2 emu·K/mol. An increase is observed at 32 K to reach a

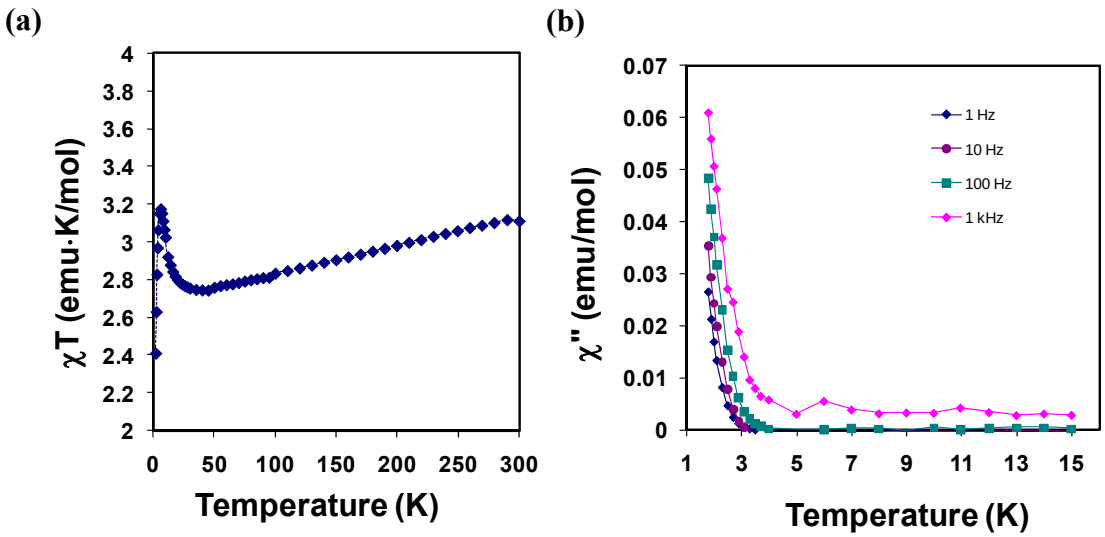

Figure 59. (a) Temperature dependence of χT from 300 K to 2 K for the Ni_3Ru_2 PB prepared in methanol. (b) The imaginary part (χ'') of AC magnetic susceptibility at different frequencies (H_{AC} = 3 Oe and H_{DC} = 0 Oe) indicating an ordering temperature near 2 K.

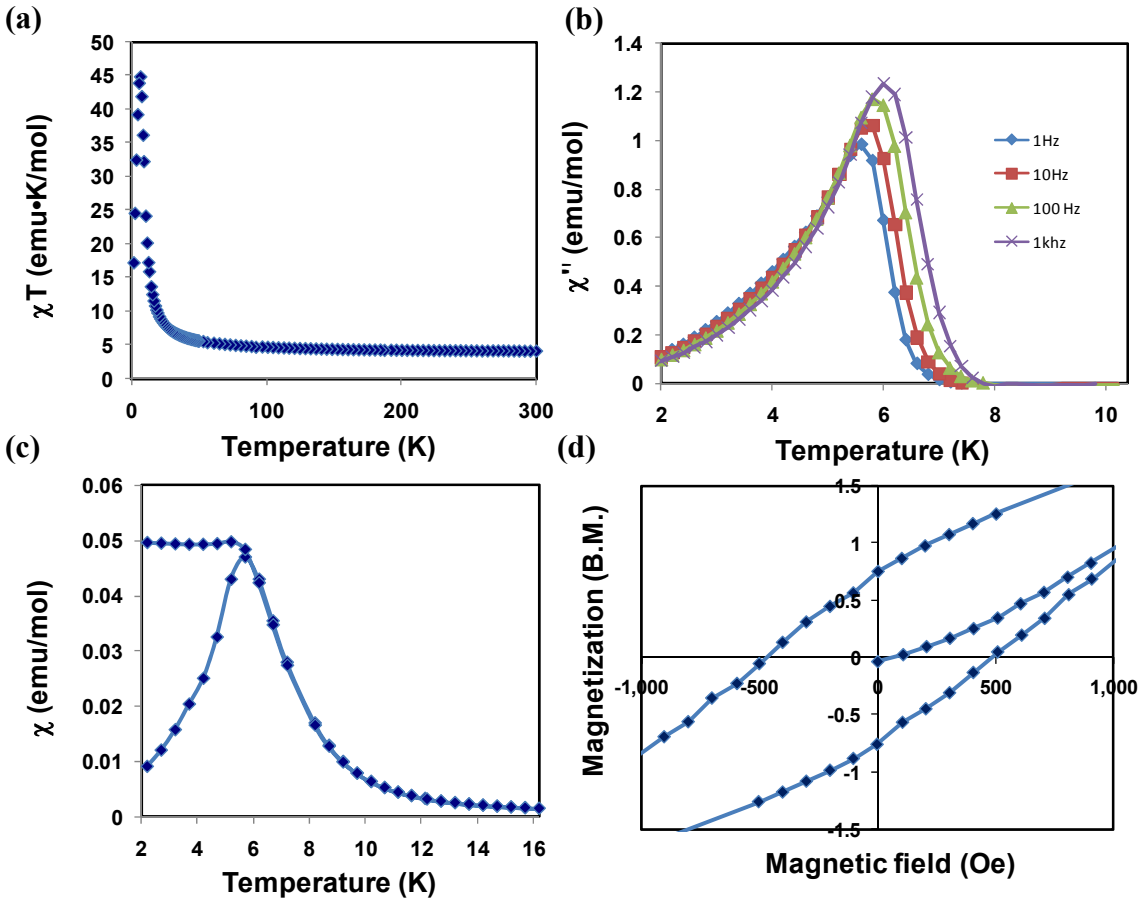

Figure 60. (a) Temperature dependence of χT from 300 K to 2 K for the Ni_3Os_2 PB prepared in methanol. (b) Imaginary part (χ'') of AC magnetic susceptibility at different frequencies (H_{AC} = 3 Oe and H_{DC} = 0 Oe) that reveals magnetic ordering near 5 K (c) and confirmed by ZFC/FC divergence at 5.5 K. (d) The hysteresis loop measured at 1.8K with H_c = 400 Oe.

maximum of 44.8 emu·K/mol for the Ni_3Os_2 anlaog. These data indicate that ferromagnetic coupling and ordering is occurring. AC susceptibility measurements are in accord with this conclusion. The Ni_3Ru_2 PB exhibits an out-of-phase signal near 1.8K. AC measurements and ZFC measurements for the Ni_3Os_2 PB sample show an ordering at 5.5 K with hysteresis and a coercivity of 500 Oe. These samples show slightly improved magnetic properties over the earlier discussed ones which can be attributed to the better crystallinity of the solids.

$Ni_3[Ru(CN)_6]_2 \cdot 20H_2O \cdot 2MeOH$ and $Ni_3[Os(CN)_6]_2 \cdot 4H_2O$ prepared in H_2O/MeOH . In terms of magnetic properties, the most interesting of the analogs came from the reactions performed in the H_2O/MeOH solvent mixture. Room temperature χT values for Ni_3Ru_2 (Figure 61) and Ni_3Os_2 (Figure 62) are 3.75 and 3.65 emu·K/mol respectively which are very close to the expected idealized value of 3.75 emu·K/mol. As the temperature decreases, the χT value for both materials is fairly constant until ~30 K where an increase is observed to reach maximum χT values of 35 emu·K/mol and 38 emu·K/mol for the for Ni_3Ru_2 and Ni_3Os_2 respectively. Clearly ferromagnetic coupling and ordering is operative at low temperatures. AC susceptibly, ZFC/FC, and hysteresis measurements for the Ni_3Ru_2 and Ni_3Os_2 PB samples lead to ordering temperatures of 8.2K and 6.2 K respectively. Hysteresis measurements show that both materials are soft magnets with H_c values for Ni_3Ru_2 PB and Ni_3Os_2 of 800 and 500 Oe respectively.

A trend is evident in the aforementioned results as depicted in Figure 63. As noted previously in the literature the use of non-aqueous media have a negative impact on the chemistry to produce crystalline phases of PBs. In some cases the materials are

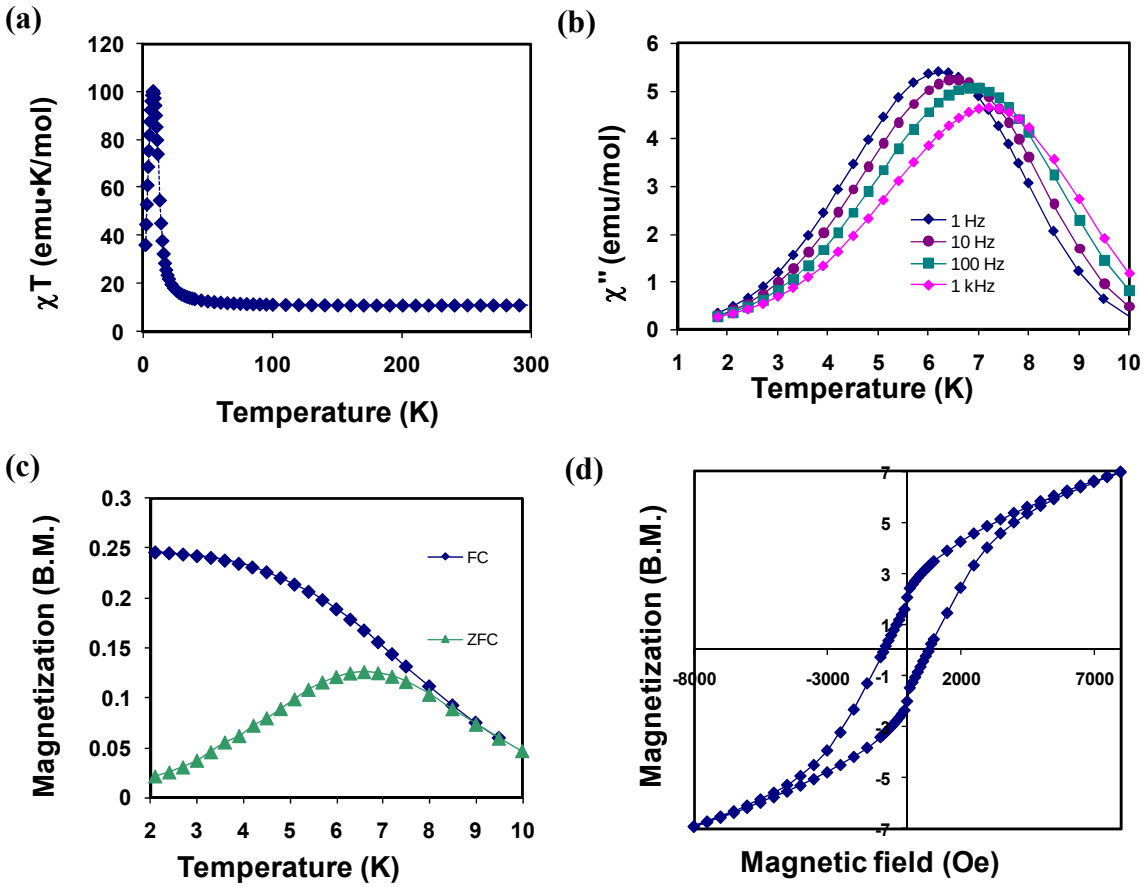

Figure 61. (a) The temperature dependence of χT in the range 300 K to 2 K for the Ni_3Ru_2 PB phase prepared in methanol/H_2O. (b) The imaginary part (χ'') of AC magnetic susceptibility at different frequencies (H_{AC} = 3 Oe and H_{DC} = 0 Oe) demonstrating ordering near 7 K (c) and confirmed by ZFC/FC divergence at 8 K. (d) The hysteresis loop measured at 1.8 K with a H_c value of 500 Oe.

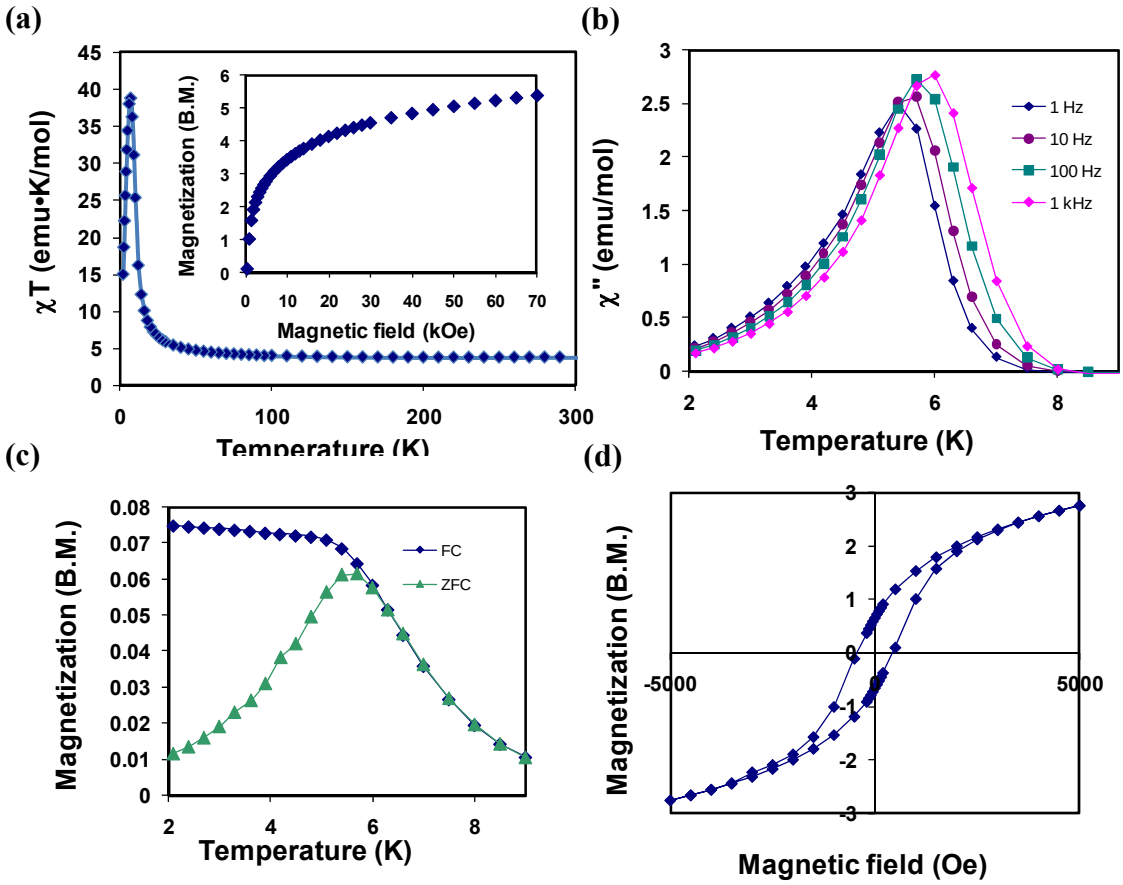

Figure 62. Temperature dependence of χT from 300 K to 2 K for the Ni_3Os_2 PB phases prepared in methanol/H_2O. Inset: magnetization versus field. (b) The imaginary part (χ") of AC magnetic susceptibility at different frequencies (H_{AC} = 3 Oe and H_{DC} = 0 Oe) demonstrating the ordering near 5 K (c) which is confirmed by ZFC/FC divergence at 6.0 K. (d) The hysteresis loop measured at 1.8K with an H_c value of 500 Oe.

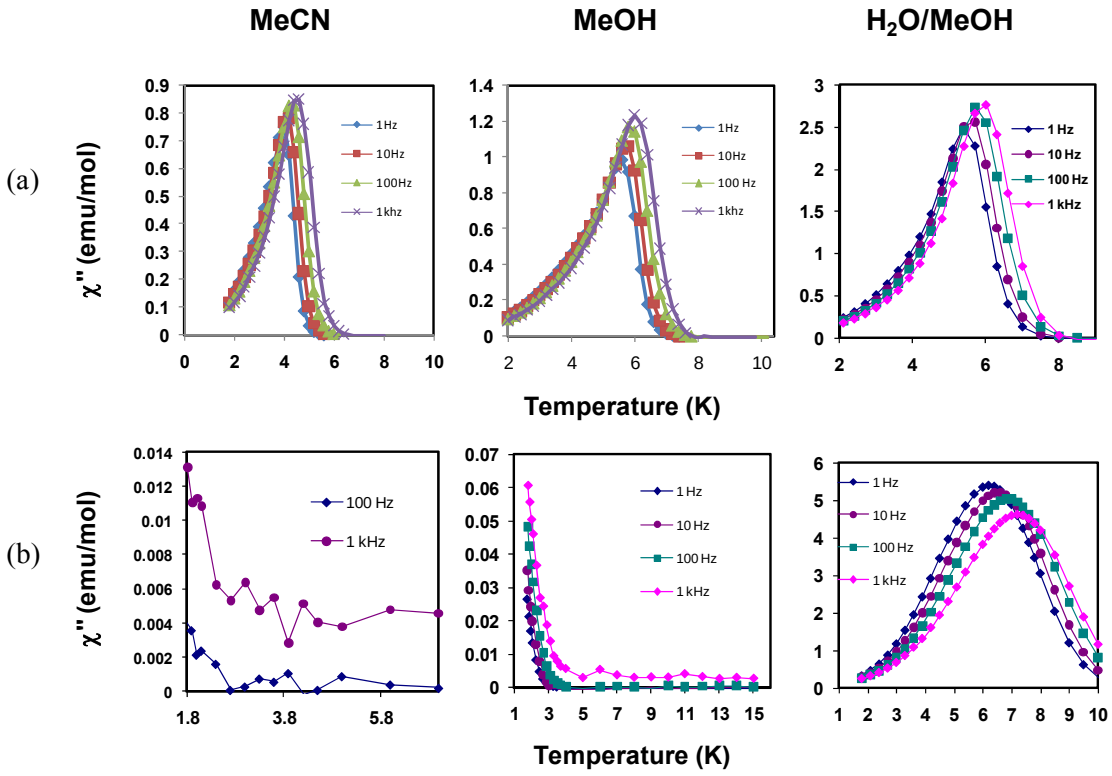

Figure 63. (a) The trend observed in the ordering temperatures for the Ni_3Os_2 PB analogs and (b) Ni_3Ru_2 PB analogs. The ordering temperature increases from MeCN-prepared to MeOH/H_2O-prepared samples.

amorphous and the samples are highly variable from one batch to another which points to the importance of hydrogen bonding interactions as facilitated by chemistry performed in water. In the present study, in going from a solvent with no potential for H-bonding such as acetonitrile, to an alcohol that can participate in weak H-bonding like methanol, and finally to a mixture of methanol and water aqueous system leads to an increase in the magnetic ordering temperatures. This represents the first time that a systematic study has been where the only variable that is altered is the solvent. The fact that both the Ru and Os materials behave in a similar fashion lends strong support to the importance of synthetic conditions on the reproducibility and properties of PB analogs materials. It is also noted on a positive note that magnetic ordering was observed for the methanol prepared samples in both cases and for the acetonitrile Ni_3Os_2 phase which lends hope to the notion that it may be possible to avoid water for some of the sensitive cyanometallates and still observe desired properties, although the most favorable reaction conditions are clearly water which should be used whenever possible.

General Discussion of Magnetic Properties

The structure and formula of Prussian Blue analogs leads to the intrinsic properties evident in the materials. Depending on a variety of conditions, such as alkali metal ion content, solvent and the ratios of the reagents, the general formula $M_xA[B(CN)_6]_z \cdot nH_2O$ (x = amount of cation, z = stoichoimety of cyanometallate unit, and n = water content) can be easily manipulated. For systems such as those presented in this chapter, the alkali metal ion content is zero since none was added to the reaction. Although the elemental analysis indicated the presence of a small percentage of the

Table 15. Summary of Magnetic Data for the new Prussian Blue materials based on Ru and Os.

Compound	**Coupling**	**T_c**	***J* cm^{-1}**
$Mn_3[Ru(CN)_6]_2 \cdot 22H_2O \cdot MeOH$	negligible A.F.	-	
$Mn_3[Os(CN)_6]_2 \cdot 18H_2O$	A.F.	very weak <1.8K	
$PPN_{0.6}Fe_{2.7}[Ru(CN)_6]_2 \cdot 14H_2O \cdot 2MeCN$	A.F.	-	
$Fe_3[Os(CN)_6]_2 \cdot 19H_2O$	A.F.	-	
$Ni_3[Ru(CN)_6]_2 \cdot 20H_2O \cdot MeCN$ From MeCN	negligible	-	
$Ni_3[Os(CN)_6]_2 \cdot 20H_2O \cdot 2MeCN$ From MeCN	F.	4.0	0.93
$PPN_{0.2}Ni_{2.9}[Ru(CN)_6]_2 \cdot 16H_2O \cdot 2MeOH$ From MeOH	F.	1.8	0.42
$Ni_3[Os(CN)_6]_2 \cdot 20H_2O \cdot MeOH$ From MeOH	F.	5.5	1.27
$Ni_3[Ru(CN)_6]_2 \cdot 20H_2O \cdot 2MeOH$ From H_2O/MeOH	F.	8.0	1.85
$Ni_3[Os(CN)_6]_2 \cdot 4H_2O$ From H_2O/MeOH	F.	6.0	1.39
$Ni_3[Fe(CN)_6]_2 \cdot nH_2O$*	F.	23	
$Co_3[Cr(CN)_6]_2 \cdot nH_2O$*	F.	19	
$Fe_3[Cr(CN)_6]_2 \cdot 4H_2O$*	F.	16	
$Co_3[Fe(CN)_6]_2 \cdot nH_2O$ *	A.F.	14	
$Mn_3[Fe(CN)_6]_2 \cdot nH_2O$ *	A.F.	9	

* n is unreported

PPN^+ cation in two of the PB products, these cations are too large to be able to play the role of occupying defect sites. The general formula would be $A[B(CN)_6]_{2/3}\cdot 18\text{-}22H_2O$ with statistically distributed vacancies in 1/3 of the cyanometallate sites throughout the extended 3D array. It should be noted that defects are dictated by the electroneutrality of the phase and not random factors. A large number of vacancies in the materials is responsible for the low magnetic ordering temperatures but the ordering is also affected strongly by the weak coupling through the $[Ru(CN)_6]^{3-}$ and $[Os(CN)_6]^{3-}$ building blocks to the 3d transition metal ions as noted throughout the discussion in this dissertation. The magnetic exchange interactions J_{Ni-Os} and J_{Ni-Ru} were estimated from the Langevin–Weiss–Neél equation[141] as shown in Table 15. In general, Prussian Blue analogs with the two-thirds stoichiometry exhibit T_c values below 30K,[18, 142] (bottom of Table 15) which is the case with all of our new compounds.

As noted earlier, a convenient comparison of properties is possible for the $Ni[Fe(CN)_6]_{2/3}\cdot nH_2O$ Prussian Blue phase which is a close relative of the new ferromagnets $Ni[Ru(CN)_6]_{2/3}\cdot nH_2O$ and $Ni[Os(CN)_6]_{2/3}\cdot nH_2O$ reported herein. The Fe containing material exhibits ferromagnetic coupling as well as a low ordering temperature of 23 K, albeit higher than the Ru and Os anaogs. The difference in ordering temperatures must be related to the role of orbital overlap through the CN bridging ligand as one moves down the Fe family from Ru to Os. The closest match of compounds in the series is between the materials prepared in the H_2O/MeOH solvent system to $Ni[Fe(CN)_6]_{2/3}\cdot nH_2O$ Prussian Blue phase prepared in H_2O. In this family

$Ni[M(CN)_6]_{2/3}\cdot nH_2O$ the ordering temperature goes from 23 K to 7.9 K to 6.0 K for M = Fe, Ru and Os, respectively.

Conclusions

The new Prussian Blue analogs described herein open up a new chapter in Prussian Blue chemistry based on 4d and 5d paramagnetic hexacyanometallates (Table 15). The collective magnetic data for the Ni_3Ru_2 and Ni_3Os_2 PB analogs indicate that they are soft ferromagnets with low T_c values ranging from 1.8 K to 7.9 K. In this new series of PB analogs, the Fe based PB's represent the closest compound to Turnbull's Blue to be reported to date, but detailed Mossbauer experiments must to be performed in order to elucidate the exact nature of the oxidation states of the metal ions in the system. The magnetic data suggest that both the Fe_3Ru_2 and Fe_3Os_2 phases are able to exist with HS Fe^{II} but no spin crossover behavior has been observed for these materials; suitable modifications to the chemical formulae may lead to new properties however.[30]

The main message of this Chapter Is that solvent has a strong effect on the properties of Prussian Blue and its analogs. Recent theoretical work has been undertaken in an effort to understand the effect that water plays on the Prussian Blue properties.[143] In our work we can clearly see a trend that acetonitrile leads to very poor properties and that methanol and a mixture of methanol and water leads to increases in the ordering temperatures, with the latter solvent mixture leading to the highest T_c values. Due to the vacancies inherent in these materials future work will be focused on the incorporation of alkali metal ions, especially sodium and potassium, in order to

synthesize stoichiometrically equivalent Prussian Blue analogs of the type $M_1A[B(CN)_6]\cdot nH_2O$. A decrease in vacancies should lead to improved exchange interactions and higher T_c values.

CHAPTER VI

CONCLUSIONS AND OUTLOOK

The work in this dissertation focuses on exploring the fundamental chemistry of materials prepared from cyanometallate building blocks and detailed studies of their magnetic properties.[118] In Chapter II, four molecules were prepared with the purpose of investigating the effect that the geometry of the cluster as well as the metal ion has on the magnetic properties of the material. It was discovered that only one molecule of the four exhibited SMM behavior, namely the Ni_9W_6 pentadecanuclear cluster. In addition to this exciting result, the exchange coupling constants for both of the pentadecanuclear clusters were extracted from a full analysis, the first time the entire cluster had been treated with magnetic modeling, to give J = 12.0 cm^{-1} and J = 12.2 cm^{-1} for the Ni_9W_6 and Ni_9Mo_6 clusters respectively. This analysis provided the first opportunity for validating theoretical models on the exchange coupling of the pentadecanuclear complexes. Indeed, the theoretical results of 12.4 and 11.9 cm^{-1} for the clusters based on the same core are in excellent agreement with the experimental data.[109]

The research presented in Chapter III is a foray into a new area of cyanide magnetochemistry, namely the study of the building blocks $[Ru(CN)_6]^{3-}$ and $[Os(CN)_6]^{3-}$, the reactivity of which has not been explored to any extent. Given the previous success of the Dunbar group in preparing a large number of model clusters of the trigonal bipyramidal geometry[69], this cluster type was selected as a target for the 4*d* and 5*d*

Table 16. Examples of characterized TBP clusters.

$[M(CN)_6]^{3-}$ \ M^{2+}	V^{II}	Cr^{II}	Mn^{II}	Fe^{II}	Co^{II}	Ni^{II}	Zn^{II}
Cr^{III}		✓	✓	✓	✓	✓	✓
Mn^{III}			✓				
Fe^{III}			✓	✓	✓	✓	✓
Co^{III}			✓	✓	✓	✓	✓
Mo^{III}	✓		✓	✓	✓	✓	
Ru^{III}		✓	✓	✓		✓	
Os^{III}			✓	✓		✓	

Group 8 congeners. The advantage of working with such a large homologous series of clusters is obvious; the topology of the cluster remains constant and even the space group of the crystals are the same in all but a few cases. Given this situation, one can make a direct comparison between different cyanometallate bulding blocks with the same co-ligands and metal ions an example of which is noted in Table 16. A major driving force for the work is also the fact that theoretical studies published in the recent literature led to the conclusion that the incorporation of the $[Os(CN)_6]^{3-}$ ion into the TBP geometry with Mn^{II} and possibly Ni^{II} ions could yield new SMM's.[83, 144] The work in this chapter led to the first molecules to contain these building blocks, the most notable examples of which are the ferromagnetically coupled Ni_3Os_2[102] and Ni_3Ru_2 TBP clusters. In the case of the Ni_3Os_2 TBP the magnetic data were fit to a model that took into account anisotropic magnetic exchange interactions, which is the origin of the anisotropy in the cluster. [129] Another significant achievement was in the isolation of the Mn_3Os_2 TBP, which as predicted from theory to have a large barrier to the reversal of magnetization. Unfortunately this was not case, but there does seem to be potential SMM behavior exhibited below 1.8 K which needs to be further evaluated by low temperature measurements, one method being microSQUID at temperatures as low as 0.04 K which will be performed at Grenoble. The fact that we have essentially refuted the theory reported for SMM behavior of the Mn_3Os_2 TBP is important because the understanding of the influence of the 4*d* and 5*d* metals in cyanide assemblies is very poor at this stage and the theories must be tested and refined by having actual experimental data in hand. Future work will be directed at theoretical work on the

Ni_3Ru_2 TBP and obtaining the structure of the Mn_3Ru_2 TBP analog to provide more information on the properties of 4*d* and 5*d* metal ions bridged by cyanide to first row transition metal ions.

Chapter IV describes the unique behavior of the Fe_3Os_2 and Fe_3Ru_2 TBP clusters, which undergo CTIST and a combination of CTIST and spin crossover respectively. One of the most valuable aspects of this work is that the study provides the only complete study on a family of isostructural clusters in which a trend in the SCO/CTCST properties is correlated to a single variable, namely the identities of the metal ion of the cyanometallate; on this case all of them are Group 8 LS d^5 metal ions. As one traverses down the family from 3d to 5d ions, it can be seen that the Fe_3Fe_2 complex exhibits SCO behavior, the Fe_3Ru_2 exhibits a mixture of CTCST and SCO phenomena, and finally the Fe_3Os_2 cluster exhibits only CTCST behavior. Future directions will involve following up on the hydration experiment of the Fe_3Os_2 TBP cluster. This experiment provided evidence that the crystals of the cluster remain stable and can exchange interstitial solvent without dissolving and recrystallizing, the result is a dramatic change in the physical properties. This discovery will allow for a direct study of solvent effects on CTIST and spin crossover which is very little understood in the molecular magnetism field.

Typically, cyanide bridged clusters are modeled after a particular Prussian Blue analog, either to elicit similar properties or for simple comparison sake. For the clusters presented in the thesis based on $[Ru(CN)_6]^{3-}$ and $[Os(CN)_6]^{3-}$ there are no corresponding PB analogs. To fill in the gaps in the literature, the preparation of new Prussian Blue

analogs is presented in Chapter V. The experiments are based on the same metal ion combinations of the clusters reported in Chapters III and IV. The literature cites a number of examples in which the synthesis of Prussian Blue analogs in non-aqueous media leads to amorphous products but the results in this chapter indicate that PB analogs with a degree of crystallinity may be synthesized in organic media as well as mixtures of organic solvents and water. Only one particular combination with the Ru^{III} and Os^{III} building blocks, namely those with Ni^{II},[102] yielded products that undergo long range ordering at low temperatures. With this in mind, the Ni^{II} Prussian Blue analogs were subjected to a solvent dependent study, in which the reaction was performed in acetonitrile, methanol, and a mixture of methanol and water. The goal was to determine the effect on the ordering temperature of using solvents capable of engaging in hydrogen bonding interactions (methanol and water) versus one that does not (acetonitrile). The results are interesting in that there is a clear trend in moving from acetonitrile to methanol and finally to methanol/water. There is both an increase in the crystallinity as well as in the ordering temperature for the materials (range is 1.8 K to 7.2 K). It is important to note however, that crystallinity was observed even in the products which were synthesized from MeCN and MeOH, demonstrating that powder x-ray characterization was possible even in non-aqueous media by judicious combinations of starting materials. Further work on these systems is in order, mostly in the vein of alkali metal inclusion in order to decrease the number of vacancies in the structure. Ideally, these changes in the material should lead to an increase the overall crystallinity and in the ordering temperature of the materials.

The molecules presented in this thesis provide clear evidence for the usefulness and versatility of the 4*d* and 5*d* metal ions in both discrete and extended materials. The new chemistry that was performed with $[Mo(CN)_8]^{3-}$ and $[W(CN)_8]^{3-}$ proved to be valuable for bridging theory with experiment on the topic of SMM behavior. The incorporation of the $[Ru(CN)_6]^{3-}$ and $[Os(CN)_6]^{3-}$ building blocks into clusters that exhibit fascinating properties such as CTIST and spin crossover and into extended networks that exhibit magnetic ordering demonstrate the general utility of these six-coordinate anions as building blocks for magnetic materials. These ions will have a profound impact not only on the development of new materials, but also in expanding and refining current theoretical models, which may lead to more precise predictions for magnetic behavior so that "designer" magnetic materials can be developed. The work in this thesis constitutes a significant contribution to the field of molecular magnetism and coordination chemistry by expanding the experimental knowledge of the physical properties exhibited by 4*d* and 5*d* cyanometallates, and also for providing new experimental data which will be valuable to theoreticians seeking to understand the intrinsic nature of magnetic phenomena.

Finally, advances in the field of molecular magnetism are important for the acquisition of fundamental knowledge as well as for keeping pace with the demand for new technologies. One of the key fields of direct relevance to work in molecular nanomagnets is that of spintronics,[145-147] which makes use of the spin of the electron as well as the charge to store information and perform computations. The new physics behind this idea has resulted in new devices such as terabyte hard drives, and is also

crucial for the hopes of fabricating new higher performing transistors. This area of research takes advantage of quantum mechanics, which makes the use of molecular magnets highly appealing for incorporation into spintronic devices; indeed this topic has been the focus of a number of high profile publications since 2008.[54, 94, 95] It is important to always bear in mind, however, that the quest for useful materials to use in applications is not the only goal. We must gain a fundamental understanding of molecular magnetism in order to fully maximize the potential of this area.

REFERENCES

1. Dunbar, K. R.; Heintz, R. A., *Prog. Inorg. Chem.* **1997,** *45*, 283-391.

2. Shatruk, M.; Avendano, C.; Dunbar, K. R., *Prog. Inorg. Chem.* **2009,** *56*, 155-334.

3. Duimstra, J. A.; Stern, C. L.; Meade, T. J., *Polyhedron* **2006,** *25*, 2705-2709.

4. Ferbinteanu, M.; Miyasaka, H.; Wernsdorfer, W.; Nakata, K.; Sugiura, K.; Yamashita, M.; Coulon, C.; Clerac, R., *J. Am. Chem. Soc.* **2005,** *127*, 3090-3099.

5. Smith, J. A.; Galan-Mascaros, J.-R.; Clerac, R.; Dunbar, K. R., *Chem. Commun.* **2000**, 1077-1078.

6. Miyasaka, H.; Matsumoto, N.; Re, N.; Gallo, E.; Floriani, C., *Inorg. Chem.* **1997,** *36*, 670-676.

7. Konishi, Y.; Tokoro, H.; Nishino, M.; Miyashita, S., *J. Phys. Soc. Jpn.* **2006,** *75*, 114603/1-114603/9.

8. Podgajny, R.; Nitek, W.; Rams, M.; Sieklucka, B., *Cryst. Growth Des.* **2008,** *8*, 3817-3821.

9. Clima, S.; Hendrickx, M. F. A.; Chibotaru, L. F.; Soncini, A.; Mironov, V.; Ceulemans, A., *Inorg. Chem.* **2007,** *46*, 2682-2690.

10. Holmes, S. M.; Girolami, G. S., *J. Am. Chem. Soc.* **1999,** *121*, 5593-5594.

11. Woodward, J., *Philos. Trans.* **1724,** *33*, 15-17.

12. Stahl, G. E., *Experimenta, Observationes, Animadversiones CCC Numero, Chymicae et Physicae* **1731**.

13. Powell, H. M., *Proceedings of the Chemical Society of London* **1959**, *3*, 73-75.

14. Ware, M., *J. Chem. Educ.* **2008,** *85*, 612-618.

15. Anderson, P. W., *Physical Review* **1959,** *115*, 2-13.

16. Sato, O., *J. Solid State Electrochem.* **2007,** *11*, 773-779.

17. Entley, W. R.; Girolami, G. S., *Science* **1995,** *268*, 397-400.

18. Verdaguer, M.; Girolami, G. S., *Magnetism: molecules to materials V,* Wiley-VCH: New York, 2005, 283-346.

19. Chapman, K. W.; Southon, P. D.; Weeks, C. L.; Kepert, C. J., *Chem. Commun.* **2005**, 3322-3324.

20. Mayoh, B.; Day, P., *J. Chem. Soc., Dalton. Trans.* **1976**, 1483-1486.

21. Ferlay, S.; Mallah, T.; Ouahes, R.; Veillet, P.; Verdaguer, M., *Nature* **1995,** *378*, 701-703.

22. Sato, O.; Tao, J.; Zhang, Y. Z., *Angew. Chem. Int. Ed.* **2007,** *46*, 2152-2187.

23. Ohkoshi, S.; Yorozu, O.; Iyoda, A.; Fujishima, A.; Hashimoto, K., *Appl. Phys. Lett.* **1997,** *70*, 1040-1044.

24. Kosaka, W.; Nomura, K.; Hashimoto, K.; Ohkoshi, S. I., *J. Am. Chem. Soc.* **2005,** *127*, 8590-8591.

25. Sato, O.; Iyoda, T.; Fujishima, A.; Hashimoto, K., *Science* **1996,** *272*, 704-705.

26. Bleuzen, A.; Lomenech, C.; Dolbecq, A.; Villain, F.; Goujon, A.; Roubeau, O.; Nogues, M.; Varret, F.; Baudelet, F.; Dartyge, E.; Giorgetti, C.; Gallet, J. J.; Moulin, C. C. D.; Verdaguer, M., *Mol. Cryst. Liq. Cryst. Sci. Tech Sec A* **1999,** *334*, 965-974.

27. Hatlevik, O.; Buschmann, W. E.; Zhang, J.; Manson, J. L.; Miller, J. S., *Adv. Mat.* **1999,** *11*, 914-918.

28. Dujardin, E.; Ferlay, S.; Phan, X.; Desplanches, C.; Moulin, C. C. D.; Sainctavit, P.; Baudelet, F.; Dartyge, E.; Veillet, P.; Verdaguer, M., *J. Am. Chem. Soc.* **1998,** *120*, 11347-11352.

29. Mallah, T.; Thiebaut, S.; Verdaguer, M.; Veillet, P., *Science* **1993,** *262*, 1554-1557.

30. Shimamoto, N.; Ohkoshi, S.-i.; Sato, O.; Hashimoto, K., *Inorg. Chem.* **2002,** *41*, 678-684.

31. Kaye, S. S.; Long, J. R., *J. Am. Chem. Soc.* **2005,** *127*, 6506-6507.

32. Segal, M. G., *Sci. Total Environ.* **1993,** *137*, 31-48.

33. Voigt, G., *Sci. Total Environ.* **1993,** *137*, 205-225.

34. Ludi, A., *J. Chem. Educ.* **1981,** *58*, 1013-1013.

35. Cambi, L.; Szego, L., *Ber. Deut. Chem. Ges.* **1931,** *64*, 2591-2598.

36. Koenig, E.; Madeja, K., *Chem. Commun.* **1966,** *No. 3*, 61-62.

37. Shatruk, M.; Dragulescu-Andrasi, A.; Chambers, K. E.; Stoian, S. A.; Bominaar, E. L.; Achim, C.; Dunbar, K. R., *J. Am. Chem. Soc.* **2007,** *129*, 6104-6116.

38. Letard, J. F., *J. Mater. Chem.* **2006,** *16*, 2550-2559.

39. Guetlich, P.; Goodwin, H. A., *Top. Curr. Chem.* **2004,** *233*, 1-47.

40. Murray, K. S.; Kepert, C. J., *Top. Curr. Chem.* **2004,** *233*, 195-228.

41. Nihei, M.; Ui, M.; Yokota, M.; Han, L.; Maeda, A.; Kishida, H.; Okamoto, H.; Oshio, H., *Angew. Chem., Int. Ed.* **2005,** *44*, 6484-6487.

42. Letard, J. F.; Guionneau, P.; Goux-Capes, L., *Towards spin crossover applications*. Springer-Verlag: Berlin, 2004; Vol. 235, p 221-249.

43. Berlinguette, C. P.; Dragulescu-Andrasi, A.; Sieber, A.; Guedel, H. U.; Achim, C.; Dunbar, K. R., *J. Am. Chem. Soc.* **2005,** *127*, 6766-6779.

44. Berlinguette, C. P.; Dragulescu-Andrasi, A.; Sieber, A.; Galan-Mascaros, J. R.; Guedel, H. U.; Achim, C.; Dunbar, K. R., *J. Am. Chem. Soc.* **2004,** *126*, 6222-6223.

45. Li, D.; Clerac, R.; Roubeau, O.; Harte, E.; Mathoniere, C.; Le Bris, R.; Holmes, S. M., *J. Am. Chem. Soc.* **2008,** *130*, 252-258.

46. Shatruk, M.; Chambers, K. E.; Prosvirin, A. V.; Dunbar, K. R., *Inorg. Chem.* **2007,** *46*, 5155-5165.

47. Neel, L., *Compt. Rend.* **1949,** *228*, 664-666.

48. Spaldin, N., *Magnetic materials: fundamentals and device applications*. Cambridge University Press, Cambridge, 2003; p 250

49. Sessoli, R.; Gatteschi, D.; Caneschi, A.; Novak, M. A., *Nature* **1993,** *365*, 141-143.

50. Lis, T., *Acta. Crys. Sec. B* **1980,** *36*, 2042-2046.

51. Tsai, H. L.; Eppley, H. J.; Devries, N.; Folting, K.; Christou, G.; Hendrickson, D. N., *Chem. Commun.* **1994**, 1745-1746.

52. Gatteschi, D.; Sessoli, R., *Angew.Chem., Int.Ed.* **2003,** *42*, 268-297.

53. Thomas, L.; Barbara, B., *J. Low Temp. Phys.* **1998,** *113*, 1055-1060.

54. Bogani, L.; Wernsdorfer, W., *Nat. Mater.* **2008,** *7*, 179-186.

55. Leuenberger, M. N.; Loss, D., *Nature* **2001,** *410*, 789-793.

56. Ako, A. M.; Hewitt, I. J.; Mereacre, V.; Clerac, R.; Wernsdorfer, W.; Anson, C. E.; Powell, A. K., *Angew. Chem. Int. Ed.* **2006,** *45*, 4926-4929.

57. Li, D.; Parkin, S.; Wang, G.; Yee, G. T.; Prosvirin, A. V.; Holmes, S. M., *Inorg. Chem.* **2005,** *44*, 4903-4905.

58. Tasiopoulos, A. J.; Wernsdorfer, W.; Abboud, K. A.; Christou, G., *Inorg. Chem.* **2005,** *44*, 6324-6338.

59. Rebilly, J. N.; Mallah, T., *Structure and Bonding* **2006,** *122*, 103-131.

60. Murugesu, M.; Takahashi, S.; Wilson, A.; Abboud, K. A.; Wernsdorfer, W.; Hill, S.; Christou, G., *Inorg. Chem.* **2008,** *47*, 9459-9470.

61. Schelter, E. J.; Karadas, F.; Avendano, C.; Prosvirin, A. V.; Wernsdorfer, W.; Dunbar, K. R., *J. Am. Chem. Soc.* **2007,** *129*, 8139-8149.

62. Berlinguette, C. P.; Vaughn, D.; Canada-Vilalta, C.; Galan-Mascaros, J. R.; Dunbar, K. R., *Angew. Chem., Int. Ed.* **2003,** *42*, 1523-1526.

63. Sessoli, R.; Tsai, H. L.; Schake, A. R.; Wang, S.; Vincent, J. B.; Folting, K.; Gatteschi, D.; Christou, G.; Hendrickson, D. N., *J. Am. Chem. Soc.* **1993,** *115*, 1804-1816.

64. Bagai, R.; Christou, G., *Chem. Soc. Rev.* **2009,** *38*, 1011-1026.

65. Freedman, D. E.; Jenkins, D. M.; Iavarone, A. T.; Long, J. R., *J. Am. Chem. Soc.* **2008,** *130*, 2884-2885.

66. Kim, J.; Han, S.; Lim, J. M.; Choi, K. Y.; Nojiri, H.; Suh, B. J., *Inorg. Chim. Acta* **2007,** *360*, 2647-2652.

67. Palii, A. V.; Ostrovsky, S. M.; Klokishner, S. I.; Tsukerblat, B. S.; Schelter, E. J.; Prosvirin, A. V.; Dunbar, K. R., *Inorg. Chim. Acta* **2007,** *360*, 3915-3924.

68. Sokol, J. J.; Hee, A. G.; Long, J. R., *J. Am. Chem. Soc.* **2002,** *124*, 7656-7657.

69. Funck, K. E.; Hilfiger, M. G.; Berlinguette, C. P.; Shatruk, M.; Wernsdorfer, W.; Dunbar, K. R., *Inorg. Chem.* **2009,** *48*, 3438-3452.

70. Tasiopoulos, A. J.; Vinslava, A.; Wernsdorfer, W.; Abboud, K. A.; Christou, G., *Angew. Chem. Int. Ed.* **2004,** *43*, 2117-2121.

71. Waldmann, O., *Inorg. Chem.* **2007,** *46*, 10035-10037.

72. Ruiz, E.; Cirera, J.; Cano, J.; Alvarez, S.; Loose, C.; Kortus, J., *Chem. Commun.* **2008**, 52-54.

73. Freedman, D. E.; Bennett, M. V.; Long, J. R., *Dalton Trans.* **2006**, 2829-2834.

74. Song, Y.; Zhang, P.; Ren, X. M.; Shen, X. F.; Li, Y. Z.; You, X. Z., *J. Am. Chem. Soc.* **2005,** *127*, 3708-3709.

75. Podgajny, R.; Desplanches, C.; Sieklucka, B.; Sessoli, R.; Villar, V.; Paulsen, C.; Wernsdorfer, W.; Dromzee, Y.; Verdaguer, M., *Inorg. Chem.* **2002,** *41*, 1323-1327.

76. Larionova, J.; Gross, M.; Pilkington, M.; Andres, H.; Stoeckli-Evans, H.; Gudel, H. U.; Decurtins, S., *Angew. Chem., Int. Ed.* **2000,** *39*, 1605-1609.

77. Bonadio, F.; Gross, M.; Stoeckli-Evans, H.; Decurtins, S., *Inorg. Chem.* **2002,** *41*, 5891-5896.

78. Lim, J. H.; Yoon, J. H.; Kim, H. C.; Hong, C. S., *Angew. Chem., Int. Ed.* **2006,** *45*, 7424-7426.

79. Venkatakrishnan, T. S.; Rajamani, R.; Ramasesha, S.; Sutter, J.-P., *Inorg. Chem.* **2007,** *46*, 9569-9574.

80. Schelter, E. J.; Prosvirin, A. V.; Dunbar, K. R., *J. Am. Chem. Soc.* **2004,** *126*, 15004-15005.

81. Tsukerblat, B. S.; Palii, A. V.; Ostrovsky, S. M.; Kunitsky, S. V.; Klokishner, S. I.; Dunbar, K. R., *J. Chem. Theory Comput.* **2005,** *1*, 668-673.

82. Tregenna-Piggott, P. L. W.; Sheptyakov, D.; Keller, L.; Klokishner, S. I.; Ostrovsky, S. M.; Palii, A. V.; Reu, O. S.; Bendix, J.; Brock-Nannestad, T.; Pedersen, K.; Weihe, H.; Mutka, H., *Inorg. Chem.* **2009,** *48*, 128-137.

83. Mironov, V. S., *Dok. Phys. Chem.* **2007,** *415*, 199-204.

84. Mironov, V. S.; Chibotaru, L. F.; Ceulemans, A., *J. Am. Chem. Soc.* **2003,** *125*, 9750-9760.

85. Palii, A. V.; Ostrovsky, S. M.; Klokishner, S. I.; Tsukerblat, B. S.; Berlinguette, C. P.; Dunbar, K. R.; Galan-Mascaros, J. R., *J. Am. Chem. Soc.* **2004,** *126*, 16860-16867.

86. Palii, A. V.; Ostrovsky, S. M.; Klokishner, S. I.; Tsukerblat, B. S.; Schelter, E. J.; Prosvirin, A.; Dunbar, K. R., *Inorg. Chim. Acta* **2007,** *360*, 3915-3924.

87. Clemente-Juan, J. M.; Coronado, E.; Gaita-Arino, A.; Gimenez-Saiz, C.; Chaboussant, G.; Gudel, H. U.; Burriel, R.; Mutka, H., *Chem. Eur. J.* **2002,** *8*, 5701-5708.

88. Palii, A.; Ostrovsky, S. M.; Klokishner, S. I.; Tsukerblat, B. S.; Dunbar, K. R., *ChemPhysChem* **2006,** *7*, 871-879.

89. Herchel, R.; Boca, R.; Gembicky, M.; Kozisek, J.; Renz, F., *Inorg. Chem.* **2004,** *43*, 4103-4105.

90. Real, J. A.; Gaspar, A. B.; Munoz, M. C.; Gutlich, P.; Ksenofontov, V.; Spiering, H., *Top. Curr. Chem.* **2004,** *233*, 167-193.

91. Mathoniere, C.; Podgajny, R.; Guionneau, P.; Labrugere, C.; Sieklucka, B., *Chem.Mater.* **2005,** *17*, 442-449.

92. Li, D.; Parkin, S.; Clerac, R.; Holmes, S. M., *Inorg. Chem.* **2006,** *45*, 7569-7571.

93. Beedle, C. C.; Stephenson, C. J.; Heroux, K. J.; Wernsdorfer, W.; Hendrickson, D. N., *Inorg. Chem.* **2008,** *47*, 10798-10800.

94. Bogani, L.; Wernsdorfer, W., *Inorg. Chim. Acta* **2008,** *361*, 3807-3819.

95. Winpenny, R. E. P., *Angew. Chem. Int. Ed.* **2008,** *47*, 7992-7994.

96. Buser, H. J.; Schwarzenbach, D.; Petter, W.; Ludi, A., *Inorg. Chem.* **1977,** *16*, 2704-2710.

97. Galan-Mascaros, J. R.; Dunbar, K. R., *Angew. Chem., Int. Ed.* **2003,** *42*, 2289-2293.

98. Bellouard, F.; Clemente-Leon, M.; Coronado, E.; Galan-Mascaros, J. R.; Gomez-Garcia, C. J.; Romero, F.; Dunbar, K. R., *Eur. J. Inorg. Chem.* **2002**, 1603-1606.

99. Palii, A. V.; Ostrovsky, S. M.; Klokishner, S. I.; Reu, O. S.; Sun, Z. M.; Prosvirin, A. V.; Zhao, H. H.; Mao, J. G.; Dunbar, K. R., *J. Phys. Chem. A* **2006,** *110*, 14003-14012.

100. Van Langenberg, K.; Batten, S. R.; Berry, K. J.; Hockless, D. C. R.; Moubaraki, B.; Murray, K. S., *Inorg. Chem.* **1997,** *36*, 5006-5015.

101. Smith, J. A.; Galan-Mascaros, J. R.; Clerac, R.; Sun, J. S.; Ouyang, X.; Dunbar, K. R., *Polyhedron* **2001,** *20*, 1727-1734.

102. Hilfiger, M. G.; Shatruk, M.; Prosvirin, A.; Dunbar, K. R., *Chem. Commun.* **2008**, 5752-5754.

103. Yoon, J. H.; Lim, J. H.; Kim, H. C.; Hong, C. S., *Inorg. Chem.* **2006,** *45*, 9613-9615.

104. Lim, J. H.; Yoo, H. S.; Yoon, J. H.; Koh, E. K.; Kim, H. C.; Hong, C. S., *Polyhedron* **2008,** *27*, 299-303.

105. Sieklucka, B.; Podgajny, R.; Przychodzen, P.; Korzeniak, T., *Coord. Chem. Rev.* **2005,** *249*, 2203-2221.

106. Zhong, Z. J.; Seino, H.; Mizobe, Y.; Hidai, M.; Fujishima, A.; Ohkoshi, S. I.; Hashimoto, K., *J. Am. Chem. Soc.* **2000,** *122*, 2952-2953.

107. Ruiz, E.; Rajaraman, G.; Alvarez, S.; Gillon, B.; Stride, J.; Clerac, R.; Larionova, J.; Decurtins, S., *Angew. Chem., Int. Ed.* **2005,** *44*, 2711-2715.

108. Berlinguette, C. P.; Galan-Mascaros, J. R.; Dunbar, K. R., *Inorg. Chem.* **2003,** *42*, 3416-3422.

109. Zhang, Y. Q.; Luo, C. L., *Dalton Trans.* **2008**, 4575-4584.

110. L. D. C. Bok, J. G. L., S. S. Basson,, *Z. Anorg. Chem.* **1975,** *415*, 81-83.

111. *SMART and SAINT,Siemens Analytical X-ray Instruments Inc*, Madison,WI, 1996.

112. Sheldrick, G. M. *SADABS*, University of Gottingen, Germany, 1997.

113. Sheldrick, G. M., *Acta Cryst. Sec. A* **2008,** *64*, 112-122.

114. Barbour, L. J., *J. Supramol. Chem.* **2001,** *1*, 189-191.

115. Borras-Almenar, J. J.; Clemente-Juan, J. M.; Coronado, E.; Tsukerblat, B. S., *J. Comput. Chem.* **2001,** *22*, 985-991.

116. Chibotaru, L. F.; Mironov, V. S.; Ceulemans, A., *Angew. Chem. Int. Ed.* **2001,** *40*, 4429-4435.

117. Shores, M. P.; Sokol, J. J.; Long, J. R., *J. Am. Chem. Soc.* **2002,** *124*, 2279-2292.

118. Hilfiger, M. G.; Zhao, H. H.; Prosvirin, A.; Wernsdorfer, W.; Dunbar, K. R., *Dalton Trans.* **2009**, 5155-5163.

119. Gillon, B.; Larionova, J.; Ruiz, E.; Nau, Q.; Goujon, A.; Bonadio, F.; Decurtins, S., *Inorg. Chim. Acta* **2008,** *361*, 3609-3615.

120. Krause, R. A.; Violette, C., *Inorg. Chim. Acta* **1986,** *113*, 161-162.

121. Bendix, J.; Steenberg, P.; Sotofte, I., *Inorg. Chem.* **2003,** *42*, 4510-4512.

122. Albores, P.; Slep, L. D.; Baraldo, L. M.; Baggio, R.; Garland, M. T.; Rentschler, E., *Inorg. Chem.* **2006,** *45*, 2361-2363.

123. Alexander, J. J.; Gray, H. B., *J. Am. Chem. Soc.* **1968,** *90*, 4260-4271.

124. Inoue, H.; Yanagisa.S, *J. Inorg. Nuc. Chem.* **1974,** *36*, 1409-1411.

125. Crean, F. M.; Schug, K., *Inorg. Chem.* **1984,** *23*, 853-857.

126. Cauzzi, D. A.; Mori, G.; Predieri, G.; Tiripicchio, A.; Cavatorta, F., *Inorg. Chim. Acta* **1993,** *204*, 181-187.

127. Eller, S.; Fischer, R. D., *Inorg. Chem.* **1990,** *29*, 1289-1290.

128. Alexande.Jj; Gray, H. B., *J. Am. Chem. Soc.* **1968,** *90*, 4260-4272.

129. Palii, A. V.; Reu, O. S.; Ostrovsky, S. M.; Klokishner, S. I.; Tsukerblat, B. S.; Hilfiger, M.; Shatruk, M.; Prosvirin, A.; Dunbar, K. R., *J. Phys. Chem. A* **2009,** *113*, 6886-6890.

130. Li, D.; Parkin, S.; Wang, G.; Yee, G. T.; Clerac, R.; Wernsdorfer, W.; Holmes, S. M., *J. Am. Chem. Soc.* **2006,** *128*, 4214-4215.

131. Raghunathan, R.; Ramasesha, S.; Mathoniere, C.; Marvaud, V., *Phys.Rev.B: Condens.Matter Mater.Phys.* **2006,** *73*, 045131/1-045131/7.

132. Ohkoshi, S.; Hamada, Y.; Matsuda, T.; Tsunobuchi, Y.; Tokoro, H., *Chem. Mater.* **2008,** *20*, 3048-3054.

133. Castro, M.; Rodriguez-Velamazan, J. A.; Boukheddaden, K.; Varret, F.; Tokoro, H.; Ohkoshi, S., *EPL,* **2007,** *79,* 27007p1-27007p6.

134. Park, J. H.; Frye, F.; Anderson, N. E.; Pajerowski, D. M.; Huh, Y. D.; Talham, D. R.; Meisel, M. W., *J. Magn. Magn. Mater.* **2007,** *310*, 1458-1459.

135. Guionneau, P.; Marchivie, M.; Bravic, G.; Letard, J. F.; Chasseau, D., *Top. Curr. Chem.* **2004,** *234*, 97-128.

136. Ruiz, E.; Rodriguez-Fortea, A.; Alvarez, S.; Verdaguer, M., *Chem.--Eur.J.* **2005,** *11*, 2135-2144.

137. Beauvais, L. G.; Long, J. R., *J. Am. Chem. Soc.* **2002,** *124*, 2110-2111.

138. Nelson, K. J.; Miller, J. S., *Inorg. Chem.* **2008,** *47*, 2526-2533.

139. Robin, M. B., *Inorg. Chem.* **1962,** *1*, 337-342.

140. Behera, J. N.; Dâ€™Alessandro, D. M.; Soheilnia, N.; Long, J. R., *Chem. Mater.* **2009,** *21*, 1922-1926.

141. Neel, L., *Annales de Physique* **1948,** *3*, 137-198.

142. Juszczyk, S.; Johansson, C.; Hanson, M.; Ratuszna, A.; Malecki, G., *J. Phys. Cond. Mat.* **1994,** *06*, 5707-5716.

143. Wojdel, J. C., *J. Mol. Mod.* **2009,** *15*, 567-572.

144. Mironov, V. S., *Dok. Phys. Chem.* **2006,** *408*, 130-136.

145. Dagotto, E., *Science* **2005,** *309*, 257-262.

146. Wolf, S. A.; Awschalom, D. D.; Buhrman, R. A.; Daughton, J. M.; von Molnar, S.; Roukes, M. L.; Chtchelkanova, A. Y.; Treger, D. M., *Science* **2001,** *294*, 1488-1495.

147. Zutic, I.; Fabian, J.; Das Sarma, S., *Reviews of Modern Physics* **2004,** *76*, 323-410.

APPENDIX A

PHYSICAL METHODS

Infrared Spectroscopy

Infrared (IR) spectra were measured as Nujol mulls between KBr plates on a Nicolet 740 Fourier transform IR spectrometer. Solution IR spectra were collected by evaporating the desired compound onto a KBr plate.

Magnetic Susceptibility Measurements

Magnetic susceptibility and magnetization measurements were carried out with a Quantum Design SQUID magnetometer MPMS-XL. DC magnetic measurements were performed with an applied field of 1000 G in the 2 - 300 K temperature range. AC magnetic susceptibility measurements were performed in a 3 Oe AC field at a operating frequencies in the 1-1500 Hz range. Magnetization data were collected in the 0-7 T range starting at zero field at 2 K and were corrected for the diamagnetic contributions calculated from the Pascal constants. Unless otherwise noted, all magnetic data in this dissertation were collected on crushed single crystals which were structurally confirmed by unit cell determination. Samples were placed into plastic bags and rolled into a cylindrical shape and placed into a plastic tube for measurements. The diagmagnetic background of the sample holder is subtracted from previously measurements on the empty bags.

^{57}Fe Mössbauer Spectroscopy

Mössbauer spectra were collected on constant acceleration instruments using cryostats that allowed the sample temperature to be varied between 1.5 and 300 K in external fields up to 7 T (Carnegie Mellon University). Spectral simulations were generated using WMOSS (WEB Research, Edina, MN), and isomeric shifts were reported relative to an Fe metal standard at room temperature. Samples of freshly prepared crystals were placed in a Teflon® Mossbauer cup, sealed tightly and sent over dry ice for measurement. At Carnegie Mellon University, the samples are stored under liquid N2 when measurements are not being performed.

Single Crystal X-Ray Crystallography

In a typical experiment, the crystal selected for study was suspended in paraffin oil and mounted on a cryoloop which was placed in an N_2 cold stream. Single crystal X-ray data were collected on a Bruker APEX diffractometer equipped with a CCD detector at 110 K (Table 1). The data sets were recorded as ω-scans at a 0.3° step width and integrated with the Bruker SAINT[111] software package. The absorption correction (SADABS[112]) was based on fitting a function to the empirical transmission surface as sampled by multiple equivalent measurements. Solution and refinement of the crystal structures were carried out using the SHELX[113] suite of programs and the graphical interface X-SEED.[114] All the structures were solved by direct methods which resolved the positions of all the metal atoms and most of the C and N atoms. The remaining non-hydrogen atoms were located by alternating cycles of least squares refinements and difference Fourier maps. Hydrogen atoms were placed at calculated positions, with the

exception of some water molecules, for which the hydrogen atoms were located from the difference Fourier maps. Whenever disordered solvent molecules were present in a structure, their bond distances were restrained to chemically meaningful values. The final refinement was carried out with anisotropic thermal parameters for all non-hydrogen atoms, except for the non-hydrogen atoms of the disordered solvent molecules which were refined isotropically.

Powder X-ray Diffraction

All samples were collected on a holder composed of a single silicon crystal to minimize background interference on a Bruker D8 Advance X-ray diffractometer with LynxEye detector using Cu K-α radiation. Samples were ground and gently pressed onto the surface and the data were collected from 5 – 55° in 2θ at room temperature.

APPENDIX B

POWDER DIFFRACTION OF PB ANALOGS

Indexing and Fitting analysis courtesy of Dr.Bhuvanesh

$Ni_3[Os(CN)_6]_2 \cdot 20H_2O \cdot MeOH$

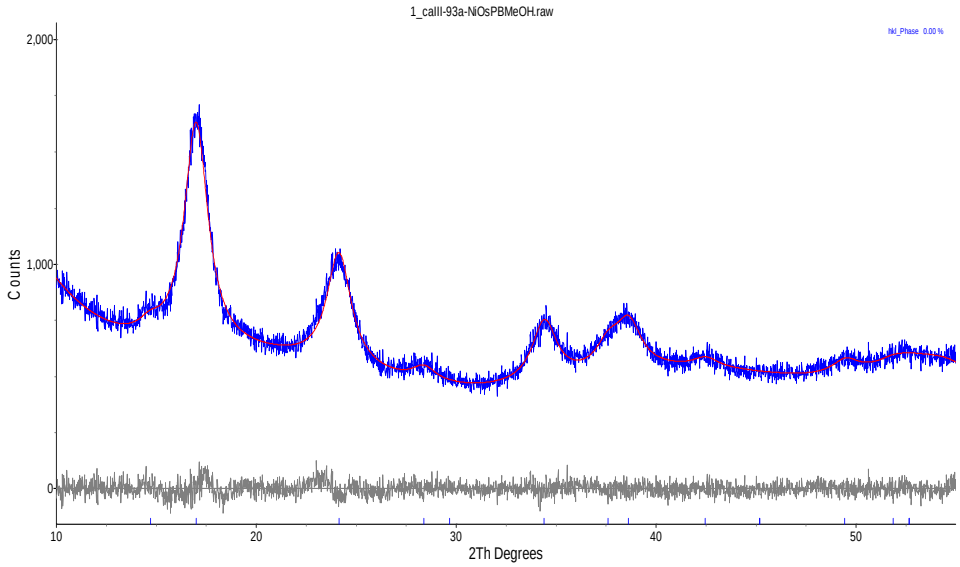

Analysis Report

Data Files

Data file 1 :
F:\Bhuv_F\Powder\Dunbar\2009_09_08_Matt_Hilfiger_PrussianBlue\prussian blue raw files\1_caIII-93a-NiOsPBMeOH.raw

Global R-Values

Rexp : 3.85 Rwp : 4.19 Rp : 3.32 GOF : 1.09
Rexp`: 15.45 Rwp`: 16.78 Rp` : 17.38 DW : 1.66

Quantitative Analysis - Rietveld

Phase 1 : hkl_Phase 0.000 %

Background

One on X		164.1174
Chebychev polynomial, Coefficient	0	583.4743
	1	-102.1657
	2	122.5122
	3	-42.39992
	4	16.3213
	5	-9.060725
	6	23.55685
	7	-21.89018
	8	-14.92695

Instrument

Primary radius (mm)	250
Secondary radius (mm)	250
Linear PSD 2Th angular range (°)	3.3
FDS angle (°)	1
Full Axial Convolution	
Filament length (mm)	12
Sample length (mm)	15
Receiving Slit length (mm)	12
Primary Sollers (°)	2.3
Secondary Sollers (°)	2.3

Corrections

Specimen displacement	-0.1459438
LP Factor	0

Miscellaneous

Start X	10

hkl Phase - 1 Pawley method

Phase name	hkl_Phase
R-Bragg	26.019
Spacegroup	Fm-3m
Cell Mass	0.000
Cell Volume (Å^3)	1140.72981
Wt% - Rietveld	0.000
Crystallite Size	
Cry size Lorentzian (nm)	6.2
Lattice parameters	
a (Å)	10.4486680

h	k	l	m	d	Th2	I
1	1	1	8	6.03254	14.67231	1.2
0	0	2	6	5.22433	16.95769	26
0	2	2	12	3.69416	24.07100	27.3
3	1	1	24	3.15039	28.30559	5.19
2	2	2	8	3.01627	29.59232	0.32
0	0	4	6	2.61217	34.30170	32.2
3	3	1	24	2.39709	37.48885	14.8
0	4	2	24	2.33639	38.50057	32.1
4	2	2	24	2.13283	42.34330	7.97
5	1	1	24	2.01085	45.04812	0.00781
3	3	3	8	2.01085	45.04812	0.00781
0	4	4	12	1.84708	49.29511	17.8
5	3	1	48	1.76615	51.71647	6.89
0	0	6	6	1.74144	52.50563	2.59
4	4	2	24	1.74144	52.50563	2.59

$Ni_3[Os(CN)_6]_2 \cdot 20H_2O \cdot 2MeCN$

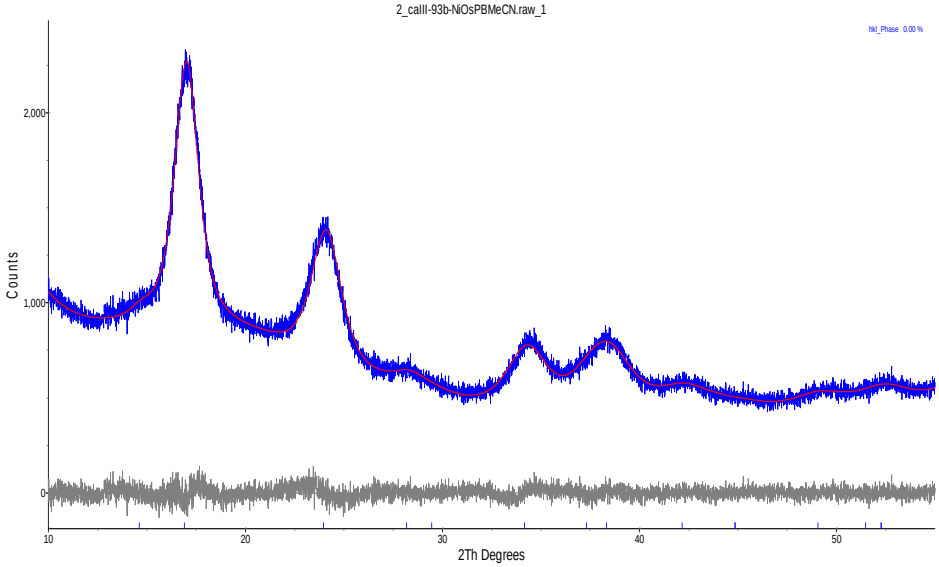

Analysis Report

Data Files

Data file 1 :
F:\Bhuv_F\Powder\Dunbar\2009_09_08_Matt_Hilfiger_PrussianBlue\prussian blue raw files\2_caIII-93b-NiOsPBMeCN.raw_1

Global R-Values

Rexp : 3.59	Rwp : 3.94	Rp : 3.12	GOF : 1.10
Rexp` : 11.15	Rwp` : 12.23	Rp` : 10.90	DW : 1.69

Quantitative Analysis - Rietveld

Phase 1 : hkl_Phase		0.000 %

Background

One on X		1008.764
Chebychev polynomial, Coefficient	0	584.8813
	1	-244.1442
	2	100.0918
	3	22.34046
	4	-16.45962
	5	12.84476
	6	46.56714
	7	-15.75756
	8	2.951002

Instrument

Primary radius (mm)	250
Secondary radius (mm)	250
Linear PSD 2Th angular range (°)	3.3
FDS angle (°)	1
Full Axial Convolution	
Filament length (mm)	12
Sample length (mm)	15
Receiving Slit length (mm)	12
Primary Sollers (°)	2.3
Secondary Sollers (°)	2.3

Corrections

Specimen displacement	-0.3100853
LP Factor	0

Miscellaneous

Start X	10

hkl Phase - 1 Pawley method

Phase name	hkl_Phase
R-Bragg	28.475
Spacegroup	Fm-3m
Cell Mass	0.000
Cell Volume (Å^3)	1155.37120
Wt% - Rietveld	0.000
Crystallite Size	
Cry size Lorentzian (nm)	10.4
Strain	
Strain L	1.324279
Strain G	4.918021
e0	1.41685
Lattice parameters	
a (Å)	10.4931814

h	k	l	m	d	Th2	I
1	1	1	8	6.05824	14.60972	0.815
0	0	2	6	5.24659	16.88523	31.8
0	2	2	12	3.70990	23.96736	39.4
3	1	1	24	3.16381	28.18303	6.93
2	2	2	8	3.02912	29.46393	2.22
0	0	4	6	2.62330	34.15171	46
3	3	1	24	2.40730	37.32393	19.6
0	4	2	24	2.34635	38.33086	52.5
4	2	2	24	2.14191	42.15508	22.5
5	1	1	24	2.01941	44.84660	3.1
3	3	3	8	2.01941	44.84660	3.1
0	4	4	12	1.85495	49.07216	46.4
5	3	1	48	1.77367	51.48098	1.17
0	0	6	6	1.74886	52.26600	40
4	4	2	24	1.74886	52.26600	40

$PPN_{0.2}Ni_{2.9}[Ru(CN)_6]_2 \cdot 16H_2O \cdot 2MeOH$

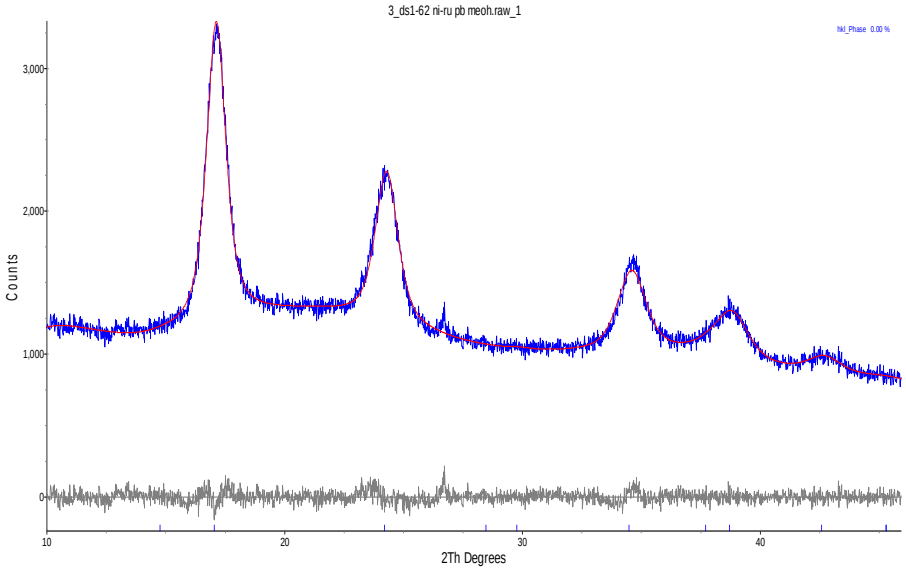

Analysis Report

Data Files

Data file 1 :
F:\Bhuv_F\Powder\Dunbar\2009_09_08_Matt_Hilfiger_PrussianBlue\prussian blue raw files\3_ds1-62 ni-ru pb meoh.raw_1

Global R-Values

Rexp : 2.80	Rwp : 3.10	Rp : 2.45	GOF : 1.11
Rexp`: 8.30	Rwp`: 9.20	Rp` : 8.03	DW : 1.62

Quantitative Analysis - Rietveld

Phase 1 : hkl_Phase		0.000 %

Background

One on X		4792.286
Chebychev polynomial, Coefficient	0	834.2949
	1	-22.47659
	2	-127.2512
	3	44.29494
	4	-3.752332
	5	-32.07196
	6	35.7891
	7	17.91366

	8	-29.62914

Instrument

Primary radius (mm)	250
Secondary radius (mm)	250
Linear PSD 2Th angular range (°)	3.3
FDS angle (°)	1
Full Axial Convolution	
Filament length (mm)	12
Sample length (mm)	15
Receiving Slit length (mm)	12
Primary Sollers (°)	2.3
Secondary Sollers (°)	2.3

Corrections

Specimen displacement	-0.2025734
LP Factor	0

Miscellaneous

Start X	10

hkl Phase - 1 Pawley method

Phase name	hkl_Phase
R-Bragg	25.156
Spacegroup	Fm-3m
Cell Mass	0.000
Cell Volume (Å^3)	1122.72454
Wt% - Rietveld	0.000
Crystallite Size	
Cry size Lorentzian (nm)	12.3
Strain	
Strain L	0.0003228485
Strain G	3.013291
e0	0.75337
Lattice parameters	
a (Å)	10.3934023

h	k	l	m	d	Th2	I
1	1	1	8	6.00063	14.75076	0.0967
0	0	2	6	5.19670	17.04853	33.5
0	2	2	12	3.67462	24.20092	39
3	1	1	24	3.13373	28.45927	0.0391
2	2	2	8	3.00032	29.75329	0.846
0	0	4	6	2.59835	34.48980	51.3
3	3	1	24	2.38441	37.69568	5.79
0	4	2	24	2.32404	38.71343	39.3
4	2	2	24	2.12154	42.57938	20.1
5	1	1	24	2.00021	45.30093	0.0313
3	3	3	8	2.00021	45.30093	0.0313

$Mn_3[Os(CN)_6]_2 \cdot 18H_2O$

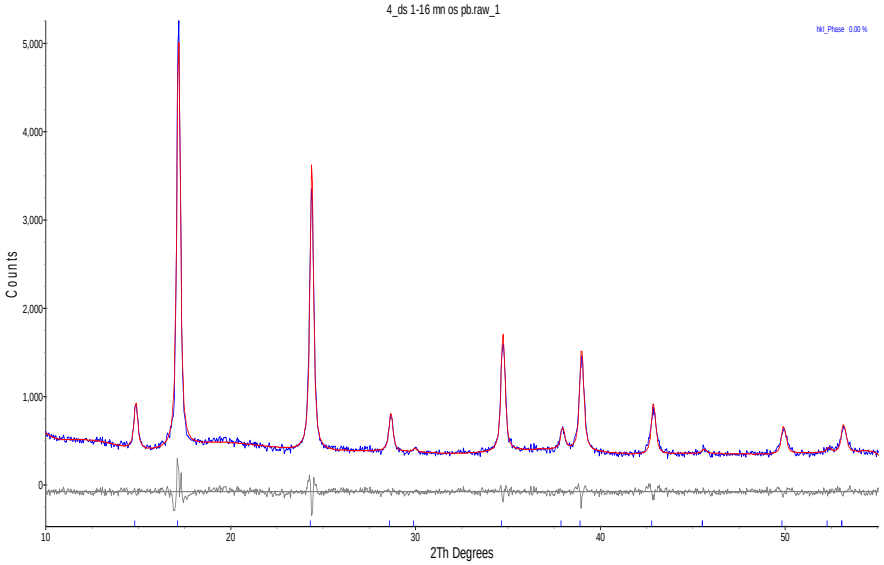

Analysis Report

Data Files

Data file 1 :
F:\Bhuv_F\Powder\Dunbar\2009_09_08_Matt_Hilfiger_PrussianBlue\prussian blue raw files\4_ds 1-16 mn os pb.raw_1

Global R-Values

Rexp : 4.40	Rwp : 5.93	Rp : 4.70	GOF : 1.35
Rexp` : 12.38	Rwp` : 16.68	Rp` : 21.20	DW : 1.29

Quantitative Analysis - Rietveld

Phase 1 : hkl_Phase 0.000 %

Background

Chebychev polynomial, Coefficient	0	412.4902
	1	-75.68565
	2	38.90756
	3	-14.11265
	4	14.09953
	5	-9.510432
	6	9.643042
	7	-13.94276
	8	-6.4397
	9	10.13489
	10	-6.687668
	11	-6.565882

12	4.387571
13	-13.18502
14	10.82359
15	-2.929157
16	-10.09343

Instrument

Primary radius (mm)	250
Secondary radius (mm)	250
Linear PSD 2Th angular range (°)	3.3
FDS angle (°)	1
Full Axial Convolution	
Filament length (mm)	12
Sample length (mm)	15
Receiving Slit length (mm)	12
Primary Sollers (°)	2.3
Secondary Sollers (°)	2.3

Corrections

Specimen displacement	-0.1628275
LP Factor	0

Miscellaneous

Start X	10

hkl Phase - 1 Pawley method

Phase name	hkl_Phase
R-Bragg	61.692
Spacegroup	Fm-3m
Cell Mass	0.000
Cell Volume (Å^3)	1107.63392
Wt% - Rietveld	0.000
Crystallite Size	
Cry size Lorentzian (nm)	52.7
Lattice parameters	
a (Å)	10.3466260

h	k	l	m	d	Th2	I
1	1	1	8	5.97363	14.81782	1.56
0	0	2	6	5.17331	17.12618	18.2
0	2	2	12	3.65808	24.31200	26.4
3	1	1	24	3.11963	28.59066	5.1
2	2	2	8	2.98681	29.89093	0.501
0	0	4	6	2.58666	34.65064	24.7
3	3	1	24	2.37368	37.87257	5.6
0	4	2	24	2.31358	38.89548	28.7
4	2	2	24	2.11200	42.78133	18.2
5	1	1	24	1.99121	45.51720	0.934
3	3	3	8	1.99121	45.51720	0.934
0	4	4	12	1.82904	49.81421	14.9
5	3	1	48	1.74890	52.26486	2.89
0	0	6	6	1.72444	53.06369	9.23
4	4	2	24	1.72444	53.06369	9.23

$Ni_3[Ru(CN)_6]_2 \cdot 20H_2O \cdot 2MeOH$

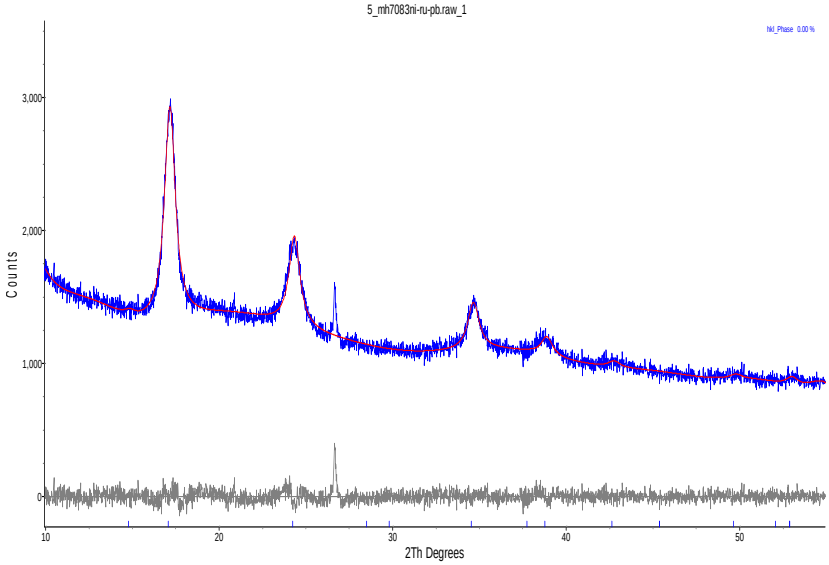

Analysis Report

Data Files

Data file 1 :
F:\Bhuv_F\Powder\Dunbar\2009_09_08_Matt_Hilfiger_PrussianBlue\prussian blue raw files\5_mh7083ni-ru-pb.raw_1

Global R-Values

Rexp : 2.85	Rwp : 3.43	Rp : 2.63	GOF : 1.20
Rexp`: 21.75	Rwp`: 26.15	Rp` : 34.96	DW : 1.49

Quantitative Analysis - Rietveld

Phase 1 : hkl_Phase		0.000 %

Background

Chebychev polynomial, Coefficient	0	1156.877
	1	-361.219
	2	55.1113
	3	-27.05582
	4	33.62465
	5	-21.768
	6	33.59256
	7	-16.51916
	8	-9.952398
	9	22.72157
	10	2.325728
	11	-15.24436
	12	8.294374
	13	-5.892254
	14	2.685722

15	-5.20991
16	-7.892924

Instrument

Primary radius (mm)	250
Secondary radius (mm)	250
Linear PSD 2Th angular range (°)	3.3
FDS angle (°)	1
Full Axial Convolution	
Filament length (mm)	12
Sample length (mm)	15
Receiving Slit length (mm)	12
Primary Sollers (°)	2.3
Secondary Sollers (°)	2.3

Corrections

Specimen displacement	-0.2388603
LP Factor	0

Miscellaneous

Start X	10

hkl Phase - 1 Pawley method

Phase name	hkl_Phase
R-Bragg	14.748
Spacegroup	Fm-3m
Cell Mass	0.000
Cell Volume (Å^3)	1118.28455
Wt% - Rietveld	0.000
Crystallite Size	
Cry size Lorentzian (nm)	12.2
Lattice parameters	
a (Å)	10.3796834

h	k	l	m	d	Th2	I
1	1	1	8	5.99271	14.77036	0.329
0	0	2	6	5.18984	17.07123	21.7
0	2	2	12	3.66977	24.23339	19
3	1	1	24	3.12959	28.49768	0.0313
2	2	2	8	2.99636	29.79353	0.0313
0	0	4	6	2.59492	34.53681	21.7
3	3	1	24	2.38126	37.74739	0.351
0	4	2	24	2.32097	38.76664	11.6
4	2	2	24	2.11874	42.63841	4.67
5	1	1	24	1.99757	45.36414	0.0313
3	3	3	8	1.99757	45.36414	0.0313
0	4	4	12	1.83489	49.64480	4.74
5	3	1	48	1.75449	52.08588	0.586
0	0	6	6	1.72995	52.88155	5.94
4	4	2	24	1.72995	52.88155	5.94

$Mn_3[Ru(CN)_6]_2 \cdot 22H_2O \cdot MeOH$

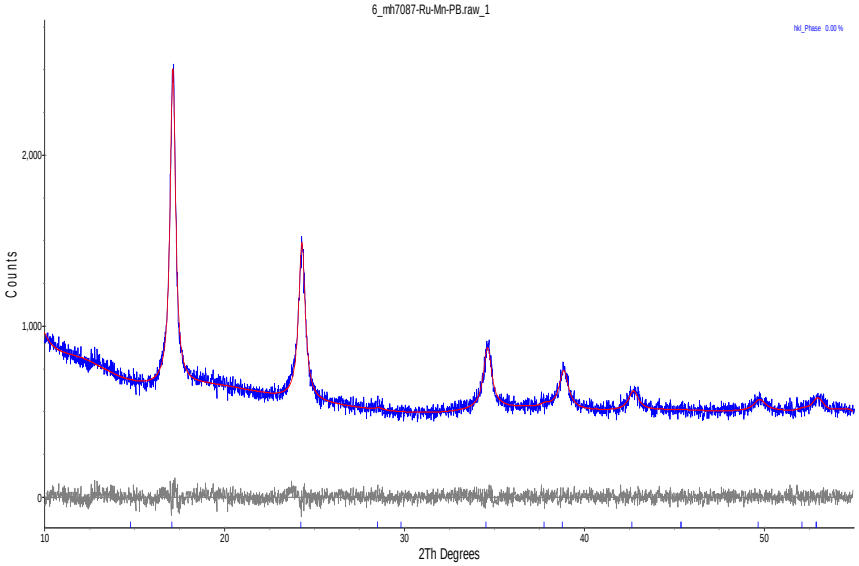

Analysis Report

Data Files

Data file 1 :
F:\Bhuv_F\Powder\Dunbar\2009_09_08_Matt_Hilfiger_PrussianBlue\prussian blue raw files\6_mh7087-Ru-Mn-PB.raw_1

Global R-Values

Rexp : 3.99	Rwp : 4.24	Rp : 3.37	GOF : 1.06
Rexp`: 21.76	Rwp`: 23.13	Rp` : 32.41	DW : 1.80

Quantitative Analysis - Rietveld

Phase 1 : hkl_Phase 0.000 %

Background

Chebychev polynomial, Coefficient	0	597.6695
	1	-164.1201
	2	94.83751
	3	-42.07856
	4	14.49006
	5	-8.736563
	6	18.04265
	7	-8.544789
	8	-0.9176945
	9	9.441099
	10	-1.552613
	11	-5.626745
	12	3.615344
	13	-6.943583
	14	4.764669

15	-6.40491
16	-2.794345

Instrument

Primary radius (mm)	250
Secondary radius (mm)	250
Linear PSD 2Th angular range (°)	3.3
FDS angle (°)	1
Full Axial Convolution	
Filament length (mm)	12
Sample length (mm)	15
Receiving Slit length (mm)	12
Primary Sollers (°)	2.3
Secondary Sollers (°)	2.3

Corrections

Specimen displacement	-0.1429099
LP Factor	0

Miscellaneous

Start X	10

hkl Phase - 1 Pawley method

Phase name	hkl_Phase
R-Bragg	3.171
Spacegroup	Fm-3m
Cell Mass	0.000
Cell Volume (Å^3)	1117.90037
Wt% - Rietveld	0.000
Crystallite Size	
Cry size Lorentzian (nm)	67.4
Strain	
Strain L	1.238647
Strain G	0.000805606
e0	0.30964
Lattice parameters	
a (Å)	10.3784947

h	k	l	m	d	Th2	I
1	1	1	8	5.99203	14.77206	0.00781
0	0	2	6	5.18925	17.07320	11.5
0	2	2	12	3.66935	24.23621	14.5
3	1	1	24	3.12923	28.50101	0.289
2	2	2	8	2.99601	29.79702	0.00781
0	0	4	6	2.59462	34.54089	15.6
3	3	1	24	2.38099	37.75187	0.91
0	4	2	24	2.32070	38.77126	13.8
4	2	2	24	2.11850	42.64353	9.42
5	1	1	24	1.99734	45.36963	0.0904
3	3	3	8	1.99734	45.36963	0.0904
0	4	4	12	1.83468	49.65088	8.74
5	3	1	48	1.75429	52.09230	2.95
0	0	6	6	1.72975	52.88808	7.72

4	4	2	24	1.72975	52.88808	7.72

$Fe_3[Os(CN)_6]_2 \cdot 19H_2O$

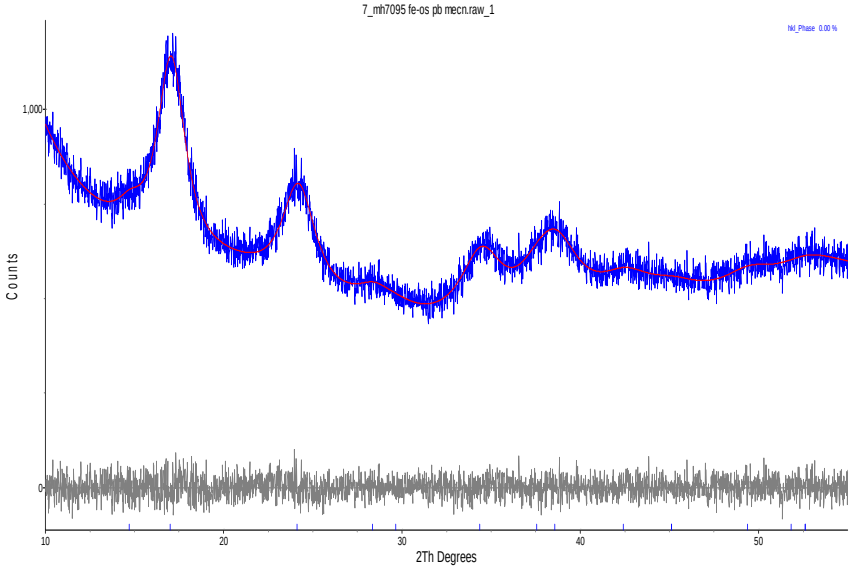

Analysis Report

Data Files

Data file 1 :
F:\Bhuv_F\Powder\Dunbar\2009_09_08_Matt_Hilfiger_PrussianBlue\prussian blue raw files\7_mh7095 fe-os pb mecn.raw_1

Global R-Values

Rexp : 3.91	Rwp : 4.07	Rp : 3.25	GOF : 1.04
Rexp`: 19.82	Rwp`: 20.65	Rp` : 19.61	DW : 1.94

Quantitative Analysis - Rietveld

Phase 1 : hkl_Phase 0.000 %

Background

Chebychev polynomial, Coefficient

0	590.3937
1	-127.3692
2	141.2592
3	-39.48018
4	15.07859
5	-11.58171
6	20.98117
7	-8.916863
8	-5.337848

Instrument

Primary radius (mm)	250
Secondary radius (mm)	250
Linear PSD 2Th angular range (°)	3.3
FDS angle (°)	1
Full Axial Convolution	
Filament length (mm)	12
Sample length (mm)	15
Receiving Slit length (mm)	12
Primary Sollers (°)	2.3
Secondary Sollers (°)	2.3

Corrections

Specimen displacement	-0.1938704
LP Factor	0

Miscellaneous

Start X	10

hkl Phase - 1 Pawley method

Phase name	hkl_Phase
R-Bragg	18.486
Spacegroup	Fm-3m
Cell Mass	0.000
Cell Volume (Å^3)	1134.98837
Wt% - Rietveld	0.000
Crystallite Size	
Cry size Lorentzian (nm)	6.8
Strain	
Strain L	2.298476
Strain G	3.871971
e0	1.31467
Lattice parameters	
a (Å)	10.4311087

h	k	l	m	d	Th2	I
1	1	1	8	6.02240	14.69714	1.24
0	0	2	6	5.21555	16.98645	15.9
0	2	2	12	3.68795	24.11212	19.7
3	1	1	24	3.14510	28.35424	5.39
2	2	2	8	3.01120	29.64327	1.99
0	0	4	6	2.60778	34.36124	32
3	3	1	24	2.39306	37.55431	15.8
0	4	2	24	2.33247	38.56794	37.6
4	2	2	24	2.12924	42.41801	18.5
5	1	1	24	2.00747	45.12813	5.87
3	3	3	8	2.00747	45.12813	5.87
0	4	4	12	1.84398	49.38364	29.5
5	3	1	48	1.76318	51.80998	0.16
0	0	6	6	1.73852	52.60079	15.8
4	4	2	24	1.73852	52.60079	15.8

$Ni_3[Ru(CN)_6]_2 \cdot 20H_2O \cdot MeCN$

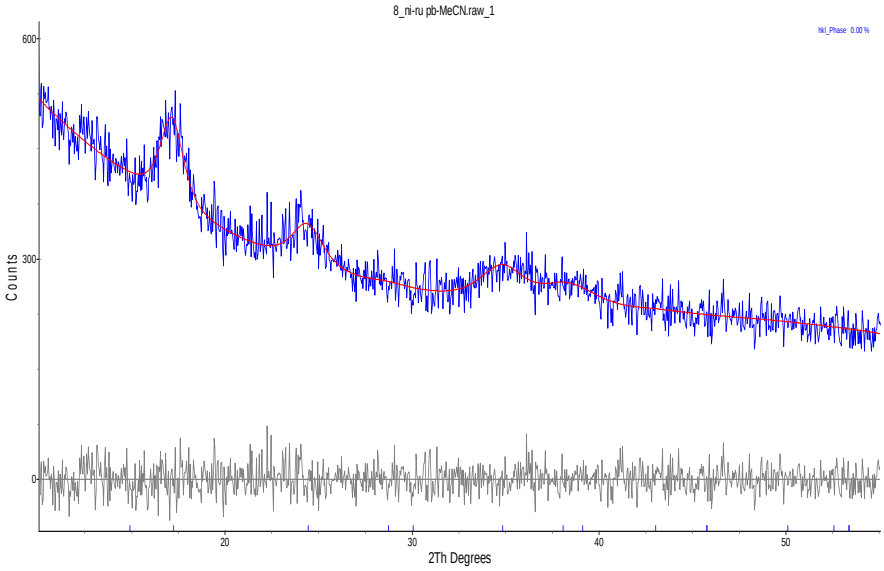

Analysis Report

Data Files

Data file 1 :
F:\Bhuv_F\Powder\Dunbar\2009_09_08_Matt_Hilfiger_PrussianBlue\prussian blue raw files\8_ni-ru pb-MeCN.raw_1

Global R-Values

Rexp : 5.72	Rwp : 6.01	Rp : 4.66	GOF : 1.05
Rexp`: 55.61	Rwp`: 58.46	Rp` : 57.56	DW : 1.90

Quantitative Analysis - Rietveld

Phase 1 : hkl_Phase	0.000 %

Background

Chebychev polynomial, Coefficient	0	300.1995
	1	-137.3514
	2	56.35056
	3	-22.27055
	4	1.351231

Instrument

Primary radius (mm)	250
Secondary radius (mm)	250
Linear PSD 2Th angular range (°)	3.3
FDS angle (°)	1
Full Axial Convolution	
Filament length (mm)	12

Sample length (mm)	15
Receiving Slit length (mm)	12
Primary Sollers (°)	2.3
Secondary Sollers (°)	2.3

Corrections

Specimen displacement	0.1142858
LP Factor	0

Miscellaneous

Start X	10

hkl Phase - 1 Pawley method

Phase name	hkl_Phase
R-Bragg	73.074
Spacegroup	Fm-3m
Cell Mass	0.000
Cell Volume (Å^3)	1090.51580
Wt% - Rietveld	0.000
Crystallite Size	
Cry size Lorentzian (nm)	25.4
Strain	
Strain L	4.989433
Strain G	4.986983
e0	2.04583
Lattice parameters	
a (Å)	10.2930477

h	k	l	m	d	Th2	I
1	1	1	8	5.94269	14.89539	0.000244
0	0	2	6	5.14652	17.21601	3.01
0	2	2	12	3.63914	24.44050	4.01
3	1	1	24	3.10347	28.74268	0.504
2	2	2	8	2.97135	30.05018	0.000244
0	0	4	6	2.57326	34.83676	9.94
3	3	1	24	2.36139	38.07728	5.83
0	4	2	24	2.30160	39.10616	3.26
4	2	2	24	2.10106	43.01507	1.21
5	1	1	24	1.98090	45.76754	0.000244
3	3	3	8	1.98090	45.76754	0.000244
0	4	4	12	1.81957	50.09133	0.000244
5	3	1	48	1.73984	52.55767	0.000244
0	0	6	6	1.71551	53.36170	0.000244
4	4	2	24	1.71551	53.36170	0.000244

$PPN_{0.6}Fe_{2.7}[Ru(CN)_6]_2 \cdot 14H_2O \cdot 2MeCN$

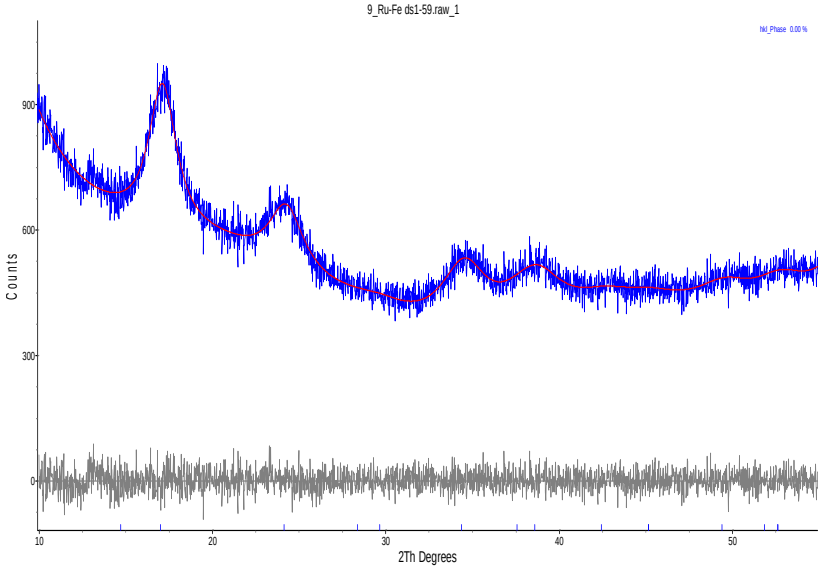

Analysis Report

Data Files

Data file 1 :
F:\Bhuv_F\Powder\Dunbar\2009_09_08_Matt_Hilfiger_PrussianBlue\prussian blue raw files\9_Ru-Fe ds1-59.raw_1

Global R-Values

Rexp : 4.21	Rwp : 4.25	Rp : 3.33	GOF : 1.01
Rexp`: 24.63	Rwp`: 24.84	Rp` : 22.81	DW : 1.95

Quantitative Analysis - Rietveld

Phase 1 : hkl_Phase	0.000 %

Background

Chebychev polynomial, Coefficient	0	515.9448
	1	-184.5291
	2	111.2625
	3	-23.59946
	4	9.822525
	5	-3.838967
	6	31.34748

Instrument

Primary radius (mm)	250
Secondary radius (mm)	250
Linear PSD 2Th angular range (°)	3.3
FDS angle (°)	1

Full Axial Convolution	
Filament length (mm)	12
Sample length (mm)	15
Receiving Slit length (mm)	12
Primary Sollers (°)	2.3
Secondary Sollers (°)	2.3

Corrections

Specimen displacement	-0.3095359
LP Factor	0

Miscellaneous

Start X	10

hkl Phase - 1 Pawley method

Phase name	hkl_Phase
R-Bragg	14.919
Spacegroup	Fm-3m
Cell Mass	0.000
Cell Volume (Å^3)	1133.86116
Wt% - Rietveld	0.000
Crystallite Size	
Cry size Lorentzian (nm)	8.3
Strain	
Strain L	4.306544
Strain G	3.686538
e0	1.62612
Lattice parameters	
a (Å)	10.4276543

h	k	l	m	d	Th2	I
1	1	1	8	6.02041	14.70204	0.0156
0	0	2	6	5.21383	16.99212	10.9
0	2	2	12	3.68673	24.12023	11.8
3	1	1	24	3.14406	28.36383	0.708
2	2	2	8	3.01020	29.65332	1.97
0	0	4	6	2.60691	34.37297	29.6
3	3	1	24	2.39227	37.56722	5.67
0	4	2	24	2.33169	38.58123	26.7
4	2	2	24	2.12854	42.43275	8.98
5	1	1	24	2.00680	45.14391	4.71
3	3	3	8	2.00680	45.14391	4.71
0	4	4	12	1.84337	49.40109	43.8
5	3	1	48	1.76260	51.82842	0.367
0	0	6	6	1.73794	52.61955	38.2
4	4	2	24	1.73794	52.61955	38.2

VITA

MATTHEW GARY HILFIGER
Development Scientist Baker Hughes
12645 West Airport Blvd Sugar Land, TX 77478
Email: matthew.hilfiger@bakerhughes.com

EDUCATION

Texas A&M University, College Station, Texas

Ph.D. *Chemistry* (2010)

Advisor: Prof. Kim R. Dunbar

Grove City College, Grove City, PA

B.S. *Chemistry* (2004)

RESEARCH EXPERIENCE

Texas A&M University, College Station, Texas

NSF-REU Participant, Department of Chemistry. (May 2003-September 2003)

Research Assistant, Department of Chemistry. (August 2004-September 2009)

Teaching Assistant, Department of Chemistry. (2004-2009)

Bariod Research and Development, Halliburton, Houston, Texas

Intern (Summer 2008)

Baker Hughes Petrolite Division, Sugarland, Texas

Scientist IV (October 2009 – Present)

NSF-GK 12 Fellow (May 2007 – May 2008)

AFFILIATIONS

Sigma Xi (2003 – Present)

American Chemical Society (2004 – Present)

Phi Lambda Upsilon Chemistry Honors Society (2006 – Present)

Society of Petroleum Engineers (2006 – Present)